

Kinetic and Mechanistic Investigation of the Atmospheric Oxidation of Selected Partially Oxygenated Hydrocarbons

Dissertation

zur Erlangung des akademischen Grades eines
Doktor der Naturwissenschaften (Dr. rer. nat.)

vorgelegt von

Jan Niklas Illmann

Bergische Universität Wuppertal
Fakultät für Mathematik und Naturwissenschaften
Physikalische und Theoretische Chemie

unter Leitung von
Prof. Dr. Peter Wiesen

Wuppertal, Februar 2022

The PhD thesis can be quoted as follows:

urn:nbn:de:hbz:468-20220420-105114-3

[<http://nbn-resolving.de/urn/resolver.pl?urn=urn%3Anbn%3Ade%3A468-20220420-105114-3>]

DOI: 10.25926/72r0-4046

[<https://doi.org/10.25926/72r0-4046>]

Erklärung

“Ich versichere, die Arbeit selbstständig verfasst zu haben, nur die in der Dissertation angegebenen Hilfsmittel benutzt und alle wörtlich oder inhaltlich übernommenen Stellen als solche gekennzeichnet zu haben.“

Wuppertal, Februar 2022

Jan Niklas Illmann

Danksagung

Ich danke allen Menschen von ganzem Herzen, die auf verschiedenste Art und Weise zur Entstehung dieser wissenschaftlichen Arbeit beigetragen und mich auf diesem Weg begleitet haben.

Zusammenfassung

In der vorliegenden Arbeit wurden die Mechanismen der OH-initiierten Oxidation von 3-Penten-2-on, 3-Methyl-3-penten-2-on und 4-Methyl-3-penten-2-on sowie die Ozonolysereaktionen für eine größere Reihe α,β -ungesättigter Ketone bestehend aus Methylvinylketon, 3-Penten-2-on, 3-Methyl-3-penten-2-on, 4-Methyl-3-penten-2-on und Ethylvinylketon untersucht. Die Experimente wurden in zwei atmosphärischen Simulationskammern der Bergischen Universität Wuppertal, Deutschland, mit einem Gesamtvolumen von 480 L bzw. 1080 L unter Verwendung von Langweg-FTIR-Spektroskopie durchgeführt. Ausgewählte Experimente wurden durch ein PTR-ToF-MS Instrument unterstützt.

Die Studien der OH-Mechanismen wurden unter Bedingungen durchgeführt, bei denen nahezu alle Peroxy-Radikale mit NO_x ($= \text{NO} + \text{NO}_2$) reagieren. Da die Netto-Bildung von Peroxyacetylnitrat (PAN) von dem NO_2/NO -Verhältnis abhängt, wobei nur ein Teil der gebildeten Acetylperoxy-Radikale in PAN konvertiert, wurde ein Summenparameter PAN + CO_2 eingeführt, um die Ausbeute von Acetylperoxy-Radikalen als Maß für das primäre PAN-Bildungspotential zu bestimmen. Daher wurden die experimentellen Bedingungen optimiert, um eine Quantifizierung von CO_2 zu ermöglichen. Damit wurde gezeigt, dass die OH-Reaktion aller untersuchten Reaktionssysteme zur direkten Bildung von Acetylperoxy-Radikalen mit molaren Ausbeuten von $56 \pm 14 \%$ für 3-Penten-2-on, $60 \pm 7 \%$ für 3-Methyl-3-penten-2-on und $24 \pm 6 \%$ für 4-Methyl-3-penten-2-on führt. Weiterhin wurde gezeigt, dass beinahe alle übrigen Reaktionsprodukte zur Bildung von Acetylperoxy-Radikalen in deren nachfolgenden Gasphasenoxidationen führen.

Die Kinetik der Ozonolysereaktionen einer Serie α,β -ungesättigter Carbonyle wurde im Hinblick auf Reaktivitätstrends analysiert. In diesem Zusammenhang wurde ein semi-quantitativer Ansatz entwickelt, in dem die Reaktionsgeschwindigkeitskonstante einer Zielverbindung in Beziehung zu der Reaktionsgeschwindigkeitskonstante einer geeigneten Grundstruktur gesetzt wird. Dieses Relativverhältnis wurde als Reaktivitätsfaktor x_r definiert und als Instrument zur Vorhersage der Geschwindigkeitskonstanten für die Ozonolysereaktionen einer Serie α,β -ungesättigter Carbonyle verwendet. Dieses Konzept ändert den aktuellen Standpunkt zum Aufbau von Struktur-Aktivitäts-Beziehungen.

Die Mechanismen der Ozonolysereaktionen wurden in Gegenwart ausreichender Mengen von Kohlenstoffmonoxid (CO) durchgeführt, um die im Reaktionssystem gebildeten OH-Radikale abzufangen. Um die Ausbeute stabilisierter Criegee Intermediate

(sCl) abzuschätzen und deren Sekundärchemie zu unterdrücken, wurde eine Reihe von Experimenten durchgeführt, in denen SO_2 der Reaktionsmischung zugegeben wurde. In diesem Zusammenhang wurde beobachtet, dass alle untersuchten Ketone organische Säuren bilden, wobei die Summe der molaren Ausbeuten organischer Säuren bis zu 50 % des konsumierten Ketons entsprachen. Mögliche Bildungsmechanismen basierend auf dem experimentellen Nachweis werden für alle untersuchten Reaktionssysteme diskutiert.

Abstract

In the present work the mechanisms of the OH-initiated oxidation of 3-penten-2-one, 3-methyl-3-penten-2-one, and 4-methyl-3-penten-2-one as well as the ozonolysis reactions for a larger series of α,β -unsaturated ketones comprising methyl vinyl ketone, 3-penten-2-one, 3-methyl-3-penten-2-one, 4-methyl-3-penten-2-one, and ethyl vinyl ketone have been studied. The experiments were performed in two atmospheric simulation chambers at the University of Wuppertal, Germany, with a total volume of 480 L and 1080 L, respectively, using long-path FTIR spectroscopy. Selected experiments were supported by a PTR-ToF-MS instrument.

The studies regarding the OH-mechanism were conducted under conditions, where virtually all peroxy radicals react with NO_x ($= \text{NO} + \text{NO}_2$). Since the net peroxyacetyl nitrate (PAN) formation depends on the NO_2/NO ratio, where only a fraction of the formed acetyl peroxy radicals converts into PAN, a sum parameter PAN + CO_2 was introduced in order to determine the yield of acetyl peroxy radicals as a measure of the first-generation PAN forming potential. Therefore, the experimental conditions were optimized to allow the quantification of CO_2 . Accordingly, it was found that for all investigated systems the OH reaction generated directly the formation of acetyl peroxy radicals with molar yields of $56 \pm 14 \%$ for 3-penten-2-one, $60 \pm 7 \%$ for 3-methyl-3-penten-2-one, and $24 \pm 6 \%$ for 4-methyl-3-penten-2-one, respectively. Further, it is demonstrated that nearly all other reaction products form also acetyl peroxy radicals in their further gas-phase oxidation.

The kinetics of the ozonolysis reaction for a series of α,β -unsaturated carbonyls was analysed in terms of reactivity trends. In this respect, a semi-quantitative approach is designed for which the rate coefficient of the target species is related to the rate coefficient of a suitable core structure. This relative ratio was defined as a reactivity factor x_r and used as a tool to predict ozonolysis rate coefficients for a series of α,β -unsaturated carbonyls. This concept amends the current point of view used to build structure-activity relationships models.

The mechanisms of the ozonolysis reactions were investigated in the presence of sufficient amounts of carbon monoxide (CO) to scavenge OH radicals formed in the reaction system. In order to estimate the stabilized Criegee intermediate (sCI) yield and to suppress their secondary reactions, a number of experiments were performed, where SO_2 was added to the reaction mixture. In this respect, it was observed that all investigated ketones form organic acids where the sum of the molar yields of acids formed accounts for up to

50 % of the ketone consumption. Possible formation mechanisms evolving from the experimental evidence are discussed for all explored reaction systems.

Contents

1	Introduction	19
2	Gas-phase oxidation processes in the troposphere	23
2.1	Mechanisms of the OH-initiated oxidation	23
2.2	Mechanisms of ozonolysis reactions	28
3	Gas-phase reactivity of α,β-unsaturated carbonyls towards ozone	33
3.1	Abstract	33
3.2	Introduction	33
3.3	Experimental	36
3.3.1	Materials	36
3.4	Results and discussion	37
3.4.1	Rate coefficients	37
3.4.2	Reactivity trends	42
3.4.3	Dependence of x_r on the alkyl chain length	49
3.4.4	Structure-activity relations	53
3.5	Conclusions	57
4	Atmospheric oxidation of α,β-unsaturated ketones: kinetics and mechanism of the OH radical reaction	59
4.1	Abstract	59
4.2	Introduction	59
4.3	Experimental	61
4.3.1	1080 L chamber	62
4.3.2	480 L chamber	62
4.3.3	Materials	63
4.3.4	Experimental protocol	64
4.3.5	Relative rate method	65
4.3.6	Product identification and quantification	65
4.3.7	Modelling	66
4.4	Results and discussion	68
4.4.1	Kinetic study	68
4.4.1.1	Reactivity	70
4.4.2	Infrared cross sections	72
4.4.3	Product study of the OH reaction	74
4.4.3.1	3-Methyl-3-penten-2-one + OH	74
4.4.3.2	4-Methyl-3-penten-2-one + OH	77
4.4.3.3	Product yields correction and further oxidation processes	80
4.4.3.4	ROONO ₂ formation	85
4.4.3.5	RONO ₂ formation	87
4.4.4	Atmospheric implication and conclusions	88

5	Biomass burning plume chemistry: OH-radical initiated oxidation of 3-penten-2-one and its main oxidation product 2-hydroxypropanal	91
5.1	Abstract	91
5.2	Introduction	91
5.3	Experimental	93
5.3.1	480 L chamber	93
5.3.2	1080 L chamber	93
5.3.3	Methods	94
5.3.4	Materials	96
5.4	Results and discussion	96
5.4.1	3-Penten-2-one + OH kinetics	96
5.4.2	In situ generation of 2-hydroxypropanal	97
5.4.3	3-Penten-2-one + OH mechanism	99
5.4.4	2-Hydroxypropanal + OH and modelling	104
5.5	Atmospheric implication and conclusion	113
6	Formation of organic acids in the ozonolysis of α,β-unsaturated ketones exemplified by the case study of ethyl vinyl ketone + ozone	117
6.1	Introduction	117
6.2	Experimental	119
6.2.1	EVK + O ₃	119
6.2.2	In situ generation of peracids	120
6.3	Results and discussion	121
6.3.1	In situ generation of peracids	121
6.3.2	Primary carbonyls and sCl yield	124
6.3.3	HC(O)OH and HC(O)OC(O)H formation	130
6.3.4	Fate of the carbonyl-substituted Cl	132
6.4	Conclusion	140
7	Ozonolysis of α,β-unsaturated ketones: 3-alken-2-ones	143
7.1	Introduction	143
7.2	Experimental	143
7.3	Results and discussion	144
7.3.1	Primary carbonyls and sCl yield	144
7.3.2	Main fate of the Criegee Intermediates	148
7.3.2.1	4-Methyl-3-penten-2-one	151
7.3.2.2	Methyl vinyl ketone	162
7.3.2.3	3-Penten-2-one	169
7.3.2.4	3-Methyl-3-penten-2-one	176
7.4	Conclusion	188
8	Summary and outlook	191
9	Annex	195
9.1	Supplementary information to Chapter 4	195

9.2	Supplementary information to Chapter 5	202
9.3	Further supplementary material	205
References		207

List of Figures

2.1	Generalized ozonolysis mechanism	29
3.1	Relative rate plots of the ozonolysis kinetics study	40
3.2	Determination of the analogue structures of MMA and MCrot	43
3.3	Dependence of reactivity factors on the alkyl chain length	52
4.1	Relative-rate plots for the OH and Cl reaction of 3M3P2 and 4M3P2	69
4.2	Exemplary FTIR spectra of a 3M3P2 + OH product study experiment	75
4.3	Proposed mechanism for 3M3P2 + OH	76
4.4	Exemplary FTIR spectra of a 4M3P2 + OH product study experiment	78
4.5	Residual spectra of a 4M3P2 + OH product study experiment	79
4.6	Proposed mechanism for 4M3P2 + OH	80
4.7	Experimental and simulated time profiles obtained for a 3M3P2 + OH experiment	83
4.8	Experimental and simulated time profiles obtained for a 4M3P2 + OH experiment	84
4.9	NO ₂ /NO dependence of the PAN/CO ₂ formation ratio and the PAN + CO ₂ yield	86
5.1	Relative-rate plots for 3P2 + OH	98
5.2	Formation of 2-hydroxypropanal through the ozonolysis of 3-buten-2-ol and 3-penten-2-ol	100
5.3	Yield plots of identified reaction products of 3P2 + OH	101
5.4	Proposed mechanism for 3P2 + OH	102
5.5	Residual spectra assigned to 2HPr	103
5.6	Proposed mechanism for 2HPr + OH	105
5.7	Experimental and simulated time profiles for a 3P2 & 2HPr + OH experiment	107
5.8	Experimental and simulated time profiles for a 3P2 + OH experiment	111
6.1	Reference spectra of acids and peracids	123
6.2	Proposed mechanism for EVK + O ₃	126
6.3	Residual spectra assigned to 2-oxobutanal	128
6.4	Yield plots for formic anhydride and formic acid	131
6.5	Residual and reference spectra	133
6.6	Yield plots for ethyl hydroperoxide, perpropionic acid and acetaldehyde	134
6.7	Chemistry of the propionyl peroxy and ethyl peroxy radical	135
7.1	Generic reaction scheme for the ozonolysis of α,β-unsaturated ketones	145
7.2	Yield plots for the primary carbonyls and the dicarbonyl/carbonyl ratio	147
7.3	Chemistry of the acetyl peroxy and methyl peroxy radical	150
7.4	Chemistry of the acetonyl peroxy radical	153
7.5	Residual spectra	154
7.6	Product yields depending on the [HO ₂]/[CH ₃ C(O)CH ₂ O ₂] ratio	157

7.7	Experimental and simulated time profiles of 4M3P2, hydroxyacetone, HCHO, peracetic acid, methyl hydroperoxide, and methyl glyoxal	159
7.8	Proposed mechanism for the fate of the carbonyl-substituted Cl (methyl glyoxal oxide)	161
7.9	Hypothetically possible formation of formic acetic anhydride	162
7.10	Yield plots for formic anhydride, formic acid, m/z 47, m/z 61, and m/z 73	164
7.11	Product yields depending on the $[HO_2]/[CH_3C(O)CH_2O_2]$ ratio	168
7.12	Yield plots for methyl hydroperoxide, peracetic acid, glyoxal, methane, ketene, and formic acetic anhydride	171
7.13	Fate of the <i>E</i> -CH ₃ CHOO and <i>Z</i> -CH ₃ CHOO according to available literature data	172
7.14	Proposed pathways for the further chemistry of both CH ₃ C(O)C(CH ₃)OO isomers (= BiOx)	179
7.15	Residual spectra of the 3M3P2 + O ₃ system	182
9.1	Calibration plots for acetoin, 3M3P2, 4M3P2, and HMPPr	195
9.2	Calibration plots for biacetyl	196
9.3	Subtraction procedure for 3M3P2 + OH	197
9.4	FTIR spectra of 3M3P2 and 4M3P2 in the gas-phase	198
9.5	Subtraction procedure for 4M3P2 + OH	199
9.6	Yield plots of identified reaction products of 3M3P2 + OH	200
9.7	Yield plots of identified reaction products of 4M3P2 + OH	201
9.8	Correlation between the integrated absorption band of 2HPr and its concentration	202
9.9	Non-linear plot for the formation of 2HPr from the 3P2 + OH reaction ...	203
9.10	Ratio of the obtained yields of acetaldehyde and methyl glyoxal from 3P2 + OH in dependence of the 2HPr yield used in the model	203
9.11	Sum of the obtained yields of acetaldehyde and methyl glyoxal from 2HPr + OH in dependence of the 2HPr yield used in the model	204
9.12	Obtained branching ratios k_a and k_b for the formation of acetaldehyde and methyl glyoxal from 2HPr + OH in dependence of the 2HPr yield used in the model	204
9.13	Scheme of the 1080 L chamber	205

List of Tables

3.1	General structure of α,β -unsaturated carbonyls and substitution pattern	35
3.2	Summary of results of the ozonolysis kinetics study	38
3.3	Summary of the rate coefficients of the gas-phase ozonolysis of α,β -unsaturated ketones, esters and aldehydes	44
3.4	Summary of the rate coefficients of the gas-phase ozonolysis of α,β -unsaturated acids and esters with longer <i>n</i> -alkyl chain	50
3.5	Predicted and observed rate coefficients of selected α,β -unsaturated carbonyls	54
4.1	Structures of α,β -unsaturated ketones and related literature	61
4.2	Results of the kinetic study of the OH and Cl reaction of 3M3P2 and 4M3P2	70
4.3	Integrated absorption cross sections	73
4.4	Uncorrected and corrected molar yields of the 3M3P2 + OH system	82
4.5	Uncorrected and corrected molar yields of the 4M3P2 + OH system	82
4.6	Estimated tropospheric lifetimes	89
5.1	Results of the 3P2 + OH kinetic experiments	99
5.2	Simplified reaction sequence used for the modelling of 3P2 + OH and 2HPr + OH	109
5.3	Uncorrected yields and first-generation yields obtained for 3P2 + OH	113
6.1	Quantified reaction products and assigned masses of the EVK + O ₃ reaction	125
6.2	Reaction sequence needed for the modelling of the temporal behaviour of acetaldehyde, ethyl hydroperoxide, and perpropionic acid	136
7.1	Structures of investigated Criegee intermediates	144
7.2	Yields of the primary carbonyls for MVK, 3P2, 3M3P2, and 4M3P2	146
7.3	Quantified reactions products and assigned masses of 4M3P2 + O ₃	152
7.4	Reaction sequence used for the modelling of the temporal behaviour of products accounted for the acetyl peroxy radical further chemistry	156
7.5	Quantified reactions products and assigned masses of MVK + O ₃	163
7.6	Quantified reactions products and assigned masses of 3P2 + O ₃	170
7.7	Quantified reactions products and assigned masses of 3M3P2 + O ₃	177
9.1	Parameters used for modelling of 3M3P2 + OH	201
9.2	Parameters used for modelling of 4M3P2 + OH	202

Abbreviations

BB	biomass burning
BVOC	biogenic volatile organic compound
CI	Criegee intermediate
EVK	ethyl vinyl ketone
FA	formic anhydride
FAA	formic acetic anhydride
FID	flame ionization detector
FTIR	Fourier-transform infrared
GC	gas chromatography
HOM	highly oxidized molecule
HOMO	highest occupied molecular orbital
HMP _r	2-hydroxy-2-methylpropanal
MCM	Master Chemical Mechanism
MCrot	methyl crotonate
MIBK	methyl isobutyl ketone
MMA	methyl methacrylate
MS	mass spectrometry
MTig	methyl tiglate
MVK	methyl vinyl ketone
M3M2B	methyl 3-methyl-2-butenolate
NMHC	non-methane hydrocarbon
OVOC	oxygenated volatile organic compound
PAN	peroxyacetyl nitrate
POZ	primary ozonide
SAR	structure-activity relationships
sCI	stabilized Criegee intermediate
SOZ	secondary ozonide
VOC	volatile organic compound
2HPr	2-hydroxypropanal
3B2OL	3-buten-2-ol
3M3P2	3-methyl-3-penten-2-one
3P2	3-penten-2-one

3P2OL

3-penten-2-ol

4M3P2

4-methyl-3-penten-2-one

1 Introduction

Partially oxygenated hydrocarbons are ubiquitous in the troposphere (the lower part of the atmosphere). If not emitted directly as an oxygenated volatile organic compound (OVOC), any hydrocarbon, once released into the atmosphere, undergoes an oxidative transformation, where, besides subsequent fragmentation of the molecule, oxygen will add in any case at a certain point of the oxidation process. Observing the diversity of organic species entering the troposphere, from both biogenic and anthropogenic sources, this process results necessarily in a tremendous variety of OVOCs. To give an example, Calvert et al. (2011) summarized the formation of about 65 oxygenated species originating from the oxidation of n-butane. Understanding these processes and their outcomes is crucial due to their contribution to particle and ozone formation and consequently their effects on air quality, health and climate.

Due to its high emission rate from biogenic sources (Guenther et al., 2006) isoprene is still subject of intense research, which implies also a rising interest for the consecutively formed reaction products (Wennberg et al., 2018 and references therein). According to the currently established degradation scheme for isoprene, included in the Master Chemical Mechanism (MCM), about 34 % (molar) of isoprene results in the formation of methyl vinyl ketone (MVK, 3-buten-2-one) under conditions, for which virtually all peroxy radicals react with NO, whereas even higher yields ($\approx 47\%$) are found at NO levels of about 100 pptV, present in pristine environments (Jenkin et al., 2015). It is hence not surprising that the OH-initiated oxidation of MVK was examined by several groups under a variety of experimental conditions (Tuazon and Atkinson, 1989; Grosjean et al., 1993b; Galloway et al., 2011; Praske et al., 2015; Fuchs et al., 2018). Nevertheless detailed mechanistic investigations for structural analogue ketones were missing, although they might be theoretically formed in the oxidation of any biogenic volatile organic compound (BVOC) possessing two (substituted) conjugated C=C double bonds. For instance, α,β -unsaturated ketones like 3-penten-2-one were identified in laboratory experiments representative of biomass burning (BB) emissions (Ciccioli et al., 2001; Hatch et al., 2017), which suggests their formation either from the atmospheric oxidation of BVOCs or from further processes taking place in biomass burning plumes.

In 2020 the IUPAC (International Union of Pure and Applied Chemistry) task group on atmospheric chemical kinetic data evaluation published a review article on ozonolysis reactions together with comprehensive and updated recommendations (Cox et al., 2020).

These comprise overall rate coefficients for ozonolysis reactions and mechanistic schemes as well as rate coefficients for stabilized Criegee intermediates (sCI). Yet, these data sets are limited to small alkenes and a range of monoterpenes. In the case of Criegee intermediates (CI), information is reported up to C₄ species. Data on ozonolysis reactions of multifunctional species containing at least one hetero atom (usually O atoms) are entirely missing, which suggests strongly a fundamental gap of knowledge and gives a motivation for studies such as the present one. Indeed, methyl vinyl ketone was subject of only two previous studies, which yielded at least partly contradictory results (Grosjean et al., 1993b; Ren et al., 2017). In addition, the product identification was rather limited to the primary carbonyls and the fate of the carbonyl-substituted CI was completely missing. The same applies to the homologue ethyl vinyl ketone (Grosjean et al., 1996). However, the importance of ozonolysis reactions of OVOCs appears to be largely overlooked. For instance, observing the rate coefficients for the reaction with OH (Mellouki et al., 2021) and ozone (e. g. Treacy et al., 1992; Neeb et al., 1998) together with the average concentrations of the respective atmospheric oxidants (e. g. Bloss et al., 2005), about 15–20 % of methyl vinyl ketone (MVK) are removed by O₃ rather than OH during the day, although, in principle, MVK reacts quite slowly with ozone. This implies that to date, up to 20 % of the daytime MVK loss processes are poorly characterized.

The aim of this work is to identify and close the gaps, where important information on the oxidative mechanisms of α,β -unsaturated ketones were incomplete or missing altogether, which, in turn, focused on the reactions with OH radicals and ozone.

The results and discussions of the present work are divided into two parts. Part A contains findings that were already published in peer-reviewed journals in 2021 (Illmann et al., 2021a; 2021b; 2021d), whereas part B presents the results not published to date.

In order to assess the reactivity of α,β -unsaturated carbonyls (for a broader range of compounds including also esters), firstly the kinetics of the ozonolysis reactions was determined and analysed in detail, since these offers the unique possibility to regard the C=C bond as a unit. When this work started, no easily applicable, well-predicting structure-activity relationships (SAR) were available but for the gas-phase reaction of VOCs with OH (Kwok and Atkinson, 1995; Jenkin et al., 2018a; 2018b). Jenkin et al. (2020) published structure-activity relationships for ozonolysis reactions immediately before submission of the manuscript (Illmann et al., 2021a, Chapter 3). Since the OH reaction is the dominating loss process during daytime conditions, this chapter is followed by investigations on the OH-initiated oxidation mechanisms for α,β -unsaturated ketones, where literature data were rather incomplete (4-methyl-3-penten-2-one, Gaona-Colmán et al., 2017) or not at all

existent (3-penten-2-one, 3-methyl-3-penten-2-one). In this respect, a simple modelling approach was used in order to correct the product yields for secondary processes (and hence obtain first-generation yields). In Chapter 5 this approach was used also to investigate the OH-initiated oxidation of a first-generation product of the 3-penten-2-one + OH reaction, which is not easy accessible as a pure compound and hence difficult to investigate separately. Finally, detailed examination on the ozonolysis mechanism for α,β -unsaturated ketones is presented, which, for a comprehensive analysis, was performed for a larger series of compounds (methyl vinyl ketone, 3-penten-2-one, 3-methyl-3-penten-2-one, 4-methyl-3-penten-2-one, and ethyl vinyl ketone). Experimental details are provided for each chapter separately. For a better understanding, the key aspects addressing current scientific issues related to the performed investigations are presented in each chapter's introduction.

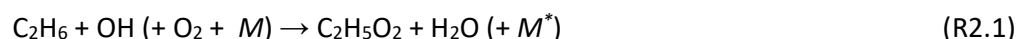
Introduction

2 Gas-phase oxidation processes in the troposphere

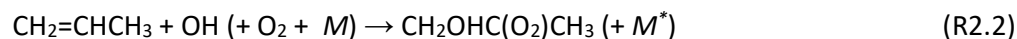
In the following chapter a brief overview is given on the current state of knowledge concerning the general mechanisms of the OH-radical-initiated oxidation and ozonolysis reactions of VOCs.

2.1 Mechanisms of the OH-initiated oxidation

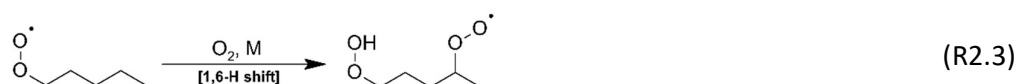
The OH-radical-initiated oxidation of saturated organic species proceeds through the abstraction of H atoms as exemplarily shown below for ethane (C₂H₆).



In the case of unsaturated organics the OH radical adds predominantly (in many reactions almost exclusively) to the C=C double bond, as shown exemplarily for propene.



For both pathways this results in the formation of a peroxy radical (RO₂), those further fate can proceed generally either via bimolecular reactions with NO, NO₂, HO₂ or other RO₂ radicals, or isomerization yielding initially a hydroperoxide, as shown below for an 1,6-H shift of the 1-pentyl peroxy radical. Accordingly, the fate of RO₂ radicals depends on the availability of the respective reaction partners comparative to rate coefficients for isomerization for a given RO₂ radical.



Particularly H-shift isomerizations of RO₂, well reputed from combustion processes, were subject of extensive research during the last years upon discovery of their occurrence at ambient temperatures (Bianchi et al., 2019 and references therein). For instance, Crouse et al. (2009) confirmed experimentally the formation of hydroperoxyaldehydes in the isoprene oxidation, which could be solely justified through H shift isomerizations of the initially formed peroxy radicals following the isoprene + OH reaction. Ehn et al. (2012) proposed the formation of highly oxidized molecules (later on defined as HOMs) based on

the investigation of monoterpene ozonolysis in laboratory experiments, where mass spectra indicated high molecular weight ions (300–650 Da) similar to field observations from boreal forests. Shortly after, Crouse et al. (2013) suggested that autoxidation, defined as an H atom abstraction by peroxy radicals, is an important process in atmospheric oxidation accounting for the formation of multifunctional carbonyls and hydroperoxides found in atmospheric aerosol. This finding was based on the experimental investigation of the OH-initiated oxidation of 3-pentanone, chosen as a model system, and further supported by ab initio calculations for a broader range of substituted VOCs. As can be seen from Reaction (R2.3), the H shift isomerization yields a new RO₂ after addition of O₂, which is, in principle, subject to several different possible transformation pathways including further isomerizations. As a consequence, the molecules are rapidly oxidized via addition of several O atoms included in different functional groups like carbonyls and hydroperoxides, which results in highly polar species that exhibit a low volatility. In summary, RO₂ H shift isomerizations are currently seen as important atmospheric processes owing to the fact that they regenerate radicals (OH, HO₂) and deliver the formation of highly oxidized molecules (HOMs).

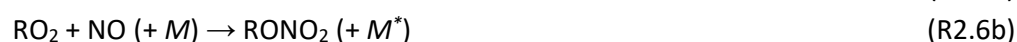
The experimental studies of these reactions remains challenging due to their nature as chain reactions, which resulted in extensive theoretical work on H shift isomerization reactions. Vereecken and Nozière (2020) proposed a SAR approach based mainly on theoretical calculations, which predicts H shift isomerization to be particularly rapid for functionalized RO₂, for instance the ones containing an aldehyde functionality. However, the authors state also that barrier heights of RO₂ H shift isomerization reactions are relatively large and thus, in many cases, they cannot compete with conventional bimolecular reactions.

Among the bimolecular loss processes the RO₂ + NO₂ reaction represents a special case, considered to be relevant in the lower troposphere solely for the case of acyl peroxy radicals. It is accepted to form peroxy nitrates (ROONO₂) in an association reaction, which was found to be highly reversible.



The thermal dissociation of peroxyalkyl nitrates results in lifetimes < 1 s at 298 K, whereas for peroxyacyl nitrates (e. g. peroxyacetyl nitrate = PAN) it reaches 1 h, allowing them to act as NO_x (= $\text{NO} + \text{NO}_2$) reservoir species (Calvert et al., 2015; Jenkin et al., 2019).

The $\text{RO}_2 + \text{NO}$ reaction is expected to dominate over $\text{RO}_2 + \text{RO}_2$ or $\text{RO}_2 + \text{HO}_2$ typically for NO levels < 1 ppbV present in anthropogenically influenced urban areas. It is commonly accepted, mainly based on work from Atkinson and co-workers (e. g. Atkinson et al., 1983), that the reaction can be written as simplified shown below.



The majority of RO_2 is generally converted into the corresponding alkoxy radical (RO), whereas Reaction (R2.6b) is obviously a radical loss process. The branching ratios depend on pressure, temperature and the nature of R (Carter and Atkinson, 1989; Arey et al., 2001). The reaction is associated with a considerable amount of exothermicity; reaction enthalpies were found to range between -46 kJ mol^{-1} and -71 kJ mol^{-1} (Orlando et al., 2003 and references therein, Calvert et al., 2015). As a consequence the nascent RO^* radical exhibits chemical activation which promotes potentially fragmentation of the radical. For instance, although the barrier towards decomposition was shown to be low for the β -hydroxyethoxy radical, formed following the OH-reaction of ethene, the decrease of the branching ratio towards decomposition with a decrease in temperatures is much less pronounced than accounted for by a thermal dissociation (Orlando et al., 2003 and references therein). Calvert et al. (2015) summarized the overall mechanism of $\text{RO}_2 + \text{NO}$ (based on the current understanding) as follows:



where $*$ denotes nascent species with vibrational excitation (chemically activated). However, the importance of chemical activation depends heavily on the decomposition barrier comparative to the excitation of RO^* . For instance, while this is not relevant for many alkoxy radicals, β -hydroxyalkoxy radicals possess almost exclusively very low energy

barriers towards fragmentation (Orlando et al., 2003 and references therein). Information are missing on β -hydroxyalkoxy radicals, where the substitution pattern allows a stabilization through intramolecular H bonding, as is the case for α,β -unsaturated ketones.

By contrast, alkoxy radicals formed following a RO_2 permutation reaction exhibit almost no excitation, since these reactions are believed to be nearly thermoneutral (Orlando et al., 2003). An additional channel of the RO_2 self-reaction accounts for the direct formation of closed-shell species, namely carbonyls and alcohols. As shown below, a third channel might yield an organic peroxide, which at least for small peroxy radicals has never been positively identified (Orlando and Tyndall, 2012).



For RO_2 cross-reactions, the pathways presented above are generally also accessible, although the variety of reaction products is obviously larger due to R and R'.



The reaction of peroxy radicals with HO_2 was considered as particularly important under conditions where NO is low enough to allow other bimolecular loss reactions to dominate. $\text{RO}_2 + \text{HO}_2$ was long believed to be solely a sink for HO_x (= OH + HO_2) radicals, which suppresses consequently O_3 formation due to the radical terminating reaction. This was due to the formation of hydroperoxides, which, however, turned out to be the sole pathway only for small alkyl peroxy radicals like the methyl or ethyl peroxy radical (Wallington and Japar, 1990; Wallington, 1991).



Investigations on the acetyl peroxy radical reaction with HO₂ proved the formation of acetic acid (besides peracetic acid), which suggested the existence of a second channel in RO₂ + HO₂ reactions (Niki et al., 1985; Horie and Moortgat, 1992; Crawford et al., 1999).



However, Sulbaek Andersen et al. (2003) investigated the reaction of a fluorinated acyl peroxy radical with HO₂ and found an alternative pathway yielding OH.



Subsequently, Hasson et al. (2004) confirmed the missing channel in the acetyl peroxy radical + HO₂ reaction, which implies a radical-propagating component in RO₂ + HO₂ reactions.

In typical atmospheric simulation chamber experiments the radical level is reasonably high, which results necessarily in the predominance of bimolecular losses for the generated RO₂. Investigations of OH reactions where methyl nitrite photolysis is used to generate OH involve NO levels favouring the predominance of RO₂ + NO.



By contrast, due to the titration reaction of NO with ozone, the NO level is virtually zero during ozonolysis reactions. Consequently, the further fate of RO₂ radicals formed following the VOC + O₃ reaction is dominated rather by RO₂ + RO₂ and RO₂ + HO₂ reactions.

2.2 Mechanisms of ozonolysis reactions

Ozonolysis reactions proceed, in the majority of cases almost exclusively, via a 1,3-dipolar cycloaddition, which yields a five-membered primary ozonide (POZ) in the initial stage (Fig. 2.1). Due to the exothermicity of ozonolysis reactions, the POZ will decompose immediately via two possible pathways yielding a stable carbonyl and a Criegee intermediate (CI), which is currently suggested to exist in its zwitterionic structure also in the gas-phase (Cox et al., 2020 and references therein). The excess energy is anticipated to be distributed through the decomposition products. Hence, in particular the nascent CIs possess a certain degree of excitation. As a consequence, in contrast to interactions observed in the liquid phase between carbonyl oxides and the solvent, excited CIs are mainly prone to a prompt decomposition in the gas-phase. However, Cox and Penkett (1971) were the first to show that Criegee intermediates can undergo also bimolecular reactions, which was proven by a rapid oxidation of SO₂ in alkene–O₃–mixtures and the subsequent formation of H₂SO₄ aerosol. In the following, it has been proposed that a fraction of the carbonyl oxides is stabilized by collisional energy transfer, which was proven by the pressure-dependence of the H₂SO₄ aerosol yield (Hatakeyama et al., 1984). In particular during the last decade, extensive work yielded rate coefficients for bimolecular reactions with stabilized Criegee intermediates (sCIs) (Cox et al., 2020 and references therein). For instance, rate coefficients of sCI + organic acids were found to be near the collision limit (Chhantyal-Pun et al., 2018). However, theoretical calculations suggest that in many cases the further fate of a significant sCI fraction, hence although thermalized, is still dominated by unimolecular rather than bimolecular loss (Vereecken et al., 2017).

Unimolecular decomposition of CIs proceeds mainly through two different pathways, where the further fate of the carbonyl oxides depends strongly on its conformation. In principle, each asymmetric Criegee Intermediate is formed potentially in two stereoisomers (Fig. 2.1), where the *E/Z* nomenclature is usually defined by the orientation of the outer O atom towards a specific substituent. For example, *E*-CH₃CHOO denotes the acetaldehyde oxide isomer where the outer O atom is oriented towards the H atom and hence possesses an *E*-configuration relative to the methyl group. For smaller CIs, possessing an H atom on the β-carbon (e. g. *Z*-CH₃CHOO), the 1,4-H shift isomerization into a chemically activated vinyl hydroperoxide is expected to be the dominant loss process (Cox et al., 2020 and references therein). This is exemplarily shown in Reaction (R2.14) for the acetone oxide, (CH₃)₂COO. Niki et al. (1987a) showed that in 2,3-dimethyl-2-butene–O₃–mixtures (*p* ≈ 700 torr) the alkene + OH reaction accounted for the excess consumption of

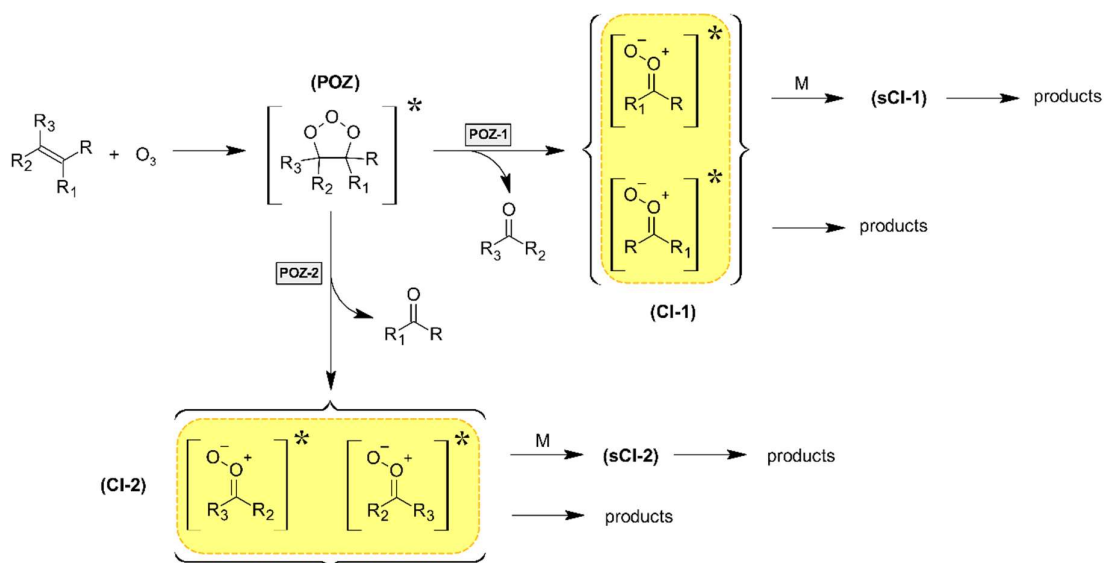
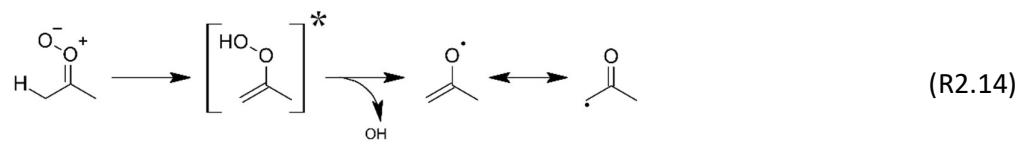
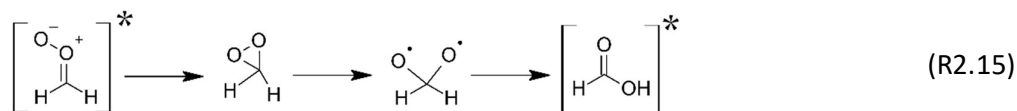


Figure 2.1. Generalized mechanism for the gas-phase ozonolysis of unsaturated organic species proceeding through the initially formed primary ozonide (POZ) and subsequent possible decomposition pathways (POZ-1 and POZ-2) yielding a stable carbonyl species and a Criegee intermediate (CI). Two stereoisomers are possibly formed for each CI, which results in four possible CIs in total.

the alkene comparative to O_3 . They confirmed for the first time the release of OH through the subsequent decomposition of the activated vinyl hydroperoxide according to Reaction (R2.14), which turned out to represent the major source of OH radicals from ozonolysis reactions (Cox et al., 2020). In most cases, the remaining radical will form a stabilized RO_2 under atmospheric conditions, those further fate proceeds as discussed in Sect. 2.1.



In the case of mono-substituted CIs the 1,4-H shift isomerization is unavailable for the *E*-isomer (e. g. *E*- CH_3CHOO). In this case, the major pathway is expected to be a 1,3-ringclosure into a dioxirane intermediate. This, in turn, isomerizes first into a bis(oxy) biradical followed by further isomerization into an acid, as exemplarily shown below for the smallest CI (CH_2OO).



The term “hot” acid is commonly used in the literature to mark its vibrational excitation (Johnson and Marston, 2008; Cox et al., 2020). Further, the excess energy is supposed to result in the fragmentation of the intermediate acid. For instance, for $[\text{HC}(\text{O})\text{OH}]^*$ decomposition into radicals and closed-shell species (CO , CO_2) has been reported.



Kroll et al. (2002) inspected the OH and OD production from *E3*-hexene, *Z3*-hexene and their analogues deuterated on the C=C double bond. They found that the OH yield from the undeuterated hexene isomers were indistinguishable from the OH + OD yield from the deuterated isomers. Due to the absence of a detectable primary kinetic isotope effect, this was interpreted as a confirmation of the existence of a pathway analogue to Reaction (R2.16d). This implies that Reaction (2.16d) accounts for the small OH yield observed for the ethene + O₃ system. The formation of ketene ($\text{CH}_2=\text{C}=\text{O}$), methanol and methane was, however, assigned to $[\text{CH}_3\text{C}(\text{O})\text{OH}]^*$ based on investigations on the ozonolysis of propene and the 2-butene isomers, where *E*- CH_3CHOO is formed (Cox et al., 2020 and references therein). Information on such reaction pathways is limited to the above mentioned excited acids, namely vibrationally excited formic and acetic acid.

Part A:
Cumulative Part

3 Gas-phase reactivity of acyclic α,β -unsaturated carbonyls towards ozone

Reproduced from "Illmann, J. N., Patroescu-Klotz, I., and Wiesen, P.: Gas-phase reactivity of acyclic α,β -unsaturated carbonyls towards ozone, *Phys. Chem. Chem. Phys.*, 23, 3455 – 3466, <https://doi.org/10.1039/D0CP05881E>, 2021" with permission from the PCCP Owner Societies.

3.1 Abstract

We evaluated different approaches to discuss the reactivity of α,β -unsaturated carbonyls comparative to alkene analogues. It was found that the reactivity factors x_r , defined as the relative ratio between the rate coefficient of the carbonyl and a core structure, allow a semi-quantitative estimation of substituent effects in α,β -unsaturated acids, aldehydes and esters when the carbonyl containing substituent is replaced by a hydrogen atom. By contrast, it can be shown that the reactivity of the corresponding ketones differs from the other carbonyls. A linear correlation is presented between the x_r – values and the number of carbon atoms of the alkyl group of the unsaturated esters, which can be used to predict ozonolysis rate coefficients. For this systematic analysis the following rate coefficients (in $10^{-18} \text{ cm}^3 \text{ molecule}^{-1} \text{ s}^{-1}$) have been determined at $298 \pm 2 \text{ K}$ and $990 \pm 15 \text{ mbar}$ and under dry conditions using the relative rate method: $k(\text{O}_3 + \text{methyl methacrylate}) = 7.0 \pm 0.9$, $k(\text{O}_3 + \text{methyl crotonate}) = 5.5 \pm 1.4$, $k(\text{O}_3 + \text{methyl 3-methyl-2-butenate}) = 1.3 \pm 0.3$, $k(\text{O}_3 + \text{methyl tiglate}) = 65 \pm 11$, $k(\text{O}_3 + 3\text{-penten-2-one}) = 31 \pm 7$, $k(\text{O}_3 + 3\text{-methyl-3-penten-2-one}) = 80 \pm 19$, $k(\text{O}_3 + 4\text{-methyl-3-penten-2-one}) = 8.4 \pm 0.8$.

3.2 Introduction

Unsaturated carbonyls are a particular class of OVOCs (Oxygenated Volatile Organic Compounds) emitted into the atmosphere from biogenic and anthropogenic sources. Esters like methyl methacrylate are important intermediates in polymer industry (Bauer, 2011). Unsaturated ketones are mainly used in the food and fragrances industry (Chapuis and Jacoby, 2001; Bickers et al., 2003). 4-methyl-3-penten-2-one is also utilized for the production of methyl isobutyl ketone (MIBK), a common polar solvent with wide applications in the manufacturing of pharmaceuticals, paints and coatings (Sifniades et al., 2011).

Once released into the atmosphere, the α,β -unsaturated carbonyls are removed by the reaction with atmospheric oxidants like OH and NO_3 radicals, O_3 or halogen atoms.

Considering the time profile of atmospheric concentrations for these species the oxidation by OH radicals will be the dominating process during daytime (Calvert et al., 2011) whereas NO₃ radical reactions can only contribute during night due to their rapid photolysis. The ozonolysis reactions potentially play a role during both day and night. In depth investigation of these processes are relevant for completion of data sets to be used in chemical modelling.

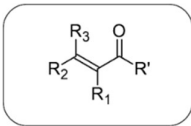
Several studies have shown that unsaturated carbonyls exhibit an unexpected high reactivity towards OH radicals indicating a mechanism other than the simple addition to an olefinic bond (Blanco et al., 2012; Colomer et al., 2013). The kinetics of the ozonolysis reactions of a moderate number of α,β -unsaturated carbonyls have been studied using both the absolute and relative rate method (Atkinson et al., 1981; Treacy et al., 1992; Grosjean et al., 1993a; Greene and Atkinson, 1994; Atkinson et al., 1995; Grosjean et al., 1996; Grosjean and Grosjean, 1998; Neeb et al., 1998; Grosjean and Grosjean, 1999; Sato et al., 2004; Gai et al., 2009; Al Mulla et al., 2010; Bernard et al., 2010; Gaona Colmán et al., 2013; 2015a; 2015b; Wang et al., 2015; Kalalian et al., 2018; Ren et al., 2019; Wang et al., 2019). However, the systematic analysis of their reactivity towards O₃ is at best at the beginning (Jenkin et al., 2020).

It is quite common to relate a target compound to the reactivity of its core structure in order to explain and/or predict its behaviour towards one of the atmospheric oxidants. In literature, these core structures were obtained by replacing the substituent of interest with -H, -CH₃ or the elimination of the carbonyl group as the most common approaches. However, in the case of ozonolysis reactions the resulting conclusion is usually just that carbonyls are less reactive than their core structure due to the deactivating inductive effect of the carbonyl moiety upon olefinic bonds. Neither a comparison of the different approaches nor a systematic analysis of different functional groups has been carried out yet.

In this work a critical comparison of the various selection methods for the core reference structure was performed and tested on the quantification of substituent effects in series of α,β -unsaturated acids, aldehydes, ketones and esters.

In order to enlarge the kinetics data base for reactivity and modelling studies we determined the rate coefficients for the compounds summarised in Table 3.1 using the relative rate technique and FTIR spectrometry. This work, to the best of our knowledge, represents the first determination of the rate coefficients for methyl 3-methyl-2-butenoate and methyl tiglate with O₃. For methyl crotonate and 3-methyl-3-penten-2-one we report here the first rate constant determination using FTIR spectrometry.

Table 3.1. General structure of α,β -unsaturated carbonyls and substitution pattern of the compounds studied within this work. Replacement of R' with -H or -OH would lead to the corresponding α,β -unsaturated aldehydes and acids, respectively.

Structure	R'	R ₁	R ₂	R ₃	Compound IUPAC nomenclature	Other name	Abbreviation
	-CH ₃	-H	-CH ₃	-H	Pent-3-en-2-one	3-Penten-2-one	3P2
	-CH ₃	-CH ₃	-CH ₃	-H	(<i>E</i>)-3-Methylpent-3-en-2-one	3-Methyl-3-penten-2-one	3M3P2
	-CH ₃	-H	-CH ₃	-CH ₃	4-Methylpent-3-en-2-one	4-Methyl-3-penten-2-one	4M3P2
	-OCH ₃	-H	-CH ₃	-H	Methyl (<i>E</i>)-but-2-enoate	Methyl crotonate	MCrot
	-OCH ₃	-CH ₃	-H	-H	Methyl 2-methylprop-2-enoate	Methyl methacrylate	MMA
	-OCH ₃	-CH ₃	-CH ₃	-H	Methyl (<i>E</i>)-2-methylbut-2-enoate	Methyl tiglate	MTig
	-OCH ₃	-H	-CH ₃	-CH ₃	Methyl 3-methylbut-2-enoate	Methyl 3,3-dimethyl-acrylate	M3M2B

3.3 Experimental

All experiments were carried out in a 1080 L quartz-glass reaction chamber in (990 ± 15) mbar of synthetic air at (298 ± 2) K. Only a brief description of the chamber will be given here as further details can be found in the previous literature (Barnes et al., 1994). The chamber is closed at both ends by metal flanges bearing several ports for the injection of reactants, addition of bath gases and coupling with analytical devices. The pumping system consists of a turbo-molecular pump backed by a double-stage rotary fore pump. The chamber can be evacuated to 10^{-4} mbar. Homogeneity of the reaction mixtures is achieved by three magnetically coupled Teflon mixing fans which are evenly placed in the chamber. A White-type mirror system is installed inside the chamber to monitor reaction mixtures via FTIR spectrometry in the spectral range $4000 - 700 \text{ cm}^{-1}$ and a resolution of 1 cm^{-1} . The system whose base length is (5.91 ± 0.01) m was operated at 82 traverses which yields a total optical path length of (484.7 ± 0.8) m. Spectra were recorded using a Nicolet iS50 instrument equipped with a liquid nitrogen cooled mercury-cadmium-telluride (MCT) detector.

During each experiment 50–120 interferograms were co-added per spectrum which results in an averaging period of about 80–190 s. Typically, 15 spectra were recorded per experiment and the first five spectra were collected without oxidant over a period of 20–30 min to check for potential wall losses of the target compound and the reference. After that the reaction was started by single or multiple injection of O_3 which was generated by passing a stream of pure oxygen through an electrical discharge in a homemade device. The observed reaction time was usually 20–40 min.

The initial mixing ratios in ppmV ($1 \text{ ppmV} = 2.46 \times 10^{13} \text{ molecules cm}^{-3}$ at 298 K) were: 0.6–0.8 for methyl methacrylate (MMA), 0.6–0.8 for methyl crotonate (MCrot), 0.3 for methyl 3-methyl-2-butenate (M3M2B), 0.6–0.7 for methyl tiglate (MTig), 1.0–1.2 for 3-penten-2-one (3P2), 1.3–1.8 for 3-methyl-3-penten-2-one (3M3P2), 1.2–1.8 for 4-methyl-3-penten-2-one (4M3P2), 1.3–1.7 for cyclohexene, 1.1 for isoprene, 0.8–0.9 for ethene, 0.9–1.9 for 2-methylpropene, 0.8–1.9 for *E*-2-butene, 0.9–1.9 for 1,3-butadiene and 6000–17000 for carbon monoxide.

3.3.1 Materials

The following chemicals were used without further purification (purities as stated by the suppliers): 2-methylpropene (Aldrich, 99%), ethene (Aldrich, 99.5%), *E*-2-butene (Messer, >99%), 1,3-butadiene (Messer, >99%), cyclohexene (Aldrich, 99%), isoprene (Aldrich, 99%),

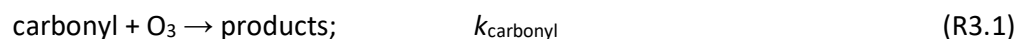
carbon monoxide (Air Liquide, 99.97%), methyl methacrylate (Aldrich, 99%), methyl crotonate (Aldrich, 98%), methyl 3-methyl-2-butenate (Aldrich, 97%), methyl tiglate (Alfa Aesar, 98%), 3-penten-2-one (Alfa Aesar, tech. 85%), 3-methyl-3-penten-2-one (Aldrich, tech. 90%), 4-methyl-3-penten-2-one (Aldrich, tech. 90%), synthetic air (Messer, 99.9999%), oxygen (Messer, 99.5%). The cis/trans isomer ratio for commercially available 3-penten-2-one is not specified

3.4 Results and Discussion

The rate coefficients for the gas-phase ozonolysis reactions of selected α,β -unsaturated carbonyls were determined relative to the O_3 reactions of at least two references for each target compound. The results are shown in Table 3.2. Preliminary results of *n*-butyl acrylate and *n*-hexyl methacrylate have been included in the discussion of reactivity trends. As these data will be part of a separate publication no experimental details are given here.

3.4.1 Rate coefficients

The relative rate technique relies on the assumption that both target compound and reference are solely removed by the oxidant as follows



However the unsaturated carbonyls are potentially subject of an irreversible first-order wall loss:



Considering all these processes the following equation can be derived:

$$\ln\left(\frac{[\text{carbonyl}]_0}{[\text{carbonyl}]_t}\right) - k_{\text{wall}} \times t = \frac{k_{\text{carbonyl}}}{k_{\text{reference}}} \ln\left(\frac{[\text{reference}]_0}{[\text{reference}]_t}\right) \quad (3.1)$$

where $[X]_t$ is the concentration of the species X at time t. If the initial assumption is correct, a plot of $\left\{\ln\left(\frac{[\text{carbonyl}]_0}{[\text{carbonyl}]_t}\right) - k_{\text{wall}} \times t\right\}$ against $\left\{\ln\left(\frac{[\text{reference}]_0}{[\text{reference}]_t}\right)\right\}$ should yield a straight line where the slope represents the relative ratio between k_{carbonyl} and $k_{\text{reference}}$. The relative rate

Table 3.2. Ozonolysis of unsaturated carbonyls. Summary of the results of the relative rate study.

Compound	Reference	No. of runs	Consumption/% Min–Max	$k_{\text{carbonyl}}/k_{\text{reference}}$	$k_{\text{carbonyl}} \times 10^{18}/$ $\text{cm}^3 \text{ molecule}^{-1} \text{ s}^{-1}$
Methyl methacrylate	2-Methylpropene	5		0.61 ± 0.03	6.9 ± 2.3
	Ethene	3		4.57 ± 0.30	7.3 ± 2.4
			31–53	average	7.0 ± 0.9
Methyl crotonate	2-Methylpropene	3		0.45 ± 0.01	5.1 ± 1.6
	Ethene	3		3.88 ± 0.20	6.2 ± 1.9
	1,3-Butadiene	1		0.69 ± 0.03	4.4 ± 1.3
			41–60	average	5.5 ± 1.4
Methyl 3-methyl-2-butenolate	1,3-Butadiene	3		0.19 ± 0.01	1.2 ± 0.4
	Ethene	3		0.90 ± 0.03	1.4 ± 0.4
			15–27	average	1.3 ± 0.3
Methyl tiglate	Cyclohexene	4		0.87 ± 0.04	68 ± 11
	<i>E2</i> -Butene	3		0.32 ± 0.02	60 ± 22
			35–65	average	65 ± 11
3-Penten-2-one	Cyclohexene	3		0.38 ± 0.02	30 ± 5
	2-Methylpropene	1		2.76 ± 0.06	31 ± 9
	Isoprene	1		2.64 ± 0.04	34 ± 9
			26–64	average	31 ± 7
3-Methyl-3-penten-2-one	2-Methylpropene	3		6.33 ± 0.34	72 ± 22
	Cyclohexene	3		0.98 ± 0.04	77 ± 11
	<i>E2</i> -Butene	3		0.48 ± 0.01	92 ± 32
			32–67	average	80 ± 19
4-Methyl-3-penten-2-one	2-Methylpropene	5		0.72 ± 0.02	8.1 ± 2.5
	1,3-Butadiene	3		1.39 ± 0.02	8.7 ± 2.7
			34–62	average	8.4 ± 0.8

plots of the investigated species are shown in Fig. 3.1. The loss rates were typically in the range of $(1-4) \times 10^{-5} \text{ s}^{-1}$ for the wall loss and $(1-7) \times 10^{-4} \text{ s}^{-1}$ for the loss due to the ozonolysis reaction. Only 3-penten-2-one and methyl crotonate showed a higher variability of the wall loss rate ranging from $0.6 \times 10^{-4} \text{ s}^{-1}$ to $2.4 \times 10^{-4} \text{ s}^{-1}$ and from $0.1 \times 10^{-4} \text{ s}^{-1}$ to $1.6 \times 10^{-4} \text{ s}^{-1}$, respectively. Ozonolysis reactions are known to produce OH radicals with yields up to unity and beyond (Calvert et al., 2000). To scavenge any OH radical formed in the experimental system an excess of CO was added. The linear fit of all kinetic plots are going through the origin within a statistical error of 3σ resulting from the regression analysis. Both scavenger efficiency and insignificant intercepts lead to the conclusion that secondary reactions can be neglected in the present experimental set-up. Hence, the obtained relative ratios $k_{\text{carbonyl}}/k_{\text{reference}}$ listed in Tab. 3.2 solely result from the ozonolysis reaction. The errors represent the 2σ statistical error of the linear regression analysis.

The relative ratios were put on an absolute basis using the following rate coefficients for room temperature recommended by Calvert et al. (2000) in $10^{-18} \text{ cm}^3 \text{ molecule}^{-1} \text{ s}^{-1}$: $k(\text{O}_3 + \text{ethene}) = 1.59 \pm 30 \%$, $k(\text{O}_3 + 2\text{-methylpropene}) = 11.3 \pm 30 \%$, $k(\text{O}_3 + E2\text{-butene}) = 190 \pm 35 \%$, $k(\text{O}_3 + 1,3\text{-butadiene}) = 6.3 \pm 30 \%$ and $k(\text{O}_3 + \text{isoprene}) = 12.8 \pm 25 \%$. For cyclohexene the latest recommendation given by Stewart et al (2013) has been used: $k(\text{O}_3 + \text{cyclohexene}) = (7.8 \pm 1.1) \times 10^{-17} \text{ cm}^3 \text{ molecule}^{-1} \text{ s}^{-1}$. The rate coefficients for the target species determined with each reference are listed in Tab. 3.2. The errors represent the statistical error from the regression analysis and the uncertainty of the reference rate coefficient. For the final results given as the mean of all determinations the arithmetic and the weighted means were compared and found to be insignificantly different. However, the error of the weighted average becomes quite small in some cases. Therefore, to cover all experimental uncertainties we thus prefer to indicate the arithmetic mean together with the corresponding 2σ error.

The following rate coefficients (in $10^{-18} \text{ cm}^3 \text{ molecule}^{-1} \text{ s}^{-1}$) were determined: $k(\text{O}_3 + \text{MMA}) = 7.0 \pm 0.9$, $k(\text{O}_3 + \text{MCrot}) = 5.5 \pm 1.4$, $k(\text{O}_3 + \text{M3M2B}) = 1.3 \pm 0.3$, $k(\text{O}_3 + \text{MTig}) = 65 \pm 11$, $k(\text{O}_3 + 3\text{P2}) = 31 \pm 7$, $k(\text{O}_3 + 3\text{M3P2}) = 80 \pm 19$, $k(\text{O}_3 + 4\text{M3P2}) = 8.4 \pm 0.8$. The rate coefficients for methyl methacrylate and 4-methyl-3-penten-2-one are in excellent agreement with previous determinations (Grosjean et al., 1993a; Sato et al., 2004; Bernard et al., 2010; Ren et al., 2019). The ozonolysis of 3-penten-2-one has been subject of three previous studies (Atkinson et al., 1981; Greene and Atkinson, 1994; Sato et al., 2004). While consistent with Greene and Atkinson (1994) and Sato et al. (2004) the rate coefficient determined in this work is around 30 % higher than the first determination reported in

Gas-phase reactivity of acyclic α,β -unsaturated carbonyls towards ozone

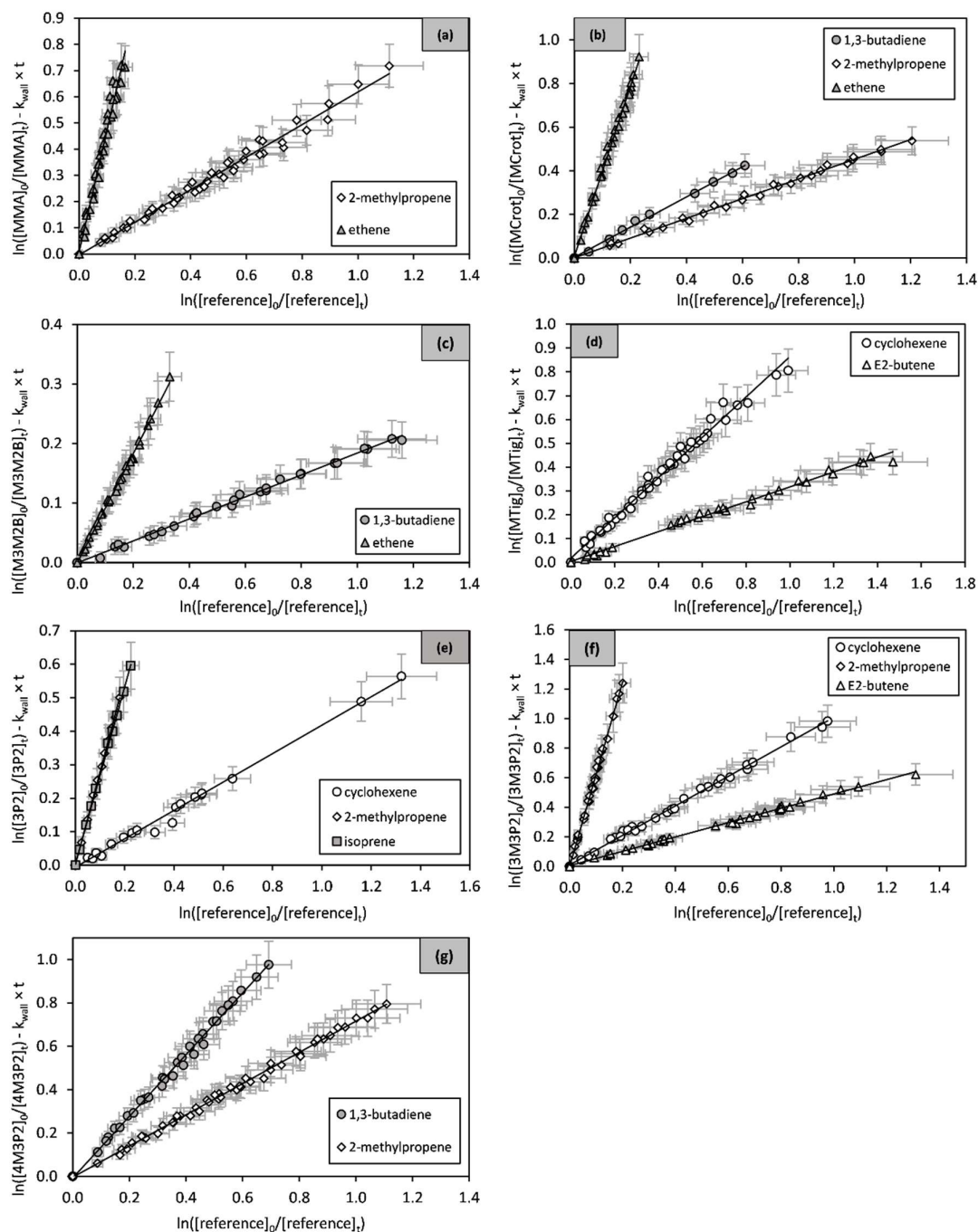


Figure 3.1. Relative rate plots of a) methyl methacrylate, b) methyl crotonate, c) methyl 3-methyl-2-butenate, d) methyl tiglate, e) 3-penten-2-one, f) 3-methyl-3-penten-2-one and g) 4-methyl-3-penten-2-one. The error bars consist of a 10 % systematic error estimated from evaluation uncertainties.

literature (Atkinson et al., 1981). However, as already pointed out by Greene and Atkinson (1994), the first determination via an absolute rate technique was probably affected by an impurity present in the samples, namely 4-methyl-3-penten-2-one. Thus, this value will not be considered further in the following discussion about reactivity trends.

The kinetics of 3-methyl-3-penten-2-one with ozone has been theoretically (Wang et al., 2019) and experimentally (Wang et al., 2015) investigated, once each. The theoretical investigation by RRKM theory yielded a rate coefficient of $2.28 \times 10^{-16} \text{ cm}^3 \text{ molecule}^{-1} \text{ s}^{-1}$ (Wang et al., 2019), which is around three times larger than the value of (80.1 ± 18.7)

$\times 10^{-18} \text{ cm}^3 \text{ molecule}^{-1} \text{ s}^{-1}$ determined in this work. On the other hand, the rate coefficient reported by Wang and co-workers (Wang et al., 2015) is 50 % smaller. They determined $k(\text{O}_3 + 3\text{M3P2})$ with an absolute method by observing the decay of ozone, using a commercial O_3 -analyzer, at different concentrations of 3-methyl-3-penten-2-one. Ozone monitors based on UV absorption are known to be affected by an interference caused by UV absorbing species (Turnipseed et al., 2017). Even when negligible under atmospheric conditions this effect becomes more relevant at higher levels of the undesired absorber (Dunlea et al., 2006; Williams et al., 2006; Fiedrich et al., 2017). Preliminary tests in our laboratory have shown 3-methyl-3-penten-2-one to photolyze when irradiated at 254 nm. Besides, Wang and co-workers do not report any test on possible interferences (Wang et al., 2015). Hence, this effect would have been undetected in their experimental set-up and subsequently have led to an underestimation of the decay of ozone. The same reason could apply for methyl crotonate. The rate coefficient determined in this work is, within the experimental uncertainties, still in satisfactory agreement with the previous study by Grosjean et al. (1993a).

The rate coefficients for methyl 3-methyl-2-butenate and methyl tiglate were experimentally determined within this work for the first time. Gallego-Iniesta and co-workers (Gallego-Iniesta et al., 2014) predicted both to be $10.5 \times 10^{-18} \text{ cm}^3 \text{ molecule}^{-1} \text{ s}^{-1}$ using a SAR approach with group-reactivity factors given by Pfrang et al. (2007). While their predictions overestimate the rate coefficients for methyl 3-methyl-2-butenate by a factor of 8 they underestimate $k(\text{O}_3 + \text{MTig})$ by a factor of 6. A similar divergence is observed using the recent SAR approach by Jenkin et al. (2020), which yields a predicted rate coefficient of $6.5 \times 10^{-18} \text{ cm}^3 \text{ molecule}^{-1} \text{ s}^{-1}$ for both species. The reason for these differences will be tentatively explained in the following sections.

3.4.2 Reactivity trends

It is commonly accepted that ozonolysis reactions proceed via a concerted 1,3 – dipolar cycloaddition with the electrophilic character of the dipole being dominant. Therefore the rate coefficients should be related to the electron density in the olefinic bond. Different groups were building SAR correlations in an attempt to fill the gaps where experimental determination of rate constants is missing. McGillen et al. (2011a) developed a SAR method for the prediction of ozonolysis rate constants for heteroatomic unsaturated species based on the summation of steric and inductive effects and concluded that, even when not negligible, the steric effects are of minor importance. Besides, the compounds studied here do not contain bulky alkyl substituents and differ only in the number and position of the methyl groups attached to the olefinic bond. Hence, it should be possible to explain the reactivity in terms of inductive effects only.

However, a weakness in reactivity discussions is identifying the core structure, to which the kinetics of the target compounds is related. Here, in order to identify the effect of the carbonyl containing substituent a useful approach is the comparison with the structural analogue alkene. As an attempt to quantify the substituent effects a non-dimensional reactivity factor x_r is used defined as the ratio between k_{carbonyl} and k_{alkene} .

$$x_r = k_{\text{carbonyl}}/k_{\text{alkene}} \quad (3.2)$$

However, in the literature different approaches for establishing analogue structures can be found by replacing the substituent of interest by either (a) a hydrogen atom (Sato et al., 2004; Gai et al., 2009; Colomer et al., 2013) or (b) a methyl group (Blanco et al., 2012) or by (c) elimination of the $-\text{C}(\text{O})-$ or $-\text{C}(\text{O})\text{O}-$ moiety (Calvert et al., 2011; Ren et al., 2019). In Fig. 3.2 these methods are explained using as examples methyl methacrylate and methyl crotonate. For both compounds the first method yields propene as analogue structure, thus (a) is not able to distinguish between certain substitution patterns. Nevertheless, a hydrogen atom would be the only neutral species without substituent effect.

According to method (b) and (c), on the other hand, the analogue alkenes are 2-methylpropene and *E*2-butene, respectively. Since $k(\text{O}_3 + \text{propene}) \approx k(\text{O}_3 + 2\text{-methylpropene})$ all approaches yield the same x_r - value in the case of methyl methacrylate. For methyl crotonate though the results differ significantly due to the much larger rate coefficient of *E*2-butene compared to propene caused by the inductive effect of the trans-

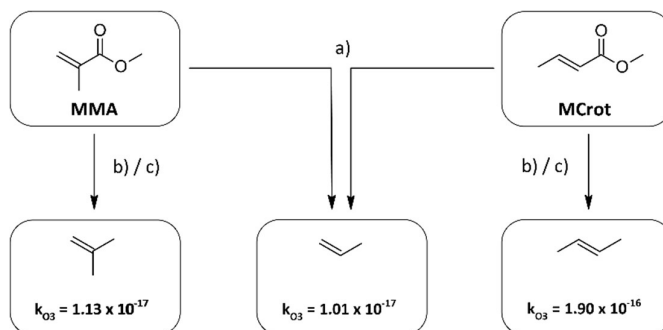


Figure 3.2. Determination of the analogue structures of methyl methacrylate (MMA) and methyl crotonate (MCrot) according to the different methods. The rate constants for the alkenes are taken from Calvert et al. (2000).

substituted methyl group. Thus method (b) potentially overestimates the deactivating effect of the carbonyl substituent.

Table 3 summarises reactivity factors calculated for a series of unsaturated esters, ketones and aldehydes using the rate coefficients obtained in the present study and literature data, where available. Only species where α - and β -position are substituted with either $-H$ or $-CH_3$ are taken into account. The recommended values given by Calvert et al. (2000) have been used for the rate coefficients of the analogue alkenes. To compare the different approaches, we considered that the analogue alkenes resulted from replacing the $-C(O)R$ moiety by both (a) a hydrogen atom and (b) a methyl group. For the compounds listed here method (c), i.e. the elimination of the $-C(O)-$ or $-C(O)O-$ moiety, leads to the same structures as method (b) for the ketones and methyl esters and method (a) for the aldehydes, respectively.

Based on the electron-withdrawing inductive effect of the carbonyl group and the resonance (mesomeric effect) due to the conjugated olefinic bond one would expect α,β -unsaturated carbonyls to be less reactive than the analogue alkenes and thus $x_r < 1$ for both methods. Method (b) yields reactivity factors between 0.003 and 0.66. This large deviation can be observed even when aldehydes, ketones and methyl esters are treated separately. Besides that, there is no information on a tendency or strength of the deactivating effect of the carbonyl moiety to be gained from this method. Thus, the replacement of the substituent by a methyl group seems not to yield further conclusions.

On the other hand, the replacement by a hydrogen atom, method (a), leads to more consistent results. Except for methyl 3-methyl-2-butenate whose reactivity toward ozone

Table 3.3. Summary of the rate coefficients of the gas-phase ozonolysis of α,β -unsaturated ketones, esters and aldehydes and their corresponding reactivity factors according to method (a) and (b). The errors of x_r represent the 2σ statistical error of the mean value. If only one determination is available, the error reflects the relative error of the rate coefficient.

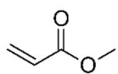
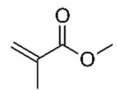
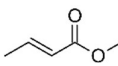
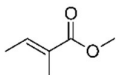
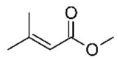
Compound	Reference	T/K	$k_{\text{carbonyl}} \times 10^{18}/$ $\text{cm}^3 \text{ molecule}^{-1} \text{ s}^{-1}$	Alkene analogue ^{a)}	x_r ^{a)}	Alkene analogue ^{b)}	x_r ^{b)} $\times 10^2$
	Grosjean and Grosjean (1998)	291	1.05 ± 0.15	Ethene	0.66	Propene	10.4
	Al Mulla et al. (2010)	298 ± 3	1.19 ± 0.11	Ethene	0.75	Propene	11.8
	Al Mulla et al. (2010)	298 ± 3	1.00 ± 0.05	Ethene	0.63	Propene	9.9
	Bernard et al. (2010)	294	0.95 ± 0.07	Ethene	0.60	Propene	9.4
	average		1.1 ± 0.2		0.66 ± 0.13		10.4 ± 2.1
	Grosjean et al. (1993a)	291	7.5 ± 0.9	Propene	0.74	2-Methylpropene	66.4
	Bernard et al. (2010)	294	6.7 ± 0.9	Propene	0.66	2-Methylpropene	59.3
	Al Mulla et al. (2010)	298 ± 3	5.75 ± 0.52	Propene	0.57	2-Methylpropene	50.9
	Al Mulla et al. (2010)	298 ± 3	6.66 ± 0.60	Propene	0.66	2-Methylpropene	58.9
	Ren et al. (2019)	291	6.63 ± 0.38	Propene	0.66	2-Methylpropene	58.7
	this work	298 ± 2	7.0 ± 0.9	Propene	0.70	2-Methylpropene	62.3
	average		6.7 ± 1.2		0.66 ± 0.11		59.4 ± 10.2
	Grosjean et al. (1993a)	291	4.4 ± 0.3	Propene	0.44	<i>E2</i> -Butene	2.3
	this work	298 ± 2	5.5 ± 1.4	Propene	0.54	<i>E2</i> -Butene	2.9
	average		4.9 ± 1.5		0.49 ± 0.15		2.6 ± 0.8
Methyl tiglate	this work	298 ± 2	65 ± 11	<i>Z2</i> -Butene	0.52 ± 0.08	2-Methyl-2-butene	16.0 ± 2.6
							
Methyl 3-methyl-2-butenate	this work	298 ± 2	1.3 ± 0.3	2-Methyl-propene	0.12 ± 0.03	2-Methyl-2-butene	0.3 ± 0.1
							

Table 3.3. (Continued)

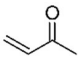
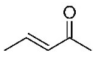
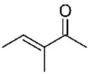
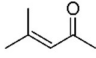
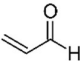
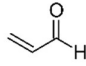
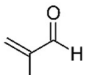
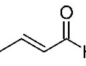
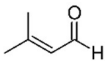
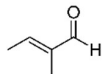
Compound	Reference	T/K	$k_{\text{carbonyl}} \times 10^{18}/$ $\text{cm}^3 \text{ molecule}^{-1} \text{ s}^{-1}$	Alkene analogue ^{a)}	$x_r^{a)}$	Alkene analogue ^{b)}	$x_r^{b)} \times 10^2$
Methyl vinyl ketone 	Atkinson et al. (1981)	296	4.77 ± 0.59	Ethene	3.00	Propene	47.2
	Treacy et al. (1992)	298 ± 4	4.20 ± 0.40	Ethene	2.64	Propene	41.6
	Grosjean and Grosjean (1998)	291	5.84 ± 0.39	Ethene	3.67	Propene	57.8
	Neeb et al. (1998)	296 ± 2	5.4 ± 0.6	Ethene	3.40	Propene	53.5
	Al Mulla et al. (2010)	298 ± 3	4.16 ± 0.33	Ethene	2.62	Propene	41.2
	Al Mulla et al. (2010)	298 ± 3	4.48 ± 0.20	Ethene	2.82	Propene	44.4
	average		4.8 ± 1.4		3.02 ± 0.86		47.6 ± 13.5
3-Penten-2-one 	Greene and Atkinson (1994)	296	36.6 ± 1.6	Propene	3.62	<i>E</i> 2-Butene	19.2
	Sato et al. (2004)	298	29.5 ± 4.1	Propene	2.92	<i>E</i> 2-Butene	15.5
	this work	298 ± 2	31 ± 7	Propene	3.07	<i>E</i> 2-Butene	16.3
	average		32.4 ± 7.4		3.20 ± 0.74		17.0 ± 3.9
3-Methyl-3-penten-2-one 	this work	298 ± 2	80 ± 19	<i>Z</i> 2-Butene	0.64 ± 0.15	2-Methyl-2-butene	19.9 ± 4.6
4-Methyl-3-penten-2-one 	Sato et al. (2004)	298	8.3 ± 1.1	2-Methyl-propene	0.73	2-Methyl-2-butene	2.1
	this work	298 ± 2	8.4 ± 0.8	2-Methyl-propene	0.74	2-Methyl-2-butene	2.1
	average		8.3 ± 0.1		0.74 ± 0.01		2.1 ± 0.1
Acrolein 	Atkinson et al. (1981)	296	0.28 ± 0.05	Ethene	0.18	Propene	2.8
	Treacy et al. (1992)	298 ± 4	0.30 ± 0.04	Ethene	0.19	Propene	3.0
	Grosjean et al. (1993a)	286	0.26 ± 0.05	Ethene	0.16	Propene	2.6
	Al Mulla et al. (2010)	298 ± 3	0.363 ± 0.035	Ethene	0.23	Propene	3.6
	Al Mulla et al. (2010)	298 ± 3	0.336 ± 0.022	Ethene	0.21	Propene	3.3
	average		0.31 ± 0.08		0.19 ± 0.05		3.1 ± 0.8

Table 3.3. (Continued)

Compound	Reference	T/K	$k_{\text{carbonyl}} \times 10^{18}/$ $\text{cm}^3 \text{ molecule}^{-1} \text{ s}^{-1}$	Alkene analogue ^{a)}	$x_r^{a)}$	Alkene analogue ^{b)}	$x_r^{b)} \times 10^2$
Acrolein 	Atkinson et al. (1981)	296	0.28 ± 0.05	Ethene	0.18	Propene	2.8
	Treacy et al. (1992)	298 ± 4	0.30 ± 0.04	Ethene	0.19	Propene	3.0
	Grosjean et al. (1993a)	286	0.26 ± 0.05	Ethene	0.16	Propene	2.6
	Al Mulla et al. (2010)	298 ± 3	0.363 ± 0.035	Ethene	0.23	Propene	3.6
	Al Mulla et al. (2010)	298 ± 3	0.336 ± 0.022	Ethene	0.21	Propene	3.3
	average		0.31 ± 0.08		0.19 ± 0.05		3.1 ± 0.8
Methacrolein 	Atkinson et al. (1981)	296	1.12 ± 0.13	Propene	0.11	2-Methylpropene	9.9
	Treacy et al. (1992)	298 ± 4	1.1 ± 0.2	Propene	0.11	2-Methylpropene	9.7
	Grosjean and Grosjean (1998)	290	1.08 ± 0.20	Propene	0.11	2-Methylpropene	9.6
	Neeb et al. (1998)	296 ± 2	1.3 ± 0.14	Propene	0.13	2-Methylpropene	11.5
	average		1.2 ± 0.2		0.11 ± 0.02		10.2 ± 1.8
Crotonaldehyde 	Atkinson et al. (1981)	296	0.90 ± 0.18	Propene	0.09	<i>E2</i> -Butene	0.5
	Grosjean and Grosjean (1998)	290	1.74 ± 0.20	Propene	0.17	<i>E2</i> -Butene	0.9
	Sato et al. (2004)	298 ± 2	1.58 ± 0.23	Propene	0.16	<i>E2</i> -Butene	0.8
	average		1.4 ± 0.9		0.14 ± 0.09		0.7 ± 0.5
3-Methyl-2-butenal 	Sato et al. (2004)	298 ± 2	1.82 ± 0.26	2-Methyl- propene	0.16 ± 0.02	2-Methyl-2-butene	0.5 ± 0.1
Tiglic aldehyde 	Sato et al. (2004)	298 ± 2	5.34 ± 0.73	<i>Z2</i> -Butene	0.04 ± 0.01	2-Methyl-2-butene	1.3 ± 0.2

is less than the analogue alkene by a factor of 10, for all unsaturated methyl esters in Table 3.3 the average x_r - value calculated with method (a) is 0.58 ± 0.19 . For the α,β -unsaturated aldehydes a reactivity factor of 0.13 ± 0.11 can be obtained which has been similarly reported by Sato et al. (2004). Tiglic aldehyde is at the lower limit of the reactivity range, however, up to date only one value was reported (Sato et al., 2004).

It can be concluded that the $-\text{C}(\text{O})\text{OCH}_3$ moiety reduces the reactivity of the olefinic bond towards ozone by 23–61 % whereas the $-\text{C}(\text{O})\text{H}$ moiety yields a reduction of reactivity by 76–98 %. These findings agree well with fundamentals of organic chemistry postulating that the strength of the $-I$ effect varies as following:



The x_r - values for 3-methyl-3-penten-2-one and 4-methyl-3-penten-2-one are 0.64 ± 0.15 and 0.74 ± 0.01 , respectively, and thereby close to the reactivity of the methyl esters. For methyl vinyl ketone (MVK) and 3-penten-2-one (3P2) though the factors are 3.02 ± 0.86 and 3.20 ± 0.74 . Hence, while consistent for α,β -unsaturated methyl esters and aldehydes, this approach seems not to be commonly valid for the unsaturated ketones. This is even more surprising as $x_r \gg 1$ indicates a significant enhancement of reactivity towards ozone compared to the structural analogue alkene. Intuitively, this is a contradiction to the well-known deactivating effect of a single carbonyl substituent. Earlier studies have shown that α,β -unsaturated ketones like 3-penten-2-one exhibit also an unexpected high reactivity towards OH radicals (Blanco et al., 2012), which was tentatively attributed to the formation of a hydrogen-bonded transition state (Smith and Ravishankara, 2002; Mellouki et al., 2003). However, the formation of such a complex is not possible in case of ozone.

One can argue that experimentally determined rate coefficients might be influenced by the secondary reaction of stabilized CI (= Criegee Intermediate) with carbonyl compounds. Higher than expected rate coefficients of ozonolysis reactions have been reported for acrylic and methacrylic acid when working without sufficient quantities of a CI scavenger (Neeb et al., 1998). By contrast, no such effect was detected for MVK (Neeb et al., 1998). For 3-penten-2-one no such experimental results are available but a similar behaviour toward CIs is expected. Hence it seems plausible to assume that the high rate coefficients obtained here and reported previously (Greene and Atkinson, 1994; Sato et al., 2004) are not the product of secondary consumption by CIs.

Several attempts have been made for the prediction of ozonolysis rate coefficients at room temperature. King et al. (1999) used perturbation frontier molecular orbital theory

(PFMO) and correlated the natural logarithm of the rate coefficients with the energy of the highest occupied molecular orbital (HOMO) over a small range of E_{HOMO} . Pfrang and co-workers updated this concept, originally developed for the prediction of OH, NO_3 and O_3 reactions of alkenes and conjugated dialkenes only, and extended its applicability to unsaturated ketones, esters, alcohols and ethers (Pfrang et al., 2006a; 2006b; 2007; 2008). These studies yielded structure-activity relations with group-reactivity factors whose predictability has been shown to be less accurate for O_3 than for OH and NO_3 (Pfrang et al., 2007). McGillen et al. (2011a) improved the predictability of rate coefficients for ozonolysis reactions of heteroatomic unsaturated species by parameterisation of steric and inductive effects which yielded the definition of a new SAR index (x_{H}). In the case of 3-penten-2-one the rate coefficient calculated based on Pfrang et al. (2007) and McGillen et al. (2011a) is $3.9 \times 10^{-18} \text{ cm}^3 \text{ molecule}^{-1} \text{ s}^{-1}$ and $5.4 \times 10^{-18} \text{ cm}^3 \text{ molecule}^{-1} \text{ s}^{-1}$, respectively. This would indicate a lower reactivity towards ozone than propene which is contradicted by the experimentally obtained values. Thus none of these approaches captures the significant increase of reactivity compared to the alkene analogue (resulting from replacement of the carbonyl containing substituent by a hydrogen atom) as observed here for methyl vinyl ketone and 3-penten-2-one. By contrast, the very recent SAR method by Jenkin et al. (2020) predicts both ketones to be more reactive than their alkene analogues. However, the authors stated that, in contrast to the SAR modifications for alkenes, generic rate coefficients had to be assigned for α,β -unsaturated carbonyls (referred to as “vinylic oxygenated compounds”) simply based on the experimental data of these ketones (Jenkin et al., 2020).

In the liquid phase, α,β -unsaturated carbonyls are known to exhibit a reactivity other than the reactivity of an olefinic bond or a carbonyl group, respectively, but characteristic conjugate addition reactions (see for example: Rossiter and Swingle (1992) and references therein). Due to conjugation, the olefinic bond and the carbonyl group are examined as a unit where π -electrons are delocalised thus lowering the electron density in the olefinic bond and reducing the reactivity towards electrophiles. The delocalisation of π -electrons is though limited to planar or nearly planar conformations. Hence, if resonance besides inductive effects significantly impacts the reduced reactivity of the α,β -unsaturated aldehydes and methyl esters, it may be possible that in 3P2 and MVK non-planar conformations are energetically favoured and therefore their reactivity cannot be compared directly with the α,β -unsaturated esters. However, this is just speculation and detailed quantum mechanical calculations are needed to whether support or refuse this hypothesis.

One could intuitively also imagine that the reactivity of 3P2 and MVK indicates an ozonolysis mechanism other than a 1,3 – dipolar cycloaddition yielding a 1,2,3-trioxolane. Criegee (1975a) already discussed the alternative formation of a σ -complex or a peroxy-epoxide in the liquid phase for systems in which epoxides have been observed. However, if this is rate-determining for 3P2 and MVK it should be reflected in the product distribution. At least for MVK methylglyoxal and formaldehyde have been identified as main products, which is in agreement with the initially formed trioxolane (Grosjean et al., 1993b; Ren et al., 2017). This reasoning may thus be ruled out.

The outstandingly low rate coefficient for methyl 3-methyl-2-butenate in comparison to the other α,β -unsaturated methyl esters indicates additional effects reducing its reactivity towards ozone. One could intuitively imagine that the *Z*-substituted methyl group and the $-\text{C}(\text{O})\text{OCH}_3$ moiety could repel each other in the initially formed trioxolane. However, this effect cannot be observed in the ketone analogue (4-methyl-3-penten-2-one) whose reactivity is close to the other methyl esters. Besides, as previously mentioned, steric effects are expected to play a minor role. Currently there is no convincing explanation for the low reactivity of methyl 3-methyl-2-butenate towards ozone.

3.4.3 Dependence of x_r on the alkyl chain length

Literature data are even scarcer for ozonolysis reactions of α,β -unsaturated carbonyls with larger linear alkyl substituents attached to the carbonyl moiety. Among α,β -unsaturated ketones only rate coefficients for ethyl vinyl ketone (Grosjean et al., 1993a) and 4-hexen-3-one (Grosjean and Grosjean, 1999) have been reported up to date. In the case of esters kinetic data were published for C_2 (4 compounds) (Gai et al., 2009; Bernard et al., 2010; Gaona-Colmán et al., 2013; 2015a; Ren et al., 2019), C_3 (1 compound) (Ren et al., 2019) and C_4 (2 compounds) (Gai et al., 2009; Ren et al., 2019). These information are shown in Table 3.4. In addition, preliminary results on the kinetics of *n*-butyl acrylate and *n*-hexyl methacrylate performed were included for a more comprehensive analysis. Very recently, Ren et al. (2019) reported the kinetics of C_1 – C_4 alkyl methacrylates and concluded that longer alkyl substituents may enhance the reactivity of the olefinic bond towards ozonolysis. They further interpreted their results as a proof that the ozonolysis reaction is an electrophilic process.

In order to establish a possible relationship between the alkyl chain length and the kinetics of ozonolysis reactions reactivity factors have been calculated for α,β -unsaturated

Table 3.4. Summary of the rate coefficients of the gas-phase ozonolysis of α,β -unsaturated acids and esters with longer n -alkyl chain. For each determination the error of x_r represents the relative error of the rate coefficient. The errors of the average x_r for each C_n are the 2σ statistical error of the average if more than one determination is available.

Alkyl rest	Compound	Reference	T/K	$k_{\text{carbonyl}} \times 10^{18}/$ $\text{cm}^3 \text{ molecule}^{-1} \text{ s}^{-1}$	x_r^a
Acid (n = 0)	Acrylic acid	Neeb et al. (1998)	296 ± 2	0.65 ± 0.13	0.41 ± 0.08
		Al Mulla et al. (2010)	298 ± 3	0.76 ± 0.05	0.48 ± 0.03
		Al Mulla et al. (2010)	298 ± 3	0.79 ± 0.07	0.49 ± 0.04
					0.46 ± 0.09
Ethyl (n = 2)	Ethyl acrylate	Bernard et al. (2010)	294	1.3 ± 0.1	0.82 ± 0.06
	Ethyl methacrylate	Gai et al. (2009)	293 ± 1	7.68 ± 0.88	0.76 ± 0.09
		Ren et al. (2019)	291	7.74 ± 0.41	0.77 ± 0.04
		average		7.71 ± 0.09	0.76 ± 0.01
	Ethyl 3,3-dimethylacrylate	Gaona-Colman et al. (2015a)	298 ± 2	8.2 ± 1.9	0.73 ± 0.17
Ethyl crotonate	Gaona-Colman et al. (2013)	298 ± 2	8.0 ± 1.8	0.79 ± 0.18	
				0.77 ± 0.08	
<i>n</i> -Propyl (n = 3)	<i>n</i> -Propyl methacrylate	Ren et al. (2019)	291	8.46 ± 0.36	0.84 ± 0.04
<i>n</i> -Butyl (n = 4)	<i>n</i> -Butyl acrylate	Gai et al. (2009)	293 ± 1	2.40 ± 0.29	1.51 ± 0.18
		preliminary results ^a		1.9 ± 0.2	1.19 ± 0.11
		average		2.2 ± 0.3	1.35 ± 0.45
	<i>n</i> -Butyl methacrylate	Ren et al. (2019)	291	9.78 ± 0.58	0.97 ± 0.06
		Gaona-Colman et al. (2013)	298 ± 2	10.0 ± 3.0	0.99 ± 0.30
				0.98 ± 0.03	
				1.16 ± 0.51	
<i>n</i> -Hexyl (n =6)	<i>n</i> -Hexyl methacrylate	preliminary results ^b		13.6 ± 1.4	1.35 ± 0.14

^a Ongoing study in our laboratory (measured relative to ethene and 1,3-butadiene), ^b ongoing study in our laboratory (measured relative to propene, 1,3-butadiene and isoprene).

esters according to method (a) using averaged data derived from all available literature references. Following this rationale, the alkyl substituent with zero carbon atoms corresponds to the α,β -unsaturated acids. Up to now, only two studies reported rate coefficients for acrylic and methacrylic acid (Neeb et al., 1998; Al Mulla et al., 2010). While consistent for acrylic acid the rate coefficients for methacrylic acid differ by a factor of two. Al Mulla and co-workers pointed out that, based on the given experimental details, no error in the experimental set-up could be identified and the discrepancies remain unexplained (Al Mulla et al., 2010). The latter compound is therefore not considered further. As for the C_1 esters, methyl 3-methyl-2-butenolate, as discussed previously, has been excluded.

A plot of the averaged x_r - values against the carbon number of the alkyl chain yields a straight line with a surprisingly high correlation coefficient (Fig. 3.3). For a better overview the average values of each substance are also included. The variation of x_r for C_4 is unsatisfactorily large for one reason mainly. The literature references for *n*-butyl methacrylate (Gaona-Colmán et al., 2013; Ren et al., 2019) agree well and yield an average of $x_r = 0.98$ which would be much closer to the regression line. For *n*-butyl acrylate the unpublished rate coefficient determined in our laboratory is around 30 % smaller ($x_r = 1.19$) than previously reported by Gai et al. (2009) ($x_r = 1.51$). This difference, even when acceptable within experimental uncertainties, significantly increases the average reactivity factor for C_4 and its statistical error.

The consistency of the x_r - values observed for the α,β -unsaturated methyl esters is exhibited also in the case of the C_2 esters where besides C_1 esters most data are available. Their reactivity towards ozone can be explained in the way the carbonyl containing substituent adjacent to the olefinic bond affects it. Even when different approaches exist in literature for the interpretation and quantification of substituent effects the addition principle, first introduced by Taft (1952) and related to inductive and steric effects, has been generally accepted. Resonance effects have been included later on (Ehrenson et al., 1973). Furthermore, resonance, if its influence on the reactivity is measurable in comparison to the inductive effects, results from the conjugation between the olefinic bond and the carbonyl group only and thus should be nearly the same for all α,β -unsaturated esters. This fact is supported by the x_r - values obtained here for methyl esters (Tab. 3.3). Hence, the increasing reactivity factors with the alkyl chain length solely result from the positive inductive effect of the alkyl group. Linear regression analysis yields an intercept of 0.45 ± 0.09 (2σ). Consequently, the pure $-C(O)O-$ moiety, present in the unsaturated acids, reduces the reactivity of the olefinic bond by 46–64 %. Irrespective of

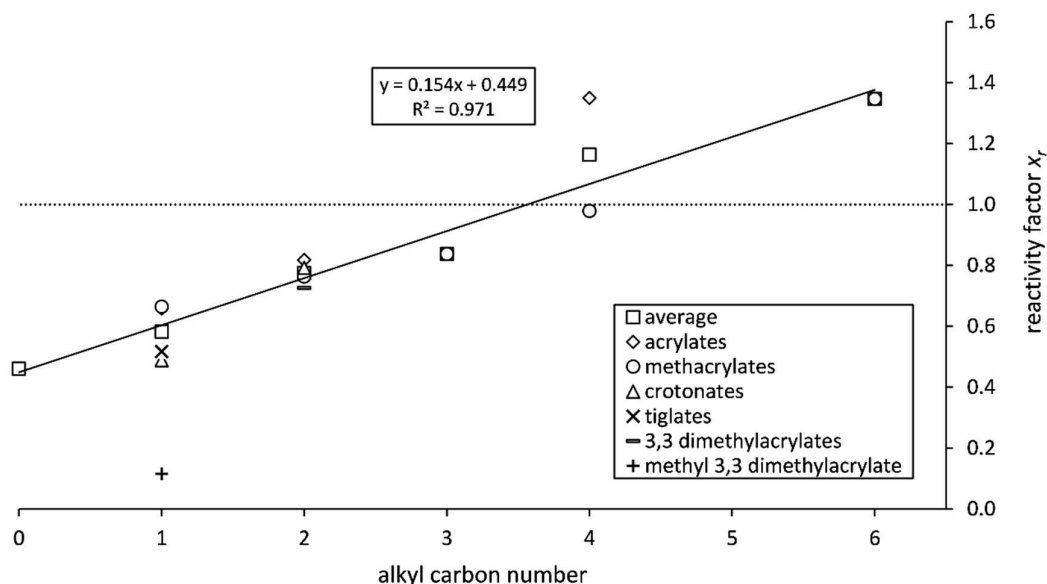


Figure 3.3. Dependence of reactivity factors on the alkyl chain length. Error bars are not included for clarity. Methyl 3,3-dimethylacrylate (= methyl 3-methyl-2-butenolate) is, as discussed previously, not included in the correlation. The dashed line represents the alkene reactivity.

the experimental uncertainties this deactivation is a factor of 1.3 larger than for the unsaturated methyl esters. This is in agreement with the previously mentioned conclusion by Ren et al. (2019) and in contradiction to earlier findings by Pfrang and co-workers who stated the influence of R being rather small (Pfrang et al., 2007).

The transmission of an inductive effect σ through a molecule has been discussed in two originally alternative mechanisms: by either transmission along bonds or interaction through space (as reviewed for example by Exner (1999) and references therein). The magnitude of σ according to the latter mechanism, irrespective of its total strength, has been described in literature (Exner, 1999) by different functions in dependence of r^{-n} where r is the distance between the atom of interest and the reactive centre of the molecule. This is equivalent to the intuitive notion that the effect of a substituent becomes smaller the more remote it is located. Hence, a logarithmic-like correlation between x_r and the number of carbon atoms would be expected where the reactivity factors for the esters with $n > 3$ become indistinguishable. However, the correlation between x_r and the number of carbon atoms shows a remarkable linearity indicating an inductive influence up to C₆ for the α,β -unsaturated esters. It would furthermore imply that the influence of every added methylene group is independent from the distance to the olefinic bond and no attenuation

of the inductive influence would be visible. It would thus be more general to say for the unsaturated esters that while a carbonyl group has an electron-withdrawing effect, electron-donating alkyl groups are thus lowering the cumulative deactivating effect of the $-C(O)OR$ substituent. The increase of the $+I$ effect with the length of the alkyl group leads to an overcompensation of the electron-withdrawing effect in case of C_4 (= *n*-butyl) hence exceeding the reactivity of the alkene analogue (Fig. 3.3). It should be emphasized that these observations contradict our understanding of the inductive influence's transmission. The invariance of the reactivity of terminal alkenes towards ozone is well documented (see for example McGillen et al. (2011b) and references therein). Thus, longer alkyl groups attached to the olefinic bond do not further enhance the $C=C$ double bond's reactivity. The presented correlation, on the other hand, unambiguously shows the influence of longer alkyl substituents. Based on that, there seems to be a fundamental difference when the alkyl group is adjacent to the oxygen atom of the $-C(O)O-$ moiety. This effect needs to be further investigated both experimentally and theoretically.

3.4.4 Structure-activity relations

The correlation in Fig. 3.3 allows to derive a formula for the group-reactivity factor of the carbonyl moiety:

$$f(-C(O)OC_nH_{2n+1}) = (0.154 \pm 0.026) \times n + (0.449 \pm 0.088) \quad (3.4)$$

where n is the number of carbon atoms attached to the oxygen atom and the errors represent the 2σ statistical error resulting from linear regression analysis. The rate coefficient of the ozonolysis reaction can be predicted using the relation:

$$k_{O_3} = k_{basic} \times f(-C(O)OC_nH_{2n+1}) \quad (3.5)$$

where k_{basic} is the rate coefficient of the alkene analogue resulting from replacing the $-C(O)OR$ substituent by a hydrogen atom. This is a fundamental difference to previous SAR approaches where the basic structure reflects the number and position of all substituents and a methyl group is supposed to be neutral ($f(-CH_3) = 1$) (Pfrang et al., 2007; Gallego-Iñiesta et al., 2014). Table 5 summarises measured and predicted rate coefficients for all α,β -unsaturated carbonyls (except ketones) where literature data are available. Predicted

Table 3.5. Predicted and observed rate coefficients (in $10^{18} \text{ cm}^3 \text{ molecule}^{-1} \text{ s}^{-1}$) of selected α,β -unsaturated carbonyls. If not indicated, the observed rate coefficients are taken from Tab. 3.3 and Tab. 3.4.

Compound (IUPAC nomenclature)	Other name	CAS	Alkene analogue	$k_{\text{obs.}}$	$k_{\text{pred.}}$ _a	r^a	$k_{\text{pred.}}$ _b	r^b
Prop-2-enal	Acrolein	107-02-8	Ethene	0.31	0.21	1.49		
2-Methylprop-2-enal	Methacrolein	78-85-3	Prop-1-ene	1.2	1.3	1.14	1.2	1.04
(<i>E</i>)-But-2-enal	Crotonaldehyde	123-73-9	Prop-1-ene	1.4	1.3	1.07	1.4	1.00
3-Methylbut-2-enal	3-Methyl-2-butenal	107-86-8	2-Methylprop-1-ene	1.8	1.5	1.24	1.8	1.01
(<i>E</i>)-2-Methylbut-2-enal	Tiglic aldehyde	497-03-0	(<i>Z</i>)-But-2-ene	5.3	16	3.05	5.7	1.07
2-Methylidenebutanal	2-Ethyl acrolein	922-63-4	But-1-ene ^c	1.1 ^d	1.3	1.22	1.4	1.33
(<i>E</i>)-Pent-2-enal	<i>E</i> 2-Pentenal	1576-87-0	But-1-ene ^c	1.4 ^e	1.3	1.09	1.7	1.18
2-Methyl-2-pentenal ^f	2-Methyl-2-pentenal	623-36-9	(<i>Z</i>)-Pent-2-ene ^g	1.6 ^h	17	10.87	6.8	4.29
			(<i>Z</i>)-Pent-2-ene	7.1 ⁱ	17	2.42	6.8	1.05
(<i>E</i>)-Hex-2-enal	<i>E</i> 2-Hexenal	6728-26-3	Pent-1-ene ^c	1.6 ^j	1.3	1.19	1.9	1.25
(<i>E</i>)-Hept-2-enal	<i>E</i> 2-Heptenal	18829-55-5	Hex-1-ene ^c	2.5 ^k	1.3	1.90	2.2	1.12
(<i>E</i>)-Oct-2-enal	<i>E</i> 2-Octenal	2548-87-0	Hept-1-ene ^c	2.4 ^k	1.3	1.82	2.5	1.04
(<i>E</i>)-Non-2-enal	<i>E</i> 2-Nonenal	18829-56-6	Octe-1-ene ^c	2.1 ^k	1.3	1.58	2.7	1.33
Prop-2-enoic acid	Acrylic acid	79-10-7	Ethene	0.73	0.71	1.03		
2-Methylprop-2-enoic acid	Methacrylic acid	79-41-4	Prop-1-ene	4.1 ^l	4.5	1.11	2.3	1.78
(<i>E</i>)-But-2-enoic acid	Crotonic acid	107-93-7	Prop-1-ene		4.5		2.3	
(<i>E</i>)-2-Methylbut-2-enoic acid	Tiglic acid	80-59-1	(<i>Z</i>)-But-2-ene		56		2.3	
(<i>E</i>)-Pent-2-enoic acid	<i>E</i> 2-Pentenoic acid	13991-37-2	But-1-ene ^c	3.1 ^m	4.5	1.46	2.7	1.12
Methyl prop-2-enoate	Methyl acrylate	96-33-3	Ethene	1.0	0.96	1.09	1.5	1.43
Methyl 2-methylprop-2-enoate	Methyl methacrylate	80-62-6	Prop-1-ene	6.7	6.1	1.10	6.5	1.03
Methyl (<i>E</i>)-but-2-enoate	Methyl crotonate	623-43-8	Prop-1-ene	4.9	6.1	1.24	6.5	1.32
Methyl (<i>E</i>)-2-methylbut-2-enoate	Methyl tiglate	6622-76-0	(<i>Z</i>)-But-2-ene	65	75	1.17	6.5	9.94
Methyl 3-methylbut-2-enoate	Methyl 3,3-dimethylacrylate	924-50-5	2-Methylprop-1-ene	1.3	6.8	5.21	6.5	4.96
Ethyl prop-2-enoate	Ethyl acrylate	140-88-5	Ethene	1.3	1.2	1.08	1.8	1.37
Ethyl 2-methylprop-2-enoate	Ethyl methacrylate	97-63-2	Prop-1-ene	7.7	7.7	1.01	7.7	1.00
Ethyl (<i>E</i>)-but-2-enoate	Ethyl crotonate	623-70-1	Prop-1-ene	8.0	7.7	1.05	7.7	1.03
Ethyl (<i>E</i>)-2-methylbut-2-enoate	Ethyl tiglate	5837-78-5	(<i>Z</i>)-But-2-ene		95		7.7	

Table 3.5. (Continued)

Compound (IUPAC nomenclature)	Other name	CAS	Alkene analogue	$k_{\text{obs.}}$	$k_{\text{pred.}}$ _a	r^a	$k_{\text{pred.}}$ _b	r^b
Ethyl 3-methylbut-2-enoate	Ethyl 3,3-dimethylacrylate	638-10-8	2-Methylprop-1-ene	8.2	8.6	1.04	7.7	1.06
Propyl prop-2-enoate	Propyl acrylate	925-60-0	Ethene		1.5		2.1	
Propyl 2-methylprop-2-enoate	Propyl methacrylate	2210-28-8	Prop-1-ene	8.5	9.2	1.09	9.0	1.06
Butyl prop-2-enoate	<i>n</i> -Butyl acrylate	141-32-2	Ethene	2.1	1.7	1.26	2.4	1.10
Butyl 2-methylprop-2-enoate	<i>n</i> -Butyl methacrylate	97-88-1	Prop-1-ene	9.9	11	1.09	10	1.03
Butyl (<i>E</i>)-but-2-enoate	<i>n</i> -Butyl crotonate	591-63-9	Prop-1-ene		11		10	
Pentyl 2-methylprop-2-enoate	<i>n</i> -Amyl methacrylate	2849-98-1	Prop-1-ene		12		11	
Hexyl prop-2-enoate	<i>n</i> -Hexyl acrylate	2499-95-8	Ethene		2.2		2.9	
Hexyl 2-methylprop-2-enoate	<i>n</i> -Hexyl methacrylate	142-09-6	Prop-1-ene	14	14	1.02	13	1.07
Hexyl (<i>E</i>)-but-2-enoate	<i>n</i> -Hexyl crotonate	1617-25-0	Prop-1-ene		14		13	

^a Based on equations (3.4) and (3.5), ^b based on Jenkin et al. (2020), ^c an average value of $1.0 \times 10^{17} \text{ cm}^3 \text{ molecule}^{-1} \text{ s}^{-1}$ has been used for the C₄ – C₈ alk-1-enes, ^d Grosjean et al. (1993a), ^e average of the rate coefficients determined by Sato et al. (2004) and Kalalian et al. (2018), ^f *trans*-substitution has been assumed for the calculation, ^g the rate coefficient of Avzianova and Ariya (2002) has been used for the calculation, ^h Kalalian et al. (2018), ⁱ Gaona Colmán et al. (2015a), ^j average of the rate coefficients determined by Atkinson et al. (1995), Grosjean et al. (1996) and Kalalian et al. (2018), ^k Gaona Colmán et al. (2015b), ^l Neeb et al. (1998), ^m McGillen et al. (2011a).

values are given as well for a series of species where, to the best of our knowledge, no experimental data are available. To rate the predictability for each measured species a ratio r between the predicted and observed rate coefficient was calculated according to an equation previously used by McGillen and co-workers (McGillen et al., 2011a):

$$r = (k_{\text{pred.}}/k_{\text{obs.}})^y \quad (3.6)$$

where $y = 1$ if $k_{\text{pred.}} > k_{\text{obs.}}$ and $y = -1$ if $k_{\text{pred.}} < k_{\text{obs.}}$.

For most of the listed species the predicted rate coefficients using the Eq. (3.4) and (3.5) are similar to those based on the Jenkin approach (Jenkin et al., 2020). Huge discrepancies are found for substances where Z2-butene is the analogue structure according to method (a) as for “vinylic esters and acids” Jenkin and co-workers only differentiate between two categories of substitution patterns, namely ethene and higher substituted alkenes (Jenkin et al., 2020). More experimental data are thus required. However, for the same reason the recent SAR method underestimates the experimentally determined rate coefficient of methyl tiglate by a factor of 10.

According to a similar rationale α,β -unsaturated aldehydes could be classified as C₀, 3-alken-2-ones as C₁, 4-alken-3-ones as C₂, and so on. However, an attempt to apply this treatment for aldehydes and ketones proved difficult first due to lack of reference data. For longer alkyl chains ($n > 2$) kinetic information are missing for target carbonyls. Even so the reactivity factors x_r for ethyl vinyl ketone and 4-hexen-3-one should be much lower than the values one obtains using method (a) directly, i.e. 3.77 and 6.34, respectively. The cause of the significant enhancement of the reactivity towards ozone observed for ketones comparative to other α,β -unsaturated carbonyls cannot be satisfactorily explained yet.

Nevertheless, the x_r -value determined for the aldehydes can also be applied to predict longer chain or higher substituted α,β -unsaturated aldehydes according to Eq. (3.5) when using $f(-\text{CHO}) = 0.130$ instead of $f(-\text{C}(\text{O})\text{OC}_n\text{H}_{2n+1})$. In doing so the r -values are < 1.25 for methacrolein, crotonaldehyde, 3-methyl-2-butenal, 2-ethyl acrolein, *E2*-pentenal and *E2*-hexenal (Tab. 3.5). Exceptions are, as previously mentioned, tiglic aldehyde ($r = 3.05$) and 2-methyl-2-pentenal. For the latter compound two determinations of the rate coefficient (in $10^{-18} \text{ cm}^3 \text{ molecule}^{-1} \text{ s}^{-1}$) are found in the literature: 7.1 ± 1.6 ($r = 3.83$) (Gaona-Colmán et al., 2015a) and 1.58 ± 0.20 ($r = 17.21$) (Kalalian et al., 2018). Kalalian et al. (2018) argued that the difference of a factor of 5 can be attributed to an OH interference in the other study. On the contrary, Gaona Colmán et al. (2015a) argued that any influence of OH cannot be very significant based on similar results when determining the rate coefficient relative

to the ozonolysis reaction of either 2-methylpropene or 1,3-butadiene. Thus, before rating the predictability of this species a re-determination of the rate coefficient is needed. On the other hand the predictive capacity of Eq. (3.5) applied for aldehydes seems to be less accurate for longer *E2*-alkenals. But given that rate coefficients for C_7 – C_9 *E2*-alkenals have only been determined once in the absence of an OH scavenger (Gaona-Colmán et al., 2015b) it could also be worth re-investigating these compounds.

3.5 Conclusions

Room-temperature rate coefficients for the gas-phase ozonolysis of a series of acyclic α,β -unsaturated carbonyls have been determined using the relative rate technique. The discussion of reactivity in terms of a relative ratio between the target compound and a core structure has already been quite common. However, we have shown here that only the replacement of the carbonyl containing substituent by a hydrogen atom provides a useful tool for the quantification of the deactivating effect of the carbonyl moiety upon the olefinic bond in the case of ozonolysis reactions. This concept is validated by the consistency of the x_r - values of the α,β -unsaturated acids, esters with different *n*-alkyl chain length and aldehydes. The linearity between x_r and the number of carbon atoms up to C_6 further indicates a cumulative nature of the positive inductive effect of the alkyl group in the case of the esters. This is in contradiction to the intuitive notion that the influence of a substituent on a reactive centre is smaller the more remote it is located. This effect needs to be further investigated for a larger pool of substances to proof if the presented correlation is able to well predict rate coefficients for ozonolysis reactions. On the other hand, this concept points out that the reactivity of most of the ketones differs from other α,β -unsaturated carbonyls as shown by the large x_r - values. This effect solely becomes visible using method (a). In order to explain the complex reactivity of the ketones detailed quantum mechanical calculations are needed.

4 Atmospheric oxidation of α,β -unsaturated ketones: kinetics and mechanism of the OH radical reaction

This chapter has been reprinted from “Illmann, N., Gibilisco, R. G., Bejan, I. G., Patroescu-Klotz, I., and Wiesen, P.: Atmospheric oxidation of α,β -unsaturated ketones: kinetics and mechanism of the OH radical reaction, *Atmos. Chem. Phys.*, 21, 13667–13686, <https://doi.org/10.5194/acp-21-13667-2021>, 2021”, used under CC BY 4.0 (<https://creativecommons.org/licenses/by/4.0/>). The typeset, numbering of tables and figures, and the numbering of references were modified from the original.

4.1 Abstract

The OH-radical-initiated oxidation of 3-methyl-3-penten-2-one and 4-methyl-3-penten-2-one was investigated in two atmospheric simulation chambers at 298 ± 3 K and 990 ± 15 mbar using long-path FTIR spectroscopy. The rate coefficients of the reactions of 3-methyl-3-penten-2-one and 4-methyl-3-penten-2-one with OH radicals were determined to be $(6.5 \pm 1.2) \times 10^{-11} \text{ cm}^3 \text{ molecule}^{-1} \text{ s}^{-1}$ and $(8.1 \pm 1.3) \times 10^{-11} \text{ cm}^3 \text{ molecule}^{-1} \text{ s}^{-1}$, respectively. To enlarge the kinetics data pool the rate coefficients of the target species with Cl atoms were determined to be $(2.8 \pm 0.4) \times 10^{-10} \text{ cm}^3 \text{ molecule}^{-1} \text{ s}^{-1}$ and $(3.1 \pm 0.4) \times 10^{-10} \text{ cm}^3 \text{ molecule}^{-1} \text{ s}^{-1}$, respectively. The mechanistic investigation of the OH-initiated oxidation focuses on the $\text{RO}_2 + \text{NO}$ reaction. The quantified products were acetoin, acetaldehyde, biacetyl, CO_2 and peroxyacetyl nitrate (PAN) for the reaction of 3-methyl-3-penten-2-one with OH radicals and acetone, methyl glyoxal, 2-hydroxy-2-methylpropanal, CO_2 and peroxyacetyl nitrate (PAN) for the reaction of 4-methyl-3-penten-2-one with OH, respectively. Based on the calculated product yields an upper limit of 0.15 was determined for the yield of RONO_2 derived from the OH reaction of 4-methyl-3-penten-2-one. By contrast, no RONO_2 formation was observed for the OH reaction of 3-methyl-3-penten-2-one. Additionally, a simple model is presented to correct product yields for secondary processes.

4.2 Introduction

The α,β -unsaturated ketones are a particular class of oxygenated volatile organic compounds (OVOCs) emitted either from biogenic and/or anthropogenic sources or generated in the oxidation of airborne VOCs in the atmosphere. The most prominent representative among this class is methyl vinyl ketone (MVK). MVK is, on the one hand,

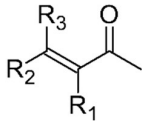
emitted from the polymer, pharmaceutical and fungicide manufacturing industries (Siegel and Eggersdorfer, 2000). On the other hand, it is formed in the troposphere, mainly through the gas-phase oxidation of isoprene, the NMHC which is most abundantly emitted into the atmosphere, with an estimated annual emission up to 750 Tg (Calvert et al., 2000; Guenther et al., 2006). Other α,β -unsaturated ketones, like 3-methyl-3-penten-2-one (3M3P2) are used in the fragrances and food industry (Chapuis and Jacoby, 2001; Bickers et al., 2003, Wang et al., 2020). Furthermore, 4-methyl-3-penten-2-one (4M3P2), commonly known as mesityl oxide, is a precursor of methyl isobutyl ketone used extensively as solvent in the fabrication of paints and coatings. Production rates as high as 0.1 Tg yr⁻¹ were reported in the US (Sifniades et al., 2011). α,β -Unsaturated ketones were also identified in laboratory studies on emissions from different fuels representative of biomass burning (Hatch et al., 2017).

During daytime the main loss process of α,β -unsaturated ketones, once released into or formed in the atmosphere, is probably the oxidation initiated by OH radicals, which has a direct impact on the atmospheric ozone and secondary organic aerosol formation (Kanakidou et al., 2005; Calvert et al., 2011). However, our knowledge about the oxidation mechanisms of species presented in Table 4.1 is rather limited. To date, only the OH radical reaction of MVK has been intensively studied (Tuazon and Atkinson, 1989; Galloway et al., 2011; Praske et al., 2015; Fuchs et al., 2018). Under high-NO conditions, where virtually all peroxy radicals react with NO, glycolaldehyde and methyl glyoxal together with formaldehyde and PAN were identified as first-generation products. Praske et al. (2015) found also a low RONO₂ yield of about 4 %. Some attention was given also to the reaction of both 3M3P2 and 4M3P2, investigated in the present study, with O₃ and to the 3M3P2 + Cl and 3M3P2 + NO₃ system (Sato et al., 2004; Canosa-Mas et al., 2005; Wang et al., 2015; Illmann et al., 2021a; Li et al., 2021). Gaona-Colmán et al. (2017) investigated the OH radical reaction of 4M3P2. They identified qualitatively though only formaldehyde and acetone (GC-MS detection). Hence, the mechanism remains rather incomplete.

In this work, we present an in-depth investigation of the OH-radical-initiated oxidation of two di-substituted α,β -unsaturated ketones, namely 3M3P2 and 4M3P2. Beside the first determination of the rate coefficient for the reaction of OH radicals with 3M3P2, we report kinetic data for Cl atom reactions.

In order to correct the formation yields of products formed in target reactions within complex experimental systems it is quite common to use the Tuazon formalism (Tuazon et al., 1986). This is based on the assumption that reaction products are subsequently consumed in secondary processes like photolysis, wall loss, and oxidation by OH radicals.

Table 4.1. Structures of α,β -unsaturated ketones and related literature on the corresponding OH-radical-initiated oxidation mechanism.

Structure	R ₁	R ₂	R ₃	Name	Reference
	-H	-H	-H	Methyl vinyl ketone (3-Buten-2-one)	Tuazon and Atkinson, (1989); Galloway et al., (2011); Praske et al., (2015); Fuchs et al., (2018)
	-H	-CH ₃	-H	3-Penten-2-one	Illmann et al., (2021c)
	-CH ₃	-H	-H	3-Methyl-3-buten-2-one	-
	-CH ₃	-CH ₃	-H	3-Methyl-3-penten-2-one	This work
	-H	-CH ₃	-CH ₃	4-Methyl-3-penten-2-one	Gaona-Colmán et al., (2017); This work

Thus, their formation yields in the target reactions are underestimated when determined from plotting the formed product against the consumed compound of interest and the yields increase when corrected. However, the formalism is difficult to apply for products with secondary sources in the reaction system. In this case, the formation yields are overestimated without proper corrections. For this purpose, we present a simple model to correct molar formation yields in the target reactions, which accounts for both consumption and secondary formation processes.

The study investigates the contribution of the OH-initiated oxidation of both 3M3P2 and 4M3P2 to the formation of NO_x reservoir species, like peroxyacetyl nitrate (PAN), in the atmosphere. Apart for being an important NO_x reservoir species for the atmosphere, PAN is a phytotoxic air pollutant (Vyskocil et al. 1998) with sources that are still unaccounted for (Fischer et al., 2014). PAN formation depends strongly on temperature and the levels of NO₂ and NO. The study stresses the importance of determining either the ratio between PAN and CO₂/HCHO or the PAN yield together with the NO₂/NO ratio within the experiment since these give more comprehensive information on NO_x reservoir species production than the PAN yield alone. Therefore experiments were conducted under varying NO₂/NO ratios.

4.3 Experimental

Experiments were carried out in a 1080 L and a 480 L reaction chamber in 990 ± 15 mbar of synthetic air at 298 ± 3 K. In the following section is given an updated description of both chambers. A major improvement of both chambers is the addition of heatable injection blocks (< 100 °C). A controlling unit allows the temperature to be adjusted for a better

transfer of samples into the reaction chamber, according to the thermal stability of the investigated substances. Graphic representations of the chambers were published already by Barnes and co-workers (Barnes et al., 1993; 1994).

4.3.1 1080 L chamber

The 1080 L chamber consists of two joint quartz-glass tubes with a total length of 6.2 m and an inner diameter of 0.47 m connected via a middle flange. It is closed at both ends by metal flanges bearing several ports for the injection of reactants, addition of bath gases and coupling with analytical devices. A total of 32 superactinic fluorescent lamps (Philips TL05 40W: 300–460 nm, max. intensity at ca. 360 nm) and 32 low-pressure mercury vapour lamps (Philips TUV 40W: max. intensity at 254 nm) can be used to irradiate the reaction mixture. These lamps are wired in parallel and spaced evenly around the reaction vessel. The pumping system consists of a turbo-molecular pump backed by a double-stage rotary fore pump. The chamber is cleaned between experiments by evacuating it to 10^{-4} mbar for at least 30 minutes. Cleanliness of the chamber is proved by FTIR. Homogeneity of the reaction mixtures is achieved by three magnetically coupled Teflon mixing fans, which are placed on the end and middle flanges. A White-type mirror system is installed inside the chamber to monitor reaction mixtures via FTIR spectroscopy in the spectral range 4000–700 cm^{-1} at a resolution of 1 cm^{-1} . The system whose base length is (5.91 ± 0.01) m was operated at 82 traverses which yields a total optical path length of (484.7 ± 0.8) m. Spectra were recorded using a Nicolet iS50 instrument equipped with a liquid nitrogen cooled mercury-cadmium-telluride (MCT) detector.

The initial mixing ratios in the 1080 L experiments, in ppmV (1 ppmV = 2.46×10^{13} molecules cm^{-3} at 298 K), were: 0.7–1.3 for 3-methyl-3-penten-2-one (3M3P2), 0.9–1.8 for 4-methyl-3-penten-2-one (4M3P2), 1.1 for isoprene, 0.9–1.4 for propene, 0.9–1.4 for isobutene, 0.9–1.4 for 1,3-butadiene, 0.9–1.9 for methyl nitrite, 0.9–1.9 for Cl_2 , 2–4 for NO and 0–2.5 for NO_2 .

4.3.2 480 L chamber

The smaller chamber in the Wuppertal laboratory consists of a borosilicate glass cylinder with a total volume of 480 L (length of 3 m and 0.45 m inner diameter). The tube is closed at both ends by aluminium flanges containing various ports for the introduction of reactants and bath gases, sampling and instruments monitoring the physical parameters inside the chamber. To ensure homogeneous mixing of the reactants a magnetically

coupled fan is mounted on the front flange inside the chamber. A total of 32 fluorescent lamps (Philips TLA 40 W, $300 \leq \lambda \leq 460$ nm, $I_{\max} = 360$ nm) are mounted in four boxes and spaced evenly around the chamber. The lamp housings are cooled with air and their inner surface is encased in reflective steel sheets. The lamps can be switched individually to allow a variation of the photolysis frequency and consequently the radical level during photolysis experiments. The pumping system consists of a rotary vane pump and a root pump yielding an end vacuum of up to 10^{-3} mbar. For a typical cleaning procedure between two experiments the chamber is completely evacuated and filled up to 200–300 mbar of synthetic air or nitrogen. This procedure is repeated until it is certain that no signals related to the previous experiment are detected. Reactants and products are monitored using in situ FTIR spectroscopy. For this purpose, a White-type mirror system (base length: 2.80 ± 0.01 m) is installed inside the chamber and coupled to a Nicolet 6700 FTIR spectrometer (MCT detector). The system is operated at 18 traverses which yields a total optical path length of 50.4 ± 0.2 m. FTIR spectra are recorded in the spectral range 4000–700 cm^{-1} at a resolution of 1 cm^{-1} .

The initial mixing ratios in the 480 L experiments in ppmV (1 ppmV = 2.46×10^{13} molecules cm^{-3} at 298 K) were: 5.0–6.1 for 3-methyl-3-penten-2-one (3M3P2), 5.0–6.0 for 4-methyl-3-penten-2-one (4M3P2), 5.0–5.7 for methyl valerate, 4.2–6.3 for propene, 4.2–6.3 for isobutene, 4.2–6.3 for 1,3-butadiene, 10–16 for methyl nitrite, 13–16 for Cl_2 , and 20–27 for NO.

4.3.3 Materials

The following chemicals were used without further handling, with purities as stated by the suppliers: isobutene (Sigma Aldrich, 99 %), propene (Air Liquide, 99.95 %), 1,3-butadiene (Messer, > 99 %), isoprene (Aldrich, 99 %), methyl valerate (Alfa Aesar, 99 %), 3-methyl-3-penten-2-one (Sigma Aldrich, tech. 90 %), 4-methyl-3-penten-2-one (Sigma Aldrich, tech. 90 %), acetoin (Sigma Aldrich, 96 %), biacetyl (Sigma Aldrich, 97 %), 2-methyl-3-buten-2-ol (Sigma Aldrich, 98 %), carbon monoxide (Air Liquide, 99.97 %), nitrogen monoxide (Air Liquide, 99.5 %), nitrogen dioxide (Messer Griesheim, > 98 %), Cl_2 (Air Liquide, 99.8 %), synthetic air (Messer, 99.9999 %), nitrogen (Messer, 99.9999 %). Methyl nitrite was synthesized by dropping sulphuric acid in an ice cooled aqueous solution of sodium nitrite and methanol (Taylor et al., 1980). The product was collected and stored in a cooling trap at -78 °C. The purity of methyl nitrite was confirmed via FTIR spectroscopy.

4.3.4 Experimental protocol

OH radicals were generated by methyl nitrite photolysis in synthetic air at 360 nm:



NO was added to the reaction system to suppress ozone formation and hence the formation of NO_3 radicals. Cl atoms were generated by photolysis of molecular chlorine in either synthetic air or nitrogen at 360 nm:



In both chambers, the target compound and the products formed during the reaction (mechanistic investigation), and the target and reference compound (kinetic study experiments) were monitored using FTIR spectroscopy. Typically, 50–70 interferograms were co-added per spectrum, which results in averaging period of about 80–113 s, and 15–20 spectra were recorded per experiment. In each run the first five spectra were collected in the dark, over a period of 10–20 min, to check for a potential wall loss of the unsaturated ketones and the reference compounds. Afterwards, the reaction was started by switching on the lamps. In the product study experiments, the reaction was terminated after the record of a maximum of 10 spectra. In selected experiments additionally 5 spectra were collected in the dark, after termination, over a time interval of 10–20 min to investigate the significance of the wall loss for the products of the oxidation reaction in the experimental system.

Usually, the housing which enfolds the transfer optics between FTIR spectrometer and chamber is flushed with purified dry air. Therefore, quantification of CO_2 is, due to a slight variability in the dry air supply, unreliable under normal laboratory conditions. To be able to quantify CO_2 , in selected product study experiments performed in the 1080 L chamber, the transfer optics housing was flushed with ultrapure N_2 evaporated from a liquid nitrogen tank.

4.3.5 Relative rate method

The rate coefficients for the reaction of OH radicals and Cl atoms with the α,β -unsaturated ketones were determined by relating the consumption of the ketone to the consumption of at least two reference compounds:



Both, ketones and references, could potentially be subject to an irreversible first-order wall loss:



Considering these processes the following equation can be derived:

$$\ln\left(\frac{[\text{ketone}]_0}{[\text{ketone}]_t}\right) - k_{\text{loss,ketone}} \times t = \frac{k_{\text{ketone}}}{k_{\text{ref.}}} \times \left(\ln\left(\frac{[\text{ref.}]_0}{[\text{ref.}]_t}\right) - k_{\text{loss,ref.}} \times t \right) \quad (4.1)$$

where $[X]_t$ is the concentration of the species X at time t and $t = 0$ corresponds to the time where the lamps were switched on. According to Eq. (4.1) a plot of $\{\ln([\text{ketone}]_0/[\text{ketone}]_t) - k_{\text{loss,ketone}} \times t\}$ against $\{\ln([\text{ref.}]_0/[\text{ref.}]_t) - k_{\text{loss,ref.}} \times t\}$ should yield a straight line with zero intercept where the slope represents the rate coefficient ratio $k_{\text{ketone}}/k_{\text{ref.}}$.

4.3.6 Product identification and quantification

The quantification of identified products was done by subtraction of calibrated reference IR spectra. The corresponding concentrations of the reference spectra were calculated based on cross sections either taken from literature references, from the Wuppertal laboratory's database or determined within this work. For methyl glyoxal we used the cross sections determined by Talukdar et al. (2011). When employing the values reported by Profeta et al. (2011) the obtained mixing ratios of methyl glyoxal are, however, almost identical. Peroxyacetyl nitrate (PAN) has been quantified using the absorption cross section reported by Allen et al. (2005). Cross sections for acetone and acetaldehyde were taken

from the Wuppertal database. The absorption cross sections of 3-methyl-3-penten-2-one, 4-methyl-3-penten-2-one, 3-hydroxy-2-butanone (acetoin) and 2,3-butanedione (biacetyl) were determined within this work by either injecting different volumes of the pure compound into the chamber, evaporating weighted solid samples (in the case of acetoin) into a flow of bath gas or by injecting aliquot volumes of a solution containing the target species according to a method previously described by Etzkorn et al. (1999). Reference spectra of 2-hydroxy-2-methylpropanal (HMPr) were generated in situ by the ozonolysis of 2-methyl-3-buten-2-ol in the presence of CO to scavenge any OH radical formed in the reaction system. CO₂ was quantified by integration of the absorption features in the range 2400–2349 cm⁻¹ and a polynomial calibration function derived from the injection of various volumes of CO₂ using a calibrated gas-tight syringe.

4.3.7 Modelling

In order to correct the experimentally determined product yields for both secondary formation and consumption a simple model was established based on the Euler-Cauchy method, which can be written down using a commercially available calculation program. In doing so, the rates $d[X]/dt$ for each species X are calculated for constant time intervals Δt based on the rate equation and the concentration of the species X in the previous time interval. This allows the calculation of concentration changes for each time interval, which, when added to the concentration of the previous time interval, yield the concentration of X at time t . The model assumes simplified reaction mechanisms as exemplarily shown below.



The simplest version of this approach assumes a steady-state (sst) concentration of OH radicals that can be determined from the individual loss rate of the target species A during the irradiation period of each experiment. This hypothesis is valid as long as pseudo-first order conditions are proven by a linear correlation between $\{\ln([A]_0/[A]_t) - k_{\text{wall}} \times t\}$ and the

time t . The modelled concentration time profiles are obtained by the input of $[A]_0$, $[OH]_{sst}$ and the rate coefficients of all listed Reactions (R4.9)–(R4.14). The yield y_x for each product of the target reaction is included as parameter to be varied until the simulated concentration-time profile of each species matches the experimental data. However, for traceability and potential future applications, we prefer to outline in detail the stepwise procedure which turned out as best practice after several tests.

1. The rate equations for each species are written according to the simplified exemplary mechanism shown above in Reactions (R4.9)–(R4.14), where kinetic data and molar formation yields for the secondary reactions are taken from literature references. Values for the first-order rate coefficients of each species' wall loss are included if they are measured in the same experiment (thus measured before and after the irradiation of the reaction mixture). If they are not measured, values for k_{wall} are first set to zero and included as additional variable. Molar formation yields for the target reaction are included as variable y_x .
2. Time intervals Δt and the total duration t are adjusted and the initial concentration $[A]_0$ of A is included for $t = 0$ according to the experimental data.
3. If the experimental logarithmic decay of the concentration of A demonstrates pseudo-first order conditions, a constant OH concentration is included based on the consumption of A during the irradiation. If pseudo-first order conditions are not accomplished within the experiment the OH concentration has to be described as a function of t based on the consumption of A . However, including the OH concentration yields a simulated time profile for A which should reproduce the experimental data of A well
4. Finally, the parameters y_x for the target reaction are varied until the time profile of each species matches the experimental data, starting with y_x corresponding to species X , which is the less affected by secondary reactions. Thus, one would start with y_d and y_b rather than y_c in the given example. The uncorrected molar yields y_x , derived from plotting the measured mixing ratio of product X against the consumed target species A , are appropriate as starting point of the iterative process. If wall losses were not determined within the experiments one should try to match the time profile for the first data points where secondary processes are less significant.

After that the wall loss parameters are varied to match the whole time profile. However, for this procedure it is mandatory to know the reasonable range of k_{wall} for each species in the experimental set-up.

The time intervals used for the simulations were typically $\Delta t < 0.1$ s. The yields errors associated with the model were found to be in the range of 0.02. If it is not possible to reproduce the time profiles with the model this will indicate either an error in the spectra evaluation, the used simplified mechanism or the conducted experiments.

4.4 Results and discussion

All experiments were conducted at a total pressure of 990 ± 15 mbar and 298 ± 3 K. Irreversible first-order wall losses of 3M3P2 and 4M3P2 were found to be negligible in the 480 L chamber and in the range $(1-6) \times 10^{-5} \text{ s}^{-1}$ and $(1-8) \times 10^{-5} \text{ s}^{-1}$ in the 1080 L chamber, respectively. In separate control experiments, containing the target species in the bath gas only, no difference was observed for the wall loss in the dark and when the mixture was irradiated over the typical length of an experiment. Hence, an increased wall loss rate due to convection induced by heated walls could be ruled out. Dark reactions between the radical source and the target species were tested as well in separate experiments and were found to be negligible in both reaction chambers. Photolysis of the unsaturated ketones was likewise found to be negligible under the experimental conditions.

4.4.1 Kinetic study

Relative-rate plots according to Eq. (4.1) are presented in Fig. 4.1 for all conducted kinetic experiments. Three reference compounds have been used to determine the rate coefficient of each investigated reaction system. The relative-rate plots for individual experiments display a high linearity, with correlation coefficients from linear regression analysis being $R^2 > 0.95$ and zero intercepts within a 2σ statistical error. The calculated relative ratios $k_{\text{carbonyl}}/k_{\text{ref.}}$ are summarized in Tab. 4.2. They were found to be independent of the initial concentration of the unsaturated ketone and the irradiation time. In the case of the Cl reactions, the relative ratios were independent of using either synthetic air or nitrogen as bath gas. Therefore, the obtained relative ratios likely result solely from each target reaction and any interfering process can be neglected in the present experimental set-up.

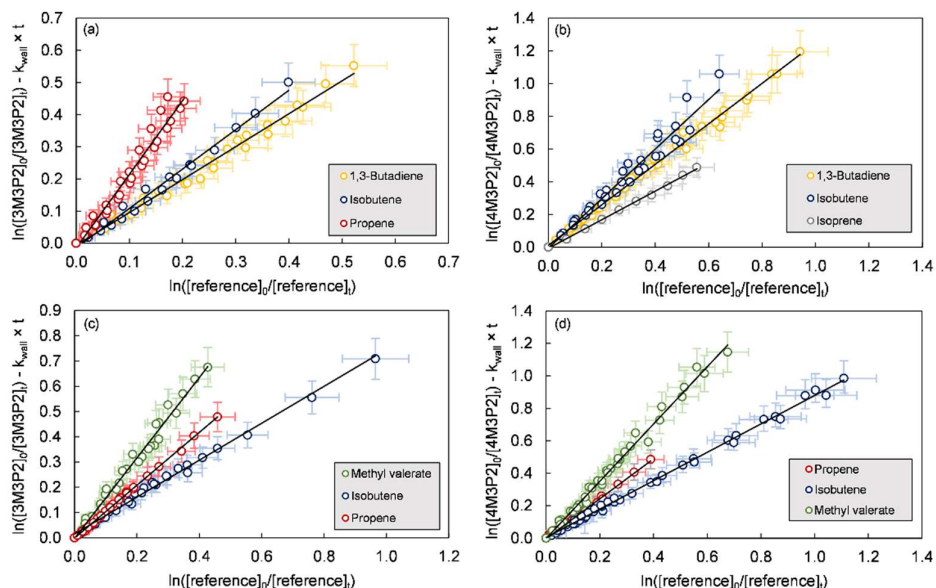


Figure 4.1. Relative-rate plots of all experiments according to Eq. (4.1) for the reaction of (a) 3-methyl-3-penten-2-one + OH, (b) 4-methyl-3-penten-2-one + OH, (c) 3-methyl-3-penten-2-one + Cl and (d) 4-methyl-3-penten-2-one + Cl. The error bars consist of a systematic uncertainty and an additional 10 % relative error to cover uncertainties derived from the experimental and evaluation procedure, respectively.

The rate coefficients were calculated based on the determined relative ratios using the following reference data: $k(\text{isobutene} + \text{OH}) = (5.1 \pm 1.0) \times 10^{-11} \text{ cm}^3 \text{ molecule}^{-1} \text{ s}^{-1}$ (Mellouki et al., 2021), $k(\text{propene} + \text{OH}) = (2.9 \pm 0.8) \times 10^{-11} \text{ cm}^3 \text{ molecule}^{-1} \text{ s}^{-1}$ (Atkinson et al., 2006), $k(1,3\text{-butadiene} + \text{OH}) = (6.66 \pm 1.33) \times 10^{-11} \text{ cm}^3 \text{ molecule}^{-1} \text{ s}^{-1}$ (Calvert et al., 2000), $k(\text{isoprene} + \text{OH}) = (1.0 \pm 0.2) \times 10^{-10} \text{ cm}^3 \text{ molecule}^{-1} \text{ s}^{-1}$ (Mellouki et al., 2021), $k(\text{isobutene} + \text{Cl}) = (3.40 \pm 0.28) \times 10^{-10} \text{ cm}^3 \text{ molecule}^{-1} \text{ s}^{-1}$ (Ezell et al., 2002), $k(\text{propene} + \text{Cl}) = (2.64 \pm 0.21) \times 10^{-10} \text{ cm}^3 \text{ molecule}^{-1} \text{ s}^{-1}$ (Ezell et al., 2002), $k(\text{methyl valerate} + \text{Cl}) = (1.7 \pm 0.2) \times 10^{-10} \text{ cm}^3 \text{ molecule}^{-1} \text{ s}^{-1}$ (Notario et al., 1998).

In Tab. 4. 2 the calculated rate coefficients are given as an average for each reference together with the corresponding error as a combination of the relative ratio's statistical error and the error of the reference's rate coefficient. The determinations with different reference compounds agree within $< 4 \%$ for the Cl reactions and $< 17 \%$ for the OH reactions, respectively. The final rate coefficients for the target reactions are given as the weighted average of all experimental determinations: $k(3\text{M3P2} + \text{OH}) = (6.5 \pm 1.2) \times 10^{-11} \text{ cm}^3 \text{ molecule}^{-1} \text{ s}^{-1}$, $k(4\text{M3P2} + \text{OH}) = (8.1 \pm 1.3) \times 10^{-11} \text{ cm}^3 \text{ molecule}^{-1} \text{ s}^{-1}$, $k(3\text{M3P2} + \text{Cl}) = (2.8 \pm 0.4) \times 10^{-10} \text{ cm}^3 \text{ molecule}^{-1} \text{ s}^{-1}$ and $k(4\text{M3P2} + \text{Cl}) = (3.1 \pm 0.4) \times 10^{-10} \text{ cm}^3 \text{ molecule}^{-1} \text{ s}^{-1}$. The quoted errors represent the 2σ statistical error of the weighted mean and an additional

Table 4.2. Results of the kinetic study using different reference compounds.

Reaction	Reference	No. of runs	Ketone [ppm] ₀	Ketone Max. consumption	$k_{\text{carbonyl}}/k_{\text{ref.}}$	$k \times 10^{11} / \text{cm}^3 \text{ molecule}^{-1} \text{ s}^{-1}$
4M3P2 + OH	Isobutene	4	5.0–6.0	47 %–65 %	1.47 ± 0.31	7.5 ± 1.8
	1,3-Butadiene	6	0.9–6.0	28 %–70 %	1.29 ± 0.03	8.6 ± 1.9
	Isoprene	1	0.9	39 %	0.88 ± 0.03	8.8 ± 1.3
	Average					8.1 ± 1.3
4M3P2 + Cl	Isobutene	5	0.9–6.0	18 %–63 %	0.90 ± 0.07	30 ± 3
	Propene	3	0.9–6.0	12 %–38 %	1.18 ± 0.09	31 ± 4
	Methyl valerate	4	5.0–6.0	39 %–68 %	1.79 ± 0.12	31 ± 4
	Average					31 ± 4
3M3P2 + OH	Propene	3	0.7–6.1	34 %–37 %	2.37 ± 0.40	6.9 ± 2.1
	Isobutene	2	0.7–6.1	21 %–39 %	1.20 ± 0.02	6.1 ± 0.6
	1,3-Butadiene	3	0.9–6.1	29 %–42 %	1.01 ± 0.06	6.7 ± 1.4
	Average					6.5 ± 1.2
3M3P2 + Cl	Isobutene	4	0.7–6.1	20 %–51 %	0.80 ± 0.14	27 ± 5
	Propene	3	0.7–6.1	17 %–38 %	1.07 ± 0.04	28 ± 3
	Methyl valerate	3	5.0–6.1	37 %–49 %	1.60 ± 0.08	27 ± 3
	Average					28 ± 4

10 % relative error to cover all uncertainties derived from the experimental and evaluation procedure.

Rate coefficients for the reaction of 4M3P2 with OH radicals and Cl atoms have been previously determined by Gaona-Colmán et al. (2017), using the relative-rate technique and GC-FID as detection method. The present values are about 20 % smaller (OH reaction) and 15 % larger (Cl reaction) than reported by Gaona-Colmán et al. (2017). However, both values are found within the uncertainties of the former study, thus in good agreement. Wang et al. (2015) reported $k(3\text{M3P2} + \text{Cl}) = (3.00 \pm 0.34) \times 10^{-10} \text{ cm}^3 \text{ molecule}^{-1} \text{ s}^{-1}$ at $293 \pm 1 \text{ K}$ based on a relative-rate study (GC-FID detection) employing large initial mixing ratios for the target species (100 ppm). Nevertheless, the value determined within this work is in excellent agreement with the one reported by Wang and co-workers.

4.4.1.1 Reactivity

It is generally accepted that OH radical and Cl atom reactions of OVOCs proceed via H atom abstraction or addition to the C=C double bond, in the case of unsaturated organic species. The AOPWIN software (US EPA, 2021; Kwok and Atkinson, 1995) estimates for the OH

reaction with both investigated ketones, without discriminating, the contribution of H atom abstraction and OH addition to the olefinic bond to be $k_{\text{abs.}} = 0.4 \times 10^{-12} \text{ cm}^3 \text{ molecule}^{-1} \text{ s}^{-1}$ and $k_{\text{add.}} = 7.8 \times 10^{-11} \text{ cm}^3 \text{ molecule}^{-1} \text{ s}^{-1}$, respectively. This suggests that the OH reaction proceeds almost exclusively through the addition to the C=C double bond. This theoretical result is supported by the findings of the present product studies (see Sect. 4.4.3). The rate coefficients of 4M3P2 + OH predicted by AOPWIN and determined here experimentally agree within 4 %. However, AOPWIN does not differentiate between certain substitution patterns. Given that there is a good agreement between the results using different references, our results show 4M3P2 to be about 1.25 times more reactive towards OH radicals than 3M3P2. Therefore, the AOPWIN prediction is less accurate in the case of 3M3P2. Estimations for the rate coefficients of the reactions of both ketones with OH radicals were given as well in an earlier study ($k(3\text{M3P2} + \text{OH}) = 4.2 \times 10^{-11} \text{ cm}^3 \text{ molecule}^{-1} \text{ s}^{-1}$ and $k(4\text{M3P2} + \text{OH}) = 5.3 \times 10^{-11} \text{ cm}^3 \text{ molecule}^{-1} \text{ s}^{-1}$) based on linear free-energy relationships using ionization potentials (Grosjean and Williams, 1992). Being lower for both ketones, these predictions qualitatively reproduce, however, the experimentally observed rate coefficient ratio $k(4\text{M3P2} + \text{OH})/k(3\text{M3P2} + \text{OH}) \approx 1.26$. The same applies when the estimation of the rate constants is performed according to SAR approach by Jenkin et al. (2018a).

On the other hand, if the reaction proceeds almost solely via the electrophilic addition to the C=C double bond the reactivity can be examined in terms of the electron density associated with the olefinic bond. We have recently pointed out the importance of defining the appropriate core structure when discussing gas-phase reactivity and related substituent effects in unsaturated oxygenated compounds (Illmann et al., 2021a). In the case of the α,β -unsaturated ketones this yields a comparison with structural analogue alkenes where the acetyl moiety is replaced by an H atom, thus (*Z*)-2-butene (for 3M3P2) and isobutene (for 4M3P2) as structural analogues. Despite the deactivating (-I) effect of carbonyl groups, the ability of the carbonyl group to form hydrogen-bonded intermediates with OH radicals (Smith and Ravishankara, 2002) lead to a presumably higher reactivity of the unsaturated ketones compared to their alkene analogues. Experimental results supporting this assumption were reported previously, although the corresponding alkene were chosen in a different way (Blanco et al., 2012).

An attempt to quantify the substituent effects in oxygenated compounds was previously performed by defining a non-dimensional reactivity factor $x_r = k_{\text{ketone}}/k_{\text{alkene}}$ (Illmann et al., 2021a). By using the latest IUPAC recommendations (Mellouki et al., 2021) for the OH radical reactions of isobutene and (*Z*)-2-butene, respectively, and the results of

the present study we obtained for both ketones $x_r > 1$. This is in complete agreement with the expected enhancement of reactivity towards OH radicals. On the other hand, x_r is < 1 for both ketones in the case of the Cl atom reaction. This is not surprising as here the formation of an activating hydrogen-bonded intermediate is not possible. Therefore, the reactivity towards Cl atoms is determined by the deactivating inductive effect of the carbonyl moiety upon the olefinic bond. However, an in-depth analysis of these effects is more related to fundamentals of physical chemistry and will be included in a separate publication.

4.4.2 Infrared cross sections

Integrated absorption cross sections σ have been determined based on the Beer-Lambert law

$$\int_{\nu_1}^{\nu_2} \ln\left(\frac{I_0}{I}\right) d\nu = \sigma \times c \times l \quad (4.2)$$

by plotting the integrated absorption band between ν_1 and ν_2 against the concentration c . These values are summarised in Tab. 4.3 together with literature data where available. Plots used to determine the cross sections are shown in Figs. 9.1 and 9.2. To the best of our knowledge, there are no previous reports on the IR cross sections for 3M3P2, 4M3P2 and acetoin in the literature. Profeta and co-workers (2011) reported band intensities for the various absorptions of biacetyl in the gas-phase. The integrated cross section of the carbonyl absorption ($1690\text{--}1769\text{ cm}^{-1}$) determined within this work is almost identical with their value. The other cross sections agree within $< 10\%$, where the largest discrepancies are observed for the least intense absorption features (between $870\text{--}994\text{ cm}^{-1}$ and $2905\text{--}3053\text{ cm}^{-1}$).

We recommend to use freshly prepared or purchased samples when working with biacetyl. The investigation of an older sample stored for several months at temperatures $< 8\text{ }^\circ\text{C}$ yielded cross sections $30\%\text{--}40\%$ lower than reported by Profeta et al. (2011) while the gas-phase IR spectra were identical with the new sample. Thus, it seems likely that degradation takes place even in a cooled sample. However, the absence of foreign absorption features in the FTIR spectra of the older sample remains unexplained.

In order to determine its integrated absorption cross section, 2-hydroxy-2-methylpropanal (HMP_r) was generated in situ through the ozonolysis of 2-methyl-3-buten-

Table 4.3. Integrated absorption cross sections determined within this work (resolution: 1 cm⁻¹, apodization: Happ-Genzel, phase correction: Merck, zero-filling: 0) together with available literature references.

Compound	Range/ cm ⁻¹	This work $\sigma \times 10^{18}$ / cm molecule ⁻¹	Literature $\sigma \times 10^{18}$ / cm molecule ⁻¹	Reference
3-Methyl-3-penten-2-one	1600–1750	35 ± 4		
4-Methyl-3-penten-2-one	1675–1741	17 ± 2		
Acetoin	3100–2700	17 ± 2		
	1766–1704	14 ± 2		
Biacetyl	2905–3053	2.7 ± 0.2	2.9	Profeta et al., (2011)
	1690–1769	31 ± 2	31	Profeta et al., (2011)
	1392–1476	5.1 ± 0.4	5.5	Profeta et al., (2011)
	1297–1392	9.3 ± 0.7	10	Profeta et al., (2011)
	1078–1154	12 ± 1	13	Profeta et al., (2011)
	870–994	3.8 ± 0.4	4.2	Profeta et al., (2011)
2-Hydroxy-2-methylpropanal	2780–3010	30 ± 5	10.2 ± 1.6	Carrasco et al., (2006)

2-ol in the presence of sufficient amounts of CO to scavenge any OH radical formed during the reaction. According to the well-established gas-phase ozonolysis mechanism, the initially formed trioxolane will decompose in two possible ways to form either one or the other primary carbonyl, namely formaldehyde (HCHO) and HMP_r, and the remaining Criegee intermediate. A secondary formation of both carbonyls resulting from further reactions of the Criegee intermediates is not likely based on the known mechanism. Moreover, by comparison with FTIR spectra of commercially available epoxides, we do not find any hint for epoxide formation in the gas-phase ozonolysis of 2-methyl-3-buten-2-ol, which is in agreement with previous studies (Carrasco et al., 2007, and references therein). Therefore, the sum of the molar yields of HCHO and HMP_r should yield 100 %. The concentrations of HMP_r in each spectrum are thus obtained based on the consumption of the HMP_r-precursor 2-methyl-3-buten-2-ol and the molar formation yield of HMP_r (Y_{HMP_r})

$$Y_{\text{HMP}_r} = 1 - Y_{\text{HCHO}} \quad (4.3)$$

where Y_{HCHO} is the experimentally determined molar formation yield of HCHO. However, in doing so the determined cross section is $(30 \pm 5) \times 10^{-18}$ cm molecule⁻¹ which is about 300 % larger than the only available literature reference (Carrasco et al., 2006). If the literature reference is taken as the true value this would either indicate a fundamental underestimation of the HMP_r concentration or an erroneous determination of the 2-methyl-3-buten-2-ol concentration in our experiments. The unsaturated alcohol is highly

volatile and does not pose quantification problems. Moreover, no wall loss was measured in any of the chambers either for the alcohol nor for the HMPr (see Sect. 4.4.3). A falsely determined cross section of the HMPr precursor by a factor up to 3 is therefore very unlikely. On the other hand, using the literature cross section would result in molar yields of about 190 % for HMPr in our experiments.

Carrasco et al. (2006) synthesised and purified HMPr in the liquid phase and evaporated different amounts of the sample. The concentrations were calculated according to the ideal gas law and subtracting the amounts of formic acid and formaldehyde still present in the liquid sample despite purification. Although the authors stated that HMPr has also been synthesized in situ, similarly to the present study, the cross section seems to be calculated based solely on the liquid sample evaporation. However, the listed integrated cross section for HCHO, based on the natural logarithm as stated by the authors, differs about a factor of two from other literature references (Nakanaga et al., 1982; Gratien et al., 2007). As well as this, the used value is about 2.3 smaller than the cited literature reference (Picquet-Varrault et al., 2002). All this suggest a systematic conversion error in the previous study. Therefore, we prefer to use the HMPr cross section estimated in our group for the following product study.

4.4.3 Product study of the OH reactions

In the following subsections the terms “ α and β position” are used with respect to their position related to the carbonyl group. Thus, the C_α refers to the carbon atom adjacent the carbonyl group. Consequently, the α -RO₂ radical names the RO₂ where the molecular oxygen added in α position.

4.4.3.1 3-Methyl-3-penten-2-one + OH

Figure 4.2 shows details obtained by evaluating IR spectra recorded during a 3M3P2 + OH experiment and the references used to identify the reaction products. The range 3600–2600 cm⁻¹ was chosen solely for clarity reasons. More spectra focussing on other spectral ranges can be found in Fig. 9.3. Figure 9.4 shows reference spectra for the unsaturated ketones. The remaining absorption features present in the residual spectra after subtraction of 3M3P2, methyl nitrite, methyl nitrate, HNO₃, HONO, HCHO, NO and NO₂ can be unambiguously attributed to acetoin, biacetyl, acetaldehyde and peroxyacetyl nitrate (PAN), respectively. CO₂ formation was clearly observed by examination of its absorption

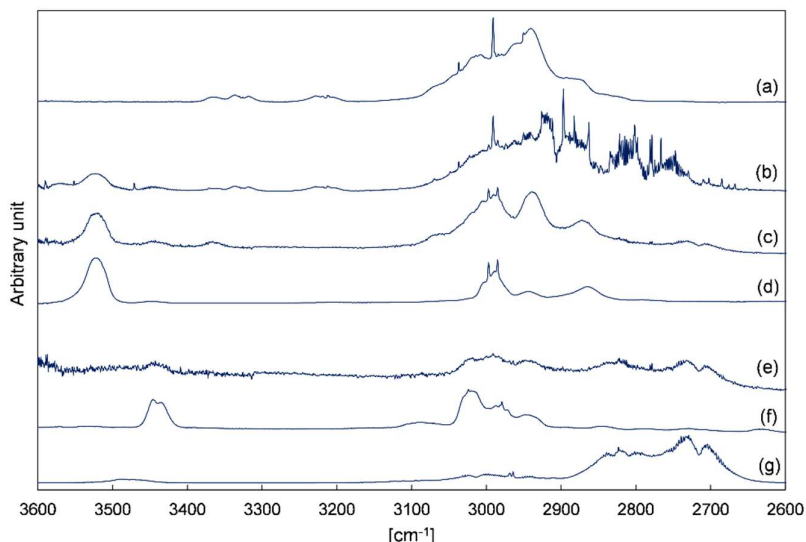


Figure 4.2. Exemplary FTIR spectra of a product study experiment of 3M3P2 + OH: (a) reaction mixture before irradiation, (b) reaction mixture at the end of the irradiation period, (c) residual spectrum after subtraction of methyl nitrite, methyl nitrate, HNO₃, HONO, NO, NO₂ and HCHO from (b), (d) reference spectrum of 3-hydroxy-2-butanone (acetoin), (e) residual spectrum after subtraction of 3M3P2 and acetoin from (c), (f) reference spectrum of 2,3-butanedione (biacetyl), and (g) reference spectrum of acetaldehyde. The spectra are shifted and scaled individually for a better overview.

features in the range 2400–2250 cm⁻¹ during the irradiation period. After subtraction of all clearly assigned spectral features the residual spectrum contains only weak absorption bands centred on 1654 cm⁻¹, 1364 cm⁻¹, 1297 cm⁻¹ and 856 cm⁻¹. Although a possible indication for the formation of organic nitrates, they are too weak to be reasonably interpreted.

The formation of the identified species can be well explained as first generation products of the OH initiated oxidation of 3M3P2, according to the proposed mechanism depicted in Fig. 4.3. The OH radical is expected to add predominantly to the C=C double bond in either α or β position followed by the addition of O₂ to form the corresponding α - or β -RO₂ radical (= hydroxyperoxy radical). Their formation and further oxidation pathways (Fig. 4.3) are consecutively defined as α_n and β_n pathways, respectively. Due to the presence of NO in excess, under these experimental conditions it is certain that virtually all RO₂ radicals will react with NO to mainly form the corresponding RO radicals (= hydroxyalkoxy radicals). The β -RO radical can undergo a bond scission (pathway β_1 , Fig. 4.3) between the α - and β - carbon (C _{α} and C _{β}) to form acetaldehyde and a hydroxyalkyl radical. This, in turn, reacts with O₂ to produce biacetyl. In principle, the H atom abstraction from

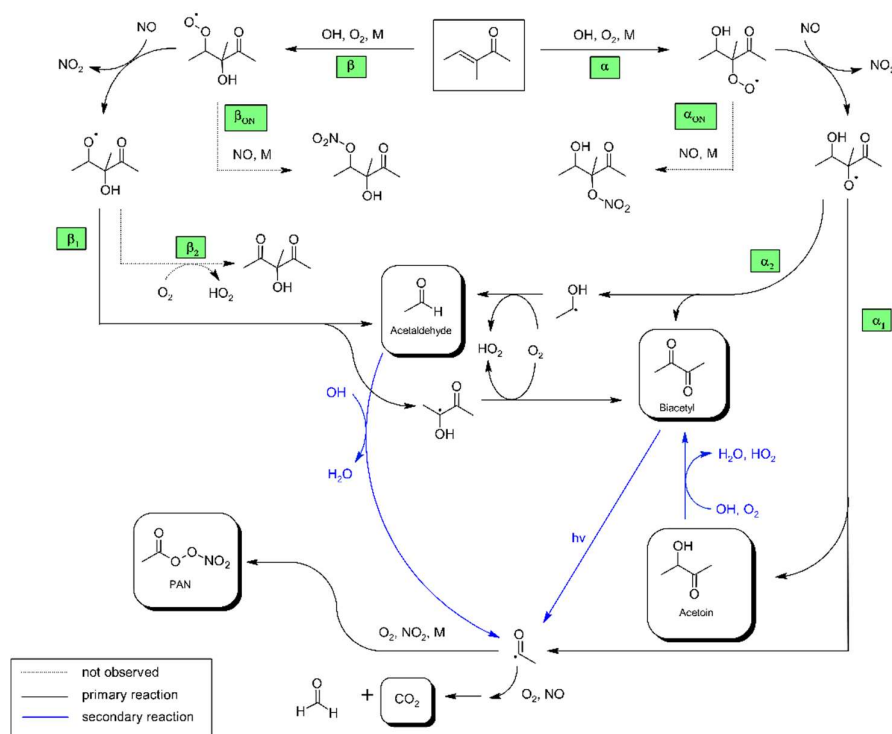


Figure 4.3. Proposed mechanism for the OH-radical-initiated oxidation of 3-methyl-3-penten-2-one and further oxidation of the first-generation products relevant under the experimental conditions.

the β -RO by O_2 might lead to the formation of a 2-hydroxy-1,3-dicarbonyl species (pathway β_2 , Fig. 4.3). However, after subtraction of all identified species there are no remaining IR absorption bands to support the occurrence of this pathway. On the other hand, the reaction of RO_2 with NO is known to be exothermic, resulting in chemically activated RO radicals potentially prone to “prompt” decomposition (Orlando et al., 2003). This pathway was shown to be important for RO radicals where energy barriers to decomposition are low, as expected for the β -RO radical according to available estimation methods (Atkinson, 2007; Vereecken and Peeters, 2009). As well as this, Atkinson (2007) concluded that decomposition will dominate compared to the reaction with O_2 in the case of 1,2-hydroxyalkoxy radicals. This also applies for the thermalized hydroxyalkoxy radicals. All this suggests that pathway β_2 does either not exist if the precursor β -RO radical is formed through $RO_2 + NO$ or its branching fraction is very low.

The addition of the OH radical in β position followed by the addition of O_2 and reaction with NO yields eventually acetoin (pathways α and α_1 , Fig. 4.3). The bond scission in the α -RO radical between C_α and the carbon atom of the carbonyl moiety (pathway α_1 , Fig. 4.3),

yields further acetyl radicals which, after addition of O_2 , can either form peroxyacetyl nitrate (through addition of NO_2) or react with NO to finally form CO_2 and $HCHO$, under the experimental conditions. The yield of $HCHO$ related to 3M3P2 oxidation cannot be experimentally determined because it is also produced in the methyl nitrite photolysis itself. On the other hand, the α -RO radical can also form biacetyl if the bond scission occurs between C_α and C_β (pathway α_2 , Fig. 4.3). In this case acetaldehyde evolves from the simultaneously formed hydroxyalkyl radical due to H atom abstraction through molecular oxygen.

4.4.3.2 4-Methyl-3-penten-2-one + OH

Figure 4.4 depicts evaluation details of IR spectra recorded during a product study experiment of 4M3P2 and references. The spectral range $3200\text{--}2600\text{ cm}^{-1}$ was chosen as mentioned above. Acetone, methyl glyoxal and peroxyacetyl nitrate are clearly identifiable in all residual spectra after subtraction of 4M3P2, methyl nitrite, methyl nitrate, HNO_3 , $HONO$, $HCHO$, NO and NO_2 . As in the 3M3P2 product studies, the CO_2 formation during the irradiation period was unambiguously observed in the range $2400\text{--}2250\text{ cm}^{-1}$ (Fig. 9.5). Trace (f) in Fig. 4.4 shows an exemplary residual spectrum after subtraction of methyl glyoxal, acetone and PAN references from the spectrum in trace (c). The spectral features are in excellent agreement, in the presented range, with a reference IR spectrum of 2-hydroxy-2-methylpropanal (see Sect. 4.4.2). This proves its formation in the OH-radical-initiated oxidation of 4M3P2. After subtraction of all assigned absorptions the remaining residual spectra, in both 480 L and 1080 L product study experiments, contain weak but well-defined absorption bands centred around 3478 cm^{-1} , 1722 cm^{-1} , 1654 cm^{-1} , 1297 cm^{-1} and 856 cm^{-1} (Fig. 4.5). The characteristic absorption pattern of the latter three bands is a strong indication for organic nitrate formation in this reaction system.

Based on the experimental results obtained here a mechanism for the reaction of OH radicals with 4M3P2 was drawn (Fig. 4.6). The OH radical will add predominantly to either the α or β carbon. The subsequent O_2 addition will yield the corresponding β - or α - RO_2 radical, respectively. As for 3M3P2, all 4M3P2 product studies were conducted under conditions where RO_2 radicals are expected to react solely with NO . Acetone can be formed from the conversion of the β - RO_2 with NO into the corresponding β -RO followed by the scission of the C-C bond between C_α and C_β (pathway β_1 , Fig. 4.6). The synchronously generated hydroxyalkyl radical might react with O_2 to yield methyl glyoxal. HMPn formation

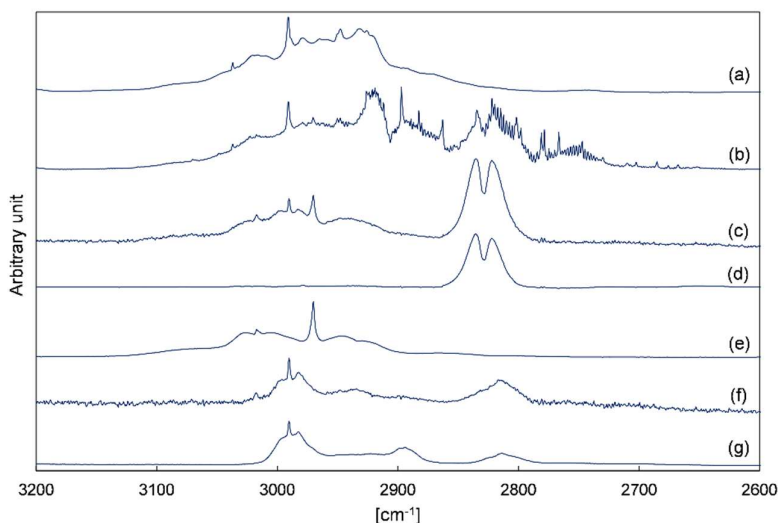


Figure 4.4. Exemplary FTIR spectra of a product study experiment of 4M3P2 + OH: (a) reaction mixture before irradiation, (b) reaction mixture at the end of the irradiation period, (c) residual spectrum after subtraction of 4M3P2, methyl nitrite, methyl nitrate, HONO, HNO₃, NO, NO₂ and HCHO from (b), (d) reference spectrum of methyl glyoxal, (e) reference spectrum of acetone, (f) residual spectrum after subtracting methyl glyoxal, acetone and PAN from (c), and (g) reference spectrum of 2-hydroxy-2-methylpropanal generated in situ. The spectra are shifted and scaled individually for a better overview.

can be explained by a bond scission between C_α and the carbon atom of the carbonyl group (pathway α_1 , Fig. 4.6). In the present experimental system, the co-generated acetyl radicals yield either PAN or CO₂ and HCHO, as discussed above. Methyl glyoxal and acetone can also be formed according to pathway α_2 (Fig. 4.6) if the bond scission in the α -RO occurs between C_α and C_β.

Hypothetically, the α -RO radical could also produce a 3-hydroxy-1,2-dicarbonyl species (pathway α_3 , Fig. 4.6) if H atom abstraction via molecular oxygen would occur rather than a C-C bond scission. However, the structure of the weak carbonyl absorption in the residual spectra seems more likely to belong to a single C=O bond rather than a vicinal diketone. There is thus no indication for the existence of this reaction pathway. Besides, the reaction RO + O₂ is not expected to be competitive to the decomposition channels of the multifunctional RO radical, as discussed above.

Organic nitrate formation, which is indicated by the residual spectra, is expected to proceed through the reaction of the α -RO₂ or β -RO₂ radical with NO (pathway α_{ON} or β_{ON} , Fig. 4.6) followed by the isomerization of the nascent ROONO adduct (Calvert et al., 2015). RONO₂ formation has also been observed through RO + NO₂ reactions of simple alkoxy

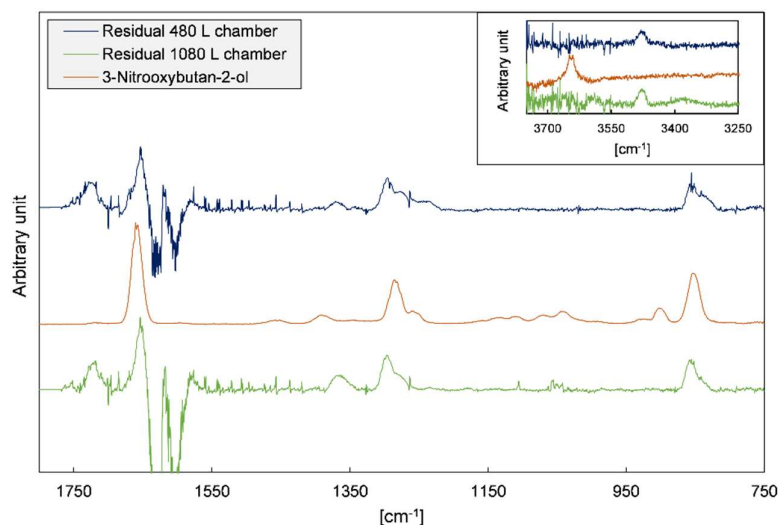


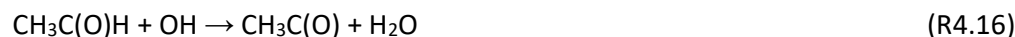
Figure 4.5. Residual spectra of 4M3P2 + OH product study experiments performed in both chambers after subtraction of all identified species and an exemplary reference spectrum of an organic nitrate recorded in our laboratory (Spittler, 2001).

radicals (Frost and Smith, 1990; Mund et al., 1998). However, high pressure rate coefficients for these types of reactions are about $(1-3) \times 10^{-11} \text{ cm}^3 \text{ molecule}^{-1} \text{ s}^{-1}$ (Atkinson et al., 2006) whereas for the reactions of RO with O_2 $k \times [\text{O}_2]$ is about $4 \times 10^4 \text{ s}^{-1}$ according to a recommendation provided by Atkinson (2007). Given that RO + O_2 seems even not to compete with unimolecular decomposition for β -hydroxyalkoxy radicals we do not expect RO + NO_2 to be experimentally and atmospherically relevant. The absorption features observed in the residual spectra, additionally to the characteristic nitrate absorptions, indicate the presence of a carbonyl (1722 cm^{-1}) and an OH-group (3478 cm^{-1}) which can be assigned to multifunctional hydroxycarbonyl nitrates as presented in Fig. 4.6. In the case of the RONO_2 species resulting from the α -RO radical, one would expect that intramolecular hydrogen bonding between the OH- and the carbonyl group stabilize the structure. This would cause, on the one hand, a broader and weaker OH absorption band and, on the other hand, a shift of the carbonyl absorption towards lower wavenumbers. Based on that, it is more likely to tentatively attribute the residual absorptions to the hydroxycarbonyl nitrate resulting from the β - RO_2 radical. The formation of organic nitrates will be further discussed in Sect. 4.4.3.5.

biacetyl, with a formation yield of about 80 %. This is also expected to be the main loss process under atmospheric conditions. Therefore, the further oxidation of acetoin is an additional source of biacetyl in the 3M3P2 experimental system. Biacetyl itself is mainly subject to photolysis (R4.15), under both the present experimental and atmospheric conditions yielding acetyl radicals.



Acetaldehyde also contributes to the formation of acetyl radicals since the aldehydic H atom abstraction (R4.16) was shown to account for about 95 % of the OH reaction (Calvert et al., 2011).



Acetone, formed in the oxidation of 4M3P2, will be mainly oxidized by OH radicals through H atom abstraction yielding acetonyl radicals which readily decompose to HCHO and acetyl radicals (Orlando et al., 2000).



However, while being a source of HCHO and acetyl radicals under atmospheric conditions, this reaction cannot play any role in the present experimental set-up, considering the lifetime of acetone with respect to OH. By contrast, HMP_r was shown to display a much higher reactivity towards OH, the reaction producing acetone with a yield of unity (Carrasco et al., 2006). Thus, this is a secondary source of acetone in our experiments. Finally, the OH reaction of methyl glyoxal will exclusively proceed via the abstraction of the aldehydic H atom. The initially formed $\text{CH}_3\text{C(O)CO}$ radical will readily dissociate into carbon monoxide and $\text{CH}_3\text{C(O)}$ radicals as well (Green et al., 1990). Based on the lamp spectrum we calculated the photolysis frequency of methyl glyoxal for all experimental conditions. The ratio between $k(\text{CH}_3\text{C(O)CHO} + \text{OH}) \times [\text{OH}]$ and $J(\text{CH}_3\text{C(O)CHO})$ was found to be typically > 7 . Hence, while photolysis of methyl glyoxal is the main loss process under most atmospheric daytime conditions the OH reaction dominates in the present experimental system.

All these processes interfere in the determination of the intrinsic yield of $\text{CH}_3\text{C(O)}$ radicals in the reaction of the unsaturated ketones with OH. As discussed above, the further

chemistry of acetyl radicals in our experiments may evolve either into PAN or CO₂/HCHO formation. However, in the atmosphere the readily formed acetyl peroxy radical may also react with HO₂ radicals to form peroxyacetic acid (CH₃C(O)OOH), acetic acid (CH₃C(O)OH), O₃ and OH radicals (Winiberg et al., 2016). Therefore, in order to evaluate the atmospheric importance of the studied ketones an estimation of the acetyl radicals yield is needed.

The product yields corrected for the secondary reactions mentioned above and wall losses in the simulation chambers were obtained using the model outlined in Sect. 4.3.7 and the kinetic parameters listed in Tab. 9.1 and Tab. 9.2 in the Annex. The molar yields for both OH reactions are summarized in Tables 4.4 and 4.5. The sum of PAN and CO₂ is equal to the molar yield of CH₃C(O) radicals. The errors represent the 2 σ statistical error resulting from the average of all experiments and an additional 10 % relative error to cover further uncertainties derived from the evaluation procedure. Exemplary experimental and simulated time profiles of the ketones and the products are shown in Figs. 4.7 and 4.8 for both investigated reaction systems.

Acetoin and acetaldehyde are only affected by secondary consumption. Hence, the model estimates an increase for both yields compared to the experimental values of the 3M3P2 oxidation. By contrast, the biacetyl yields exhibit no difference indicating that the loss by photolysis is nearly compensated by the formation through acetoin oxidation. Both acetaldehyde and biacetyl undergo further oxidation forming eventually PAN and CO₂. In compliance, the experimental concentration-time-profile for acetyl radicals is only reproduced when introducing significantly lower PAN + CO₂ formation yields in the model. In the 4M3P2 system the modelled acetone yield decreases slightly due to the further oxidation of HMPPr. Since methyl glyoxal and HMPPr are influenced only by consumption processes, their corrected yields are higher than the experimentally determined. PAN + CO₂ correction follows the same pattern as in the case of 3M3P2 + OH.

Table 4.4. Uncorrected and corrected molar yields of the 3M3P2 + OH system.

	Acetoin	PAN + CO ₂	Biacetyl	Acetaldehyde
Uncorrected	0.53 ± 0.13	0.69 ± 0.11	0.42 ± 0.13	0.36 ± 0.09
Corrected	0.60 ± 0.18	0.60 ± 0.07	0.41 ± 0.12	0.42 ± 0.15

Table 4.5. Uncorrected and corrected molar yields of the 4M3P2 + OH system.

	Acetone	Methyl glyoxal	HMPPr	PAN + CO ₂
Uncorrected	0.64 ± 0.11	0.58 ± 0.13	0.17 ± 0.05	0.27 ± 0.04
Corrected	0.62 ± 0.09	0.64 ± 0.16	0.20 ± 0.05	0.24 ± 0.06

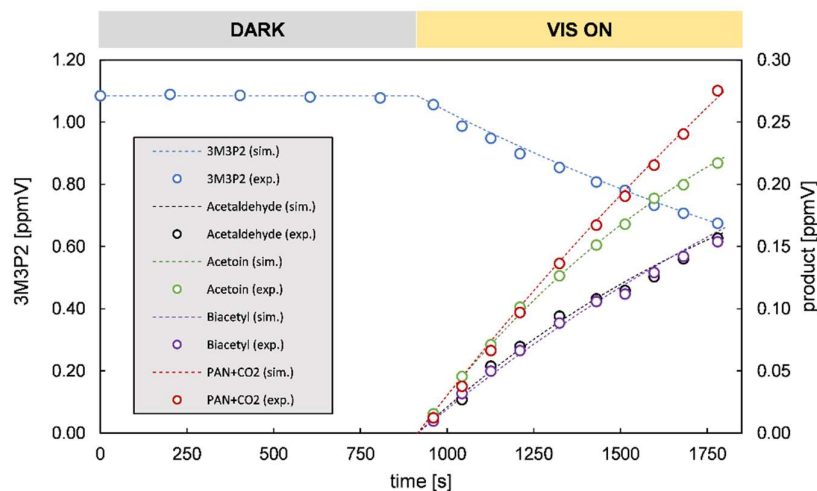


Figure 4.7. Experimental and simulated time profiles obtained for a 3M3P2 + OH experiment.

In all cases the averaged molar yields are in excellent agreement for products expected to be formed in the same reaction channel. Thus, the molar yields of acetaldehyde/biacetyl (pathway β_1 and α_2 , Fig. 4.3), acetoin/(PAN + CO₂) (pathway α_1 , Fig. 4.3), and acetone/methyl glyoxal (pathway β_1 and α_2 , Fig. 4.6) are nearly the same. In the case of 4M3P2 + OH, the yields of HMPPr/(PAN + CO₂) formed according to pathway α_1 (Fig. 4.6) are still in good agreement within the uncertainties. This supports the absorption cross section of HMPPr determined in our study. On the other hand, the results prove that the formation of acetyl radicals can be well quantified by determining the sum of PAN and CO₂ in the experimental set-up.

Among α,β -unsaturated ketones of atmospheric importance only the OH-radical-initiated oxidation of methyl vinyl ketone (MVK) has been investigated in-depth (Tuazon and Atkinson, 1989; Galloway et al., 2011; Praske et al., 2015; Fuchs et al., 2018). Tuazon and Atkinson (1989) quantified methyl glyoxal and glycolaldehyde as the main oxidation products and concluded that addition of the OH radical to the internal and terminal carbon atom accounts for $28 \pm 9\%$ and $72 \pm 21\%$, respectively. This calculation is based on the assumption that the corresponding α -RO radical will favour a bond scission between the carbonyl carbon atom and C _{α} (according to pathway α_1 in Figs. 4.3 and 4.6) due to the much lower predicted energy barrier to decomposition following this pathway (Tuazon and Atkinson, 1989). This has been confirmed by calculations performed by Praske et al. (2015) and is consistent with the SAR provided by Vereecken and Peeters (2009). Assuming $\alpha_1 \gg$

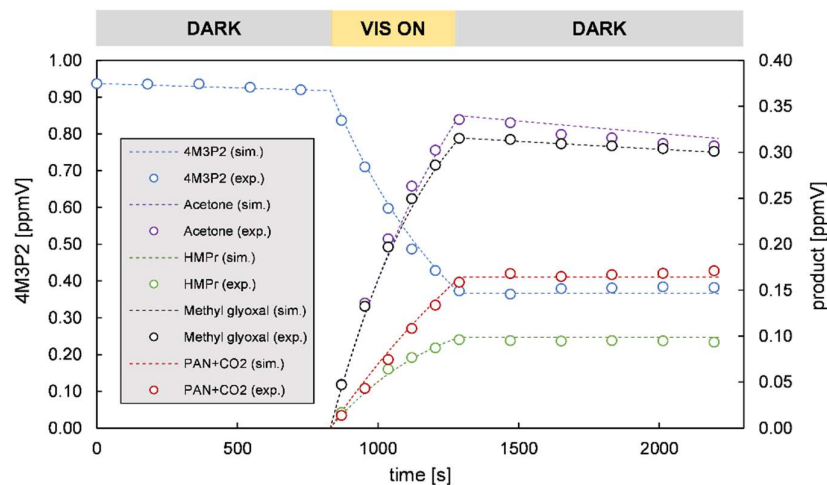


Figure 4.8. Experimental and simulated time profiles obtained for a 4M3P2 + OH experiment.

α_2 (Figs. 4.3 and 4.6) the addition of OH according to the α and β pathways accounts consequently for $60 \pm 18\%$ and $40 \pm 12\%$ for 3M3P2 and $26 \pm 8\%$ and $74 \pm 22\%$ in the case of 4M3P2, respectively, when referenced to the corresponding overall yield. However, at least for 4M3P2 the branching fraction α_2 may be important since the estimated energy barrier is lower than for α_1 according to the SAR of Vereecken and Peeters (2009). Hence, one should note that the fraction given for the addition to C_β (α pathways), respectively. In the limiting case ($\alpha_1 \gg \alpha_2$) this indicates the relationship between the branching ratios of the main channels to be $\alpha > \beta$ for MVK, $\alpha \approx \beta$ for 3M3P2 and $\alpha < \beta$ for 4M3P2 (see Figs. 4.3 and 4.6). Due to hyperconjugation the formation of the higher substituted alkyl radical should be favoured. The addition of OH to C_α leads to a primary alkyl radical in the case of MVK, a secondary for 3M3P2 and a tertiary alkyl radical in the case of 4M3P2. Therefore, while hydrogen bonding should yield a preference of the addition to the β position for all α,β -unsaturated ketones, as discussed previously with respect to the reactivity, the observed trend in the branching ratios (in the limiting case $\alpha_1 \gg \alpha_2$) is possibly related to the stability of the initially formed alkyl radicals. In the case of 4M3P2 the addition to the β -position could also be sterically hindered.

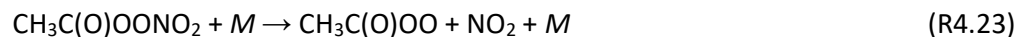
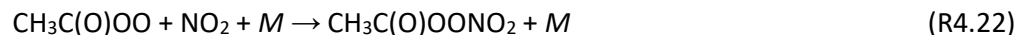
However, one should emphasize that it is not possible to derive the exact branching ratios for α and β without deciphering the branching ratios α_1 and α_2 . An attempt to obtain the corresponding rate coefficients for each decomposition channel according to

Vereecken and Peeters (2009) failed since the calculated branching ratios for α_1 and α_2 are about 0.1 and 0.9, respectively, in the case of 4M3P2 which is contradicted by the observed first-generation yields of 2HMPr and PAN + CO₂. Vereecken and Peeters (2009) stated the accuracy of the predicted rate coefficients to be within a factor of 5–10. Therefore, it is not possible to derive any further statement on the ratio $\alpha_1 : \alpha_2$.

4.4.3.4 ROONO₂ formation

To further elucidate the mechanism, experiments were conducted over a wider range of NO₂/NO ratios by adding different amounts of NO₂ to the reaction mixture. In all experiments the amount of added NO was sufficient to suppress any ozone formation.

Given that CH₃C(O) radicals instantaneously react with oxygen, under the employed experimental conditions, to form the corresponding RO₂ radical, their fate should be described by (a) the reaction with NO, (b) the reaction with NO₂ to yield peroxyacetyl nitrate (PAN), and (c) the thermal dissociation of PAN to re-generate the RO₂ radical.



Based on the Reactions (R4.20)–(R4.23) the ratio PAN/CO₂ should only depend on the NO₂/NO ratio during the reaction under constant pressure and temperature conditions. Therefore, PAN/CO₂ ratios were simulated for various NO₂/NO ratios in the experimental temperature range 295–301 K using the IUPAC recommendations (Atkinson et al., 2006) for the Reactions (R20), (R22) and (R23) (Fig. 4.9). Experimental PAN/CO₂ formation ratios were derived from plotting the generated PAN against the formed CO₂ during the irradiation period. The corresponding average NO₂/NO ratios were determined by averaging the measured mixing ratios of NO and NO₂, respectively, over the same time interval. As can be seen in Fig. 4.9, these data are qualitatively in quite good agreement with the expected ratios based on the model calculations. Hence, the fate of the CH₃C(O) radicals is well-described by the Reactions sequence (R4.19)–(R4.23) in our experiments.

However, in typical methyl nitrite photolysis experiments the NO₂/NO ratios are < 1 if NO is added to suppress ozone formation. Thus, PAN accounts for less than one third of the

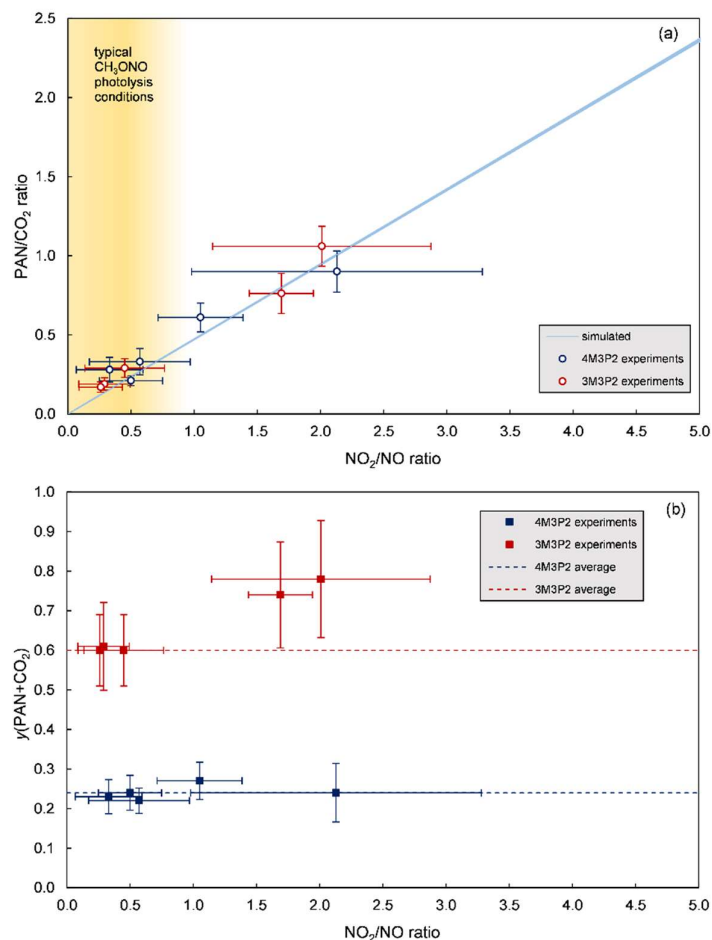


Figure 4.9. (a) Experimentally determined and simulated PAN/CO₂ formation ratio as a function of the NO₂/NO ratio. (b) Determined molar yields for acetyl radicals (as the sum of PAN and CO₂) as a function of the NO₂/NO ratio.

CH₃C(O) radical's fate (Fig. 4.9). If the experimental set-up does not allow HCHO or CO₂ to be quantified, this leads to a fundamental underestimation of the acetyl radical reaction channels. In this case, addition of NO₂ could be useful to favour PAN formation and the determination of the NO₂/NO ratio in the experiment could yield an estimation of the PAN/CO₂ ratio.

On the other hand, Fig. 4.9 clearly shows the invariance of the PAN + CO₂ yield for 4M3P2 under all experimental conditions, within the uncertainties. There is thus likely no ROONO₂ formation from the initially formed α - and β -RO₂ radicals since they are either not formed or their thermal dissociation is too large to play any role. This meets one's

expectations as, according to literature references (Calvert et al., 2015), the lifetimes of alkylperoxy nitrates are of the order of seconds at 298 K and 1 atm and so they become relevant as a NO_x reservoir when formed at lower temperatures, encountered in the upper troposphere. However, assuming an average OH concentration of $1 \times 10^6 \text{ cm}^{-3}$ (Bloss et al., 2005) the atmospheric lifetime (with respect to OH) is about 3.4 h, thus too short for 4M3P2 to enter higher altitudes. Therefore, except for PAN, ROONO_2 formation does not play any role for 4M3P2.

In the case of 3M3P2 significantly higher yields for PAN + CO_2 were observed for higher NO_2/NO ratios while being quite consistent at $\text{NO}_2/\text{NO} < 1$ (Fig. 4.9). This is actually contradictory as additional ROONO_2 formation from the initial α - and β - RO_2 radicals should lower the overall yields of the main products. However, the molar yields of biacetyl and acetaldehyde are essentially the same as in the other experiments. Thus, the carbon balance exceeds 100 % in the higher NO_2/NO ratio experiments. Unfortunately, these two experiments were the last in a series and it is quite probable that due to wall loading the wall acted as a source of $\text{CH}_3\text{C}(\text{O})$ radicals during the irradiation. The yield for PAN + CO_2 was therefore only given as an average of the experiments with $\text{NO}_2/\text{NO} < 1$.

4.4.3.5 RONO_2 formation

Given that the carbon balance is about one for 3M3P2 and about 0.85 for 4M3P2, respectively, this results in an upper limit of the overall RONO_2 yield of 0.15 for 4M3P2 while almost no RONO_2 formation occurs in the case of 3M3P2. This is qualitatively in good agreement with the residual spectra clearly indicating the presence of organic nitrates only in the case of 4M3P2. Noda et al. (2000) determined an average absorption cross section of $(1.25 \pm 0.20) \times 10^{-17} \text{ cm molecule}^{-1}$ (base 10) for the nitrooxy group absorption in the range 800–900 cm^{-1} by averaging available absorption cross sections of organic nitrates. Following this approach, an estimated RONO_2 yield of 0.06 ± 0.03 is determined which should be regarded as lower limit. While the determined wall loss is in the order of $2 \times 10^{-4} \text{ s}^{-1}$ the potentially formed RONO_2 species could also be subject of photolysis and oxidation by OH radicals. SAR methods for the prediction of OH rate coefficients were shown to fail at carbonyl nitrates (Suarez-Bertoa et al., 2012). Therefore, Suarez-Bertoa et al. (2012) proposed alternative substituent factors optimized for carbonyl nitrates in which the factor for the $-\text{ONO}_2$ group is less deactivating than in other SAR approaches. Applying this factors to the SAR of Kwok and Atkinson (1995) yields predicted rate coefficients of $1.3 \times 10^{-12} \text{ cm}^3 \text{ molecule}^{-1} \text{ s}^{-1}$ and $5 \times 10^{-13} \text{ cm}^3 \text{ molecule}^{-1} \text{ s}^{-1}$ for the α - RONO_2 and β - RONO_2 , respectively,

which would correspond to loss rates of about $1.3 \times 10^{-5} \text{ s}^{-1}$ and $5 \times 10^{-6} \text{ s}^{-1}$, respectively, due to the OH reaction. For α - and β -carbonyl nitrates it was shown that photolysis dominates over the OH initiated oxidation (Suarez-Bertoa et al., 2012; Picquet-Varrault et al., 2020). Hence, by comparison with available data (Suarez-Bertoa et al., 2012; Picquet-Varrault et al., 2020) larger loss rates result likely from photolysis of the RONO₂ species in our experiments. However, we believe that any further statement would be highly speculative. A RONO₂ yield of about 0.11 ± 0.03 has been reported for MVK based on model-assisted isoprene photooxidation experiments (Paulot et al., 2009). On the other hand, an overall RONO₂ yield of about 0.040 ± 0.006 has been determined in MVK oxidation experiments (Praske et al., 2015). Thus, the limits (0.06–0.15) reported here for the overall organic nitrate yield are consistent with the data dispersion found in the literature.

If the branching fractions for the pathways α_{ON} and β_{ON} in the 4M3P2 oxidation (Fig. 4.6) were the same this would correspond to a much larger formation yield of the multifunctional β -RONO₂ than α -RONO₂ simply due to the predominant addition of the OH radical to C _{α} . This would be consistent with the previous assignment of the residual's spectral features to the β -RONO₂. Former studies on alkenes have shown a structure-dependent RONO₂ yield derived from β -hydroxyperoxy radicals. Accordingly, the nitrate yields resulting from tertiary RO₂ were larger than those produced from secondary RO₂, which, in turn, were larger when compared to nitrate yields obtained from primary RO₂, respectively (Matsunaga and Ziemann, 2010). This would indicate $\beta_{\text{ON}} > \alpha_{\text{ON}}$ in the 4M3P2 oxidation (Fig. 4.6). Besides, Praske et al. (2015) found a 2-times-larger branching ratio for the β -RONO₂ species resulting from MVK + OH than for the α -RONO₂. They interpreted this finding in terms of a larger destabilizing effect on the initially formed ROONO complex caused by the closer carbonyl group in the case of the α -RONO₂. Both results further support the assignment of the residual absorptions to the β -RONO₂ species.

By contrast, both potentially formed RONO₂ species in the 3M3P2 oxidation would contain a quaternary C _{α} atom surrounded by bulky substituents. Thus, the almost negligible nitrate formation in the case of 3M3P2 is possibly attributed to the steric hindrance of the hypothetically resulting RONO₂ species.

4.4.4 Atmospheric implications and conclusions

Within this work we determined the rate coefficients for the OH radical and Cl atom-initiated oxidation of 3M3P2 and 4M3P2. This adds to the kinetic information concerning the reaction of these two compounds with NO₃ and O₃ reported previously (Sato et al.,

Table 4.6. Estimated tropospheric lifetimes for the studied α,β -unsaturated ketones. The lifetimes were calculated using the following concentrations: ^a global mean of 1×10^6 molecule cm^{-3} (Bloss et al., 2005), ^b 12 h average of 3×10^4 molecule cm^{-3} (Wingenter et al., 1996), ^c 24 h average of 7×10^{11} molecule cm^{-3} (Logan, 1985), and ^d 12 h average of 5×10^8 molecule cm^{-3} (Atkinson, 1991). Rate coefficients were taken from: ^e this work, ^f Illmann et al. (2021a), and ^g Canosa-Mas et al. (2005).

Compound	$\tau(\text{OH})^{\text{a}}/\text{h}$	$\tau(\text{Cl})^{\text{b}}/\text{h}$	$\tau(\text{O}_3)^{\text{c}}/\text{h}$	$\tau(\text{NO}_3)^{\text{d}}/\text{h}$
3M3P2	4.3 ^e	33.1 ^e	5.0 ^f	3.6 ^g
4M3P2	3.4 ^e	29.9 ^e	47.2 ^f	3.9 ^g

2004; Canosa-Mas et al. 2005; Illmann et al. 2021a; Li et al., 2021) in an effort to complete the gaps in the knowledge needed for modelling chemistry in the atmosphere. The yields for the identified products formed in both target reactions were found to be independent of the chamber used, the mixing ratios and the light intensity, thus giving confidence in the experimental results.

Using the kinetic data together with reasonable average concentrations for the respective oxidants (Logan, 1985; Atkinson, 1991; Wingenter et al., 1996; Bloss et al., 2005) allows to estimate tropospheric lifetimes as presented in Tab. 4.6, where $\tau(X)$ is the lifetime with respect to the oxidant X calculated according to $1/(k_x[X])$. Both unsaturated ketones did not show measurable photolysis rates in the present experimental set-up. In the atmosphere, their photodissociation lifetimes are expected to have a range of the order of days (Mellouki et al., 2015). Consequently, compared to $\tau(\text{OH})$, the photodissociation of both unsaturated ketones is evidently not an important process in the troposphere. The values in Tab. 4.6 indicate the OH radical as the dominant sink during daytime whereas the NO_3 radical plays a similar role at night. However, for 3M3P2 the O_3 reaction appears quite competitive during both day and night (Tab. 4.6). These estimated lifetimes indicate an oxidative degradation near the emission sources. Nevertheless, a further part of this work indicates that both ketones potentially impact atmospheric processes on a larger scale due to their huge potential of forming NO_x reservoir species like PAN. In this respect, we have shown that the reaction of OH with both 3M3P2 and 4M3P2 yield $\text{CH}_3\text{C}(\text{O})$ radicals by prompt decomposition of primary formed RO radicals. In the present work the sum of PAN and CO_2 could be used successfully to determine the formation yield of $\text{CH}_3\text{C}(\text{O})$ radicals in both reaction systems. Moreover, nearly all other identified oxidation products like methyl glyoxal, acetone, acetaldehyde, acetoin and biacetyl are known to generate $\text{CH}_3\text{C}(\text{O})$ radicals in their further oxidation processes - simulations based on field data collected

worldwide estimate that acetaldehyde, methyl glyoxal and acetone within the troposphere account for about 81 % of the global source for PAN formation (Fischer et al., 2014).

Among the oxidation products of both 3M3P2 and 4M3P2 at least methyl glyoxal is a well-known source of secondary organic aerosol in atmosphere (Fu et al., 2008).

On the other hand, future work is needed to identify clearly the missing products of the OH-radical-initiated oxidation of 4M3P2. The absorptions of the residual spectra could be tentatively assigned to the β -RONO₂ species. However, other detection methods are necessary for an unambiguous identification and quantification of this species.

5 Biomass burning plume chemistry: OH-radical initiated oxidation of 3-penten-2-one and its main oxidation product 2-hydroxypropanal

This chapter has been reprinted from “Illmann, N., Patroescu-Klotz, I., and Wiesen, P.: Biomass burning plume chemistry: OH-radical-initiated oxidation of 3-penten-2-one and its main oxidation product 2-hydroxypropanal, *Atmos. Chem. Phys.*, 21, 18557–18572, <https://doi.org/10.5194/acp-21-18557-2021>, 2021”, used under CC BY 4.0 (<https://creativecommons.org/licenses/by/4.0/>). The typeset, numbering of tables and figures, and the numbering of references were modified from the original.

5.1 Abstract

In order to enlarge our understanding of biomass burning plume chemistry, the OH-radical-initiated oxidation of 3-penten-2-one (3P2), identified in biomass burning emissions, and 2-hydroxypropanal (2HPr) was investigated at 298 ± 3 K and 990 ± 15 mbar in two atmospheric simulation chambers using long-path FTIR spectroscopy. The rate coefficient of $3P2 + OH$ was determined to be $(6.2 \pm 1.0) \times 10^{-11} \text{ cm}^3 \text{ molecule}^{-1} \text{ s}^{-1}$ and the molar first-generation yields for acetaldehyde, methyl glyoxal, 2HPr and the sum of PAN and CO_2 , used to determine the $\text{CH}_3\text{C}(\text{O})$ radical yield, were 0.39 ± 0.07 , 0.32 ± 0.08 , 0.68 ± 0.27 , and 0.56 ± 0.14 , respectively, under conditions where the 3P2 derived peroxy radicals react solely with NO. The $2HPr + OH$ reaction was investigated using $3P2 + OH$ as a source of the α -hydroxyaldehyde adjusting the experimental conditions to shift the reaction system towards secondary oxidation processes. The rate coefficient was estimated to be $(2.2 \pm 0.6) \times 10^{-11} \text{ cm}^3 \text{ molecule}^{-1} \text{ s}^{-1}$. Employing a simple chemical mechanism to analyse the temporal behaviour of the experiments, the further oxidation of 2HPr was shown to form methyl glyoxal, acetaldehyde and CO_2 with estimated yields of 0.27 ± 0.08 , 0.73 ± 0.08 , and 0.73 ± 0.08 , respectively.

5.2 Introduction

Unsaturated ketones are of increasing interest as more sources for their atmospheric burden are uncovered. They are potentially formed in the atmospheric oxidation of terpenes involving OH radicals or O_3 molecules. 3-Buten-2-one (methyl vinyl ketone) is the most famous representative formed through the gas-phase oxidation of the most abundantly emitted non-methane hydrocarbon (NMHC), namely isoprene (Calvert et al.,

2000). Other α,β -unsaturated ketones, however, are used in the food and fragrances industry (Bickers et al., 2003). Ciccioli et al. (2001) investigated controlled biomass burning emissions representative for the Mediterranean vegetation and identified 3-penten-2-one (3P2) in both the flaming and smoldering of pine wood. Hatch et al. (2017) identified 3P2 among various oxygenated species in the gas-phase biomass burning emissions of Chinese rice straw, Indonesian peat and boughs of ponderosa pine and black spruce during the FLAME-4 campaign. Besides, they also identified 2-methylpenta-1,3-diene (Hatch et al., 2017) which potentially yields 3P2 in the further gas-phase oxidation. All these findings pinpoint 3P2 as a likely constituent of most biomass burning (BB) plumes.

Understanding the BB plume chemistry is of global interest since their photochemical aging is believed to be a potentially significant contributor to ozone and organic aerosol formation (Jaffe et al., 2008; Yokelson et al., 2009; Alvarado et al., 2015). For instance, Jaffe et al. (2008) found a correlation between the interannual variation in O_3 and burned area in the western USA. During the next decades a drier climate, expected due to global warming, will likely result in an increase in both the number and intensity of fire events worldwide, which could consequently enlarge the influence of biomass burning on air quality. Some field measurements of BB plumes have shown that wildfires may increase significantly the ozone enhancement ratios ($\Delta O_3/\Delta CO$) (Mauzerall et al., 1998; Honrath et al., 2004) while in others a correlation between O_3 and CO could not be observed (Alvarado et al., 2010). Given typical VOC/ NO_x emission ratios from biomass burning, ozone formation is mainly limited by the availability of NO_x , which, in turn, depends on the fuel nitrogen content and the combustion efficiency (Jaffe and Wigder, 2012 and references therein). Alvarado et al. (2010) were the first to observe a fast peroxyacetyl nitrate (PAN) production in a young boreal smoke plume within the first hours after emission. Simulations of a young BB plume from a prescribed fire showed the evolution of secondary organic aerosol and O_3 to be sensitive to unidentified VOCs whose chemistry is likely characterized, amongst others, through (a) OH rate coefficients in the order of $10^{-11} \text{ cm}^3 \text{ molecule}^{-1} \text{ s}^{-1}$, (b) $RO_2 + NO$ reactions resulting mainly in fragmentation, and (c) an efficient HO_2 regeneration (Alvarado et al., 2015). However, this resulted still in a significant overestimation of downwind PAN formation (Alvarado et al., 2015). Accordingly, given the complexity of biomass burning smoke and the various conditions possible within both a young and an aged plume the chemistry is still not well characterized. In particular, the oxidation of very reactive organic species seems to be crucial for a comprehensive picture.

The present work therefore contributes expanding our understanding of BB plume chemistry by studying the oxidation processes of single species, identified in gas-phase

emissions, in simulation chamber experiments. In this respect we investigated the OH-radical-initiated oxidation of 3P2 and the fate of its main oxidation product. Up to now, to the best of our knowledge, only kinetic data were reported for the reactions of 3P2 with OH radicals and Cl atoms (Blanco et al., 2012), NO₃ radicals (Canosa-Mas et al., 2005) and O₃ (Greene and Atkinson, 1994; Sato et al., 2004; Illmann et al., 2021a).

5.3 Experimental

Kinetic and product study experiments were conducted in two indoor simulation chambers at 298 ± 3 K and in 990 ± 15 mbar of synthetic air. In both chambers OH radicals were generated by the photolysis of methyl nitrite in the presence of sufficient amounts of NO to suppress any ozone formation and consequently the generation of NO₃ radicals. Methyl nitrite has been synthesized by the dropwise addition of sulphuric acid to a saturated aqueous solution of sodium nitrite in methanol according to a method previously outlined by Taylor et al. (1980). The product was collected and stored in a cooling trap at 195 K. Its purity was verified via FTIR spectroscopy.

5.3.1 480 L Chamber

The cylindrical borosilicate glass tube with a length of 3 m and 0.45 m inner diameter is surrounded by 32 superactinic fluorescent lamps (Philips TL A 40W: 300–460 nm, I_{\max} at 360 nm) and closed at both ends by aluminium flanges. These contain various ports for the introduction of reactants and bath gas and the coupling with analytical devices. The pumping system consists of a rotary vane pump and a roots pump yielding an end vacuum up to 10^{-3} mbar. A White-type mirror system is installed inside the chamber (optical path length: 50.4 ± 0.2 m) and coupled to a Nicolet 6700 FTIR spectrometer to monitor reactants and products. Spectra are recorded in the spectral range 4000–700 cm^{-1} with a resolution of 1 cm^{-1} . The present set-up of the chamber is described with further details in the recent literature (Illmann et al., 2021b).

The initial mixing ratios in the 480 L chamber experiments in ppmV (1 ppmV = 2.46×10^{13} molecules cm^{-3} at 298 K) were: 5.8–9.4 for 3P2, 5.0 for isoprene, 8.3 for E2-butene, 10–16 for methyl nitrite, and 20–27 for NO.

5.3.2 1080 L Chamber

The 1080 L chamber consists of two joint quartz-glass tubes with a total length of 6.2 m and 0.47 m inner diameter. It is surrounded by 32 superactinic fluorescent lamps (Philips

TL05 40W: 300–460 nm, I_{\max} at 360 nm) and 32 low-pressure mercury vapour lamps (Philips TUV 40W, I_{\max} at 254 nm) which can be switched individually. The pumping system consists of a turbo-molecular pump backed by a double-stage rotary fore pump to yield an end vacuum of 10^{-4} mbar. The White-type mirror system installed inside the chamber is operated at a total optical path length of 484.7 ± 0.8 m and coupled to a Nicolet iS50 FTIR spectrometer recording FTIR spectra in the range 4000–700 cm^{-1} with a resolution of 1 cm^{-1} . A more detailed description of the chamber can be found in the recent literature (Illmann et al., 2021b).

The initial mixing ratios in the 1080 L chamber experiments, in ppmV (1 ppmV = 2.46×10^{13} molecules cm^{-3} at 298 K), were: 1.1–1.3 for 3P2, 0.9–1.1 for isoprene, 1.3–1.5 for E2-butene, 0.9–1.9 for methyl nitrite, and 2.0–3.7 for NO, 1.5–1.7 for 3-buten-2-ol, 1.3–1.4 for 3-penten-2-ol, and 13000–17000 for CO.

5.3.3 Methods

The rate coefficient of the 3P2 + OH reaction has been determined using the relative-rate technique, thus by relating the consumption of 3-penten-2-one to the consumption of a reference compound. If reactions other than presented below (Reactions R5.1–R5.3) are negligible in the experimental set-up,



the following equation can be used to determine the rate coefficient $k_{3\text{P2}}$:

$$\ln \left(\frac{[3\text{P2}]_0}{[3\text{P2}]_t} \right) - k_{\text{loss}} \times t = \frac{k_{3\text{P2}}}{k_{\text{ref}}} \times \ln \left(\frac{[\text{ref.}]_0}{[\text{ref.}]_t} \right) \quad (5.1)$$

where $[X]_t$ is the concentration of the species X at time t. The rate coefficient ratio $k_{3\text{P2}}/k_{\text{ref}}$ used to calculate $k_{3\text{P2}}$ were thus obtained from regression analysis after plotting $\left\{ \ln \left(\frac{[3\text{P2}]_0}{[3\text{P2}]_t} \right) - k_{\text{loss}} \times t \right\}$ against $\left\{ \ln \left(\frac{[\text{ref.}]_0}{[\text{ref.}]_t} \right) \right\}$.

Mixing ratios of identified species in the product study experiments were obtained by subtracting calibrated reference FTIR spectra of the target species. The cross sections we used for calibration were taken either from the literature, in the case of methyl glyoxal

(Profeta et al., 2011; Talukdar et al., 2011) and peroxyacetyl nitrate (Allen et al., 2005), the internal Wuppertal laboratory database (acetaldehyde) or determined within this work (3-penten-2-one, 2-hydroxypropanal). CO₂ was quantified by the integration of the absorption features in the spectral range 2400–2349 cm⁻¹ and a polynomial calibration function derived from the injection of various volumes of CO₂ using a calibrated gas-tight syringe. Uncorrected molar formation yields of the reaction products were calculated by plotting the mixing ratio of formed product against the mixing ratio of the consumed 3-penten-2-one. In order to obtain first-generation yields (= yields without impact of secondary reactions in the experimental set-up), the temporal behaviour of all quantified species was simulated following the approach previously outlined in the recent literature (Illmann et al., 2021b). Here, the differential equations are constructed based on the simplified reaction sequence of each species and solved by the Euler method using calculation software like Microsoft Excel. Input parameters are the rate coefficients of each of the sequence's reaction, the initial concentration of 3P2 and the time-dependent OH-concentration calculated based on the 3P2 consumption. The molar formation yields for products of the target reaction are included as variable parameters to be modified until the simulated temporal behaviour of each species matches the experimental data. The details are provided within Sect. 5.4.4.

Cross sections and reference FTIR spectra of 2HPr were obtained by the in situ generation of the aldehyde through the ozonolysis of 3-buten-2-ol and 3-penten-2-ol, respectively, in the presence of sufficient CO to scavenge any OH radical formed during the O₃ reaction, in the 1080 L chamber. In order to investigate the OH oxidation of 2HPr, the 3P2 + OH reaction was used as a source of the α -hydroxyaldehyde. An estimation of the rate coefficient was obtained following the procedure outlined previously by Baker et al. (2004). Branching ratios for the product formation were derived from modelling the temporal behaviour of the relevant species using our recently presented approach (Illmann et al., 2021b).

Typically, 15 spectra were recorded per experiment and the first five spectra were collected in the dark to determine potential wall losses in each experiment. In the product study experiments five spectra were additionally recorded after the OH reaction was terminated (the lamps were switched off) in order to check for the wall loss rates of each formed reaction product. For the 2HPr + OH investigations, a second methyl nitrite and NO injection occurred after the first irradiation period, in the dark, followed by further irradiation. About 50–70 scans were co-added per spectrum which leads to averaging

periods of about 80–115 s. Time intervals for both irradiation and dark periods of the experiments were in the order of 15 min.

For economic reasons, the housing which enfolds the transfer optics between FTIR spectrometer and chamber is flushed with purified dry air. Therefore, quantification of CO₂ is, due to a slight variability in the dry air supply, unreliable under normal laboratory conditions. To be able to quantify CO₂, in selected product study experiments, the transfer optics housing was flushed with ultrapure N₂ evaporated from a liquid nitrogen tank.

5.3.4 Materials

The following chemicals have been used without further purification and purities as stated by the suppliers: 3-penten-2-one (Alfa Aesar, technical grade 85 %), trans-2-butene (Messer, 99 %), isoprene (Aldrich, 99 %), 3-buten-2-ol (Alfa Aesar, 97 %), 3-penten-2-ol (Sigma Aldrich, 96 %), NO (Air Liquide, 99.5 %), CO (Air Liquide, 99.97 %), synthetic air (Messer, 99.9999 %). While the supplier states the predominance of the trans isomer for 3-penten-2-ol the cis/trans isomer ratio is not specified for 3-penten-2-one. The latter compound is not commercially available with purities higher than 85 %. Another sample of 70 % purity (technical grade) contains, as stated by the supplier, 30 % 4-methyl-3-penten-2-one as impurity. However, the gas-phase FTIR spectra of the 70 % sample after subtraction of the 4-methyl-3-penten-2-one content are identical to the spectra recorded for the 85 % sample. It is therefore reasonable to assume that no absorptions other than those belonging to 3-penten-2-one are present in the spectra of the used sample.

5.4 Results and discussion

The first-order wall loss of 3P2 was $< 1 \times 10^{-5} \text{ s}^{-1}$ in all 480 L chamber experiments and in the range of $(5 - 10) \times 10^{-5} \text{ s}^{-1}$ in the 1080 L chamber experiments, respectively. Typically, the consumption through OH radicals was about one order of magnitude faster than the wall loss. The reference compounds did not show any wall loss. Photolysis and dark reactions between 3P2 and the radical source were found to be negligible under all experimental conditions.

5.4.1 3-Penten-2-one + OH kinetics

Kinetic experiments were performed in both chambers under varying light intensity using isoprene and E2-butene as references. The relative-rate plots according to Eq. (5.1) are presented in Fig. 5.1 for all performed experiments. The relative ratios k_{3P2}/k_{ref} , determined

for each individual experiment following regression analysis, agree within < 13 % using isoprene and < 9 % using E2-butene as reference compound, respectively. Intercepts of the regression lines were found to be zero within a 2σ statistical error and the correlation coefficients were $R^2 > 0.99$. Given the latest IUPAC recommendations (Mellouki et al., 2021) for the rate coefficients of the OH radical reactions with E2-butene ($k = (7.1 \pm 1.1) \times 10^{-11} \text{ cm}^3 \text{ molecule}^{-1} \text{ s}^{-1}$) and isoprene ($k = (1.0 \pm 0.2) \times 10^{-10} \text{ cm}^3 \text{ molecule}^{-1} \text{ s}^{-1}$), respectively, the calculated rate constants for 3P2 derived from both references are in excellent agreement. All this suggests that secondary processes other than wall loss can be neglected in the present experimental set-up. Table 5.1 summarizes the results obtained from all conducted kinetic experiments. The weighted average rate coefficient is $(6.2 \pm 1.0) \times 10^{-11} \text{ cm}^3 \text{ molecule}^{-1} \text{ s}^{-1}$ where the quoted error results from the 2σ statistical error of the weighted mean and an additional 10 % relative error to cover uncertainties derived from the experimental and evaluation procedure.

The rate coefficient of 3P2 has been determined previously in our laboratory ($k_{3P2} = (7.22 \pm 1.74) \times 10^{-11} \text{ cm}^3 \text{ molecule}^{-1} \text{ s}^{-1}$) based on experiments employing a 3P2 sample, which contained about 30 % mesityl oxide as major impurity (Blanco et al., 2012). Nevertheless, both determinations agree within 20 % and the value obtained here is within the uncertainties of the former study.

5.4.2 In situ generation of 2-hydroxypropanal

2-Hydroxypropanal (2HPr) is one of the expected main products in the OH-radical-initiated oxidation of 3P2. This α -hydroxyaldehyde, commonly known as lactaldehyde, is available commercially only as 1 M aqueous solutions, where various dimer species coexist (Takahashi et al., 1983). Therefore, in order to obtain gas-phase FTIR spectra and cross sections of 2HPr, the ozonolysis reactions of 3-buten-2-ol (3B2OL) and 3-penten-2-ol (3P2OL) were used to generate the α -hydroxyaldehyde in situ in the 1080 L chamber. Given the wall loss of 2HPr, observed in most of the 3P2 product study experiments in the 1080 L chamber (see Sect. 5.4.3), the 3B2OL ozonolysis experiments were optimized to ensure large product formation ratios with negligible losses.

It is well established that ozonolysis reactions proceed through a 1,3-dipolar cycloaddition forming initially a five-membered primary ozonide (POZ), which readily decomposes through bond scission between the carbon atoms of the former C=C bond and one of the O-O bonds. Hence, assuming this to be the only reaction pathway taking place, each of the two possible decomposition channels results in the formation of a stable carbo-

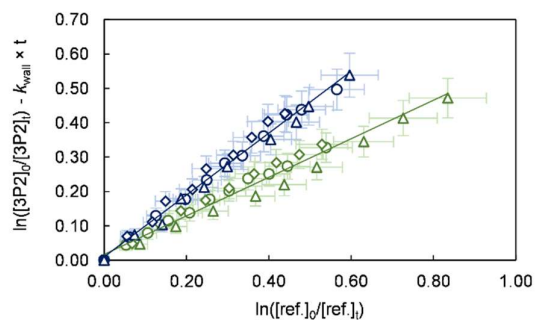


Figure 5.1. Relative-rate plots of all experiments using isoprene (green) and E2-butene (blue) as references. Different experimental runs for each reference are denoted with different symbols. The error bars consist of a systematic uncertainty and an additional 10 % relative error to cover uncertainties derived from the experimental and evaluation procedure, respectively.

nyl species and a Criegee intermediate (CI) as shown in Fig. 5.2. 3-Buten-2-ol ozonolysis leads to formaldehyde as one of the primary carbonyls. When comparing the product spectra obtained here to infrared spectra of 1,2-epoxybutane, there is no indication for epoxide formation in the 3B2OL ozonolysis spectra thus giving confidence in the correctness of the initial assumption. Since the sum of the yields of both HCHO and 2HPr, expected to be the other primary carbonyl (Fig. 5.2), should accordingly be equal to unity, then the 2HPr yield ($y_{2\text{HPr}}$) is defined as $1 - y_{\text{HCHO}}$. This allows us to derive a correlation between the integrated absorption of 2HPr and its concentration. Beside HCHO and 2HPr acetaldehyde formation can be observed unambiguously in the 3B2OL ozonolysis system. The acetaldehyde yield was reproducible throughout all 3B2OL experiments. The formation can only be explained by decomposition of the CI formed according to channel (a) (Fig. 5.2). Our results show that acetaldehyde accounts for $36 \pm 10\%$ of the CI decomposition in the 3B2OL ozonolysis. However, the fate of CIs is sensitive to the degree of excitation, which is not necessarily the same for different ozonolysis systems. Given that the same CI is formed in the 3P2OL ozonolysis (Fig. 5.2) acting as potential secondary source of acetaldehyde this experimental system turned out to be improper for a cross section determination of 2HPr. The 3P2OL ozonolysis has therefore only been used for confirmation of the 2HPr spectral features by comparison with the 3B2OL experimental system (see Sect. 5.4.3).

The observed yield for the primary aldehyde HCHO (0.38 ± 0.06) is well below 0.5, thus indicating a preference of the POZ decomposition towards 2HPr formation. Since the OH absorption band centred around 3550 cm^{-1} (integration range: $3580\text{--}3500\text{ cm}^{-1}$) is expected to be free from interferences of other unidentified species this band was chosen to

Table 5.1. Results of the 3P2 + OH kinetic experiments.

Experiment	Reference	$k_{3P2}/k_{ref.}$	$k \times 10^{11}$ ($\text{cm}^3 \text{ molecule}^{-1} \text{ s}^{-1}$)
3P2 no. 1 ^a	Isoprene	0.60 ± 0.03	6.0 ± 1.0
3P2 no. 2 ^a	E2-Butene	0.89 ± 0.04	6.3 ± 1.0
3P2 no. 3 ^a	E2-Butene	0.97 ± 0.06	6.9 ± 1.1
3P2 no. 4 ^a	Isoprene	0.63 ± 0.04	6.3 ± 1.0
3P2 no. 5 ^b	E2-Butene	0.89 ± 0.04	6.3 ± 1.0
3P2 no. 6 ^b	Isoprene	0.56 ± 0.03	5.6 ± 0.9
		Average	6.2 ± 1.0

^a Performed in the 1080 L chamber, ^b performed in the 480 L chamber.

determine a cross section for 2HPr based on the comparison of FTIR spectra of both ozonolysis systems and residuals of the 3P2 + OH system. A plot of the integrated OH absorption versus the concentration of 2HPr, calculated based on the yields as discussed above, is shown in Fig. 9.2 in the Annex. The cross section for the integrated OH absorption band was determined as $(5.0 \pm 1.5) \times 10^{-18} \text{ cm molecule}^{-1}$ (base *e*) by averaging the results of all individual experiments. The experimental results agree within 9 % but given the error of the HCHO yield and the wall loss of 2HPr we prefer, however, to assign an expanded uncertainty of 30 %.

5.4.3 3-Penten-2-one + OH mechanism

Product study experiments were carried out in both simulation chambers. After subtraction of 3P2 and the species related to the methyl nitrite photolysis itself (methyl nitrite, methyl nitrate, NO, NO₂, HONO, HNO₃, and HCHO) the FTIR spectra contain absorption features that can be attributed unambiguously to acetaldehyde, methyl glyoxal and peroxyacetyl nitrate (PAN). CO₂ formation is observed by the absorption features in the range 2400–2250 cm⁻¹. Plots of the identified products (in ppmV without corrections) versus the consumed 3P2 corrected for the wall loss (in ppmV) are presented in Fig. 5.3 for all conducted experiments. In the case of methyl glyoxal and acetaldehyde these correlations exhibit a very high linearity. This indicates clearly their formation as primary products in the OH initiated oxidation of 3P2. Molar formation yields based on averaging the results of the regression analysis of each experiment are 0.40 ± 0.07 and 0.29 ± 0.09 for acetaldehyde and methyl glyoxal, respectively, without corrections other than the 3P2 wall loss. The errors represent the corresponding precision errors. The larger relative error associated with methyl glyoxal results from a larger scattering in the experimental data.

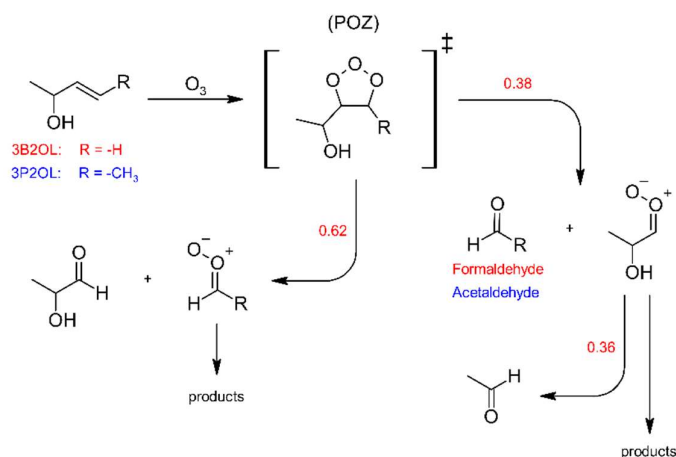


Figure 5.2. Formation of 2-hydroxypropanal through the ozonolysis of 3-buten-2-ol (3B2OL, red) and 3-penten-2-ol (3P2OL, blue) and respective average branching ratios. For readability reasons only one stereoisomer is drawn for each Criegee Intermediate.

Based on the structure-activity relationship (SAR) approach provided by Kwok and Atkinson (1995) the group rate constant is in the order of $10^{-13} \text{ cm}^3 \text{ molecule}^{-1} \text{ s}^{-1}$ for H-atom abstraction from the terminal methyl groups whereas, addition to the C=C double bond accounts for about $10^{-11} \text{ cm}^3 \text{ molecule}^{-1} \text{ s}^{-1}$. Hence, it is very likely that the OH radical will add almost exclusively to either the α - or β -carbon atom to form the corresponding α - or β -hydroxyalkyl radical. Under atmospheric conditions these radicals will react immediately with molecular oxygen yielding the corresponding hydroperoxy radicals. By employing an excess of NO virtually all RO_2 radicals will react with NO and form mainly hydroxyalkoxy radicals (Fig. 5.4). A fraction of the $RO_2 + NO$ reaction might also produce organic nitrates ($RONO_2$). The β -RO radical could react either with oxygen to yield a 1,3-dicarbonyl species (Fig. 5.4, pathway β_2) or dissociate to form acetaldehyde. The co-built hydroxyalkyl radical will react subsequently with oxygen yielding methyl glyoxal, in agreement with our experimental observations.

Formation of PAN originates from $CH_3C(O)$ radicals, generated in the reaction system through the subsequent reactions with oxygen and NO_2 . However, we recently pointed out that under the typical experimental conditions when the methyl nitrite photolysis is used as source for OH radicals, PAN formation accounts only for up to one-third of the fate of acetyl radicals (Illmann et al., 2021b). The main fate of the readily formed acetyl peroxy radical will be the reaction with NO which eventually yields CO_2 and HCHO. Since HCHO is

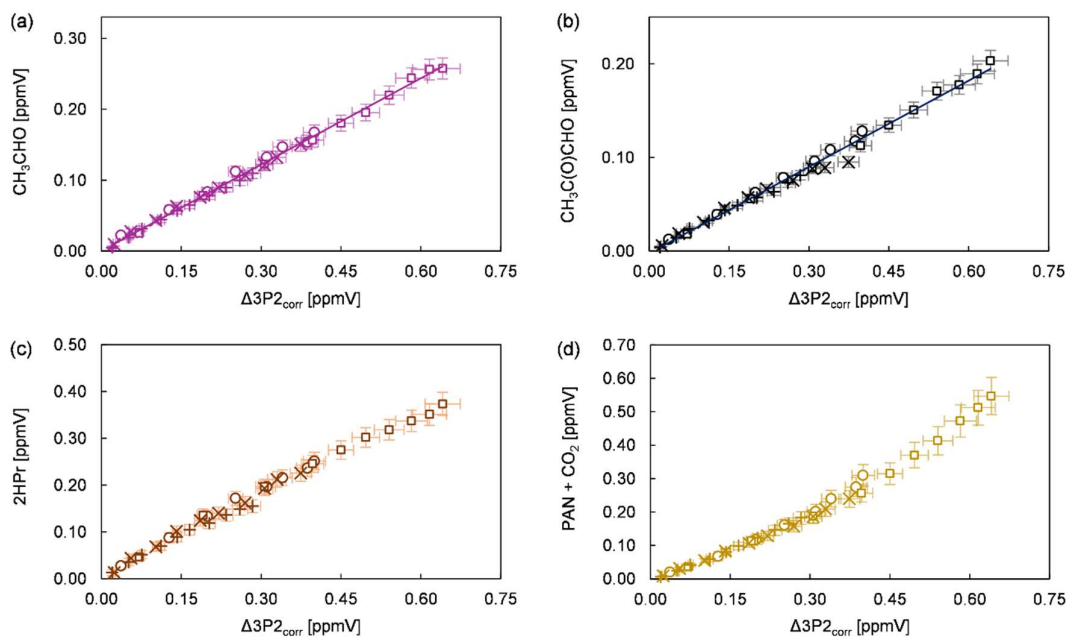


Figure 5.3. Yield plots for (a) acetaldehyde, (b) methyl glyoxal, (c) 2-hydroxypropanal, and (d) the sum of PAN and CO₂ for all conducted experiments corrected for the wall loss of 3P2. The error bars consist of the corresponding precision error. The data of the 480 L chamber experiments are multiplied with a factor of 0.1 to fit within the scale of 1080 L chamber experiments. Different experimental runs are denoted with different symbols.

formed in the methyl nitrite photolysis itself, the sum of PAN and CO₂ has been used to estimate the formation yield of CH₃C(O) radicals. The correlation between (PAN + CO₂) and $\Delta 3P2$ is strongly linear up to a consumption of about 30 % (Fig. 5.3) and becomes precisely non-linear with higher levels of the 3P2 consumption. This indicates strongly, on the one hand, the formation of CH₃C(O) radicals due to the OH reaction of 3P2. On the other hand, secondary processes like further oxidation of the first-generation products increase the formation rate of acetyl radicals at longer reaction times. The primary generation of CH₃C(O) radicals results from the bond scission between C_α and the carbonyl carbon atom of the α -RO radical (pathway α_1 , Fig. 5.4). The molar formation yield of the sum PAN + CO₂, without corrections, is 0.63 ± 0.14 based on averaging the results of the regression analysis of each experiment over the linear range.

In contrast to daytime conditions within the troposphere, the photolysis of the generated acetaldehyde and methyl glyoxal under our experimental conditions was negligible compared to the further oxidation through OH radicals. The reaction of both aldehydes with OH was shown to proceed nearly exclusively via the abstraction of the

Biomass burning plume chemistry: OH-radical initiated oxidation of 3-penten-2-one and its main oxidation product 2-hydroxypropanal

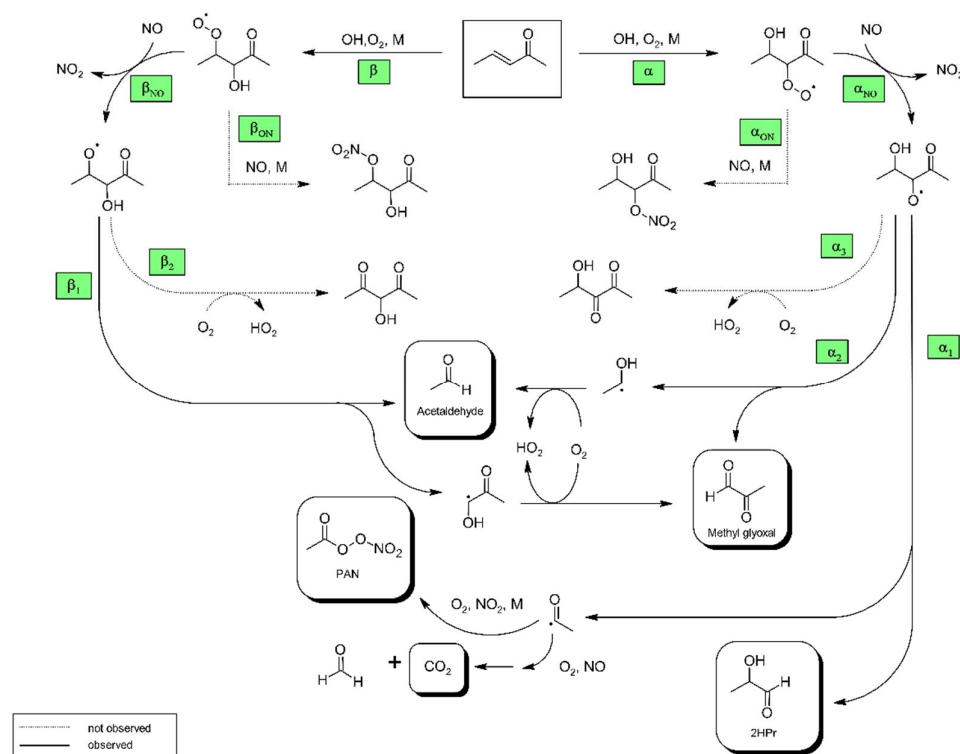


Figure 5.4. Proposed mechanism for the OH radical initiated oxidation of 3P2. The reaction pathways are named according to the position where the oxygen adds to form the peroxy radical.

aldehydic H atom, therefore being a secondary source of $\text{CH}_3\text{C}(\text{O})$ radicals with strength of 95%–100% (Calvert et al., 2011).

Similarly to the β -RO, the α -RO radical could also react with oxygen according to pathway α_3 to form a hydroxydicarbonyl species (Fig. 5.4). However, based on the observed spectral features there is no evidence to support further transformation pathways of both RO radicals other than the decomposition channels. This is in agreement with the product studies of structurally similar α,β -unsaturated ketones conducted under conditions where RO radicals are formed solely through the reaction of $\text{RO}_2 + \text{NO}$ (Tuazon and Atkinson, 1989; Galloway et al., 2011; Praske et al., 2015; Illmann et al., 2021b). The exothermicity of $\text{RO}_2 + \text{NO}$ results in RO radicals that are chemically activated and prone to decomposition (Orlando et al., 2003). For 1,2-hydroxyalkoxy radicals it was also shown that the reaction with O_2 cannot compete with the dissociation channel (Atkinson, 2007).

2-Hydroxypropanal is a co-product of $\text{CH}_3\text{C}(\text{O})$ radicals in the pathway α_1 (Fig. 5.4). Residual spectra of the 3P2 + OH system after subtraction of acetaldehyde, methyl glyoxal

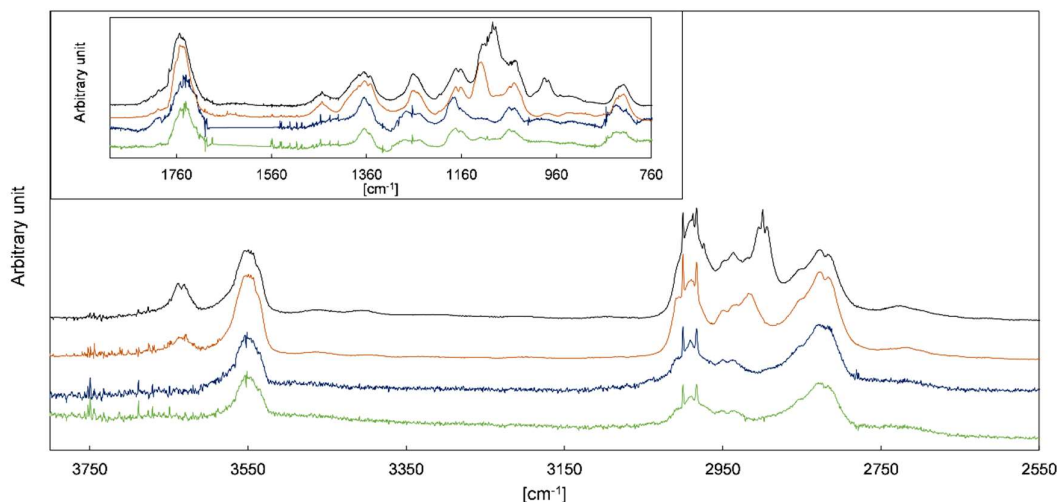


Figure 5.5. FTIR spectra of the residuals assigned to 2HPr obtained in the 1080 L chamber (green) and 480 L chamber (blue) 3P2 + OH experiments and residuals obtained from the ozonolysis of 3-penten-2-ol (brown) and 3-buten-2-ol (black).

and PAN are shown in Fig. 5.5 together with spectra recorded during the ozonolysis of 3B2OL and 3P2OL (s. Sect. 5.4.2). Absorption bands centred on 3640 cm^{-1} and in the range $1120\text{--}1090\text{ cm}^{-1}$ and centred on 3640 cm^{-1} , 980 cm^{-1} and in the range $1120\text{--}1090\text{ cm}^{-1}$ are present only in the residual spectra of the 3P2OL and 3B2OL ozonolysis experiments, respectively, indicating additional unidentified reaction products, which likely result from CI decomposition processes. However, other spectral ranges centred on 3550 cm^{-1} (O–H stretching vibration), 1750 cm^{-1} (C=O stretching vibration), 1370 cm^{-1} (C–H/O–H bending vibration), 830 cm^{-1} (C–H bending vibration), and the main parts of the characteristic absorption pattern in the range $3040\text{--}2640\text{ cm}^{-1}$ (C–H stretching vibration) agree within the spectra in both position and relative intensity, thus giving confidence in the identification of 2HPr.

Based on the integrated absorption cross section determined within this work an averaged molar yield of 0.59 ± 0.25 is derived for 2HPr in the 3P2 + OH reaction, from the regression analysis of all experiments without further corrections. One should note that the 2HPr yields of all experiments, performed in both chambers, agree within 12 % and the major uncertainty is derived from the accuracy of the absorption cross section. Nevertheless, the 2HPr yield is similar to the molar yield of PAN + CO₂ which is reflected by the proposed mechanism since these species are formed accordingly in the same reaction pathway (Fig. 5.4). On the other hand, the yield plots of 2HPr show a small but precise

curvature in each single experiment (Fig. 5.3). The wall loss of the α -hydroxyaldehyde was found to be $< 10 \times 10^{-5} \text{ s}^{-1}$ in the 1080 L chamber and $< 4 \times 10^{-5} \text{ s}^{-1}$ in the 480 L chamber, respectively. This all indicates that further oxidation of the α -hydroxyaldehyde is significant under the experimental conditions.

5.4.4 2-Hydroxypropanal + OH and modelling

Among the class of α -hydroxyaldehydes mechanistic information on the OH reaction and photolysis at atmospheric pressure were reported merely for glycolaldehyde (Niki et al., 1987b; Bacher et al., 2001; Magneron et al., 2005). Baker et al. (2004) reported rate coefficients for the OH reaction of a series of hydroxyaldehydes synthesized in situ via the reaction of OH radicals with precursor alcohols. The authors obtained $k = (1.7 \pm 0.2) \times 10^{-11} \text{ cm}^3 \text{ molecule}^{-1} \text{ s}^{-1}$ for 2HPr + OH through a non-linear least squares analysis of the data of the 2-methyl-2,4-pentandiol oxidation (Baker et al., 2004). Under tropospheric daytime conditions both photolysis and OH-initiated oxidation are important removal processes for glycolaldehyde (Bacher et al., 2001). However, assuming a similar behaviour for 2HPr, photolysis is expected to be negligible under the experimental conditions of the present study, since the OH radical level is much higher while photolysis frequencies are lower than within the troposphere. Including the above rate constant of 2HPr + OH into the model described previously (Illmann et al., 2021b) results in a corrected average yield of 0.68 ± 0.27 , which is about 15 % higher than determined from the yield plot, without proper corrections (Fig. 5.3). Hence, a significant fraction of the α -hydroxyaldehyde is subject to OH radical initiated oxidation.

Based on the SAR approach by Kwok and Atkinson (1995) and the mechanistic information reported for the glycolaldehyde oxidation (Niki et al., 1987b; Bacher et al., 2001; Magneron et al., 2005) one would expect abstraction of the aldehydic H atom to dominate compared to abstraction of the carbon-bonded H atom of the $-\text{CH}(\text{OH})-$ entity for the OH reaction of 2HPr, as presented in Fig. 5.6. The abstraction from the terminal $-\text{CH}_3$ group and the $-\text{OH}$ group is expected to be negligible due to the much lower group rate constants. The hydroxypropionyl radical formed according to channel (a) will either eliminate carbon monoxide and react with O_2 to form acetaldehyde or react with oxygen to form a hydroxypropionyl peroxy radical (Fig. 5.6). The latter radical, resulting from channel (2a), may either yield peroxyhydroxypropionyl nitrate or will be converted to the corresponding RO radical (Fig. 5.6). This species will readily eliminate CO_2 and finally form acetaldehyde as well. A theoretical investigation on the C_5 -acylperoxy radical indicates that

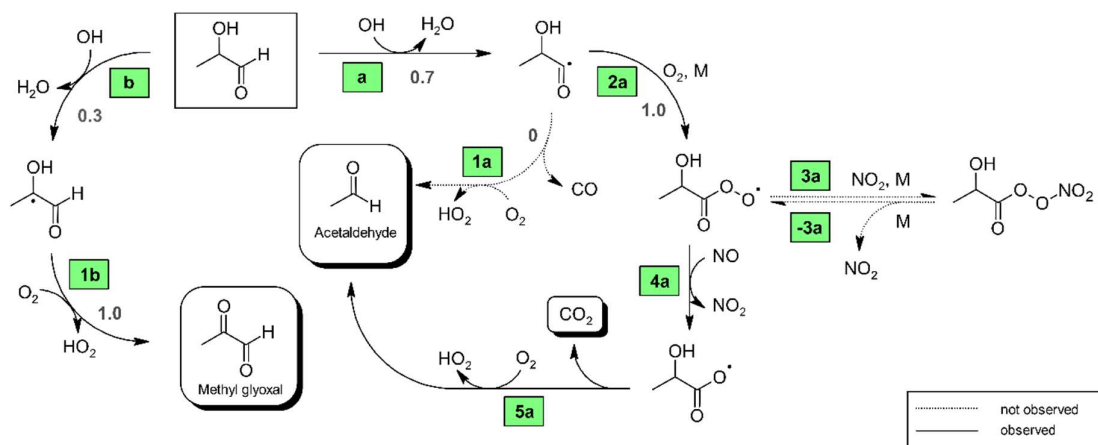


Figure 5.6. Proposed mechanism for the OH-radical-initiated oxidation of 2-hydroxypropanal (2HPr). Relevant branching ratios estimated within this work are denoted in grey next to the reaction channel.

H migration reactions (1,5-H, 1,6-H or 1,7-H shift) of larger acylperoxy radicals might be fast enough to compete with the bimolecular reactions at low parts-per-billion levels of NO (Knap and Jørgensen, 2017). However, based on the predicted effects of the substitution pattern on the reactivity towards H migration reactions (Vereecken and Nozière, 2020), one would not expect the unimolecular reaction of the smaller hydroxypropionyl peroxy radical to be competitive, at least not under our experimental conditions. By analogy to the OH-initiated oxidation of 3-hydroxy-2-butanone (Aschmann et al., 2000) one would expect reaction with oxygen to predominate over decomposition for the hydroxyalkyl radical formed following channel (b), thus leading to methyl glyoxal (Fig. 5.6). Hence, the 2HPr + OH reaction appears to be a secondary source of acetaldehyde and methyl glyoxal in the experimental system.

In order to investigate the 2HPr + OH reaction, methyl nitrite and NO were added for a second time, after a 3P2 consumption of about 70 %, to shift the reaction system towards secondary oxidation processes. Applying the approach presented by Baker et al. (2004) to these experiments, as shown in Fig. 9.9 in the Annex, allows to estimate a value of $(2.2 \pm 0.6) \times 10^{-11} \text{ cm}^3 \text{ molecule}^{-1} \text{ s}^{-1}$ for the rate coefficient of 2HPr + OH. Our estimation is about 30 % larger than previously reported (Baker et al., 2004). Taking into account that both determinations are based on the in situ generation of the α -hydroxyaldehyde, this is still an excellent agreement. In panel (c) of Fig. 5.7 it can be observed that the mixing ratio of acetaldehyde (purple circles) increases continuously over the second irradiation period, while that of methyl glyoxal (black circles) is reaching a plateau relatively fast. This is in

qualitative agreement with the proposed mechanism. Peroxy nitrates other than PAN, formed through $3P2 + OH$, could not be detected. Traces of the analogue peroxy-hydroxyacyl nitrate resulting from glycolaldehyde oxidation have only been previously observed when the corresponding RO_2 radical was generated through the reaction of glycolaldehyde with Cl atoms in the presence of NO_2 (Niki et al., 1987b). Magneron et al. (2005) did not detect any PAN-type species in the glycolaldehyde + OH system and therefore concluded that this species is probably unstable and readily dissociates. Hence, abstraction of the aldehydic H atom following channel (a) will likely result exclusively in the formation of acetaldehyde irrespective of the branching ratio between the (1a) and the (2a) channel (Fig. 5.6).

The molar formation yields of acetaldehyde and methyl glyoxal, derived from $3P2 + OH$ as well as from $2HPr + OH$, were included as parameters in a simplified model (Illmann et al., 2021b) and varied until the experimental time profiles are reproduced by the simulation. Since the OH-initiated oxidation of $2HPr$ is expected to proceed solely through the channels (a) and (b), the product yields of acetaldehyde and methyl glyoxal, from $2HPr + OH$, should correspond to the branching ratios k_a and k_b , respectively (Fig. 5.6). Their sum should, in turn, equal unity. Table 5.2 shows the simplified reaction sequences and the rate coefficients needed to describe the reaction system. These sequences do not follow the nomenclature used in the proposed mechanisms (Figs. 5.4 and 5.6) since the simplified model does not differentiate whether a product is formed directly from a parent compound through more than one pathway.

Figure 5.7 summarizes an analysis of the model sensitivity, observing also the accuracy of all quantified species. For all species but $2HPr$ accuracy was defined as a 10 % relative error plus the corresponding detection limit. The accuracy of $2HPr$ is given as a 30 % relative error plus the detection limit due to the uncertainty of the cross section determination. Panels (c)–(f) show different model runs for acetaldehyde and methyl glyoxal in which the $2HPr$ yield was set to 0.66, represented by the solid line in panel (b). As can be seen in panel (c), without considering the $2HPr + OH$ reaction the simulated profile represents roughly the experimental methyl glyoxal data during the first irradiation period. By contrast, the acetaldehyde profile matches the experimental data only in the beginning of the first irradiation corresponding to a $3P2$ consumption of < 30 %. The temporal profiles of both species completely fail in reproducing the measured data during the second irradiation, where more than 70 % of the $3P2$ is already consumed. This demonstrates unambiguously that a secondary source for both acetaldehyde and methyl glyoxal is needed to describe the experimental system, namely the α -hydroxyaldehyde oxidation. However, the match

Biomass burning plume chemistry: OH-radical initiated oxidation of 3-penten-2-one and its main oxidation product 2-hydroxypropanal

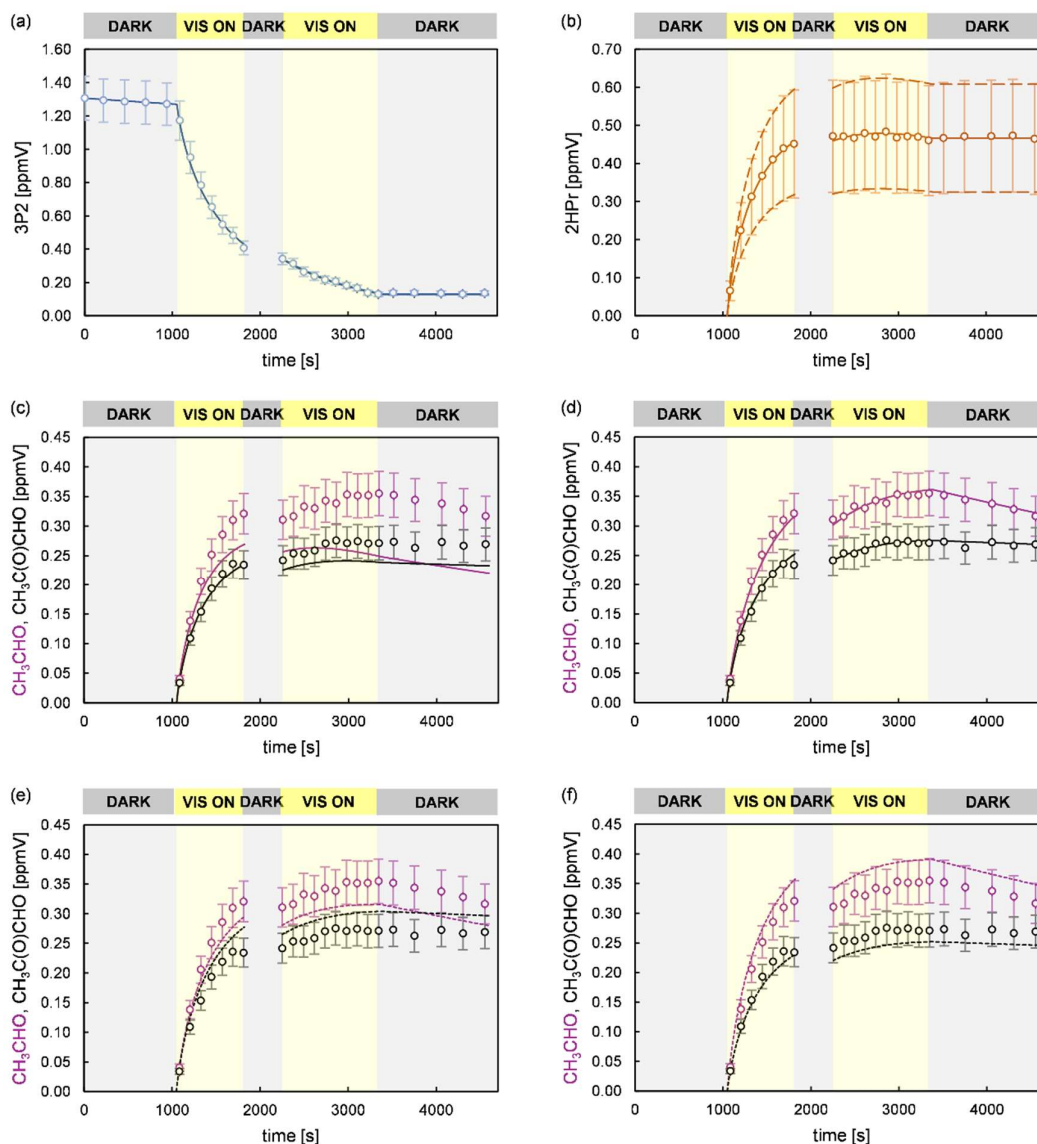


Figure 5.7. Experimental and simulated time profiles for a 3P2 + OH experiment, performed in the 1080 L chamber, with a supplementary addition of methyl nitrite and NO during the second dark phase of the experiment. The experimental set-up did not allow the quantification of CO₂. The circles represent the experimental data. The error bars represent the accuracy error for each species. The lines show the simulated profiles of (a) 3P2, and (b) 2HPr assuming the average yield (solid line) and the upper and lower limit (dashed lines). The simulated profiles of acetaldehyde and methyl glyoxal are shown considering the average 2HPr yield (c) without their secondary formation, (d) with the optimum parameters used to reproduce the experimental data, (e) for the lower and upper limit of acetaldehyde and methyl glyoxal (scenario 1), respectively, and (f) for the upper and lower limit of acetaldehyde and methyl glyoxal (scenario 2), respectively.

between the simulated and experimental time profiles in the beginning of the first irradiation allows us to set values for the first-generation yields of acetaldehyde and methyl glyoxal from $3P2 + OH$ in these experiments. Panel (d) shows the optimum model run that allows a simultaneous fit of the experimental time profiles for both acetaldehyde and methyl glyoxal. In order to assess the errors for the branching ratios k_a and k_b , two scenarios were defined which represent the limiting cases and thus enable us to determine the maximum variation of k_a and k_b . Accordingly, panel (e) shows a model run in which acetaldehyde is simulated for its lower limit of the accuracy error and methyl glyoxal for the upper limit, respectively, (scenario 1) while panel (f) represents the inverse case (scenario 2). These scenarios were modelled for different strengths of the secondary source of acetaldehyde and methyl glyoxal, meaning that the 2HPr yield from $3P2 + OH$ was varied within the limits imposed by the accuracy of the 2HPr measurement, as shown in panel (b). For both scenarios, the obtained first-generation yields of acetaldehyde and methyl glyoxal from $3P2 + OH$ were found to be independent from the 2HPr yield. Since the formation of acetaldehyde and methyl glyoxal from the $3P2 + OH$ reaction does not necessarily depend on 2HPr, this observation is rather self-consistent and serves merely as a validation of our model. Based on the proposed $3P2 + OH$ mechanism one would expect their yields to be the same, thus their ratio should equal unity. This does correspond to scenario 1 while an acetaldehyde/methyl glyoxal ratio > 1 is observed for scenario 2 (Fig. 9.10 in the Annex). Although within the accuracy errors this indicates a small bias between the acetaldehyde and methyl glyoxal quantification. The sum of the acetaldehyde and methyl glyoxal yield from $2HPr + OH$ correlates with the 2HPr yield from the $3P2 + OH$ reaction, where larger values are observed when the input 2HPr yield is lowered (Fig. 9.11 in the Annex). In order to reproduce the entire time profiles of acetaldehyde and methyl glyoxal, an overestimation of the 2HPr mixing ratio and hence the strength of the secondary acetaldehyde and methyl glyoxal source is compensated for by an underestimation of the acetaldehyde and methyl glyoxal yield in the model. Hence, this behaviour can be rationalized in terms of an antagonistic effect. The sum of the acetaldehyde and methyl glyoxal yields becomes unity when a 2HPr yield of about 0.54 and 0.61 is used in the model for scenario 1 and 2, respectively. Considering the yield of 0.66, used to match the experimental data in panel (b), this might indicate an overestimation of the 2HPr mixing ratios. However, the differences are within the accuracy due to the rather uncertain 2HPr cross section. The branching ratios k_a and k_b were obtained by scaling of the acetaldehyde and methyl glyoxal yield. These were found to be independent from the 2HPr yield within

Table 5.2. Simplified reaction sequence used for the modelling of the temporal behaviour of experimentally quantified species in order to obtain first-generation yields for the respective reactions (3P2 + OH, 2HPr + OH).

Reaction	Branching ratio	Rate coefficient	
(R4) CH ₃ CH=CHC(O)CH ₃ + OH → products		6.2 × 10 ⁻¹¹ cm ³ molecule ⁻¹ s ⁻¹	a, b
(R4a) → CH ₃ C(OH)C(O)H	0.68 ^c		
(R4b) → CH ₃ C(O)H	0.39 ^c		
(R4c) → CH ₃ C(O)C(O)H	0.32 ^c		
(R4d1) → CH ₃ C(O)OONO ₂	^d		
(R4d2) → CO ₂ + HCHO	^d		
(R5) CH ₃ CH=CHC(O)CH ₃ + wall →		≤ 1.0 × 10 ⁻⁴ s ⁻¹	a, e
(R6) CH ₃ C(O)H + OH → products		1.5 × 10 ⁻¹¹ cm ³ molecule ⁻¹ s ⁻¹	a, f
(R6a) → CH ₃ C(O)OONO ₂	a, g		
(R6b) → CO ₂ + HCHO	a, g		
(R7) CH ₃ C(O)H + wall →		≤ 1.0 × 10 ⁻⁴ s ⁻¹	a, e
(R8) CH ₃ C(O)C(O)H + OH → products		1.3 × 10 ⁻¹¹ cm ³ molecule ⁻¹ s ⁻¹	a, h
(R8a) → CO + CH ₃ C(O)OONO ₂	ⁱ		
(R8b) → CO + CO ₂ + HCHO	ⁱ		
(R9) CH ₃ C(O)C(O)H + wall →		≤ 1.0 × 10 ⁻⁴ s ⁻¹	a, e
(R10) CH ₃ C(OH)C(O)H + OH → products		1.7 × 10 ⁻¹¹ cm ³ molecule ⁻¹ s ⁻¹	a, j
(R10a) → CO ₂ + CH ₃ C(O)H	0.73 ^c		
(R10b) → CH ₃ C(O)C(O)H	0.27 ^c		
(R11) CH ₃ C(OH)C(O)H + wall →		≤ 1.0 × 10 ⁻⁴ s ⁻¹	a, e

^a Input parameter; ^b rate coefficient determined within this work; ^c average branching ratio obtained through modelling; ^d average branching ratio (R4d1+R4d2)/R4 = 0.58 obtained through modelling; ^e determined in each individual experiment; ^f rate coefficient from Atkinson et al. (2006); ^g branching ratio (R6a+R6b)/R6 = 0.95 from Atkinson et al. (2006); ^h rate coefficient from Atkinson et al. (2006); ⁱ branching ratio (R8a+R8b)/R8 = 1.0 from Atkinson et al. (2006); ^j rate coefficient from Baker et al. (2004).

the 2HPr accuracy limits and almost indistinguishable in between scenario 1 and 2 (Fig. 9.12 in the Annex). Accordingly, the average branching ratios k_a and k_b are 0.73 ± 0.08 and 0.27 ± 0.08 , respectively. Within the uncertainties, this is in agreement with SAR predictions (Kwok and Atkinson, 1995) which estimate 0.8 and 0.2 for the branching ratios, respectively, as well as previous results on the OH reaction of glycolaldehyde at atmospheric pressure (Niki et al., 1987b; Bacher et al., 2001; Magneron et al., 2005).

Based on these results, the temporal profiles of acetaldehyde and methyl glyoxal are well-reproduced for all conducted experiments. Their corrected yields in the 3P2 + OH reaction are 0.39 ± 0.07 and 0.32 ± 0.08 , respectively. Hence, while larger molar yields were observed for acetaldehyde than for methyl glyoxal without proper corrections the model predicts both first-generation yields to be the same within the accuracy errors, which indicate their formation according to the same reaction channel. The branching ratios of the simplified reaction scheme, obtained through modelling, are given in Tab. 5.2.

Figure 5.8 shows time profiles obtained from an experiment performed in the 480 L chamber, in which PAN and CO₂ were quantified, as well as simulated profiles from different model runs. As presented in panel (b), the experimental data are reproduced solely for less than the first half of the irradiation period, if only PAN and CO₂ formation from 3P2 + OH are considered in the model. This corresponds to a 3P2 consumption of < 30% which is consistent with the non-linearity of the yield plot observed for higher 3P2 consumption levels (Fig. 5.3). As discussed before, PAN and CO₂ formation are affected from the further oxidation of acetaldehyde and methyl glyoxal. However, CO₂ elimination from the 2HPr-derived RO radical (Fig. 5.6) is an additional source of CO₂ in the experimental system according to pathway (5a). Given that abstraction of the aldehydic H atom of 2HPr is expectedly leading solely to acetaldehyde, the yield of CO₂ from the 2HPr oxidation depends only on the ratio between decomposition of the hydroxypropionyl radical and its reaction with oxygen (Fig. 5.6). In order to assess the uncertainty on the sum parameter PAN + CO₂ due to secondary chemistry, the temporal profile of PAN + CO₂ was simulated assuming both acetaldehyde and methyl glyoxal at the upper (scenario 3) and lower limit (scenario 4) of the measurement accuracy (Fig. 5.8). Hence, the strength of the secondary sources of CH₃C(O) radicals in the experimental system was either maximized or minimized in the model. Moreover, the temporal behaviour of PAN + CO₂ was simulated without considering CO₂ formation from 2HPr + OH (dashed lines) and assuming the CO₂ yield to equal the acetaldehyde yield (solid lines). In both scenarios (panel d and f of Fig. 5.8) the temporal profiles are nearly indistinguishable during the first half of the irradiation time, and one obtains the same first-generation yield for the sum parameter PAN + CO₂, used to determine the CH₃C(O) radical yield. The entire profile is reproduced solely when the CO₂ yield from 2HPr + OH is equalized to the acetaldehyde yield in scenario 3 (panel d). In scenario 4, where the secondary formation of CH₃C(O) radicals was set to the lower limit, the model slightly underestimates the sum of PAN and CO₂ at the end of the experiment (panel f). However, in both scenarios the model predicts the sum of PAN + CO₂ to be significantly lower than experimentally observed at the end of the irradiation period, when the CO₂ formation from 2HPr is set to 0 (dashed lines). When introducing larger PAN + CO₂ yields for 3P2 + OH it is possible to match the observed profile for the second half of the experiment. However, in this case the model overestimates PAN + CO₂ formation in the first half of the experiment, in which secondary formation is expected to be almost negligible.

Biomass burning plume chemistry: OH-radical initiated oxidation of 3-penten-2-one and its main oxidation product 2-hydroxypropanal

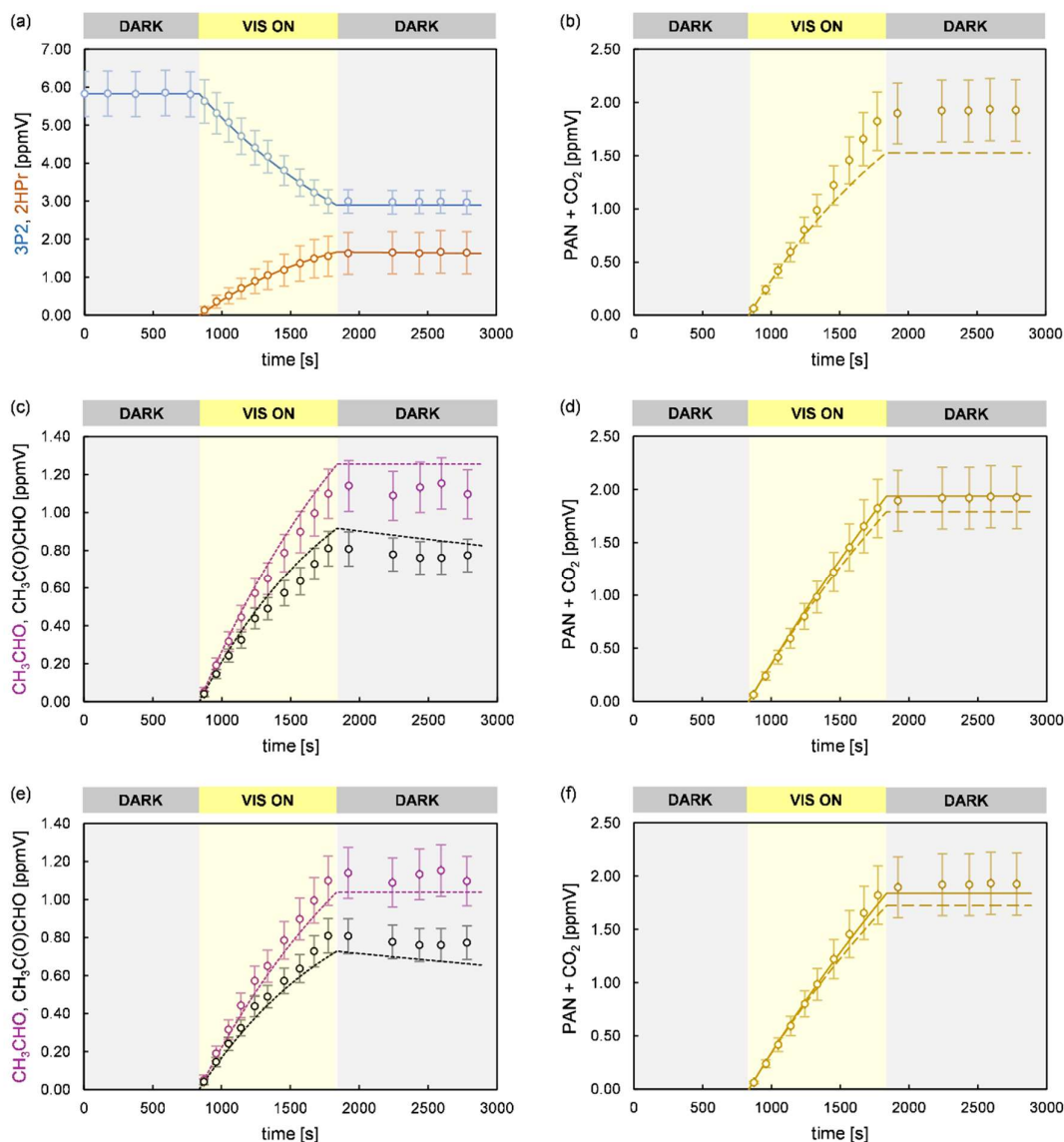


Figure 5.8. Experimental (circles) and simulated (lines) temporal behaviour of 3P2, 2HPr, acetaldehyde, methyl glyoxal and PAN + CO₂ in an experiment performed in the 480 L chamber. The error bars of the experimental data represent the accuracy error. Model runs of the sum parameter PAN + CO₂ are shown considering only the formation of PAN and CO₂ due to CH₃C(O) radicals formed in the reaction system (dashed line) and including additionally the CO₂ source from 2HPr + OH (solid line). The model run in panel (b) considers only primary PAN and CO₂ formation from 3P2 + OH. Panel (c) and (d) represent model runs according to scenario 3 (acetaldehyde and methyl glyoxal at the upper limit of the accuracy error) and panel (e) and (f) according to scenario 4 (acetaldehyde and methyl glyoxal at the lower limit of the accuracy error), respectively.

For the hydroxyacetyl radical Méreau et al. (2001) concluded, based on ab initio calculations, that decomposition cannot compete with the O₂ reaction. Niki et al. (1987b) observed CO₂ instead of CO formation in the glycolaldehyde oxidation when secondary oxidation processes were minimized in the experimental system. These findings together with the significant discrepancy of the simulated and experimental time profile for PAN + CO₂ at long irradiation times, when a CO₂ formation from 2HPr oxidation is not included in the model, suggest that decomposition of the hydroxypropionyl radical is negligible and $k_{2a}/[k_{1a} + k_{2a}] = 1$ (see Fig. 5.6). Including the additional CO₂ source in the model significantly improves the consistency between the simulated and experimental PAN + CO₂ profile at long irradiation times, although slight discrepancies remain in some experiments. One should note that in this regard the time profile no longer represent merely the formation of CH₃C(O) radicals. However, given that both the simulation with and without the additional CO₂ source are indistinguishable in the first part of the irradiation period (Fig. 5.8) it is still possible to derive the corrected average yield for PAN + CO₂ (0.56 ± 0.14) representing the yield of CH₃C(O) radicals.

As for acetaldehyde and methyl glyoxal, the yields for 2HPr and PAN + CO₂ are the same within the assigned accuracy thus indicating their formation in the same reaction channel. Since carbon dioxide formation might be easily affected from processes on the chamber walls, the corrected yield for PAN + CO₂ should, therefore, be still regarded as upper limit. A build-up of CO₂ from the walls might become relevant at longer irradiation times and this supposedly explains the remaining small discrepancies at irradiation times > 10 min in some experiments. However, the reproducibility of the yields is essentially the same as for 2HPr for experiments performed in both chambers. Besides, separate control experiments, in which synthetic air was irradiated with the same set of lamps, did not show significant CO₂ production. Therefore, the influence of off-gasing processes on its temporal behaviour is probably negligible in the beginning of the experiments, when the formation of the products in the target reaction dominates over secondary chemistry. An overestimation of the CH₃C(O) radical yield is thus unlikely. Uncorrected and corrected molar yields, namely first-generation yields, of all quantified products are summarised in Tab 5.3.

Combining the yields of the 3P2 oxidation products leads to a carbon balance close to unity (0.98 ± 0.18). The branching ratios for the pathways α_{ON} and β_{ON} (Fig. 5.4) forming RONO₂ species are expectedly very minor channels. This is in agreement with previous findings in our laboratory, where the production of RONO₂ species in the OH oxidation of

Table 5.3. Uncorrected yields and first-generation yields (yields corrected for secondary processes) of species identified in the 3P2 + OH reaction.

	2-Hydroxypropanal	PAN + CO ₂	Methyl glyoxal	Acetaldehyde
Uncorrected	0.59 ± 0.25	0.63 ± 0.14	0.29 ± 0.09	0.40 ± 0.07
Corrected	0.68 ± 0.27	0.56 ± 0.14	0.32 ± 0.08	0.39 ± 0.07

α,β -unsaturated ketones was observed only in conjunction with the formation of tertiary RO₂ radicals (Illmann et al., 2021b). Further, Praske et al. (2015) reported a low overall RONO₂ yield of 0.040 ± 0.006 for MVK oxidation.

5.5 Atmospheric implication and conclusion

The atmospheric lifetime of 3P2 with respect to OH radicals, defined as $1/(k_{3P2} \times [OH])$, is about 4.5 h when assuming a global average OH radical concentration of $1.0 \times 10^6 \text{ cm}^{-3}$ within the troposphere (Bloss et al., 2005). Calvert et al. (2011) recommended, however, an OH radical level of $2.5 \times 10^6 \text{ cm}^{-3}$ for the calculation of atmospheric lifetimes for short-lived species which leads consequently to an even shorter lifetime. Since our experiments indicate no measurable photolysis, the OH reaction is the dominant degradation process during daytime. 3P2 is thus oxidized close to the emission/formation source. A larger influence on atmospheric processes is indicated by the primary formation of CH₃C(O) radicals, which account for 22 ± 6 % of the 3P2 oxidation. As acetyl radicals ultimately yield PAN, depending on the NO₂/NO ratio, 3P2 exhibits a huge potential of forming NO_x reservoir species. The gas-phase oxidation of the first-generation product 2HPr by OH radicals would generate mainly acetaldehyde (~80 %) hence increasing the potential of forming NO_x reservoirs. However, by comparison with glycolaldehyde photolysis of 2HPr may also be competitive. On the other hand, since 2HPr is highly soluble in water, uptake into the aqueous phase (aerosols) may also be an important loss process. Hydration would increase significantly the lifetime towards photolysis and potentially lead to the formation of organic acids, as discussed previously for glycolaldehyde (Calvert et al., 2011).

Given both the short lifetime and the mechanism of the OH-initiated oxidation, 3P2 is an example of species whose chemistry explains the rapid PAN formation in young biomass burning plumes, as found previously in field observations (Alvarado et al., 2010). Acetaldehyde and methyl glyoxal form as well acetyl radicals in their further gas-phase oxidation (Calvert et al., 2011). Besides, methyl glyoxal is also known as a source of secondary organic aerosol (Fu et al., 2008). Box models yielded high average OH radical concentrations of about $7.5 \times 10^6 \text{ cm}^{-3}$ within young biomass burning plumes (Müller et al.,

2016). Based on that, once emitted from biomass burning, more than 50 % of the 3P2 carbon are converted into $\text{CH}_3\text{C}(\text{O})$ radicals in less than 3 h. Assuming gas-phase products only in the further oxidation pathways, possibly up to 2 PAN molecules are formed per 3P2 molecule consumed. The α,β -unsaturated ketone fits also well into the characteristics of unknown VOCs as deployed by Alvarado et al. (2015) to elucidate the evolution of O_3 and secondary organic aerosol in a plume of a prescribed fire in California since (a) the OH rate coefficient of 3P2 is in the order of $10^{-11} \text{ cm}^3 \text{ molecule}^{-1} \text{ s}^{-1}$, (b) the $\text{RO}_2 + \text{NO}$ reactions of 3P2 derived peroxy radicals result exclusively in fragmentation of the molecule, and (c) the mechanism proposed in this study predicts a high HO_2 regeneration level. Therefore, single-component studies as the present one contribute to a better understanding of the complex biomass burning plume chemistry.

Part B:

Non-cumulative Part

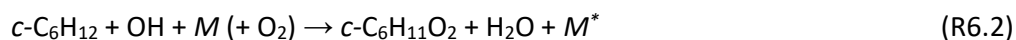
6 Formation of organic acids in the ozonolysis of α,β -unsaturated ketones exemplified by the case study of ethyl vinyl ketone + ozone

6.1 Introduction

Ozonolysis reactions are of interest in particular owing to their contribution on OH radical and aerosol formation (Johnson and Marston, 2008 and references therein). However, in many cases the mechanism and the reaction products remain poorly characterized, which is often reflected in a low overall carbon balance. This is partly due to the nature of ozonolysis reactions, which proceed almost exclusively (with some exceptions) via a 1,3-dipolar cycloaddition yielding initially a five-membered primary ozonide (POZ). This, in turn, is formed with a substantial amount of energy due to the exothermicity of ozonolysis reactions. As a consequence the POZ will decompose immediately via two possible pathways (see Fig. 2.1), where only 50 % results initially in the formation of stable carbonyl products (primary carbonyls), if the POZ channel represents the only pathway of the ozonolysis reaction. The remaining fraction yields Criegee intermediates (CIs), which are formally zwitterionic carbonyl oxides (see Fig. 2.1). Since the excess energy is necessarily distributed in the initially formed reaction products, this results in nascent CIs, which are subject to further decomposition whereas a fraction might be thermalized (stabilized CIs = sCIs) and is prone to bimolecular reactions (Cox et al., 2020). Extensive work during the last decades has shown that sCIs react very fast with SO₂ or organic acids (Cox et al., 2020 and references therein), although under atmospheric conditions sCIs will react preferentially with H₂O or the water dimer. Accordingly, different levels of H₂O in the experiments might be one reason for the varying product distributions reported for specific reaction systems. Further, ozonolysis reactions are also experimentally challenging, as they were shown to produce OH radicals (Cox et al., 2020 and references therein), which implies necessarily a competition between the O₃ and OH reaction of the target species depending on the reaction system and the OH yield of the ozonolysis reaction. In order to overcome this issue, OH scavengers like cyclohexane or CO are often used to investigate the ozonolysis system without OH interference in atmospheric simulation chamber experiments. However, in the case of CO almost any OH radical is converted into HO₂, which implies possibly a fundamental increase of the HO₂ level in the reaction system.



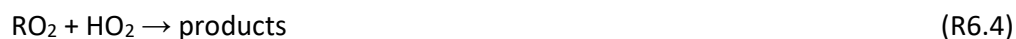
By contrast, the OH-initiated oxidation of cyclohexane forms additional RO₂ species (for instance initially the cyclohexyl peroxy radical).



Since in the presence of higher O₃ levels any background level of NO present in a simulation chamber were ultimately titrated,



the further fate of the RO₂ radicals is (besides possible isomerization if the HO₂ or RO₂ level were sufficiently low in the experiment) dominated by reactions with either HO₂ or RO₂.



Hence, the OH scavenger used might affect the observed product distribution due to its impact on the Reactions (R6.4) and (R6.5).

Despite the importance of α,β -unsaturated ketones in terms of atmospheric burden - they form in the oxidation of terpenes (e. g. methyl vinyl ketone from isoprene), their ozonolysis reactions were scarcely studied. Further, the existing studies report rather conflicting results. For example, in the case of the primary carbonyls from methyl vinyl ketone + O₃ (Grosjean et al., 1993b; Ren et al., 2017). The longer-chain analogue ethyl vinyl ketone (EVK) has solely been studied previously by Grosjean et al. (1996), the results targeting the primary carbonyl formation. They identified also acetaldehyde, although its formation remained unexplained. Combining this, the fate of carbonyl-substituted CIs, where the C=O bond is close to the C=O⁺-O⁻ moiety, seems generally to be poorly understood. For this purpose, EVK, emitted from plants after leave wounding (Fall et al., 2001), was chosen as a model study (as the first of series) in the present work, in order to obtain a more comprehensive understanding of the α,β -unsaturated ketones ozonolysis mechanism.

To keep the reaction system as simple as possible, two experimental approaches were followed. First, all experiments were performed with an excess of CO to suppress OH

reactions and exclude the formation of RO₂ radicals other than formed from EVK + O₃. In a second series of experiments, sufficient SO₂ was also added to the reaction mixture to favour the sCl + SO₂ reaction and hence suppress potential reactions of sCl with other reaction products. It is shown that combining the results of both experimental set-ups provides a more comprehensive perspective on the ozonolysis mechanism. Further, this allowed to obtain yields for the primary carbonyl 2-oxobutanal via a semi-quantitative approach, although standards of this compound are not commercially available. Evidences are found for the formation of organic acids and pathways accounting for their formation are proposed. In addition, infrared absorption features of perpropionic acid are presented.

6.2 Experimental

6.2.1 EVK + O₃

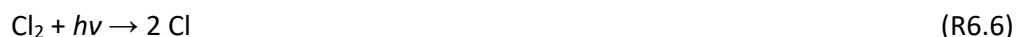
In order to investigate the EVK + O₃ system, experiments were carried out in the 1080 L chamber under dry conditions (r. h. << 0.1 %) following the procedure outlined in Chapter 3. A scheme of the 1080 L chamber is presented in the Annex (Fig. 9.13). Carbon monoxide (CO) was added in sufficient amount to scavenge any OH radical formed in the reaction system. In further experiments, SO₂ was also added to the reaction mixture to allow an estimate of the stabilized Criegee Intermediate (= sCl) yield. The initial mixing ratios were 1.5–2.3 ppmV for EVK (Alfa Aesar, 97 %), 3.1–4.0 ppmV for SO₂ (Air Liquide, 99.9 %), and 15000–20000 ppmV for CO (Air Liquide, 99.97 %).

EVK and the reaction products were quantified via FTIR by subtraction with calibrated reference spectra from the internal laboratory database. In addition to the quantification by long-path FTIR, a qualitative identification of reaction products was performed using a PTR-ToF-MS 8000 instrument (Ionicon Analytik GmbH, Innsbruck, Austria). The drift tube was operated at a temperature of 70 °C, 2.2 mbar pressure and 500 V drift voltage. Accordingly, the E/N value was about 130 Td ($1 \text{ Td} = 1 \times 10^{-17} \text{ V cm}^2$), where E is the electric field in the drift tube, and N is the gas number density. The sampling line of the instrument was operated at a temperature of 70 °C and coupled to a heated stainless steel line, which was mounted on the middle flange of the 1080 L chamber. The sample flow was 200 mL min⁻¹. In order to obtain stable signals with the PTR-MS instrument, the fan mounted on the middle flange inside the chamber was switched on during the whole experiment. The PTR-ToF-MS data were recorded and processed using the TOFDAQ data acquisition software and the PTR-MS VIEWER software (Ionicon Analytik GmbH, Innsbruck, Austria), respectively.

Simulations of the temporal evolution of reaction products, possibly formed from peroxy radical reactions, were performed following the approach outlined previously (Illmann et al., 2021b). A detailed sensitivity analysis and model validation can be found in Illmann et al. (2021d). In contrast to previous applications, an explicit chemical mechanism was used for the relevant RO₂ reactions, in order to prove if the temporal behaviour of selected reaction products is described by known reaction sequences. For this purpose, the source of the parent RO₂ was included as a simplified reaction (EVK + O₃ → RO₂) as well as an average HO₂ concentration. Both, the branching ratio towards the RO₂ formation and [HO₂] were varied to check for a match between the experimental data and the modelled time profiles for all relevant species.

6.2.2 In situ generation of peracids

Infrared spectral features of peracetic acid (= peroxyacetic acid) and perpropionic acid (= peroxypropionic acid) were generated by the irradiation (I_{\max} at 360 nm) of acetaldehyde/methanol/Cl₂ and propionaldehyde/methanol/Cl₂ mixtures, respectively, in both the 480 L and 1080 L chamber. Given that both the acetaldehyde + Cl and the propionaldehyde + Cl reaction proceed nearly exclusively via the abstraction of the aldehydic H atom, the respective RO₂ radicals are generated as follows:



In order to favour RO₂ + HO₂ reactions, the level of HO₂ is increased due to CH₃OH + Cl and the subsequent reaction sequence:



The [HO₂]/[RO₂] ratio can be adjusted by the initial [aldehyde]/[CH₃OH] ratio. Accordingly, the initial mixing ratios were set at 1.6–4.4 ppmV for acetaldehyde (Sigma Aldrich, > 99.5 %), 1.1–7.3 ppmV for propionaldehyde (Sigma Aldrich, 97 %), 1.9–16 ppmV for methanol (Sigma Aldrich, 99.9 %) and 1.9–21 ppmV for Cl₂ (Air Liquide, 99.8 %).

6.3 Results and discussion

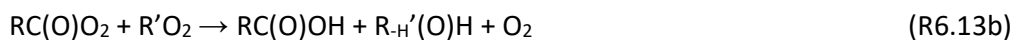
In the following sections the discussion upon the in situ generation of peracids from their aldehyde precursors precedes the presentation of the EVK + O₃ investigation results, for the generated FTIR spectra were subsequently used for the identification and quantification of perpropionic acid.

6.3.1 In situ generation of peracids

Among RO₂ + HO₂ reactions the acetyl peroxy radical + HO₂ system is one of the most investigated reactions and reasonably well characterized (Niki et al., 1985; Horie and Moortgat, 1992; Hasson et al., 2004; Jenkin et al., 2007; Dillon and Crowley, 2008; Groß et al., 2014, Winiberg et al., 2016; Hui et al., 2019). The reported investigations performed in simulation chambers were conducted mainly by irradiating acetaldehyde/methanol/Cl₂ mixtures (Hasson et al., 2004; Jenkin et al., 2007; Winiberg et al., 2016). Therefore, the in situ generation of peracetic acid was chosen to test the experimental set-up. All experiments were observed up to a maximum consumption of 60–70 % of the initial acetaldehyde. In order to promote RO₂ + HO₂ rather than RO₂ + RO₂ reactions, the initial aldehyde concentration was kept always lower than [CH₃OH]₀. In all experiments, significant amounts of hydrogen peroxide (H₂O₂) are formed. Since this can be rationalized through the HO₂ self-reaction, it indicates the HO₂ level to be near the upper experimental limit. In the case of acyl peroxy radicals, the RO₂ + HO₂ reaction was reported to proceed through 3 different channels (Hasson et al., 2004):



Accordingly, peracetic acid and acetic acid are formed in the CH₃C(O)H/CH₃OH/Cl₂ system. The alkoxy radical (R6.12c) eliminates CO₂ to yield a methyl radical, that is immediately converted into a methyl peroxy radical (CH₃O₂). The CH₃O₂ further chemistry evolves into methyl hydroperoxide and HCHO through the reaction with HO₂ and possibly into HCHO and CH₃OH through the CH₃O₂ self-reaction. However, if RO₂ + RO₂ plays a role, the cross reaction of the alkyl peroxy and acyl peroxy radical is about a factor of 10² faster and proceeds as follows (Tyndall et al., 2001):



In consequence, after the subtraction of the reaction sequence's products (acetic acid, O_3 , CO_2 , CH_3OOH , HCHO) as well as CH_3OH , HCHO , HC(O)OH , H_2O_2 and HCl , the residual spectrum of such a reaction mixture should correspond to peracetic acid. Trace (b) of Fig. 6.1 shows a residual spectrum obtained from an irradiated $\text{CH}_3\text{C(O)H/CH}_3\text{OH/Cl}_2$ mixture, which is in excellent agreement with a reference spectrum of peracetic acid from the Wuppertal laboratory database, presented in trace (a). The residual spectrum shows additional small curvatures centred at 1150 cm^{-1} and 1050 cm^{-1} . However, this can be partly explained by the subtraction of high amounts of methanol, those absorption dominates at 1050 cm^{-1} . Additionally, a curvature of the baseline was observed in this region in some experiments, which might be built artificially due to the subtraction process. Despite this, the experimental set-up was proven successful in obtaining the spectral features of peracids, as shown in Fig. 6.1.

The experiments irradiating $\text{C}_2\text{H}_5\text{C(O)H/CH}_3\text{OH/Cl}_2$ mixtures were performed until a maximum consumption of 30–60 % of propionaldehyde. Similarly to the irradiation of mixtures containing acetaldehyde, H_2O_2 formation was also observed. This indicates a high HO_2 level in the experimental system, necessary to promote the $\text{RO}_2 + \text{HO}_2$ reactions. According to the Reactions (R6.12a)–(R6.12c) perpropionic acid, propionic acid and $\text{C}_2\text{H}_5\text{C(O)O}$ radicals are formed from the $\text{C}_2\text{H}_5\text{C(O)O}_2 + \text{HO}_2$ reaction. The existence of all 3 reaction channels has been proven previously by Hasson et al. (2012). However, although FTIR spectroscopy has also been used in the Hasson et al. (2012) study, the peracid was quantified with HPLC and up to date no IR spectrum was reported for perpropionic acid.

As discussed above, in the presence of O_2 , the $\text{C}_2\text{H}_5\text{C(O)O}$ radical eliminates CO_2 to form the ethyl peroxy radical. Similarly to methyl peroxy radical, the ethyl peroxy radical further chemistry yields ethyl hydroperoxide and possibly acetaldehyde. The residual spectrum assigned to perpropionic acid was obtained by subtraction of the following species: propionaldehyde, methanol, HCHO , formic acid, CO_2 , propionic acid, ethyl hydroperoxide, O_3 , acetaldehyde, peracetic acid, H_2O_2 , and HCl . The perpropionic acid spectrum is presented in Fig. 6.1, panel (c).

The spectrum contains characteristic absorption bands centred at 3303, 1760, 1450, 1180 and 880 cm^{-1} , which are nearly identical to the absorption features of peracetic acid, and were assigned on the basis of well acknowledged rules. The position of the absorption centred at 3303 cm^{-1} is identical to the peracetic acid spectrum. This absorption band is

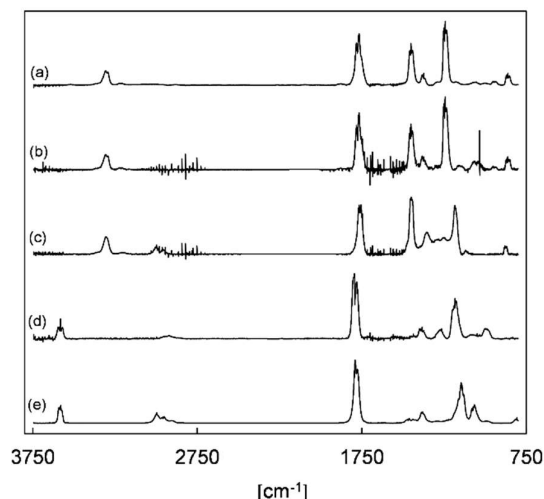


Figure 6.1. (a) Reference spectrum of peracetic acid (peroxyacetic acid), (b) residual spectrum corresponding to peracetic acid generated in a $\text{CH}_3\text{C}(\text{O})\text{H}/\text{CH}_3\text{OH}/\text{Cl}$ mixture, (c) residual spectrum assigned to perpropionic acid generated in a $\text{C}_2\text{H}_5\text{C}(\text{O})\text{H}/\text{CH}_3\text{OH}/\text{Cl}$ mixture, (d) spectrum of acetic acid, and (e) spectrum of propionic acid. The spectra were cut in the range $2400\text{--}1900\text{ cm}^{-1}$.

assigned to the strong OH stretching vibration, which is significantly shifted towards lower wavenumbers comparative to free OH stretching vibrations of alcohols and acids, for instance. This is attributed to intramolecular H-bonding, which lowers the bond strength and subsequently the wavenumber of the absorption band. In the case of peracids, this results in the formation of stable five-membered rings (Giguère and Weingartshofer Olmos, 1952). This characteristic absorption is therefore an undoubted proof for the presence of a peracid. The residual spectrum contains an absorption band at 1450 cm^{-1} , again similar to the peracetic acid spectrum, which is assigned to the OH bending vibration. The absorption bands centred at 1760 cm^{-1} and 1180 cm^{-1} are attributed to the C=O and C-O stretching vibration. Both absorption features are shifted towards lower wavenumbers comparative to the peracetic acid spectrum where a larger shift is observed for the C-O stretching vibration (from 1245 cm^{-1} to 1180 cm^{-1}). Panel (d) and panel (e) of Fig. 6.1 depict reference spectra of gas-phase acetic acid and propionic acid, those absorption bands show the same behaviour for the C=O and C-O stretching vibration. Therefore, all these findings give confidence in attributing the absorption features of the residual spectrum to perpropionic acid.

6.3.2 Primary carbonyls and sCI yield

The wall loss of EVK was found to be in the range $(1-5) \times 10^{-5} \text{ s}^{-1}$. The loss due to the O_3 reaction was about $(6-8) \times 10^{-4} \text{ s}^{-1}$ and hence at least one order of magnitude faster than the wall loss in all performed experiments. The EVK + O_3 reaction was observed until about 60–80 % of the EVK were consumed. Table 6.1 summarizes the yields of the quantified reaction products based on the FTIR measurements as well as the assigned ion signals from the PTR-MS data.

The formation of formaldehyde is unambiguously visible in the FTIR spectra recorded during the reaction, unequivocally larger than any experimental artefacts. Combining the results of all single experiments performed in the presence of CO as an OH radical scavenger results in an average formaldehyde yield of 0.31 ± 0.09 . Its formation as a primary carbonyl can be rationalized through the decomposition of the primary ozonide (POZ), which is formed through the 1,3-dipolar cycloaddition according to the well-established ozonolysis mechanism (Criegee, 1975b). The other decomposition channel generates 2-oxobutanal and the remaining Criegee intermediate formaldehyde oxide (Fig. 6.2). Due to a lack of standard, the oxoaldehyde could not, at first, be unambiguously identified in the FTIR spectra recorded for this reaction mixture. However, its formation is, on one hand, indicated by the evolution of the m/z 87 signal corresponding likely to protonated 2-oxobutanal ($\text{C}_4\text{H}_7\text{O}_2^+$). Additionally, the m/z 59 signal is observed. For the structural analogue oxoaldehyde methyl glyoxal (MH^+ at m/z 73) fragment ions were reported at m/z 45 ($\text{C}_2\text{H}_5\text{O}^+$) which corresponds to a loss of CO (Müller et al., 2012). Correspondingly, the m/z 59 signal is likely a fragment ion of 2-oxobutanal ($\text{C}_3\text{H}_7\text{O}^+$). On the other hand, the FTIR spectra show the build-up of an absorption pattern in the range $2850-2800 \text{ cm}^{-1}$ which is quite characteristic for the C–H stretching vibration of α -oxoaldehydes like glyoxal and methyl glyoxal. An attempt to perform a 2-oxobutanal quantification is presented below based on the experiments where SO_2 was added to the reaction mixture.

The fate of the simultaneously built formaldehyde oxide, CH_2OO , is reasonably well characterized based mainly on extensive work on the ethene + O_3 system (Cox et al., 2020 and references therein). The CI is expected to undergo mainly isomerization into “hot” formic acid, $[\text{HC}(\text{O})\text{OH}]^*$, following the dioxirane channel (Fig. 6.2). The further decomposition of the “hot” formic acid was shown to evolve into different channels forming either CO or CO_2 (Cox et al., 2020). Therefore, the formaldehyde oxide decomposition contributes to the CO_2 formation yield of 0.90 ± 0.21 , obtained from the FTIR data. However, an estimate of the formaldehyde oxide contribution on the built-up of

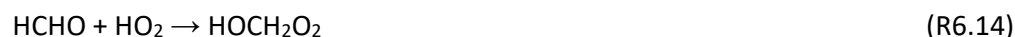
Table 6.1. Quantified reaction products and assigned masses of the EVK + O₃ reaction in the presence of CO as an OH radical scavenger and a supplementary addition of SO₂ together with available literature data. The uncertainties given for the product yields determined within this work represent a combination of the 2 σ statistical error and the accuracy error.

Species	Yield ^a	Yield ^b	Yield ^a	Yield ^c	Assigned m/z ^a
HCHO	0.31 ± 0.09	0.548 ± 0.069	0.37 ± 0.02	0.65 ± 0.12	31.018
2-oxobutanal	0.30 ± 0.07 ^d	0.444 ± 0.025	0.49 ± 0.03	0.53 ± 0.12 ^d	87.045, 59.050
Formic acid	0.034 ± 0.011			0.31 ± 0.10	47.013
Formic anhydride	0.13 ± 0.08				47.013
Acetaldehyde	0.11 ± 0.03	0.097 ± 0.001		0.15 ± 0.05	45.034
Ethyl hydroperoxide	0.13 ± 0.05				45.034
Perpropionic acid	0.066 ± 0.048			n.q.	91.040, 75.045
Propionic acid				0.17 ± 0.03	
Propionaldehyde ^e					59.050
Methyl ketene ^e					57.034
CO ₂ ^f	0.90 ± 0.21			0.54 ± 0.08	
sCl				0.40 ± 0.09	
Detection method	FTIR	LC-UV	FTIR	FTIR	PTR-MS
Reference	This work	Grosjean et al. (1996)	O'Dwyer et al. (2010)	This work	This work

^a Experiments were performed in the presence of CO as an OH radical scavenger, ^b experiments were performed in the presence of cyclohexane as an OH radical scavenger ^c experiments were performed in the presence of CO as and OH radical scavenger and SO₂, ^d the yields were obtained following a semi-quantitative approach by assuming the infrared cross section of the C=O band to equal the cross section of the structural analogue methyl glyoxal, ^e the formation is not unequivocally proven due to interfering fragment ions, ^f sum of CO₂ formed from EVK + O₃ and CO + OH.

CO₂ cannot be given, since by employing CO as a scavenger, almost any OH radical formed in the reaction system converts CO into CO₂.

The HCHO yield is well below 0.5, which is intuitively expected, if the ratio between both POZ decomposition channels were 1. An underestimation of the HCHO yield due to a potential wall loss was ruled out based on the high linearity of the yield plots. Alternatively, a conceivable loss process of HCHO to be considered might be its reaction with HO₂ (R6.14) (Barnes et al., 1985; Veyret et al., 1989), which is known to become likely relevant under higher radical concentrations present in chamber experiments.



The HOCH₂O₂ further chemistry might evolve, for instance, into formic acid (HC(O)OH) formation via the RO₂ self-reaction or the reaction with HO₂. In principle the level of HO₂ is reasonably high mainly due to the conversion of OH into HO₂ by carbon monoxide (see below). From the simulations performed on the temporal evolution of reaction products

Formation of organic acids in the ozonolysis of α,β -unsaturated ketones exemplified by the case study of ethyl vinyl ketone + ozone

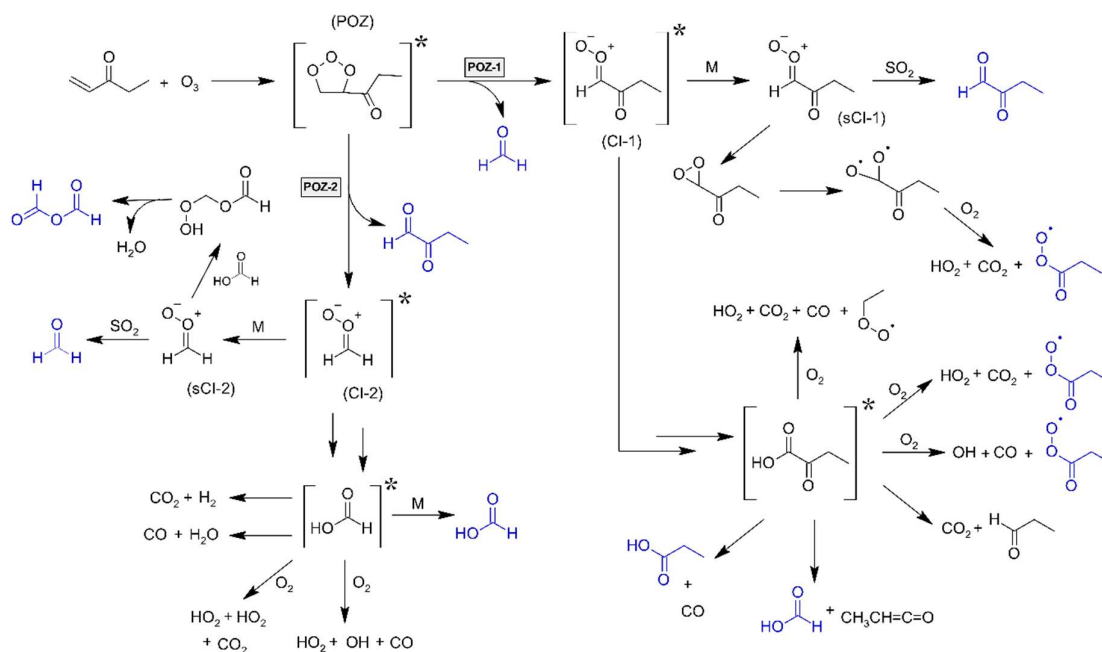


Figure 6.2. Mechanism of the EVK + O₃ reaction built upon the results of the present investigation. Structures are marked in blue for species quantified within this work and for radical species those presence is proven by the quantification of subsequently formed species. For clarity, only the *E*-isomer is drawn for the carbonyl-substituted CI (CI-1). The pathways of (CI-1) will be developed in detail in the text.

assigned to RO₂ reactions, as presented below (see Sect. 6.3.4), a mean [HO₂] of about $\approx 2 \times 10^{10} \text{ cm}^{-3}$ can be concluded for all experiments in the absence of a sCI scavenger. However, when instead the temporal evolution of HCHO is simulated for a simplified reaction system observing the Reactions (R6.14), (R6.15), HOCH₂O₂ + HOCH₂O₂ and HOCH₂O₂ + HO₂, it is found that HO₂ levels about a factor of 40–50 larger are necessary in order to observe a measurable influence on HCHO. Although the obtained value for [HO₂] provides just a rough estimate, a factor of 40–50 is far beyond the uncertainties and experimentally implausible. The observed HCHO yield is therefore not expectedly affected by a secondary consumption of HCHO by HO₂.

In the presence of SO₂ the HCHO yield increases from 0.31 ± 0.09 to 0.65 ± 0.12 while up to 20 % of the SO₂ are consumed during the EVK + O₃ reaction. SO₂ has been shown to react quite fast with Criegee Intermediates ($k(\text{SO}_2 + \text{CI}) \approx 10^{-11} - 10^{-10} \text{ cm}^3 \text{ molecule}^{-1} \text{ s}^{-1}$), converting a carbonyl oxide into the corresponding carbonyl (Cox et al., 2020). This is, however, limited to the fraction of thermally equilibrated CIs those lifetime is long enough to allow bimolecular reactions to compete with decomposition. Hence, the increase of the

HCHO yield by a factor of 2 points out that a significant fraction of the formaldehyde oxide formed in the EVK + O₃ reaction is stabilized. A plot of the consumed SO₂ vs. the consumed EVK provides an estimate of 0.40 ± 0.09 for the stabilized Criegee Intermediate (sCI) yield. With respect to SAR predictions (Vereecken et al., 2017), for a fraction of the stabilized CIs decomposition might be still faster than bimolecular reactions, therefore the sCI yield should be considered as a lower limit. However, the linearity of the plots over the whole experimental duration suggests that, even after certain amounts of acids are formed (see below), the level of SO₂ was sufficient to suppress sCI + acid reactions.

Trace (a) of Fig. 6.3 shows a residual spectrum of an experiment, performed in the presence of SO₂, after subtraction of all clearly identified species. In all experiments with added SO₂ a non-linear baseline shift is observed, which is attributed to particle formation in the system. This can be rationalized through the size-dependent scattering of IR radiation when the particle diameters are similar to the wavenumber of the radiation and the particle concentration is sufficiently high. The particle-based scattering lowers the IR radiation intensity entering the detector of the spectrometer. Hence, a broad absorption becomes visible in the FTIR spectra. Given that this effect is not observed in the absence of SO₂, this is interpreted as the formation of H₂SO₄ due to the reaction of the SO₃, formed from the reaction of SO₂ with the CIs, and the amount of H₂O still present in the bath gas.

Trace (b) shows the same residual spectrum after applying a baseline correction. Since all other identified reaction products were subtracted at this point and secondary reactions were largely minimized due to the addition of SO₂, the residual absorption bands visible in the range 3500–1600 cm⁻¹ should correspond mainly to 2-oxobutanal. For comparison, trace (c) shows a reference spectrum of gas-phase methyl glyoxal, which possesses characteristic absorption features for the C=O stretching vibrations centred on 1730 cm⁻¹ and for the C–H stretching vibration of the aldehyde moiety (as mentioned above) in the range 2860–2800 cm⁻¹. Both position and relative intensity of these absorption bands are similarly found in the residual spectrum in panel (b). Additionally, the absorption pattern around 3000 cm⁻¹ (C–H stretching vibration of alkyl groups) is quite similar to the gas-phase FTIR spectrum of propionaldehyde presented in panel (d). This all supports the assignment of the residual spectrum to 2-oxobutanal. Taking into account that absorption cross sections of characteristic vibrations usually do not show a large variability for structurally similar compounds, a quantitative FTIR spectrum of 2-oxobutanal was obtained by applying the infrared cross section of the methyl glyoxal C=O absorption band (Talukdar et al., 2011) to the baseline corrected residual spectrum. Accordingly, the 2-oxobutanal yield was found

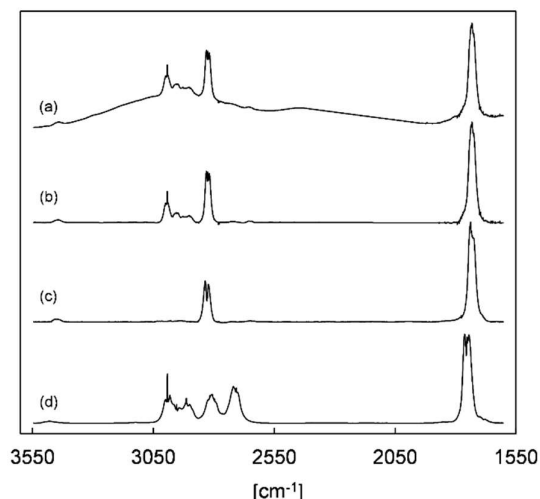


Figure 6.3. (a) Residual spectrum assigned to 2-oxobutanal from an EVK + O₃ experiment in the presence of CO used as an OH radical scavenger and SO₂ used as a sCl scavenger (the spectrum was cut in the range 2400–1900 cm⁻¹), (b) spectrum (a) after baseline correction, (c) reference spectrum of methyl glyoxal, and (d) reference spectrum of propionaldehyde.

to be 0.30 ± 0.07 in the presence of CO as an OH radical scavenger and 0.53 ± 0.12 when SO₂ was present during the reaction. In the absence of the sCl scavenger, the obtained 2-oxobutanal yield is thus identical to the HCHO yield, which indicates the ratio to be 1 in between both POZ decomposition channels. However, this implies that in the present investigation the POZ decomposition accounts solely for about 61 ± 11 % of the EVK + O₃ reaction. One might intuitively think that this indicates an overestimation of the EVK consumption which could be related either to a quantification error or to an unidentified secondary loss process of EVK. Though, even after re-analysis of the calibration data and additional control experiments there is no indication for an erroneous infrared cross section. A hypothetically secondary loss process might be the reaction of EVK with sCl. At least for the structural analogue methyl vinyl ketone (MVK) it was shown that, under experimental conditions similar to the present study, the observed kinetics of MVK + O₃ was not affected by the reaction of the unsaturated ketone with Cls (Neeb et al., 1999). It is therefore reasonable to assume that EVK + O₃ exhibits the same behaviour.

The gas-phase ozonolysis of EVK has been formerly investigated by Grosjean et al. (1996) and O'Dwyer et al. (2010). Grosjean et al. (1996) reported product yields of 0.548 ± 0.069 and 0.444 ± 0.025 for HCHO and 2-oxobutanal, respectively. The quantification of the carbonyls was done by the measurement of the 2,4-

dinitrophenylhydrazine (DNPH) derivatives by liquid chromatography after the collection of samples onto DNPH-coated cartridges (Grosjean et al., 1996). Thus, both the HCHO and the 2-oxobutanal yield determined within this work are significantly lower than reported by Grosjean et al. (1996). In contrast to the present work, the former study has been carried out at a relative humidity of 55 ± 10 %. Although the bimolecular reaction of formaldehyde oxide with H_2O is quite slow ($10^{-16} \text{ cm}^3 \text{ molecule}^{-1} \text{ s}^{-1}$, Cox et al. 2020), at least a fraction of the stabilized CH_2OO will react with H_2O under these experimental conditions. The $\text{CH}_2\text{OO} + \text{H}_2\text{O}$ as well as the $\text{CH}_2\text{OO} + (\text{H}_2\text{O})_2$ reaction have been shown to form initially the chemically activated hydroxymethyl hydroperoxide, OHCH_2OOH , (Neeb et al., 1997), which is either thermalized or decomposes into HC(O)OH and H_2O or HCHO and H_2O_2 . Therefore, an additional source of HCHO might have been present under the humid conditions of the former study. However, since at least for the reaction with the water dimer other studies provided contradictory conclusions on the relative importance of each reaction channel (Nguyen et al., 2016; Sheps et al., 2017; Cox et al., 2020), no clear statement can be made. On the other hand, no data are available for the carbonyl-substituted Cl. Due to a lack of standard, Grosjean et al. (1996) used a response factor estimated from the results of other α -dicarbonyls, where standards were available, for the quantification of 2-oxobutanal. Accordingly, they assigned a 20 % relative error to the 2-oxobutanal response factor. Therefore, the relative error of < 6 % reported for the 2-oxobutanal yield under humid conditions (Grosjean et al., 1996) is at least surprising.

By contrast, O'Dwyer et al. (2010) worked at a relative humidity < 1 %. They reported product yields of 0.37 ± 0.02 and 0.49 ± 0.03 for HCHO and 2-oxobutanal, respectively. The present value for HCHO is thus identical to O'Dwyer et al. (2010) within the assigned uncertainty. Similar to the present approach, O'Dwyer et al. (2010) quantified 2-oxobutanal by assuming the cross section of the C=O absorption to be same as for a structurally similar compound, namely *n*-butanal. Following this rationale, they obtained a 2-oxobutanal yield which is about 60 % larger than determined here. Comparing the cross section of the integrated carbonyl absorption band of methyl glyoxal (e. g. Talukdar et al., 2011) with a value for the C=O absorption band of *n*-butanal from the Wuppertal laboratory database, it is found that the cross section is about ≈ 65 % larger in the case of the α -dicarbonyl. Consequently, the experimentally observed correlation between the integrated carbonyl absorption of 2-oxobutanal and the consumption of EVK are nearly the same in the present study and that of O'Dwyer et al. (2010). The authors argue solely that the cross section of *n*-butanal was chosen due to the similarities between the residual spectrum and that of *n*-butanal. By contrast, they do not state why they expect the intensity of the C=O absorption

of an α -dicarbonyl to be the same as for an aldehyde containing only one carbonyl group, which is not plausible.

6.3.3 HC(O)OH and HC(O)OC(O)H formation

The formation of formic acid is indicated in the FTIR spectra, possibly supported by the evolution of the m/z 47 signal in the PTR-MS data. The calculated yield is 0.034 ± 0.011 . However, fragment ions of anhydrides appear as m/z of their corresponding acid. Given that formic anhydride (FA) is observed (FTIR) with a yield of about 0.13 ± 0.08 , the presence of the m/z 47 signal is probably mainly a consequence of the anhydride formation. The yield plot of FA is shown in panel (a) of Fig 6.4. In each experiment, the correlation is strongly linear, but significantly different slopes are observed, which is reflected in the large error assigned to the FA yield. Although formic acid is a likely contaminant present in chamber experiments, both the reproducibility of the HC(O)OH yield and the observation of formic anhydride indicate that HC(O)OH is formed from the EVK + O₃ reaction. Additionally, an HC(O)OH yield of 0.31 ± 0.10 was found, when the reaction was carried out in the presence of SO₂. The increase of the yield by a factor of 10 is clearly beyond a possible level of contamination although a non-linear behaviour is observed for the yield plots at long reaction times which is the likely result of a significant wall loss at higher HC(O)OH concentrations (Fig. 6.4).

The formic anhydride cannot result directly from the ozonolysis reaction itself. Its formation is expected to proceed through the bimolecular reaction of the formaldehyde oxide with formic acid resulting in the generation of hydroperoxymethyl formate (HPMF), as observed in former studies (Neeb et al., 1995; 1996). The spectral features do not support the existence of HPMF. Though, HPMF decomposition leads to H₂O and formic anhydride (Neeb et al., 1995; 1996), which is therefore an indirect evidence for the HC(O)OH formation in the system. Further, nearly all formic acid formed in the system is consumed via the fast reaction of HC(O)OH + sCl. This is confirmed, on the one hand, by the large increase of the HCHO yield in the presence of SO₂ indicating a large fraction of thermally equilibrated formaldehyde oxide prone to bimolecular reactions. On the other hand, the consumption of HC(O)OH through sCl is largely suppressed in the presence of SO₂, therefore causing the substantial increase of the observed HC(O)OH yield. Since both formic acid and HPMF influence the formation of FA, the FA yield is sensitive to the further fate of both precursor species. This supposedly explains the variation observed for the FA

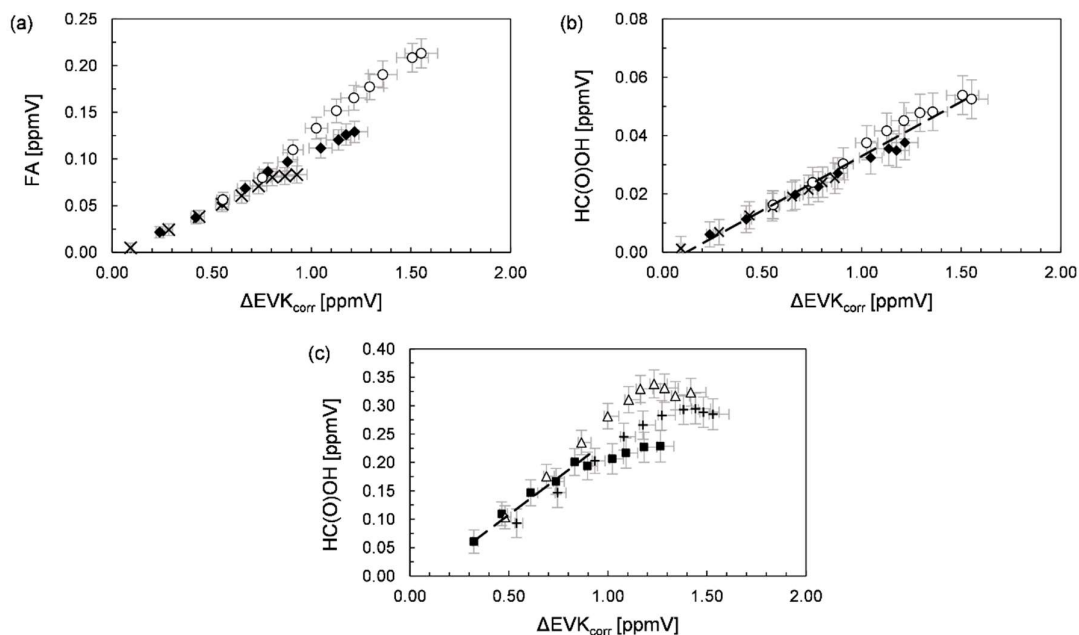


Figure 6.4. Yield plots obtained for (a) formic anhydride (FA), and (b) formic acid in the absence of SO_2 , and (c) formic acid in the presence of SO_2 . Different experimental runs are denoted with different symbols. The error bars represent a precision error as a combination of a relative error plus the corresponding detection limit under the experimental conditions.

yield. For instance, if HC(O)OH exhibits a significantly larger wall loss in one experiment, this will result necessarily in a lowering of HPMF and consequently the FA yield observed. On the other hand, due its formation from secondary reactions, one should observe larger FA yields with higher EVK consumption levels. While this might be the case for the experiment represented by the open circles, this is clearly not observed for the other experiments (Fig. 6.4). The reason for this behaviour remains unexplained.

In principle, a formation of formic acid is also possible from the $CH_2OO + SO_2$ reaction. Hatakeyama et al. (1986) suggested this reaction to proceed initially via the reversible formation of an adduct, which decomposes into HC(O)OH and SO_2 . It was further shown that higher SO_2 levels lower the HC(O)OH yield. Theoretical calculations indicate that the further fate of the initially formed adduct evolves mainly into $HCHO + SO_3$, whereas only 17 % result into the formation of a singlet bis(oxy) biradical (Vereecken et al., 2012). This, in turn, might isomerize and yield at least partly stabilized formic acid. Accordingly, a contribution of $CH_2OO + SO_2$ to the overall HC(O)OH yield is generally possible. However,

since there is a strong evidence for the formic acid formation in the absence of SO_2 (formic acid and formic anhydride), this is not the major source of formic acid.

Although HC(O)OH might be hypothetically also formed in the reaction of formaldehyde oxide with H_2O , a contribution to HC(O)OH formation can be ruled out given both the low H_2O level in the experiments and the low rate coefficient ($10^{-16} \text{ cm}^3 \text{ molecule}^{-1} \text{ s}^{-1}$) of the $\text{CH}_2\text{OO} + \text{H}_2\text{O}$ reaction (Cox et al., 2020). Chemically activated CIs were shown to possibly form dioxirane intermediates that convert to singlet bis(oxy) biradicals and subsequently isomerize to acids (or esters). In the case of formaldehyde oxide this reaction pathway provides the vibrationally excited formic acid ($[\text{HC(O)OH}]^*$). Therefore, one assumes intuitively that collisional stabilization of the vibrationally excited acid to be the source of HC(O)OH . The formation of stabilized acids has been reported following the dioxirane isomerization in the case of larger terpene-based CIs (Winterhalter et al., 2009; Nguyen et al., 2009a; 2009b). This may be interpreted in terms of a larger probability of collisional stabilization due to a larger number of vibrational modes comparative to smaller CIs, which potentially allows the excess energy to be distributed below a dissociation threshold. Accordingly, up to now only fragmentation of the molecule has been reported for the smallest CI (Cox et al., 2020). However the unexpectedly high HC(O)OH yield, measured within this work, indicates the possibility of a vibrational excitation of $[\text{HC(O)OH}]^*$ that is low enough to allow collisional stabilization. Another possible formation mechanism will be discussed below.

6.3.4 Fate of the carbonyl-substituted CI

The formation of perpropionic acid is indicated by the characteristic absorption band centred on 3303 cm^{-1} (Fig 6.5). Within PTR-MS measurements, the $\text{H}_3\text{O}^+ + \text{peracetic acid}$ reaction was shown to produce mainly ($\approx 90\%$) protonated acetic acid (Španěl et al., 2003), which hence interferes with acetic acid at m/z 61 ($\text{C}_2\text{H}_5\text{O}_2^+$). Since a similar behaviour is likely for perpropionic acid and propionic acid is not observed in the FTIR spectra when working without a sCI scavenger, the evolution of the m/z 75 signal further supports the assignment to perpropionic acid. In addition, although much less intense (by a factor of $\approx 10^2$), an increase is observed for the m/z 91 ion, which could result from the protonated perpropionic acid. Infrared cross sections of peracids were only reported for peracetic acid. Orlando et al. (2000) determined an absorption cross section of $(5.3 \pm 0.7) \times 10^{-19} \text{ cm}^2 \text{ molecule}^{-1}$ (base e) at 1251 cm^{-1} , which, as pointed out by Berasategui et al. (2020), was

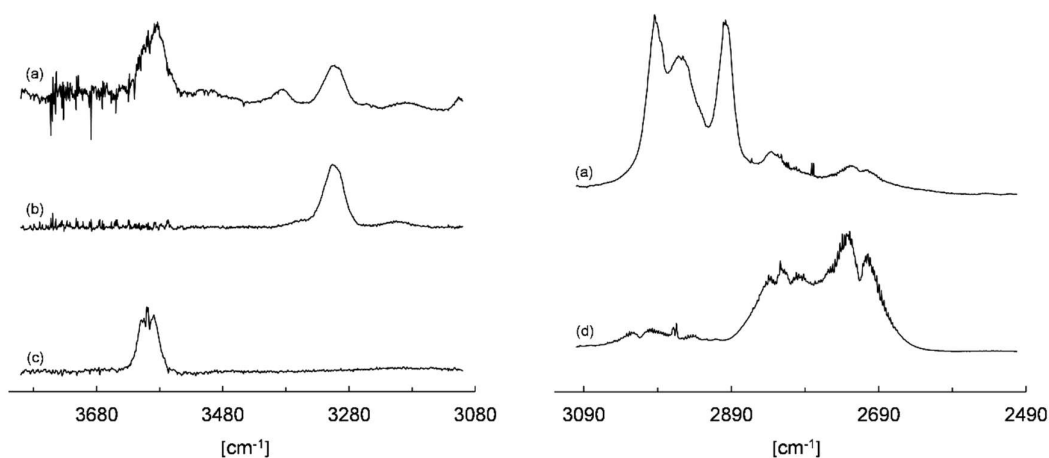


Figure 6.5. (a) Spectrum of an EVK + O₃ experiment, collected after an EVK consumption of about 70 %, after subtraction of H₂O, EVK, HCHO, HC(O)OH, and 2-oxobutanal, and reference spectra of (b) perpropionic acid, (c) ethyl hydroperoxide, and (d) acetaldehyde, respectively.

mistakenly listed as 1295 cm⁻¹. Applying this value to the reference spectrum of peroxyacetic acid produced here allows estimating a cross section for the absorption band of the C=O stretching vibration, which then was used to calculate the concentrations of peroxypropionic acid according to the semi-quantitative approach presented previously for 2-oxobutanal. Based on that, the yield of perpropionic acid was found to be 0.066 ± 0.048 for the experiments without a sCl scavenger. One can observe that between the different experimental runs there is a good agreement, as evidenced from the yield plot in panel (b) of Fig. 6.6. However, due to the semi-quantitative approach used to quantify the perpropionic acid, an expanded uncertainty of 50 % was added to the statistical error.

In the presence of SO₂ a small curvature around 3300 cm⁻¹ might indicate the formation of perpropionic acid. However, a reliable quantification is not possible due to the baseline shift during the reaction, as discussed above. Acetaldehyde and ethyl hydroperoxide are found with formation yields of 0.11 ± 0.03 and 0.13 ± 0.03 , respectively, in the absence of the sCl scavenger (Fig. 6.6). No signal was detected at m/z 63, corresponding to the hydroperoxide (C₂H₇O₂⁺). However, the fragment ion (C₂H₅O⁺), built upon elimination of H₂O, interferes with acetaldehyde at m/z 45. Hence, although the evolution of the m/z 45 ion supports the FTIR data, a differentiation between the contribution of acetaldehyde and an ethyl hydroperoxide fragment is not possible. When SO₂ was present, the acetaldehyde yield increased minimally (0.15 ± 0.05) while no indication for ethyl hydroperoxide could

Formation of organic acids in the ozonolysis of α,β -unsaturated ketones exemplified by the case study of ethyl vinyl ketone + ozone

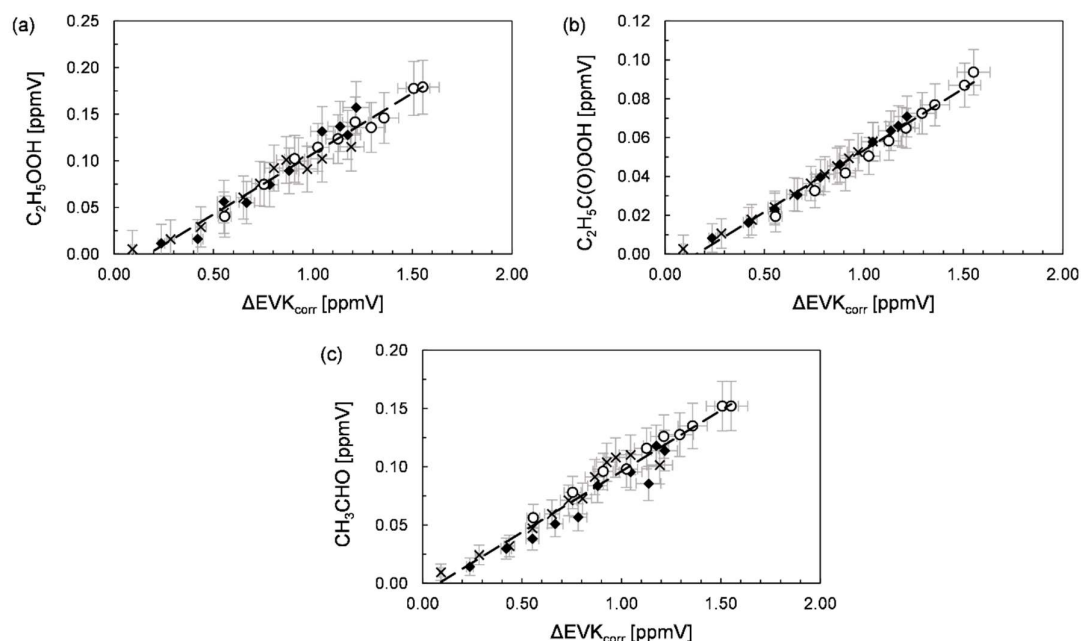


Figure 6.6. Yield plots obtained for (a) ethyl hydroperoxide, (b) perpropionic acid, and (c) acetaldehyde, respectively, in the absence of SO_2 . Different experimental runs are denoted with different symbols. The error bars represent a precision error as a combination of a relative error plus the corresponding detection limit under the experimental conditions.

be found in the FTIR spectra. Additionally, the formation of propionic acid is observed.

Perpropionic acid formation can solely be rationalized through the reaction of the propionyl peroxy radical ($C_2H_5C(O)O_2$) with HO_2 . Accordingly, the level of HO_2 in the system must be sufficiently high to allow a competition between $RO_2 + HO_2$ and $RO_2 + RO_2$ reactions. This is likely the result of OH radicals formed from the $EVK + O_3$ reaction, which in the presence of an excess of CO are converted nearly quantitatively into HO_2 radicals, or H atoms following Cl fragmentation. Up to now, the $C_2H_5C(O)O_2 + HO_2$ reaction has only been investigated by Hasson et al. (2012) who reported branching ratios of 0.35 ± 0.1 , 0.25 ± 0.1 , and 0.4 ± 0.1 for the pathways yielding perpropionic acid, propionic acid and ethyl peroxy radicals ($C_2H_5O_2$), respectively (Fig. 6.7). The latter radical itself reacts with HO_2 to form ethyl hydroperoxide. Though, the acetaldehyde formation can only proceed via $RO_2 + RO_2$ reactions. Both, the $C_2H_5C(O)O_2 + C_2H_5O_2$ reaction and the $C_2H_5O_2$ self-reaction finally produce acetaldehyde (Fig. 6.4). Since the rate coefficient of the self-reaction is 10^2 times smaller than for the $C_2H_5C(O)O_2 + C_2H_5O_2$ reaction (Le Crâne et al.,

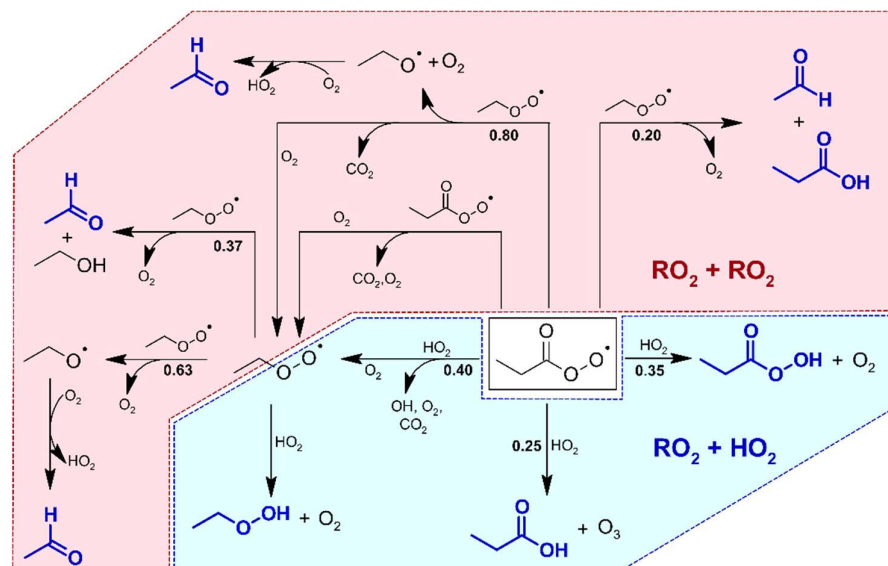


Figure 6.7. Chemistry of the propionyl peroxy and ethyl peroxy radical based on the identified reaction products (blue structures). For clarity, the reaction sequences are only shown considering a prompt propionyl peroxy radical source in the experimental system. The blue area represents the $RO_2 + HO_2$ reactions, the rose area marks the $RO_2 + RO_2$ domain. The corresponding branching ratios, given in bold numbers, are the current IUPAC recommendations (2021). For the $C_2H_5C(O)O_2 + HO_2$ reaction the values are taken from Hasson et al. (2012).

2005; Noell et al., 2010), the $C_2H_5O_2$ self-reaction is expectedly negligible in the present experiments (without SO_2).

The rate coefficient of the $C_2H_5C(O)O_2$ self-reaction is comparable to the RO_2 cross-reaction (Le Crâne et al., 2005). Hence, the self-reaction increases the level of ethyl peroxy radicals in the experiments due to the conversion from $C_2H_5C(O)O_2$ into $C_2H_5O_2$ radicals. In the absence of SO_2 the acetaldehyde yield was found to be the same as the ethyl hydroperoxide yield within the assigned uncertainties. Therefore, about 50 % of the ethyl peroxy radicals react with HO_2 , whereas the remaining 50 % react with propionyl peroxy radicals.

The observed acetaldehyde yield is in good agreement with the value (0.10) reported by Grosjean et al. (1996). However, RO_2 reactions were not considered in the former study. The authors gave no explanation for the acetaldehyde formation, which was therefore attributed to either an impurity, a secondary reaction due to non-scavenged OH radicals or an unknown mechanism (Grosjean et al., 1996).

About 20 % of $C_2H_5C(O)O_2 + C_2H_5O_2$ reaction results also in propionic acid, those formation is not observed in the absence of SO_2 . As discussed for $HC(O)OH$, this does not

Table 6.2. Reaction sequence used for modelling the temporal behaviour of acetaldehyde, ethyl hydroperoxide, and perpropionic acid.

Reaction	Branching ratio	Rate coefficient ^a
(R6.16a) ^b $\text{CH}_2=\text{CHC}(\text{O})\text{C}_2\text{H}_5 + \text{O}_3 \rightarrow \text{C}_2\text{H}_5\text{C}(\text{O})\text{O}_2$		^c
(R6.16b) ^b $\text{CH}_2=\text{CHC}(\text{O})\text{C}_2\text{H}_5 + \text{O}_3 \rightarrow \text{C}_2\text{H}_5\text{O}_2$		^c
(R6.17) $\text{C}_2\text{H}_5\text{C}(\text{O})\text{O}_2 + \text{HO}_2 \rightarrow \text{products}$		2.0×10^{-11} ^d
(R6.17a) $\text{C}_2\text{H}_5\text{C}(\text{O})\text{O}_2 + \text{HO}_2 \rightarrow \text{C}_2\text{H}_5\text{C}(\text{O})\text{OOH} + \text{O}_2$	0.35 ^e	
(R6.17b) $\text{C}_2\text{H}_5\text{C}(\text{O})\text{O}_2 + \text{HO}_2 \rightarrow \text{C}_2\text{H}_5\text{C}(\text{O})\text{OH} + \text{O}_3$	0.25 ^e	
(R6.17c) $\text{C}_2\text{H}_5\text{C}(\text{O})\text{O}_2 + \text{HO}_2 (+ \text{O}_2) \rightarrow \text{C}_2\text{H}_5\text{O}_2 + \text{OH} + \text{O}_2 + \text{CO}_2$	0.40 ^e	
(R6.18) $2 \text{C}_2\text{H}_5\text{C}(\text{O})\text{O}_2 (+ \text{O}_2) \rightarrow 2 \text{C}_2\text{H}_5\text{O}_2 + \text{O}_2 + 2 \text{CO}_2$		1.7×10^{-11} ^f
(R6.19) $\text{C}_2\text{H}_5\text{C}(\text{O})\text{O}_2 + \text{C}_2\text{H}_5\text{O}_2 \rightarrow \text{products}$		1.2×10^{-11} ^f
(R6.19a) $\text{C}_2\text{H}_5\text{C}(\text{O})\text{O}_2 + \text{C}_2\text{H}_5\text{O}_2 (+ \text{O}_2) \rightarrow \text{C}_2\text{H}_5\text{O}_2 + \text{CO}_2 + \text{CH}_3\text{C}(\text{O})\text{H} + \text{HO}_2 + \text{O}_2$	0.8 ^f	
(R6.19b) $\text{C}_2\text{H}_5\text{C}(\text{O})\text{O}_2 + \text{C}_2\text{H}_5\text{O}_2 \rightarrow \text{C}_2\text{H}_5\text{C}(\text{O})\text{OH} + \text{CH}_3\text{C}(\text{O})\text{H} + \text{O}_2$	0.2 ^f	
(R6.20) $\text{C}_2\text{H}_5\text{O}_2 + \text{HO}_2 \rightarrow \text{C}_2\text{H}_5\text{OOH} + \text{O}_2$		6.9×10^{-12} ^f
(R6.21) $2 \text{C}_2\text{H}_5\text{O}_2 \rightarrow \text{products}$		7.6×10^{-14} ^f
(R6.21a) $2 \text{C}_2\text{H}_5\text{O}_2 (+ \text{O}_2) \rightarrow 2 \text{CH}_3\text{C}(\text{O})\text{H} + 2 \text{HO}_2 + \text{O}_2$	0.37 ^f	
(R6.21b) $2 \text{C}_2\text{H}_5\text{O}_2 \rightarrow \text{CH}_3\text{C}(\text{O})\text{H} + \text{C}_2\text{H}_5\text{OH} + \text{O}_2$	0.63 ^f	

^a In [$\text{cm}^3 \text{ molecule}^{-1} \text{ s}^{-1}$], ^b either a prompt source of $\text{C}_2\text{H}_5\text{C}(\text{O})\text{O}_2$ (R6.16a) or $\text{C}_2\text{H}_5\text{C}(\text{O})\text{O}_2$ and $\text{C}_2\text{H}_5\text{O}_2$ radicals (R6.16a + R6.16b) was considered, ^c the radical source was included according to the experimental first-order loss of EVK, ^d the rate coefficient was assumed to be the same as the IUPAC recommended value for the $\text{CH}_3\text{C}(\text{O})\text{O}_2 + \text{HO}_2$ reaction, ^e Hasson et al. (2012), ^f IUPAC recommended values (2021).

mean that propionic acid is not formed in the system since virtually all propionic acid formed in the system is likely consumed due to a fast reaction with sCIs. For instance, the reaction of the formaldehyde oxide with propionic acid is expected to yield as well a hydroperoxide ester, which decomposes to formic propionic anhydride and H_2O . Accordingly, the fragment ions of the anhydride would also appear at m/z 47 and m/z 75 in the PTR mass spectra.

In order to prove, if the temporal behaviour of acetaldehyde, ethyl hydroperoxide, propionic acid and perpropionic acid can be described solely through the known RO_2 reactions, the temporal evolution of the reaction products was simulated following the approach described recently in the literature (Illmann et al., 2021b; 2021d). Table 6.2 summarizes the reaction sequences needed to describe the system. Model runs were performed assuming the $\text{EVK} + \text{O}_3$ reaction to form initially either $\text{C}_2\text{H}_5\text{C}(\text{O})\text{O}_2$ or $\text{C}_2\text{H}_5\text{C}(\text{O})\text{O}_2$ and $\text{C}_2\text{H}_5\text{O}_2$ radicals. A major uncertainty of the simulations is $[\text{HO}_2]$, given that the HO_2 concentration cannot be determined experimentally. The value is adjusted mainly by reproducing the experimental time profiles of perpropionic acid. However, when only $\text{C}_2\text{H}_5\text{C}(\text{O})\text{O}_2$ radicals are formed promptly from $\text{EVK} + \text{O}_3$, an estimation of the overall $\text{C}_2\text{H}_5\text{C}(\text{O})\text{O}_2$ radical yield is given by the sum of the acetaldehyde, ethyl hydroperoxide and

perpropionic acid yield. The temporal profiles of both acetaldehyde and ethyl hydroperoxide, whose quantification errors are much smaller than for perpropionic acid, were found to be very sensitive to the overall $\text{C}_2\text{H}_5\text{C}(\text{O})\text{O}_2$ radical yield and $[\text{HO}_2]$. Though, adjusting both $[\text{HO}_2]$ and the overall $\text{C}_2\text{H}_5\text{C}(\text{O})\text{O}_2$ radical yield allows a simultaneous fit for all temporal profiles within the uncertainties of the experimentally determined product yields. When a prompt source of $\text{C}_2\text{H}_5\text{O}_2$ radicals from the EVK + O_3 reaction is included, a match of all time profiles is achieved only for the lower accuracy limit of the perpropionic acid data. Accordingly, the overall $\text{C}_2\text{H}_5\text{C}(\text{O})\text{O}_2$ radical yield is lower than without considering a potentially prompt source of $\text{C}_2\text{H}_5\text{O}_2$ radicals, although in all model runs the $\text{C}_2\text{H}_5\text{O}_2$ source was found to be a factor of 3–4 smaller than the $\text{C}_2\text{H}_5\text{C}(\text{O})\text{O}_2$ source. Based on these results it is not possible to conclude whether the ethyl peroxy radical evolves solely from the propionyl peroxy radical further chemistry or also promptly from the CI chemistry. Nevertheless, the present results hint at the propionyl peroxy radical being the dominant RO_2 . The temporal evolution of acetaldehyde, ethyl hydroperoxide and perpropionic acid seems generally to be well described by the RO_2 reactions above listed in Tab. 6.2 for the experiments in the absence of SO_2 .

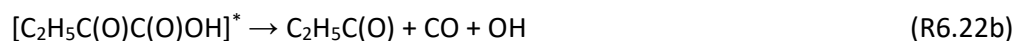
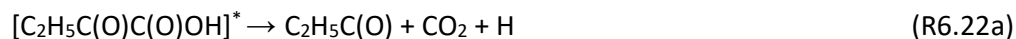
Since no hydroperoxides could be quantified, this is an indication that the RO_2 further chemistry is dominated by $\text{RO}_2 + \text{RO}_2$ reactions in the experiments in the presence of SO_2 . Therefore, there is no possibility to adjust $[\text{HO}_2]$ for the modelling approach. Although all possible $\text{RO}_2 + \text{RO}_2$ reactions shift the reaction system towards acetaldehyde formation, in the absence of SO_2 the acetaldehyde yield is about a factor of 2 smaller than the sum of the acetaldehyde, ethyl hydroperoxide and perpropionic acid yield. This indicates a much lower RO_2 level when the sCIs are scavenged with SO_2 . However, in this set-up it is not possible to decipher precisely the contribution of the $\text{C}_2\text{H}_5\text{O}_2$ self-reaction and the $\text{C}_2\text{H}_5\text{C}(\text{O})\text{O}_2 + \text{C}_2\text{H}_5\text{O}_2$ reaction towards acetaldehyde formation (Fig. 6.7). Since, contrary to ethyl hydroperoxide, the formation of perpropionic acid is at least suggested by the FTIR data, this might indicate the propionyl peroxy radical to be still the dominant RO_2 radical. Further, the formation of ethanol, following the $\text{C}_2\text{H}_5\text{O}_2$ self-reaction, was not supported by the FTIR spectra in any of the experiments.

The uncertainties of the branching ratios assigned to the $\text{C}_2\text{H}_5\text{C}(\text{O})\text{O}_2 + \text{C}_2\text{H}_5\text{O}_2$ reaction set a range of 0.0–0.4 for the propionic acid/acetaldehyde formation ratio based on the $\text{RO}_2 + \text{RO}_2$ reactions in the present experiments, which is well below the observed ratio (1.1 ± 0.4). This is a strong evidence for an additional source of propionic acid in the EVK + O_3 reaction besides the RO_2 based formation. In addition, since propionic acid is observed under conditions, where sCI reactions are largely minimized, this suggests strongly its

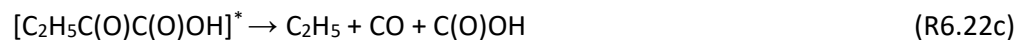
formation from chemically activated carbonyl oxides. As discussed above, the formation of stabilized acids following the dioxirane isomerization was reported for larger CIs (Winterhalter et al., 2009; Nguyen et al., 2009a; 2009b). But as the POZ decomposition yields initially a C₁- and a C₄-fragment, the above mentioned mechanism cannot account for the formation of the C₃-acid (propionic acid). This, in turn, would result into 2-oxobutanoic acid, which is observed neither in the PTR mass spectra, nor in the FTIR spectra, assuming a similar spectral structure as the infrared spectra of gas-phase pyruvic acid (2-oxopropanoic acid).

However, the prompt formation of the C₂H₅C(O)O₂ radical (and possibly of the C₂H₅O₂ radical) and the amount of propionic acid, not accounted for by RO₂ further reactions, can only originate from the C₄-fragment, which, in turn, is the carbonyl-substituted CI. The carbonyl group in α -position prohibits the possibility of an 1,4-H shift isomerization and the intermediate formation of a vinyl hydroperoxide. Therefore, this CI is expected to undergo mainly an isomerization following a 1,3-ring closure (dioxirane route), which yields probably the vibrationally excited oxobutanoic acid, [C₂H₅C(O)C(O)OH]*, irrespective of the E- or Z-configuration of the CI. This implies that both the propionyl peroxy radical and the subsequent reaction products as well as propionic acid, not accounted for by RO₂ reactions, arise from the decomposition of [C₂H₅C(O)C(O)OH]*.

Fragmentation routes of vibrationally excited acids were reported mainly for [HC(O)OH]* and [CH₃C(O)OH]*, although the data level remains relatively scarce (Cox et al., 2020 and references therein) and no such data are available for substituted acids. However, based on the observed reaction products, 6 different fragmentation routes are proposed for the vibrationally excited oxobutanoic acid. Accordingly, there are 3 fragmentation pathways following a bond cleavage, which, in turn, result in the formation of the radical species confirmed by the observed products. The bond scission may occur either between the H and O atom of the OH group or between the OH and the carbonyl group. The remaining radical will readily eliminate either CO₂ or CO. However, in both cases a propionyl radical is formed which, in the presence of O₂, is immediately converted into a propionyl peroxy radical.



A third radical-forming channel may be existent, where a bond cleavage occurs between the alkyl and the carbonyl group.



Hence, an ethyl peroxy radical, HO₂, CO and CO₂ should be ultimately formed in the presence of O₂. As discussed above, it is presently not clear, if ethyl peroxy radicals are formed promptly from the EVK + O₃ reaction or result only from the propionyl peroxy radical further chemistry. Though, even if the branching ratios were the same for each of the above mentioned decomposition channels, the formation of propionyl peroxy radicals would dominate, as concluded from the experimental results.

Since an additional source of propionic acid is inevitably related also to the chemically activated carbonyl-substituted Cl, propionic acid is suggested to arise from a molecular fragmentation pathway.



Although a direct comparison is not given, at least the fact that the fragmentation yields stable molecules is in agreement with previous observations for [HC(O)OH]^{*} and [CH₃C(O)OH]^{*} (Cox et al., 2020 and references therein).

Another possible molecular fragmentation route were the elimination of CO₂ and the consecutive formation of propionaldehyde.



However, the identification of propionaldehyde is not conclusively confirmed. Although a small absorption observed in the range 2750–2680 cm⁻¹ of the residual FTIR spectra might indicate its formation, the intensity is too low to permit a reliable assignment to the C₃-aldehyde. The evolution of the *m/z* 59 signal is as well not an unambiguous proof for propionaldehyde being more likely a fragment ion of 2-oxobutanal.

There might also be a molecular fragmentation route similar to the ketene formation as observed for the vibrationally excited acetic acid. Accordingly, one would expect the formation of methyl ketene and HC(O)OH, which would hence interfere with the suggested HC(O)OH source from the collisional stabilization of [HC(O)OH]^{*}.



Since $C_2H_5C(O)^+$ ions interfere at m/z 57, the increase of the ion signal is not a reliable proof for methyl ketene formation. Assuming $HC(O)OH$ is formed solely through the collisional stabilization of $[HC(O)OH]^*$, the reaction products (including the non-quantified co-products like CO and CO_2 from the carbonyl-substituted CI) account for about $96 \pm 16 \%$ of the C_1 -fragment and $85 \pm 13 \%$ of the C_4 -fragment in the presence of SO_2 . If $HC(O)OH$ were formed solely from the fragmentation of $[C_2H_5C(O)C(O)OH]^*$, $65 \pm 12 \%$ accounted for the C_1 -fragment and $116 \pm 17 \%$ for the C_4 -fragment. One would intuitively think the first case to be more reliable as the POZ decomposition yields necessarily both a C_1 -fragment and the C_4 -fragment, irrespective of the branching ratios of both decomposition channels. Therefore, the fractions of both the C_1 -fragment and the C_4 -fragment products should be the same within the assigned uncertainties. However, if the $[HC(O)OH]^*$ is not stabilized by collision, the only closed-shell decomposition products are CO and CO_2 those fraction cannot be determined under the present experimental conditions, as discussed above. Therefore, it is not possible to state if only one or both pathways contribute to the observed $HC(O)OH$ formation.

For the product yields indicate a lower RO_2 level in the presence of SO_2 , propionyl peroxy radicals (and possibly ethyl peroxy radicals) seem to be released also from the stabilized carbonyl-substituted CI . Theoretical calculations on the ozonolysis of β -pinene and β -caryophyllene indicated that thermally equilibrated dioxirane intermediates convert preferentially to a triplet bis(oxy) radical following an intersystem crossing and decompose subsequently into CO_2 and two radicals (Nguyen et al., 2009a; 2009b). This further supports the above hypothesis that propionyl peroxy radicals are partly generated from the sCI .

6.4 Conclusion

In the present work it was found that the $EVK + O_3$ reaction produces several carbonyls, apart from the primary carbonyls ($HCHO$ and 2-oxobutanal) following the POZ decomposition. In contrast to a former study, the propionyl peroxy radical was shown to be the dominant RO_2 species in the reaction system. Its formation was clearly assigned to the further fate of the carbonyl-substituted CI . Based on the current understanding on Criegee intermediates, it was suggested that the carbonyl-containing CI forms intermediately a vibrationally excited oxoacid. As here were no hints for a collisional stabilization of such a species, the acid is expected to decompose exclusively. Accordingly, two radical-forming fragmentation routes were proposed, which finally yield propionyl peroxy radicals. However, based on the present results it remains unclear if the ethyl

peroxy radical is formed promptly from the decomposition of the oxoacid or evolves solely from the propionyl peroxy radical chemistry. This case study emphasizes the need for a careful analysis of possible RO₂ chemistry in the experimental set-up when interpreting the results of O₃ reactions. For instance, while the reactions were dominated by RO₂ + RO₂ in the presence of SO₂, a significant fraction of RO₂ + HO₂ took place when working with CO as an OH radical scavenger solely.

The SO₂ consumption indicated that about 40 ± 9 % of the CIs formed in the EVK + O₃ reaction are stabilized and hence prone to bimolecular reactions, particularly with H₂O and (H₂O)₂ under atmospheric conditions. The formation of propionic acid was possible only when employing SO₂ to scavenge sCIs, which are known to react rapidly with organic acids. In fact, the combined organic acid yield is, within the uncertainties, almost identical to the sCI yield obtained, which indicates that without sCI scavenger nearly all the acid formed is consumed through the sCI + acid reaction. The acid-forming mechanisms found in the literature cannot account for the non-RO₂ derived propionic acid in the present reaction system. Therefore, propionic acid is suggested to arise from fragmentation of the vibrationally excited oxoacid via a molecular pathway eliminating carbon monoxide. However, the formation of HC(O)OH could not clearly be attributed to one of the proposed pathways and further investigations are needed to decipher the formation mechanism. If collisional stabilization of [HC(O)OH]^{*} contributes significantly to the overall HC(O)OH formation, the formic acid/propionic acid formation ratio possesses an unequivocal pressure dependence. However, irrespective of the pathway yielding HC(O)OH, the present study provides strong evidence that both acids are formed from chemically activated CIs. This implies that both formic and propionic acid are formed also under the humid conditions present in the troposphere. Consequently, if the acid-forming pathway is a general feature of chemically activated carbonyl oxides of the structure RC(O)CHOO, the ozonolysis of α,β -unsaturated ketones turns out as a considerable source of organic acids.

In the presence of SO₂, the product yields (considering the non-quantified co-products) account for about 87 ± 11 % of the consumed EVK, when assuming HC(O)OH to be formed from the C₁-fragment solely, and for about 106 ± 14 %, when HC(O)OH formation is assumed to originate only from the C₄-fragment. Hence, EVK + O₃ proceeds solely through the POZ decomposition.

Although the yields of both primary carbonyls are indistinguishable without a sCI scavenger, indicating a branching ratio of 0.5 for both POZ decomposition channels, they account only for about 61 ± 11 % of the expected primary carbonyls following the POZ decomposition. This contradiction remains unexplained. There is currently no better

Formation of organic acids in the ozonolysis of α,β -unsaturated ketones exemplified by the case study of ethyl vinyl ketone + ozone

explanation than an unidentified secondary consumption of both primary carbonyls exists in the experimental system.

7 Ozonolysis of α,β -unsaturated ketones: 3-alken-2-ones

7.1 Introduction

Based on the findings from the inspection of the EVK + O₃ reaction (Chapter 6), the question arose, whether the formation of an organic acid upon elimination of a carbonyl group (RC(O)OH) is a general pathway of mono-substituted C=O containing CIs (RC(O)CHOO). Since one decomposition route of the POZ derived from methyl vinyl ketone (MVK), 3-penten-2-one (3P2), and 4-methyl-3-penten-2-one (4M3P2) provides methyl glyoxal oxide, CH₃C(O)CHOO, their ozonolysis reaction would consequently account for the formation of acetic acid. In this respect, the ozonolysis reactions of methyl vinyl ketone (MVK), 3-penten-2-one (3P2), and 4-methyl-3-penten-2-one (4M3P2) were investigated employing the experimental conditions used for the ozonolysis reaction of EVK. In order to discern between the various degradation pathways of the different CIs formed in the reaction system, 3-methyl-3-penten-2-one (3M3P2) was also investigated since its ozonolysis reaction leads to acetaldehyde oxide, CH₃CHOO, which is produced also in the 3P2 ozonolysis. For a better understanding, the results targeting the fate of the CIs are presented individually for each investigated reaction system in such a way, that each discussed reaction system differs only by one of the CIs from the previous one.

7.2 Experimental

The O₃ reactions of all 3-alken-2-ones were investigated in the 1080 L chamber under dry conditions (r. h. << 0.1 %) following the procedure outlined in Chapter 3 and 6. The reactions were performed in the presence of CO to scavenge OH radicals formed in the reaction system. In further experiments, SO₂ was also added to the reaction mixture, to allow an estimate of the stabilized Criegee Intermediate (= sCI) yield. The initial mixing ratios were 2.4–3.0 ppmV for MVK (Sigma Aldrich, 90 %), 0.9–1.4 ppmV for 3P2 (Alfa Aesar, 85 %), 0.7–1.6 ppmV for 3M3P2 (Sigma Aldrich, 90 %), 1.0–1.8 ppmV for 4M3P2 (Sigma Aldrich, 90 %), 3.1–4.0 ppmV for SO₂ (Air Liquide, 99.9 %), and 15000–20000 ppmV for CO (Air Liquide, 99.97 %). In addition to the FTIR quantification, the PTR-MS instrument was used for a qualitative identification of the reaction products for the experiments targeting the mechanistic investigation without a sCI scavenger following the procedure outlined in Chapter 6. When the quantification was not possible, yield plots were constructed by relating the raw signal (either FTIR or MS) assigned to one reaction product to the reduction of the raw signal belonging to the ketone.

7.3 Results and discussion

The wall losses were found to be $< 3 \times 10^{-5} \text{ s}^{-1}$ for MVK, 3M3P2 and 4M3P2 and in the range of $(1-8) \times 10^{-5} \text{ s}^{-1}$ for 3P2. The investigated reactions were observed until a maximum consumption of 53–70 % (MVK), 50–80 % (3P2), 68–83 % (3M3P2), and 45–75 % (4M3P2) of the respective initial concentration. Table 7.1 shows an overview of the CIs formed in the investigated reaction systems.

7.3.1 Primary carbonyls and sCI yield

An overall view on the reaction of O_3 with α,β -unsaturated ketones is given in Fig. 7.1. The decomposition of the POZ formed following the 1,3-dipolar cycloaddition of O_3 to the unsaturated ketones proceeds through 2 possible routes yielding either a carbonyl or a dicarbonyl species (Fig. 7.1). Accordingly, one observes the formation of HCHO (0.35 ± 0.08) and methyl glyoxal (0.29 ± 0.05) from MVK, acetaldehyde (0.21 ± 0.07) and methyl glyoxal (0.66 ± 0.16) from 3P2, acetaldehyde (0.21 ± 0.04) and biacetyl (0.59 ± 0.13) from 3M3P2, and acetone (0.10 ± 0.04) and methyl glyoxal (0.90 ± 0.11) from 4M3P2. Table 7.1 summarizes the obtained product yields of the primary carbonyls quantified via FTIR spectroscopy from all performed experiments. The corresponding yield plots, summarized for each reaction system as the sum of both primary carbonyls in the absence and presence of SO_2 , are shown in Fig. 7.2. The panels (e) and (f) of Fig. 7.2 present the dicarbonyl/carbonyl ratio observed for the primary carbonyls of each investigated reaction system.

Primary carbonyl yields were reported previously only for the ozonolysis of MVK (Grosjean et al., 1993; Ren et al., 2017) and 3M3P2 (Wang et al., 2015). Li et al. (2021)

Table 7.1. Structures of investigated Criegee intermediates (CIs) together with their names and parent ketones. For clarity, only one stereoisomer is drawn for CIs, for which two configurations are possible.

CI					
Name	Formaldehyde oxide	Acetaldehyde oxide	Acetone oxide	Methyl glyoxal oxide	Biacetyl oxide
Parent ketone(s)	MVK	3P2, 3M3P2	4M3P2	MVK, 3P2, 4M3P2	3M3P2

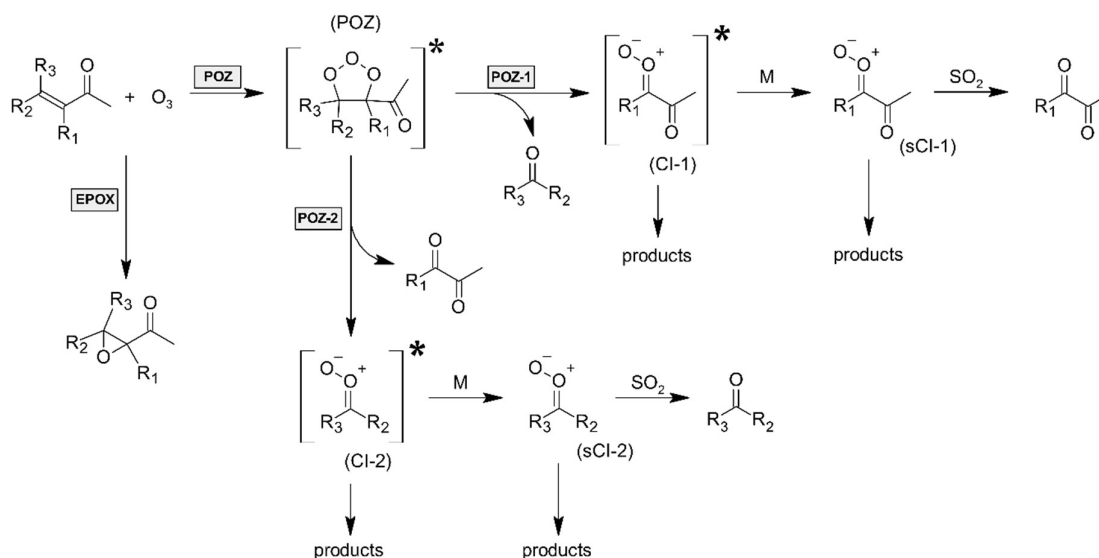


Figure 7.1. Generic reaction scheme for the gas-phase ozonolysis of α,β -unsaturated ketones, where $R_1 = R_2 = R_3 = -H$ for MVK (and EVK), $R_1 = R_3 = -H$ and $R_2 = -CH_3$ for 3P2, $R_1 = R_2 = -CH_3$ and $R_3 = -H$ for 3M3P2, and $R_2 = R_3 = -CH_3$ and $R_1 = -H$ for 4M3P2. For clarity, only one isomer is drawn for each Criegee Intermediate (CI).

investigated the 4M3P2 + O₃ reaction. However, they identified acetone and methyl glyoxal only qualitatively. The former two studies on MVK are in huge disagreement. Grosjean et al. (1993) reported a methyl glyoxal yield of 0.87, without indicating any uncertainty, based on experiments performed in the presence of cyclohexane to scavenge the OH radicals. The HCHO yield was only about 0.05. By contrast, Ren et al. (2017) reported an HCHO yield of 0.44 ± 0.05 , also in the presence of the OH scavenger cyclohexane. The authors stated that methyl glyoxal was below the detection limit of the instrument, which indicates a much lower methyl glyoxal yield than reported by Grosjean et al. (1993b). The reason for this discrepancy remained unexplained. The HCHO yield determined within the present work is slightly lower than reported by Ren et al. (2017). Interestingly, the primary carbonyl yields are quite similar to those observed for the structural analogue EVK under the same experimental conditions (see Chapter 6). Though, in contrast to EVK, the former studies on MVK + O₃ were also performed under dry conditions. Therefore, there is currently no convincing explanation for the observed distinct discrepancies.

Wang et al. (2015) observed a preference towards acetaldehyde formation in the ozonolysis of 3M3P2. They reported yields of 0.61 ± 0.07 and 0.39 ± 0.04 for acetaldehyde and biacetyl, respectively, based on PTR-MS measurements. Hence, the present data indicate the opposite trend. At least a quantification error is ruled out within the present

Tab. 7.2. Yields of the carbonyls and dicarbonyls, identified as the primary carbonyls in each studied ketone + O₃ system, for experiments in the presence of CO as an OH radical scavenger and supplementary addition of SO₂. Data obtained for EVK are included for comparison.

	MVK ^a	3P2 ^b	3M3P2 ^c	4M3P2 ^d	EVK ^a
Carbonyl ^e	0.35 ± 0.08	0.21 ± 0.07	0.21 ± 0.04	0.10 ± 0.04	0.31 ± 0.09
Dicarbonyl ^e	0.29 ± 0.05	0.66 ± 0.16	0.59 ± 0.13	0.90 ± 0.11	0.30 ± 0.07 ^f
Carbonyl ^g	0.60 ± 0.07	0.60 ± 0.10	0.80 ± 0.16	0.35 ± 0.06	0.65 ± 0.12
Dicarbonyl ^g	0.51 ± 0.05	0.68 ± 0.11	0.74 ± 0.13	0.93 ± 0.11	0.53 ± 0.12 ^f
sCl	0.32 ± 0.08	0.40 ± 0.14	0.52 ± 0.13	0.40 ± 0.09	0.40 ± 0.09

^a R₁ = R₂ = R₃ = -H, ^b R₁ = R₃ = -H, R₂ = -CH₃, ^c R₁ = R₂ = -CH₃, R₃ = -H, ^d R₂ = R₃ = -CH₃, R₁ = -H, ^e experiments were performed in the presence of CO as an OH radical scavenger, ^f the yields were obtained following a semi-quantitative approach by assuming the infrared cross section of the C=O band to equal the cross section of the structural analogue methyl glyoxal, ^g experiments were performed in the presence of CO as OH radical scavenger and SO₂.

FTIR data, since, for instance, the cross section used for biacetyl (Illmann et al., 2021b) is nearly identical to a value reported previously (Profeta et al., 2011).

As will be discussed in the following sections, the experimentally determined yields are affected by additional formation routes for HCHO from MVK, methyl glyoxal from 4M3P2 and, possibly, acetaldehyde from 3P2 and hence they do not represent solely the primary carbonyl yield. For example, in the case of 4M3P2, the secondary formation accounts for about $\approx 15\%$ of the observed methyl glyoxal yield (see below). However, when comparing the carbonyl yields obtained within this work, in the absence of a sCl scavenger, there are two trends found for all investigated α,β -unsaturated ketones. First, for 3P2 and 4M3P2 the sum of both carbonyls accounts for about $85 \pm 17\%$ and $91 \pm 13\%$ of the anticipated primary carbonyl yield, if the POZ decomposition represents the sole pathway of the O₃ reaction. By contrast, the primary carbonyl yield is slightly below 100 % for 3M3P2

($80 \pm 14\%$) and well below 100 % for MVK ($64 \pm 9\%$). This might indicate a decrease in the primary carbonyl yield, in the present experimental set-up, when the β -carbon atom is less substituted (see also EVK), although this phenomenon remains unexplained. Secondly, the ratio between the dicarbonyl and the carbonyl yield is 0.8 ± 0.1 and hence nearly one for MVK, 3.1 ± 0.9 for 3P2, 2.8 ± 0.4 for 3M3P2, and 8 ± 2 for 4M3P2. 3P2 and 3M3P2, which both possess a single CH₃ group on C _{β} , show the same dicarbonyl/carbonyl ratio although the C=C bond is higher substituted in the case of 3M3P2. Thus, the dicarbonyl/carbonyl ratio seems apparently to increase with a higher substitution on the β -carbon. A preference towards the dicarbonyl results concomitantly in the preferential formation of the β -carbon containing Cl, built upon the dicarbonyl forming POZ fragmentation route. Accordingly, the corresponding decomposition pathway leads to formaldehyde oxide (CH₂OO) from MVK, acetaldehyde oxide (CH₃CHOO) from 3P2 and

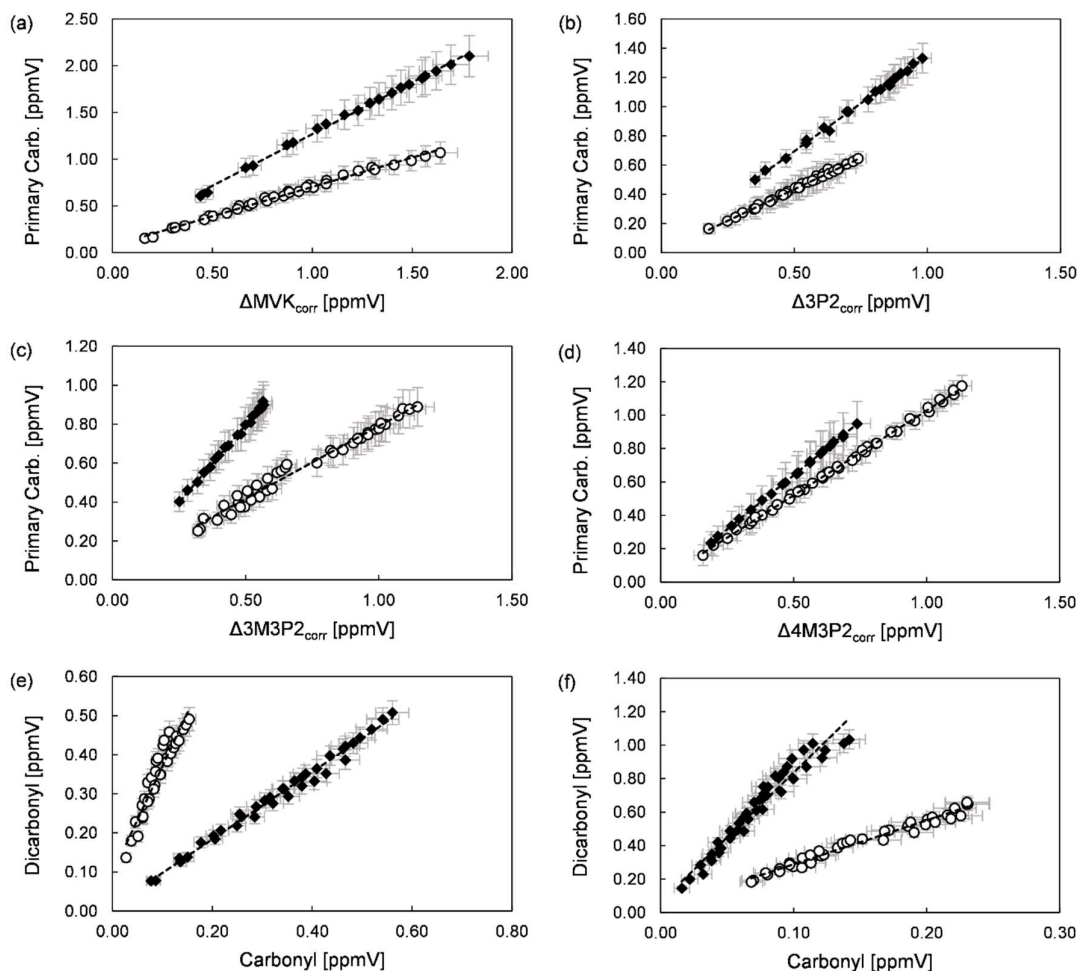


Figure 7.2. Yield plots of the sum of the primary carbonyls for (a) methyl vinyl ketone, (b) 3-penten-2-one, (c) 3-methyl-3-penten-2-one, and (d) 4-methyl-3-penten-2-one, respectively, in the absence (open circles) and presence (closed rhomb) of SO_2 . Panel (e) shows the dicarbonyl/carbonyl ratio observed for methyl vinyl ketone (closed rhomb) and 3-penten-2-one (open circles) in the absence of SO_2 , and panel (f) the dicarbonyl/carbonyl ratio observed for 4-methyl-3-penten-2-one (closed rhomb) and 3-methyl-3-penten-2-one (open circles) in the absence of SO_2 , respectively.

3M3P2 and acetone oxide ($(\text{CH}_3)_2\text{COO}$) from 4M3P2, respectively. Therefore, the observed trend is likely rationalized through the increase of the CI stability due to a higher substituted structure. A similar behaviour is observed for 1-alkenes, which yield preferentially formaldehyde (Cox et al., 2020). However, the preferential POZ fragmentation towards acetone oxide is much less pronounced (68 %) in the case of isobutene (= 2-methylpropene) than for the structural analogue ketone 4M3P2 (89 %).

The yields of the mainly primarily formed carbonyls (formaldehyde, acetaldehyde and acetone) increase for all investigated ketones by a factor of 1.7–3.5 in the presence of SO₂. By contrast, for the dicarbonyl yields no increase was observed in the case of 3P2 and 4M3P2 and only by a factor of 1.8 for MVK and 1.3 for 3M3P2. This indicates that a significant fraction of the corresponding CIs (formaldehyde oxide, acetaldehyde oxide and acetone oxide, respectively) is formed stabilized (thermally equilibrated) and prone to bimolecular reactions. The invariant methyl glyoxal yield, observed for 4M3P2 irrespective of the SO₂ presence, results from an antagonist effect, since the small contribution from the CI + SO₂ reaction is compensated for by a lowering of a secondary methyl glyoxal source (see below).

By following the consumption of SO₂ during the O₃ reactions, one obtains an estimate of the sCI yield of 0.32 ± 0.08 for MVK, 0.40 ± 0.14 for 3P2, 0.52 ± 0.13 for 3M3P2, and 0.40 ± 0.09 for 4M3P2, respectively. These yields are in excellent agreement with the increase of the overall primary carbonyl yield observed for 3P2 ($\Delta = 0.41 \pm 0.23$) and 4M3P2 ($\Delta = 0.28 \pm 0.17$), considering that the increase might be underestimated for 4M3P2 due to the secondary methyl glyoxal source. For 3M3P2, the differences observed for the primary carbonyls in the presence and absence of SO₂ agree reasonably with the determined sCI yield, although the carbonyls tend to increase more than expected from the SO₂ consumption. In the case of MVK, the sCI yield is significantly lower than the increase of the primary carbonyl yield ($\Delta = 0.47 \pm 0.13$). This phenomenon has been observed also for the structural analogue EVK (see Chapter 6), which indicates a structure-related effect. However, there is currently no convincing explanation for this behaviour.

7.3.2 Main fate of the Criegee intermediates

The formation of peracetic acid was observed for all investigated ketones within the FTIR data in the absence of SO₂. The largest yields are found for MVK (0.062 ± 0.019) and 4M3P2 (0.062 ± 0.041). For 3P2, the peracetic acid yield (0.027 ± 0.016) is about a factor of 2 smaller. In the 3M3P2 + O₃ system, traces of peracetic acid are present in the FTIR spectra, indicated by the characteristic absorption pattern around 1240 cm⁻¹. However, a quantification is not possible due to the low absorption within the spectra. In all investigated systems, the peracetic acid formation might be further supported by the evolution of the m/z 61 signal. Though in all reaction systems the FTIR data indicate the

formation of species which interfere at m/z 61 (acetic acid, formic acetic anhydride, acetic anhydride) and hence prevent an unambiguous assignment of the ion signal.

Methyl hydroperoxide (CH_3OOH) is as well observed in all reaction systems. The quantification via FTIR was achieved based on the peak absorption at 2964 cm^{-1} , but remains rather uncertain due to the low intensity. The plots of the formed CH_3OOH vs. the consumed ketone were found to be linear mainly in the beginning of the experiments. In the case of 3P2 and 4M3P2 the correlation becomes strongly non-linear with higher levels of the ketone consumption. Within PTR-MS measurements, one would expect methyl hydroperoxide to be detected as a fragment ion (CH_3O^+) at m/z 31, built upon H_2O elimination from the protonated hydroperoxide. Therefore, CH_3OOH interferes with HCHO at m/z 31. However, the evolution of the m/z 49 ion is observed also in all reaction systems, which supports qualitatively the FTIR data. In addition, the temporal profile of the m/z 49 ion is similar to the FTIR evaluation. Therefore, the non-linear behaviour, observed in some experiments at long reaction times, is likely resulting from a significant wall loss. Based on the linear range of the yield plots, the methyl hydroperoxide yield was found to be 0.10 ± 0.05 for MVK, 0.075 ± 0.017 for 3P2, and 0.10 ± 0.04 for 4M3P2. Similarly to peracetic acid, methyl hydroperoxide is also observed in the 3M3P2 + O_3 system, but the residual spectra did not allow any quantification. The yields of both peroxides decrease, when SO_2 was added to the reaction mixtures. Though, their yields possess generally a higher relative error since their evaluation, from the FTIR spectra, is assigned with a larger uncertainty due to the low amounts present in the reaction mixtures.

The only pathway of forming peracetic acid is the reaction of the acetyl peroxy radical with HO_2 . Accordingly, the O_3 reactions of all investigated ketones yield, on the one hand, acetyl radicals, which are instantaneously converted into acetyl peroxy radicals. On the other hand, similarly to the EVK + O_3 system (see Chapter 6), the HO_2 level must be sufficiently high to allow $\text{RO}_2 + \text{HO}_2$ reactions to compete with $\text{RO}_2 + \text{RO}_2$ reactions in the experimental systems. This is further supported by the fact that traces of hydrogen peroxide are visible in the FTIR spectra during the reaction in nearly all experiments without a sCl scavenger. Although hydrogen peroxide formation is generally possible from a reaction of sCl with H_2O (Cox et al., 2020), a contribution of this reaction channel is rather unlikely since the amount of H_2O is quite low in the experimental set-up. Moreover, the rate coefficients for the reactions of sCl with organic acids, which are formed in all O_3 reactions (see below), are $10^3 - 10^6$ times larger (Cox et al., 2020). Therefore, hydrogen peroxide formation is attributed to the self-reaction of HO_2 radicals, which limits the level of HO_2 in the system. The HO_2 radicals originate mainly from OH radicals, formed from the

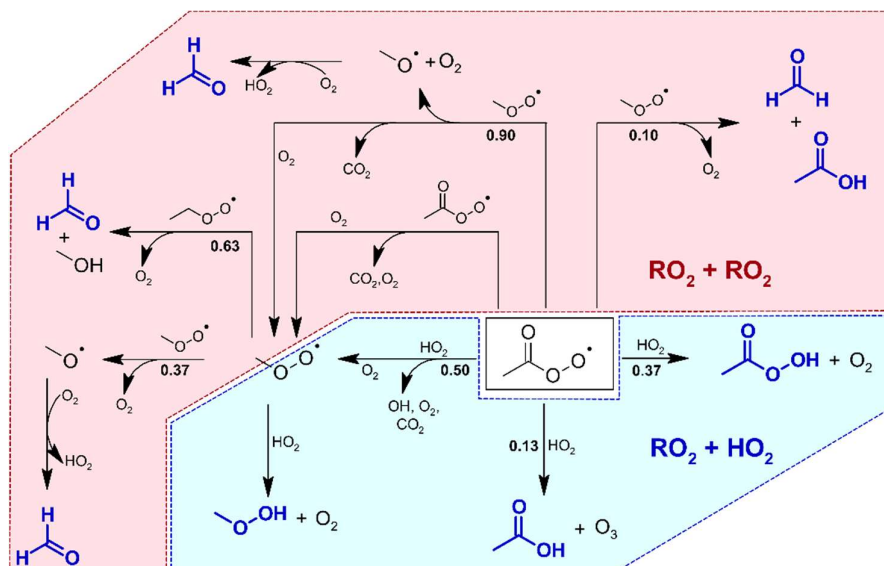


Figure 7.3 Chemistry of the acetyl peroxy and methyl peroxy radical based on the identified reaction products (bold blue structures). For clarity, the reaction sequences are shown considering only a prompt acetyl peroxy radical source in the experimental system. The blue area represents the $\text{RO}_2 + \text{HO}_2$ reactions, the rose area marks the $\text{RO}_2 + \text{RO}_2$ domain. The corresponding branching ratios, given in bold numbers, are the actual IUPAC recommended values.

CI further chemistry, and their subsequent, nearly quantitative conversion into HO_2 due to the reaction with CO (OH scavenger). Further sources of HO_2 are H abstraction reactions of formyl radicals as well as the reaction of O_2 with H atoms, possibly formed from the CI decomposition.

The $\text{CH}_3\text{C(O)O}_2 + \text{HO}_2$ reaction proceeds through three different channels yielding either (a) peracetic acid and O_2 , (b) acetic acid and O_3 , or (c) $\text{CH}_3\text{C(O)O}$, OH and O_2 (Fig. 7.3). Based on a series of studies (Niki et al., 1985; Horie and Moortgat, 1992; Hasson et al., 2004; Jenkin et al., 2007; Dillon and Crowley, 2008; Groß et al., 2014; Winiberg et al., 2016; Hui et al., 2019), the IUPAC recommends branching ratios of (a) 0.37, (b) 0.13, and (c) 0.50 for the respective reaction channels at 298 K. The $\text{CH}_3\text{C(O)O}$ radical eliminates CO_2 and is instantaneously converted into a methyl peroxy radical, which itself reacts with HO_2 to methyl hydroperoxide, as observed for all investigated ketones. Elrod et al. (2001) reported a branching ratio of ≈ 0.11 for a HCHO forming channel of the $\text{CH}_3\text{O}_2 + \text{HO}_2$ reaction. However, since this observation needs still to be confirmed, the IUPAC recommends to assign a 100 % relative error to this branching ratio.

Since about 50 % of the $\text{CH}_3\text{C}(\text{O})\text{O}_2 + \text{HO}_2$ reaction results in the formation of methyl peroxy radicals, there are at least two RO_2 species in the experimental systems, which provides the possibility of RO_2 self- and cross-reactions. Since the rate coefficient of the $\text{CH}_3\text{O}_2 + \text{CH}_3\text{O}_2$ reaction is about 30 times smaller than the $\text{CH}_3\text{C}(\text{O})\text{O}_2$ self-reaction as well as the $\text{CH}_3\text{O}_2 + \text{CH}_3\text{C}(\text{O})\text{O}_2$ reaction (Tyndall et al., 2001), the methyl peroxy self-reaction will contribute only in a minor way to the $\text{RO}_2 + \text{RO}_2$ reactions. The $\text{CH}_3\text{C}(\text{O})\text{O}_2$ self-reaction finally converts the $\text{CH}_3\text{C}(\text{O})\text{O}_2$ into a CH_3O_2 radical (Moortgat et al., 1989; Roehl et al., 1996; Maricq and Szente, 1996) and hence increases the level of methyl peroxy radicals in the system. The RO_2 cross-reaction forms mainly HCHO, as observed in all experimental systems, and additionally small amounts of acetic acid, although there remains some uncertainty on the branching ratio (Tyndall et al., 2001). A reaction scheme is presented in Fig. 7.3 summarizing the generic, possible acetyl peroxy radical further chemistry. Detailed discussions on the individual experimental systems are given in the following subsections.

7.3.2.1 4-Methyl-3-penten-2-one

The HCHO yield determined in $4\text{M3P2} + \text{O}_3$ is a factor of 2–3 larger than those for 3P2 and 3M3P2 , with and without addition of a sCl scavenger. Additionally, the formation of hydroxyacetone is observed in the FTIR spectra and the mass spectra (evolution of the m/z 75 ion) recorded during the $4\text{M3P2} + \text{O}_3$ experiments. In most of the trials, the yield plots possess a non-linear behaviour at longer reaction times similarly to the methyl hydroperoxide plots. This observation is therefore attributed mainly to a large wall loss. Based on the linear range of the plots the hydroxyacetone yield was determined as 0.091 ± 0.045 in the absence of SO_2 . Due to the low amount present in the FTIR spectra the yield exhibits a large relative uncertainty. In the presence of SO_2 , hydroxyacetone might be formed. If the increase in the peak absorption at 1289 cm^{-1} were taken as due to hydroxyacetone, this would correspond to a yield of 0.037 ± 0.012 in the presence of SO_2 . The yields of all clearly identified species as well assigned m/z ions, observed in the PTR mass spectra, are summarized in Tab. 7.3.

As discussed above, the acetone oxide, $(\text{CH}_3)_2\text{COO}$, is the predominant CI in the $4\text{M3P2} + \text{O}_3$ system. Based on preceding studies on the isobutene + O_3 system (Cox et al., 2020) the main fate of both the excited and the thermally equilibrated CI is expectedly to be the decomposition through a vinyl hydroperoxide intermediate. This results ultimately in the formation of OH and acetyl radicals, which react immediately with O_2 to give acetyl peroxy radicals. The further chemistry of the initially formed RO_2 proceeds either via its

Tab. 7.3. Quantified reaction products and assigned masses of the 4M3P2 + O₃ reaction in the presence of CO as an OH radical scavenger and in the presence of CO and SO₂. The uncertainties given for the product yields represent a combination of the 2 σ statistical error and the accuracy error.

Species	Yield ^a	Yield ^b	Assigned <i>m/z</i> ^a
Acetone	0.10 ± 0.04	0.35 ± 0.06	59.050
Methyl glyoxal	0.90 ± 0.11	0.93 ± 0.11	73.029, 45.034
HCHO	0.37 ± 0.10	0.43 ± 0.06	31.018
Formic acid		0.053 ± 0.025	47.013
Formic acetic anhydride	< 0.02		61.029, 47.013
Acetic acid		0.14 ± 0.05	61.029
Peracetic acid	0.062 ± 0.041	0.047 ± 0.022	77.024, 61.029
CH ₃ OOH	0.10 ± 0.04	0.09 ± 0.05	49.029, 31.018
Hydroxyacetone	0.091 ± 0.045		75.045
CO ₂ ^c	1.37 ± 0.37	1.31 ± 0.42	
sCl		0.40 ± 0.09	

^a Experiments were performed in the presence of CO as an OH radical scavenger, ^b experiments were performed in the presence of CO as and OH radical scavenger and SO₂, ^c sum of CO₂ formed from 4M3P2 + O₃ and CO + OH.

self-reaction, cross-reaction with subsequently formed peroxy radicals (CH₃C(O)O₂, CH₃O₂) or HO₂ (Fig. 7.4). For the self-reaction, branching ratios were reported towards the formation of methyl glyoxal + hydroxyacetone and acetonoxo radicals (Bridier et al., 1993; Jenkin et al., 1993; Emrich and Warneck, 2003). The thermal decomposition of the last produces HCHO and acetyl peroxy radicals. The acetyl peroxy radical further chemistry proceeds as discussed above. Products and assigned branching ratios of the corresponding RO₂ cross-reactions at atmospheric pressure were reported solely from a joint study on the acetonyl peroxy radical chemistry using complementary techniques (Bridier et al., 1993; Jenkin et al., 1993). Accordingly, the CH₃O₂ + CH₃C(O)CH₂O₂ reaction was shown to produce CH₃OH + methyl glyoxal, HCHO + hydroxyacetone, and CH₃O + CH₃C(O)CH₂O with branching ratios of 0.5 ± 0.1, 0.2 ± 0.1, and 0.3 ± 0.1, respectively, and the CH₃C(O)O₂ + CH₃C(O)CH₂O₂ reaction to produce acetic acid + methyl glyoxal and CH₃C(O)O + CH₃C(O)CH₂O, respectively, with branching ratios of 0.5 ± 0.2 (Jenkin et al., 1993). The complete reaction scheme of the acetonyl peroxy radical reactions based on the above discussed literature is presented in Fig. 7.4.

Since peracetic acid is observed in the 4M3P2 + O₃ system, the acetonyl peroxy radical is expected to react at least partly with HO₂. At atmospheric pressure, CH₃C(O)CH₂O₂ + HO₂ was shown to produce the corresponding alkoxy radical via the propagating channel and as well acetonyl hydroperoxide (CH₃C(O)CH₂OOH) via the radical terminating channel (Hasson et al., 2004; Dillon and Crowley, 2008; Jenkin et al., 2008; Hasson et al., 2012). Up to date, the hydroperoxide has only been positively identified based on HPLC-fluorescence meas-

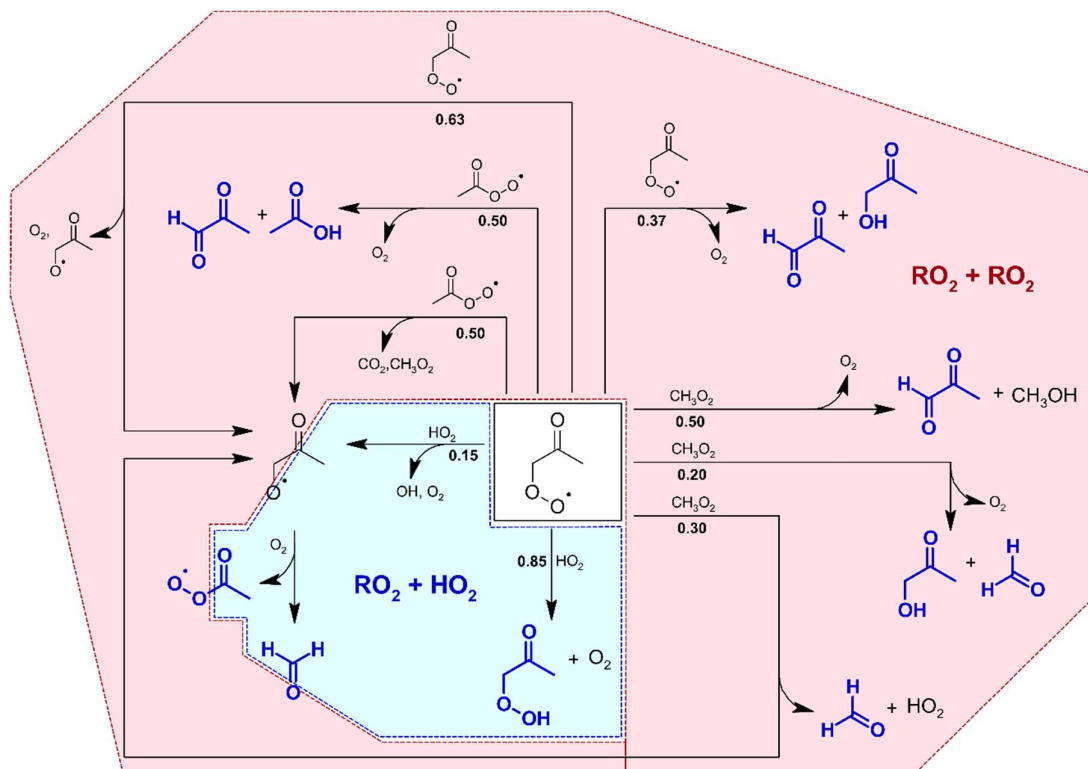


Figure 7.4. Chemistry of the acetyl peroxy radical based on the identified reaction products (bold blue structures) in the 4M3P2 + O₃ system. The blue area represents the RO₂ + HO₂ reactions, the rose area marks the RO₂ + RO₂ domain. The corresponding branching ratios, given in bold numbers, are the actual IUPAC recommended values.

measurements in two studies by the same group (Hasson et al., 2004; 2012). The authors observed a two times larger hydroperoxide yield in their second study and concluded that it was mistakenly underestimated in the former study due to an aged HPLC column (Hasson et al., 2012). However, although the conclusions were supported by FTIR measurements in both studies as well as in the study of Jenkin et al. (2008), neither residual spectra nor spectra of acetyl hydroperoxide have been reported. The only available IR spectral information was reported by Niki et al. (1987a), who suspected acetyl hydroperoxide formation in the ozonolysis of 2,3-dimethylbutene (= tetramethylethylene). The authors tried to obtain spectral features of the hydroperoxide from the photolysis of acetone/Cl₂/O₂ mixtures and found a broad absorption band at ca. 1740 cm⁻¹ similar to the residual spectrum they obtained from the ozonolysis. However, they stated further that the signal/noise ratio was too poor to allow a spectral characterization.

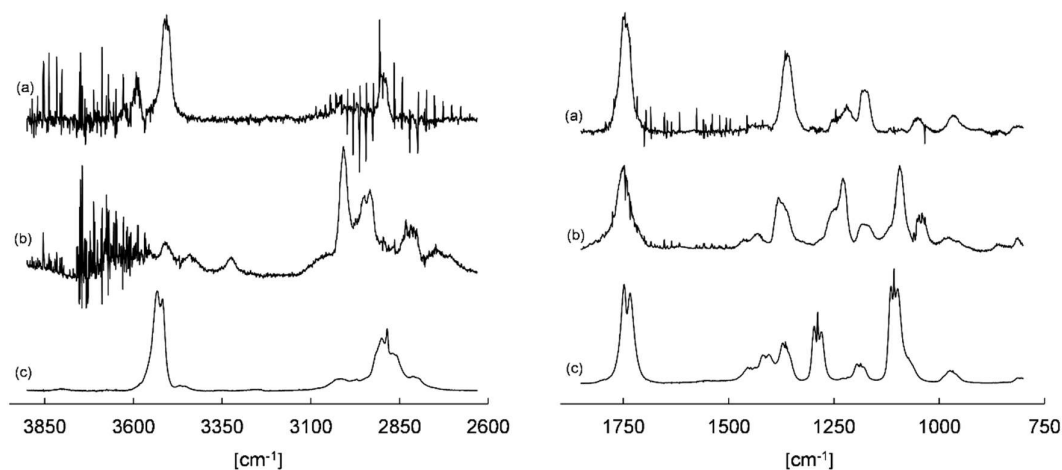


Figure 7.5. Infrared spectra of (a) a residual from an irradiated acetone/ $\text{CH}_3\text{OH}/\text{Cl}_2$ mixture assigned to acetyl hydroperoxide, (b) a residual of a 4M3P2 + O_3 experiment after subtraction of all identified species, and (c) hydroxyacetone. All traces are scaled individually for a better overview.

Trace (a) of Fig. 7.5 shows a residual spectrum of an irradiated acetone/ $\text{CH}_3\text{OH}/\text{Cl}_2$ mixture, which possesses characteristic absorptions centred at 3507 cm^{-1} (O–H stretching) and 1744 cm^{-1} (C=O stretching) similar to the hydroxyacetone spectrum presented in trace (c) and which was therefore assigned to acetyl hydroperoxide. The position of the C=O absorption band is hence similar to the observation of Niki et al. (1987a). Trace (b) contains a representative residual spectrum of the 4M3P2 + O_3 system obtained from subtraction of all unambiguously identified reaction products. The residual spectral features indicate additional unidentified reaction products containing a carbonyl group. However, the characteristic absorption band is present at 3507 cm^{-1} , which is therefore an indication for acetyl hydroperoxide formation in the system. The m/z 91 ion is not observed in the PTR data. Though, the fragment ion, generated through H_2O elimination from the protonated hydroperoxide, would appear at m/z 73 and hence interferes with the methyl glyoxal signal. Therefore, a confirmation of the hydroperoxide formation is not possible with the from PTR-MS data. Although not quantitatively, a correlation is obtained between the integrated band intensity of the absorption at 3507 cm^{-1} and the consumed 4M3P2. These plots are going through the origin but a strong linearity is observed merely in the beginning of the experiment. Since this behaviour is quite similar to hydroxyacetone and methyl hydroperoxide, this might further support the assignment to acetyl hydroperoxide.

In order to help interpreting the experimental results, simulations were performed for various $[\text{HO}_2]/[\text{CH}_3\text{C}(\text{O})\text{CH}_2\text{O}_2]$ ratios according to the methodology outlined previously (Illmann et al., 2021b; 2021c) and using the reaction sequence listed in Tab. 7.4. The variation of $[\text{HO}_2]/[\text{CH}_3\text{C}(\text{O})\text{CH}_2\text{O}_2]$ was achieved by introducing the overall acetyl peroxy radical yield as well as $[\text{HO}_2]$ as variable parameters into the model. Two different approaches were pursued. First, the product yields were simulated for a set of $[\text{HO}_2]/[\text{CH}_3\text{C}(\text{O})\text{CH}_2\text{O}_2]$ ratios independent of the experimentally observed product formation in an attempt to figure out their $[\text{HO}_2]/[\text{CH}_3\text{C}(\text{O})\text{CH}_2\text{O}_2]$ dependence. Second, the temporal behaviour was simulated for species assigned to the acetyl peroxy radical further chemistry in order to match the experimental data. Since here the purpose of modelling was not to investigate the uncertainties of the kinetic parameters listed in Tab. 7.4., the rate coefficients were taken as recommended by IUPAC without any optimization. However, it should be noted that large uncertainties in the range of $\Delta(\log k) \approx 0.2\text{--}0.3$ are assigned to nearly all recommended values of the rate coefficients given the scarce data sets published in the literature, particularly for RO_2 cross-reactions. For the second approach, $[\text{HO}_2]$ was adjusted in order to optimize the fit between the simulated time profile and the experimental FTIR based data, since $[\text{HO}_2]$ cannot be determined experimentally. Few experiments were conducted in the presence of a tracer to observe the OH production in the 4M3P2 + O_3 system. Accordingly, additional simulations indicate a lower limit of $[\text{HO}_2] \approx 1 \times 10^{10} \text{ cm}^{-3}$ considering the reaction $\text{CO} + \text{OH}$ as a major source of HO_2 .

An estimate of the $\text{CH}_3\text{C}(\text{O})\text{CH}_2\text{O}_2$ radical yield is given by the experimental data since, on the one hand, if the product distribution were described only by the $\text{CH}_3\text{C}(\text{O})\text{CH}_2\text{O}_2$ radical further chemistry, the sum of their yields would provide an estimate of the $\text{CH}_3\text{C}(\text{O})\text{CH}_2\text{O}_2$ radical yield. On the other hand, the observed acetone yield sets an upper limit for the branching ratios towards the second POZ decomposition channel and thus an upper limit for the $\text{CH}_3\text{C}(\text{O})\text{CH}_2\text{O}_2$ radical yield. Although this approach remains generally rather uncertain, the subsequently presented observations emerged from the simulations.

When $[\text{HO}_2]$ is kept constant, an increase of the input acetyl peroxy radical yield results in an increase of all product yields. The HCHO yield, in particular, is about a factor of 3–7 more sensitive to a change of the $\text{CH}_3\text{C}(\text{O})\text{CH}_2\text{O}_2$ source than hydroxyacetone, methyl glyoxal, methyl hydroperoxide and peracetic acid, respectively. On the other hand, an increase of $[\text{HO}_2]$ for a constant $\text{CH}_3\text{C}(\text{O})\text{CH}_2\text{O}_2$ radical yield, which corresponds to large changes in the $[\text{HO}_2]/[\text{CH}_3\text{C}(\text{O})\text{CH}_2\text{O}_2]$ ratio, leads to a non-linear decrease in the yields of HCHO, hydroxyacetone and methyl glyoxal, as shown in Fig. 7.6. For methyl hydroperoxide and peracetic acid one observes an increase of the formation yield, followed again by a

Table 7.4. Reaction sequence used for the modelling of the temporal behaviour of reaction products accounted for the acetylonyl peroxy radical further chemistry.

Reaction	Branching ratio	Rate coefficient ^a
(R7.1) $(\text{CH}_3)_2\text{C}=\text{CHC}(\text{O})\text{CH}_3 + \text{O}_3 \rightarrow \text{CH}_3\text{C}(\text{O})\text{CH}_2\text{O}_2$		^b
(R7.2) $\text{CH}_3\text{C}(\text{O})\text{CH}_2\text{O}_2 + \text{HO}_2 \rightarrow \text{products}$		9.0×10^{-12} ^c
(R7.2a) $\text{CH}_3\text{C}(\text{O})\text{CH}_2\text{O}_2 + \text{HO}_2 \rightarrow \text{CH}_3\text{C}(\text{O})\text{CH}_2\text{OOH} + \text{O}_2$	0.85 ^c	
(R7.2b) $\text{CH}_3\text{C}(\text{O})\text{CH}_2\text{O}_2 + \text{HO}_2 (+ \text{O}_2) \rightarrow \text{CH}_3\text{C}(\text{O})\text{O}_2 + \text{HCHO} + \text{O}_2 + \text{OH}$	0.15 ^c	
(R7.3) $2 \text{CH}_3\text{C}(\text{O})\text{CH}_2\text{O}_2 \rightarrow \text{products}$		8.0×10^{-12} ^c
(R7.3a) $2 \text{CH}_3\text{C}(\text{O})\text{CH}_2\text{O}_2 \rightarrow 2 \text{CH}_3\text{C}(\text{O})\text{CH}_2\text{O} + \text{O}_2$	0.63 ^c	
(R7.3b) $2 \text{CH}_3\text{C}(\text{O})\text{CH}_2\text{O}_2 \rightarrow \text{CH}_3\text{C}(\text{O})\text{CH}_2\text{OH} + \text{CH}_3\text{C}(\text{O})\text{C}(\text{O})\text{H} + \text{O}_2$	0.37 ^c	
(R7.4) $\text{CH}_3\text{C}(\text{O})\text{CH}_2\text{O}_2 + \text{CH}_3\text{C}(\text{O})\text{O}_2 \rightarrow \text{products}$		5.0×10^{-12} ^c
(R7.4a) $\text{CH}_3\text{C}(\text{O})\text{CH}_2\text{O}_2 + \text{CH}_3\text{C}(\text{O})\text{O}_2 (+ \text{O}_2) \rightarrow$ $\text{CH}_3\text{C}(\text{O})\text{O}_2 + \text{HCHO} + \text{CO}_2 + \text{CH}_3\text{O}_2$	0.5 ^c	
(R7.4b) $\text{CH}_3\text{C}(\text{O})\text{CH}_2\text{O}_2 + \text{CH}_3\text{C}(\text{O})\text{O}_2 \rightarrow \text{CH}_3\text{C}(\text{O})\text{C}(\text{O})\text{H} + \text{CH}_3\text{C}(\text{O})\text{OH} + \text{O}_2$	0.5 ^c	
(R7.5) $\text{CH}_3\text{C}(\text{O})\text{CH}_2\text{O}_2 + \text{CH}_3\text{O}_2 \rightarrow \text{products}$		3.8×10^{-12} ^c
(R7.5a) $\text{CH}_3\text{C}(\text{O})\text{CH}_2\text{O}_2 + \text{CH}_3\text{O}_2 \rightarrow \text{CH}_3\text{C}(\text{O})\text{C}(\text{O})\text{H} + \text{CH}_3\text{OH} + \text{O}_2$	0.5 ^c	
(R7.5b) $\text{CH}_3\text{C}(\text{O})\text{CH}_2\text{O}_2 + \text{CH}_3\text{O}_2 \rightarrow \text{CH}_3\text{C}(\text{O})\text{CH}_2\text{OH} + \text{HCHO} + \text{O}_2$	0.2 ^c	
(R7.5c) $\text{CH}_3\text{C}(\text{O})\text{CH}_2\text{O}_2 + \text{CH}_3\text{O}_2 (+ \text{O}_2) \rightarrow \text{CH}_3\text{C}(\text{O})\text{O}_2 + 2 \text{HCHO} + \text{HO}_2$	0.3 ^c	
(R7.6) $\text{CH}_3\text{C}(\text{O})\text{O}_2 + \text{HO}_2 \rightarrow \text{products}$		2.0×10^{-11} ^c
(R7.6a) $\text{CH}_3\text{C}(\text{O})\text{O}_2 + \text{HO}_2 \rightarrow \text{CH}_3\text{C}(\text{O})\text{OOH} + \text{O}_2$	0.37 ^c	
(R7.6b) $\text{CH}_3\text{C}(\text{O})\text{O}_2 + \text{HO}_2 \rightarrow \text{CH}_3\text{C}(\text{O})\text{OH} + \text{O}_3$	0.13 ^c	
(R7.6c) $\text{CH}_3\text{C}(\text{O})\text{O}_2 + \text{HO}_2 (+ \text{O}_2) \rightarrow \text{CH}_3\text{O}_2 + \text{CO}_2 + \text{OH} + \text{O}_2$	0.50 ^c	
(R7.7) $\text{CH}_3\text{C}(\text{O})\text{O}_2 + \text{CH}_3\text{C}(\text{O})\text{O}_2 (+ 2 \text{O}_2) \rightarrow 2 \text{CH}_3\text{O}_2 + 2 \text{CO}_2 + \text{O}_2$		1.6×10^{-11} ^c
(R7.8) $\text{CH}_3\text{C}(\text{O})\text{O}_2 + \text{CH}_3\text{O}_2 \rightarrow \text{products}$		1.1×10^{-11} ^c
(R7.8a) $\text{CH}_3\text{C}(\text{O})\text{O}_2 + \text{CH}_3\text{O}_2 (+ \text{O}_2) \rightarrow \text{CH}_3\text{O}_2 + \text{HCHO} + \text{CO}_2 + \text{HO}_2 + \text{O}_2$	0.9 ^c	
(R7.8b) $\text{CH}_3\text{C}(\text{O})\text{O}_2 + \text{CH}_3\text{O}_2 \rightarrow \text{HCHO} + \text{CH}_3\text{C}(\text{O})\text{OH} + \text{O}_2$	0.1 ^c	
(R7.9) $\text{CH}_3\text{O}_2 + \text{HO}_2 \rightarrow \text{CH}_3\text{OOH} + \text{O}_2$		5.2×10^{-12} ^c
(R7.10) $\text{CH}_3\text{O}_2 + \text{CH}_3\text{O}_2 \rightarrow \text{products}$		3.5×10^{-13} ^c
(R7.10a) $\text{CH}_3\text{O}_2 + \text{CH}_3\text{O}_2 (+ 2 \text{O}_2) \rightarrow 2 \text{HCHO} + \text{O}_2 + 2 \text{HO}_2$	0.37 ^c	
(R7.10b) $\text{CH}_3\text{O}_2 + \text{CH}_3\text{O}_2 \rightarrow \text{HCHO} + \text{CH}_3\text{OH} + \text{O}_2$	0.63 ^c	

^a In $[\text{cm}^3 \text{molecule}^{-1} \text{s}^{-1}]$, ^b the radical source was included according to the experimental first-order loss of 4M3P2, ^c IUPAC recommended values.

decrease, when $[\text{HO}_2]/[\text{CH}_3\text{C}(\text{O})\text{CH}_2\text{O}_2]$ is increased further (Fig. 7.6). This is rather self-consistent, since an increase of $[\text{HO}_2]/[\text{CH}_3\text{C}(\text{O})\text{CH}_2\text{O}_2]$ results expectedly in a lowering of the products, which are predominantly formed from $\text{RO}_2 + \text{RO}_2$, namely HCHO, hydroxyacetone and methyl glyoxal according to the Reactions (R7.3), (R7.4), (R7.5), (R7.7), and (R7.8). Conversely, an increase of $[\text{HO}_2]/[\text{CH}_3\text{C}(\text{O})\text{CH}_2\text{O}_2]$ shifts the system towards hydroperoxide formation (Reactions (R7.2a), (R7.6a), and (R7.9)). In the case of methyl hydroperoxide and peracetic acid the yields surpass a maximum, since their precursor RO_2 are formed from the acetylonyl peroxy radical reactions (R7.4a). Hence, the increase of the yields of both hydroperoxides is associated with the range, where the secondary RO_2 radicals favour progressively $\text{RO}_2 + \text{HO}_2$ rather than $\text{RO}_2 + \text{RO}_2$ reactions. At the same time

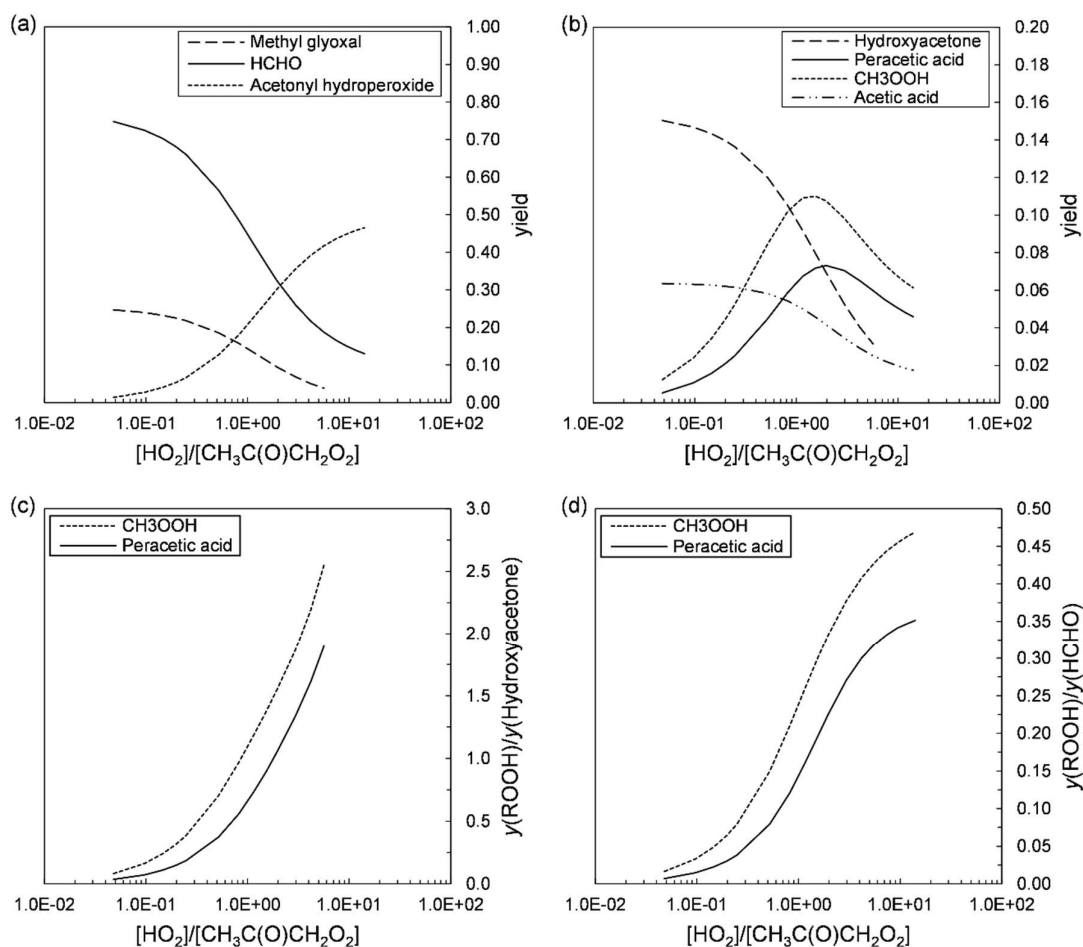


Figure 7.6. Product yields for (a) methyl glyoxal, HCHO, acetonyl hydroperoxide, and (b) hydroxyacetone, acetic acid, peracetic acid, and methyl hydroperoxide depending on the $[\text{HO}_2]/[\text{CH}_3\text{C}(\text{O})\text{CH}_2\text{O}_2]$ ratio obtained from modelling using the kinetic data from Tab. 7.4. The $\text{CH}_3\text{C}(\text{O})\text{CH}_2\text{O}_2$ radical yield from $4\text{M}3\text{P}2 + \text{O}_3$ was set to 0.6. The methyl glyoxal yield represents solely its formation from the $\text{CH}_3\text{C}(\text{O})\text{CH}_2\text{O}_2$ radical further chemistry. Panel (c) shows yield ratios between either methyl hydroperoxide or peracetic acid and hydroxyacetone, and panel (d) yield ratios between either methyl hydroperoxide or peracetic acid and HCHO depending on the $[\text{HO}_2]/[\text{CH}_3\text{C}(\text{O})\text{CH}_2\text{O}_2]$ ratio.

the increase of $[\text{HO}_2]/[\text{CH}_3\text{C}(\text{O})\text{CH}_2\text{O}_2]$ shifts the system towards $\text{CH}_3\text{C}(\text{O})\text{CH}_2\text{O}_2 + \text{HO}_2$ (R7.2), which concomitantly lowers the level of acetyl peroxy and methyl peroxy radicals in the system. By contrast, no such lowering is observed for acetonyl hydroperoxide, since it is formed directly from the parent RO_2 . However, although acetic acid is formed from both $\text{RO}_2 + \text{RO}_2$ (namely $\text{CH}_3\text{C}(\text{O})\text{CH}_2\text{O}_2 + \text{CH}_3\text{C}(\text{O})\text{O}_2$) and $\text{RO}_2 + \text{HO}_2$ (namely $\text{CH}_3\text{C}(\text{O})\text{O}_2 + \text{HO}_2$) reactions, its yield decreases with an increase of $[\text{HO}_2]/[\text{CH}_3\text{C}(\text{O})\text{CH}_2\text{O}_2]$, since first the

branching ratio towards acetic acid is much larger for $RO_2 + RO_2$ than for $RO_2 + HO_2$. Secondly, in the $[HO_2]/[CH_3C(O)CH_2O_2]$ range where $RO_2 + HO_2$ becomes dominant, the overall lowering of the $CH_3C(O)O_2$ radical level causes necessarily a decrease of the expected acetic acid yield similar to the behaviour of peracetic acid.

The profiles presented in the panels (a) and (b) of Fig. 7.6 can be translated into a $[HO_2]/[CH_3C(O)CH_2O_2]$ dependent yield ratio between the peroxides (methyl hydroperoxide, peracetic acid) and either hydroxyacetone or HCHO as presented in the panels (c) and (d). Based on that, the experimentally observed ratios indicate the $[HO_2]/[CH_3C(O)CH_2O_2]$ ratio to be in the range 1–2, when no sCl scavenger was present. Although the ratio remains rather uncertain due to the large uncertainties assigned to the quantification of both hydroperoxides, this shows $[HO_2] > [CH_3C(O)CH_2O_2]$.

When the temporal behaviour of all species were simulated following the second approach, a simultaneous match of HCHO, hydroxyacetone, methyl hydroperoxide and peracetic acid was achieved only for average values of ≈ 0.6 for the $CH_3C(O)CH_2O_2$ radical yield from 4M3P2 + O_3 and an average HO_2 level of $\approx 2 \times 10^{10} \text{ cm}^{-3}$ for experiments without addition of a sCl scavenger. This is exemplarily shown for one experiment in Fig. 7.7. In the experiments, where a non-linear behaviour was observed for the yield plots of hydroxyacetone at high 4M3P2 consumption levels, the temporal profile is matched solely in the first part of the experiment. The whole experimental time profile was reproduced when an additional first-order loss process of $\approx 4 \times 10^{-4} \text{ s}^{-1}$ was included in the model (Fig. 7.7). This value was confirmed subsequently by observing the decay of hydroxyacetone in 1 atm of synthetic air over a period of about 40 min. The non-linearity of the yield plots is therefore attributed to a first-order wall loss.

According to this simulations the formation of methyl glyoxal following the subsequent $RO_2 + RO_2$ reactions accounts for about 15 % of the observed methyl glyoxal yield in the absence of a sCl scavenger. In addition, the yield of acetyl hydroperoxide might be up to about 0.36.

The FTIR spectra indicate as well the formation of acetic acid in the experiments without a sCl scavenger. However, a reliable quantification of the low amounts supposedly present is not possible due to the spectral subtraction procedure. In addition, acetone oxide was shown to react rapidly with acetic acid (Chhantyal-Pun et al., 2018) which would consequently lower the acetic acid level expected solely from the above described simulations.

In the presence of SO_2 used to scavenge sCl, the $HCHO/CH_3OOH$ and $HCHO/CH_3C(O)OOH$ ratio indicate $[HO_2]/[CH_3C(O)CH_2O_2] \approx 1$, which is hence close to

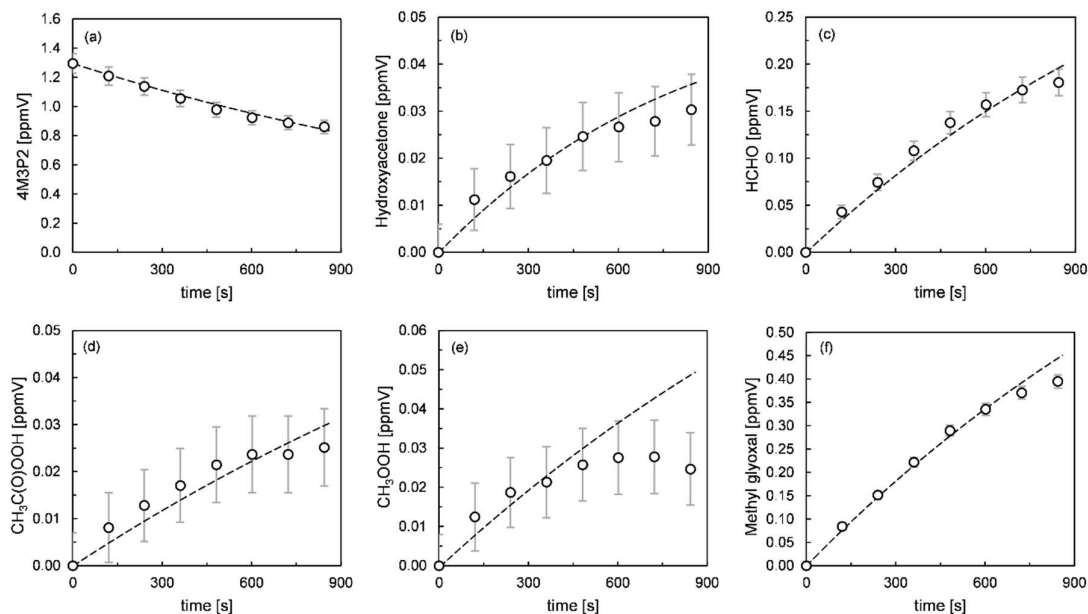


Figure 7.7. Experimental (open circles) and simulated time profiles (dashed line) of (a) 4M3P2, (b) hydroxyacetone, (c) HCHO, (d) peracetic acid, (e) methyl hydroperoxide, and (f) methyl glyoxal obtained from an experiment performed in the absence of SO_2 . The error bars represent a precision error as a combination of a relative error and the respective detection limit under the experimental conditions. Since the addition of ozone cannot be simulated, $t = 0$ was set to the time, when the first FTIR spectrum was recorded. Accordingly, the amount of products present in the first spectrum was subtracted from all data points.

$[\text{HO}_2]/[\text{CH}_3\text{C}(\text{O})\text{CH}_2\text{O}_2]$ simulated for the experiments without a sCl scavenger. Accordingly, a match of the time profiles of HCHO, peracetic acid and methyl hydroperoxide is observed merely for similar values of the $\text{CH}_3\text{C}(\text{O})\text{CH}_2\text{O}_2$ radical yield and $[\text{HO}_2]$. By contrast, the maximum amount of hydroxyacetone, which might be indicated by the FTIR spectra, is much lower than the simulated. For acetic acid, amounts are formed up to a factor of 4 larger than expected from the model runs. The methyl glyoxal temporal profile is reproduced using a slightly higher primary carbonyl yield than without a sCl scavenger, which, although within uncertainties, might indicate a small fraction of the carbonyl-substituted Cl is stabilized.

One might argue that the quantification of both hydroperoxides is rather uncertain due to their low absorptions within the FTIR spectra. However, even for HCHO solely, whose accuracy error is $< 10\%$, it is not possible to find parameters that describe simultaneously HCHO and hydroxyacetone or acetic acid. Hydroxyacetone might be possibly lost onto particles formed following the SO_2 oxidation. Though this cannot explain

a larger than expected formation, as observed for acetic acid, which points unambiguously to an additional source of acetic acid besides its formation from the $\text{RO}_2 + \text{RO}_2$ and $\text{RO}_2 + \text{HO}_2$ reactions. The acetic acid experimental time profile is well reproduced using the optimum parameters for HCHO, peracetic acid and methyl hydroperoxide and including an additional source of acetic acid from $4\text{M3P2} + \text{O}_3$ with yields of 0.08–0.11.

The formation of an organic acid beyond the possible RO_2 reactions is consistent with the observation of higher than expected propionic acid yields in the $\text{EVK} + \text{O}_3$ system (see Chapter 6). For the methyl glyoxal oxide, formed in conjunction with acetone from one POZ decomposition route, there is no vinyl hydroperoxide pathway due to the neighbouring carbonyl group. Hence, the CI may form solely a dioxirane intermediate, which isomerizes into vibrationally excited pyruvic acid, $[\text{CH}_3\text{C}(\text{O})\text{C}(\text{O})\text{OH}]^*$. In both the FTIR spectra and the PTR mass spectra there is no hint for the formation of pyruvic acid. Therefore collisional stabilization seems not to occur in the case of the oxoacid. However, fragmentation of the excited pyruvic acid proceeds possibly via 6 different pathways (Fig. 7.8) according to the mechanism proposed for the vibrationally excited oxobutanoic acid, generated in the $\text{EVK} + \text{O}_3$ system (see Chapter 6). Acetic acid is therefore likely formed following the elimination of CO from the oxoacid. Other molecular fragmentation routes may evolve either into the formation of formic acid + ketene or acetaldehyde + CO_2 . The existence of the second acid-forming pathway is supported by the observed formation of formic acid in the presence of SO_2 , although an overestimation of its measured yield cannot be ruled out completely due to a potential off-gasing from the chamber wall. Low amounts of ketene cannot be identified in FTIR spectra when working with CO as OH scavenger, since the main absorption of ketene is set in the range $2200\text{--}2100\text{ cm}^{-1}$ and hence overlapped by the saturated absorption of CO. However, preliminary results of experiments performed in the absence of an OH scavenger indicate the formation of traces of ketene, which further supports the proposed mechanism. The residual spectra of the $4\text{M3P2} + \text{O}_3$ system exhibit an absorption pattern in the range $2760\text{--}2680\text{ cm}^{-1}$, which might indicate the formation of acetaldehyde. Though this observation remains inconclusive since a baseline artefact cannot be ruled out after the multiple subtractions.

Based on the proposed mechanism for the vibrationally excited oxobutanoic acid (see Chapter 6), one might assume as well 3 different radical-forming decomposition routes for the excited pyruvic acid (Fig. 7.8), which, in the presence of O_2 , yield either acetyl peroxy or methyl peroxy radicals. The existence of these pathways is difficult to prove in the

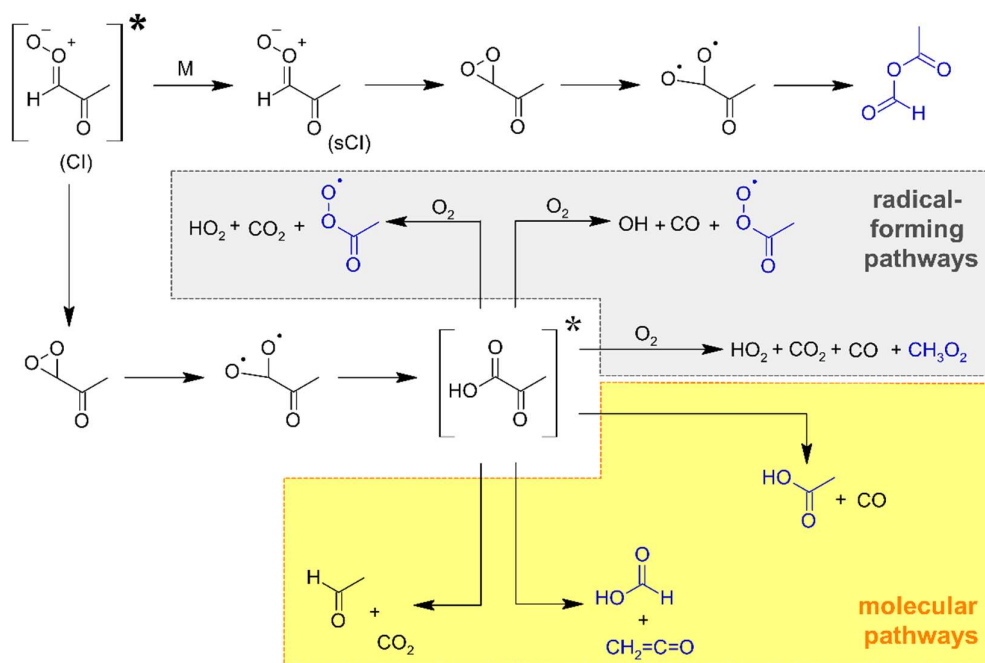


Figure 7.8. Proposed mechanism for the fate of the carbonyl-substituted CI (methyl glyoxal oxide). The grey area marks radical-forming fragmentation routes and the pale yellow area molecular fragmentation routes of the vibrationally excited pyruvic acid. Blue structures were positively identified within the experiments, although the RO_2 species cannot be assigned clearly to the shown pathways.

present reaction system. Since both RO_2 radicals are formed following the further chemistry of the predominant acetone oxide, the simulations are insensitive to additional, very small, RO_2 sources. Further, the yield needed to describe the temporal evolution of acetic acid accounts consequently for the majority of the carbonyl-substituted CI. Therefore, the radical-forming fragmentation routes, if existent for $[\text{CH}_3\text{C}(\text{O})\text{C}(\text{O})\text{OH}]^*$, are minor pathways.

The FTIR spectra indicate also the formation of formic acetic anhydride (FAA) in experiments, where only the OH scavenger was present. However, the quantification remains rather uncertain due to the spectral subtraction procedure and allows just to provide an upper limit of 0.02 for the FAA yield. Since the anhydride is not observed in the presence of SO_2 , this is a strong indication for its formation from the thermally equilibrated CIs. The formation of anhydrides in gas-phase ozonolysis reactions has been reported following the thermal decomposition of intermediately formed hydroperoxide esters, for instance hydroperoxymethyl formate, which evolve from the reaction of CIs with organic

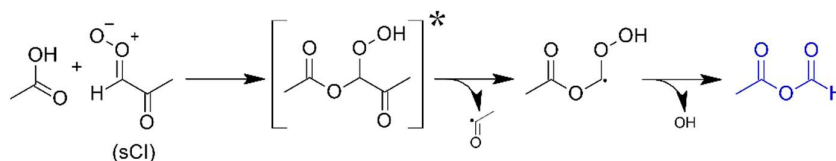


Figure 7.9. Hypothetically possible formation of formic acetic anhydride following the reaction of acetic acid with the stabilized methyl glyoxal oxide.

acids (Neeb et al., 1995; 1996). Hypothetically, one might think that the reaction of the methyl glyoxal oxide with acetic acid yields a complex hydroperoxide as shown in Fig. 7.9, which instead of H_2O elimination releases first an acetyl radical and second an OH radical to form FAA. However, presently it is not known if such a reaction sequence exists and if the release of 2 radicals will be energetically favoured. In addition, the above discussed results prove beyond doubt the acetone oxide to be the predominant CI in the $4\text{M3P2} + \text{O}_3$ system with a significant fraction of the CI formed stabilized comparative to methyl glyoxal oxide. Therefore, acetic acid will preferentially react with $(\text{CH}_3)_2\text{COO}$ rather than $\text{CH}_3\text{C}(\text{O})\text{CHOO}$ in the absence of SO_2 . According to said, it is more likely to assume that the stabilized methyl glyoxal oxide forms as well a dioxirane intermediate followed by an isomerization into an anhydride instead of an acid (Fig. 7.8).

7.3.2.2 Methyl vinyl ketone

Besides the primary carbonyls, HCHO and methyl glyoxal, the FTIR spectra attest unambiguously the formation of methyl hydroperoxide, peracetic acid, formic acid, formic anhydride (FA), and formic acetic anhydride (FAA) in the experiments where CO was added to scavenge OH radicals (Tab. 7.5). The presence of all these species is further supported by the PTR mass spectra showing the increase of characteristic ion signals, although most of the observed m/z ions do not correspond solely to one of the species. For instance, methyl hydroperoxide forms mainly a fragment ion at m/z 31 (CH_3O^+), which interferes with HCHO. Anhydrides were shown to hydrolyse and to appear as m/z of their corresponding acid, as discussed before. Thus, FA and FAA interfere very likely with $\text{HC}(\text{O})\text{OH}$ at m/z 47, and consequently, FAA also with peracetic acid at m/z 61 ($\text{C}_2\text{H}_5\text{O}_2^+$). The peracid is further supported by the m/z 77 signal ($\text{C}_2\text{H}_5\text{O}_3^+$). In addition, the PTR mass spectra indicate reaction products, which form ions at m/z 43, 45, and 87.

For all species but FAA, the yield plots are clearly linear within precision errors. In the case of FAA, the correlation might indicate a larger product formation rate at higher MVK

Tab. 7.5. Quantified reaction products and assigned masses of the MVK + O₃ reaction in the presence of CO as an OH radical scavenger and in the presence of CO and SO₂ together with available literature data. The uncertainties given for the product yields determined within this work represent a combination of the 2 σ statistical error and the accuracy error.

Species	Yield ^a	Yield	Yield	Yield ^b	Assigned m/z ^a
HCHO	0.35 ± 0.08	0.05	0.44 ± 0.05	0.60 ± 0.07	31.018
Methyl glyoxal	0.29 ± 0.05	0.87		0.51 ± 0.05	73.029, 45.034
Formic acid	0.044 ± 0.006			0.22 ± 0.04	47.013
Formic anhydride ^c	0.084 ± 0.035				47.013
Formic acetic anhydride ^c	0.028 ± 0.014				61.029, 47.013
Acetic acid				0.13 ± 0.02	61.029
Peracetic acid	0.062 ± 0.019			0.031 ± 0.012	77.024, 61.029
CH ₃ OOH	0.10 ± 0.05			0.062 ± 0.018	49.029, 31.018
Pyruvic acid		0.05			
CO			0.29 ± 0.01		
CO ₂ ^d	0.79 ± 0.16			0.57 ± 0.10	
sCl				0.32 ± 0.08	
Detection method	FTIR	HPLC-UV	FTIR, GC-MS, PTR-MS	FTIR	PTR-MS
Reference	This work	Grosjean et al. (1993)	Ren et al. (2017)	This work	This work

^a Experiments were performed in the presence of CO as an OH radical scavenger, ^b experiments were performed in the presence of CO as an OH radical scavenger and SO₂, ^c the yields were obtained from the linear range of the yield plots, ^d sum of CO₂ formed from MVK + O₃ and CO + OH.

consumption levels, which suggests its formation from secondary processes. However, in this particular case, the apparent increase may be an artefact caused by the spectral subtraction procedure. Since for the anhydrides the evaluation is based mainly on their characteristic C=O absorption pattern, this is difficult to handle due to the superposition of absorption bands, which is reflected in the larger scattering of the combined FAA data (Fig. 7.10). On the other hand, the yield plots of all anhydrides exhibit clearly a negative intercept at least in some of the experiments (Fig. 7.10), which is not observed for the primary carbonyls. The panels (c)–(e) of Fig. 7.10 present yield plots for the m/z 47, 61, and 73 signals exemplarily for one experiment (represented by the cross symbol in the FTIR data). Both, the plot for m/z 47 (CH₃O₂⁺) and m/z 61 (C₂H₅O₂⁺) do clearly indicate a significant larger yield at higher MVK consumption levels ($\Delta m/z$ 71), which is in qualitative agreement with the FAA yield plot obtained from the FTIR data. By contrast, no such effect

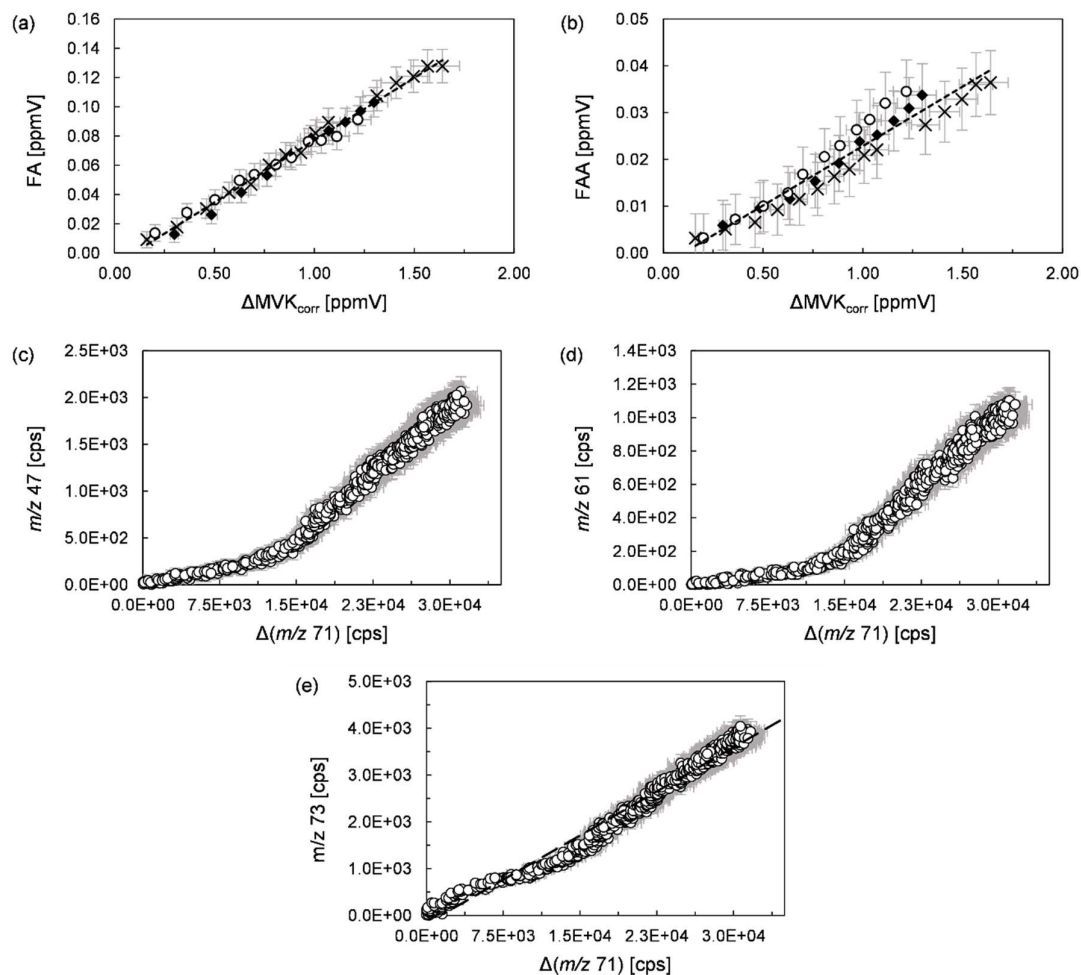


Figure 7.10. Yield plots for (a) formic anhydride, and (b) formic acetic anhydride according to the FTIR data. Different experimental runs are denoted with different symbols. Panel (c)–(e) show the yield plots for $m/z\ 47$, $m/z\ 61$, and $m/z\ 73$ for one experiment exemplarily. The error bars represent the respective precision error.

is observed in the PTR-MS data for methyl glyoxal ($m/z\ 73$), those yield plot exhibits a strong linearity over the whole experimental duration, as shown in panel (e) of Fig. 7.10. This observation suggests that the anhydrides result, at least partially, from secondary formation processes.

In the presence of SO_2 , the FTIR spectra do not confirm the formation of anhydrides. The yields for both primary carbonyls increase, whereas the peroxide (methyl hydroperoxide, peracetic acid) yields decrease roughly by a factor of 2. By contrast, a

considerable increase is observed for the HC(O)OH yield (from 0.044 ± 0.006 to 0.22 ± 0.04). In addition, acetic acid was found to be formed with a yield of 0.12 ± 0.02 .

The m/z 43 ion may be partly related to protonated ketene ($\text{CH}_2=\text{C}=\text{O}$). Its formation cannot be confirmed using FTIR data due to the overlapping CO absorption features as written above. However, preliminary results from ozonolysis experiments performed without an OH radical scavenger confirm that traces of ketene are formed. On the other hand, the temporal behaviour of the m/z 43 ion correlates strongly with the m/z 87 ion during the reaction, whereas no such correlation is observed when comparing either the m/z 43 or m/z 87 with m/z signals of clearly assigned species. This strongly suggests that both ion signals arise predominantly from the same species. Supposedly, the m/z 43 signal results mainly from $\text{CH}_3\text{C}(\text{O})^+$ ions. Among possible reaction products from both unimolecular and bimolecular reactions, the only reasonable species with m/z 87 were a protonated epoxide (α,β -epoxybutanone) formed following a pathway competing with the POZ formation (Fig. 7.1). This structure were also in agreement with the observation of m/z 43, which results likely from fragmentation of the epoxide. Gas-phase infrared absorption features of carbonyl-containing epoxides were reported in the literature only for the structurally similar glycidaldehyde (α,β -epoxypropanal) (Ma et al., 1998). The comparison proved difficult with both residual spectra of experiments performed in the presence and absence of SO_2 due to baseline problems in the spectral range characteristic for epoxides ($800\text{--}900\text{ cm}^{-1}$). In the absence of SO_2 , there remain very low absorption bands in the corresponding spectral range, which do not show the same shape as reported for glycidaldehyde (Ma et al., 1998). In contrast to the twin-peak profile of the epoxyaldehyde, the residual spectrum indicates rather two separated absorption features. However, this does not allow to derive any conclusion on a possible epoxide formation. In the presence of SO_2 , the baseline shift due to particle formation does not allow to conclude whether additional absorption bands are present in the corresponding spectral range. In summary, although the temporal evolution of both m/z 87 and m/z 43 suggest the epoxide formation, its identification remains uncertain. To evidenciate unambiguously whether the epoxide is formed during the ozonolysis reaction, further work is needed on a characterization of α,β -epoxybutanone (= 2-acetyloxirane).

The consumption of SO_2 during the ozonolysis reaction indicates the presence of thermalized carbonyl oxides, although the SO_2 consumption is considerably smaller than the increase observed for the primary carbonyl yields, as discussed above (see Sect. 7.3.1). The much larger formation yield of organic acids (formic acid, acetic acid) in the presence of SO_2 suggests that both acids are a) formed from excited CIs, and b) consumed probably

through thermalized CIs in the absence of SO_2 . For instance, the reaction of formaldehyde oxide, CH_2OO , with HC(O)OH was shown to form a vibrationally excited hydroperoxide ester (hydroperoxymethyl formate), which decomposes into H_2O and FA (Neeb et al., 1995; 1996). This, in turn, should result in a slightly curved yield plot for FA, where larger formation rates were observed with higher levels of the ketone consumption. However, besides a small negative intercept the yield plots of the FTIR data do not indicate a delayed formation. By contrast, this is strongly suggested by the yield plot for the m/z 47 signal (Fig. 7.10), which, however, originates at least partly from FAA. The presence of hydroperoxymethyl formate can neither be confirmed nor ruled out, since the residual FTIR spectra indicate that all absorption features of the hydroperoxide ester were at least superposed by absorption bands of unidentified reaction products. FA itself was shown to decompose into HC(O)OH and CO (Thomas, 1997). However, the yield plots suggest that this process is not relevant on the time scale of the experiments. In addition, this process cannot account for the HC(O)OH formation in the presence of SO_2 .

In principle, the reaction of CH_2OO with SO_2 might also form formic acid, as discussed in Chapter 6. Vereecken et al. (2012) calculated that about 17 % of the $\text{CH}_2\text{OO} + \text{SO}_2$ leads to singlet bis(oxy) biradicals. Although these, in turn, might isomerize into stabilized formic acid, this is obviously only a minor pathway. In addition, the present results evidence the formation of formic acid in the absence of SO_2 similar to the finding for the homologue ethyl vinyl ketone. Therefore, the SO_2 reaction cannot account for the majority of the observed HC(O)OH .

In contrast to the 4M3P2 ozonolysis, an analogue reaction of formaldehyde oxide with acetic acid might account for the finally formed FAA in the $\text{MVK} + \text{O}_3$ system, which is supported by the shape of the yield plot. However, it cannot be ruled out that there exists also a unimolecular channel of the methyl glyoxal oxide, as observed for $4\text{M3P2} + \text{O}_3$. The only pathway of forming peracetic acid is the reaction of its parent RO_2 with HO_2 , as discussed above. As the acetyl peroxy radical cannot result from CH_2OO , this is a further evidence that acyl radicals result from the further fate of carbonyl-substituted CIs (of the structure RC(O)CHOO), as suggested originally for the EVK-derived carbonyl oxide (see Chapter 6). This is likely rationalized through the decomposition of $[\text{CH}_3\text{C(O)C(O)OH}]^*$ formed following the further isomerization of the dioxirane intermediate (Fig. 7.8).

Methyl hydroperoxide is also formed solely from the reaction of its parent RO_2 with HO_2 . Methyl radicals, which are instantaneously converted into methyl peroxy radicals, result ultimately from the acetyl peroxy radical further reactions, either via $\text{CH}_3\text{C(O)O}_2 +$

HO_2 or via $\text{CH}_3\text{C}(\text{O})\text{O}_2 + \text{CH}_3\text{C}(\text{O})\text{O}_2$, as discussed above. However, the fragmentation of $[\text{CH}_3\text{C}(\text{O})\text{C}(\text{O})\text{OH}]^*$ might also lead directly to methyl radicals (Fig. 7.8).

Panel (a) of Fig. 7.11 shows the yields of peracetic acid, acetic acid, HCHO and methyl hydroperoxide in dependence of the $[\text{HO}_2]/[\text{CH}_3\text{C}(\text{O})\text{O}_2]$ ratio modelled for an artificial reaction producing solely acetyl peroxy radicals with a yield of 0.5 based on the kinetic parameters of the Reactions (R7.6)–(R7.10). The yield has been chosen, since the primary carbonyl yields indicate nearly a 1:1 ratio for the POZ fragmentation routes. Further, this acetyl peroxy radical yield would correspond to the upper limit, if the POZ formation and fragmentation were the only pathway and the carbonyl-substituted CI would decompose solely into acetyl radicals. The profiles of panel (a) can be translated into a yield ratio, for instance for methyl hydroperoxide and peracetic acid or methyl hydroperoxide and HCHO. The experimentally observed $\text{CH}_3\text{OOH}/\text{CH}_3\text{C}(\text{O})\text{OOH}$ ratio indicates the $[\text{HO}_2]/[\text{CH}_3\text{C}(\text{O})\text{O}_2]$ ratio to be lower in the presence than in the absence of SO_2 . However, based on the experimental $\text{CH}_3\text{OOH}/\text{CH}_3\text{C}(\text{O})\text{OOH}$ ratios together with the fact that the majority of HCHO is formed directly from the POZ decomposition (as a primary carbonyl), it is not possible to attest unambiguously a direct source of CH_3 radicals in the reaction system. The only hint for a direct CH_3 radical source is that the $\text{CH}_3\text{OOH}/\text{CH}_3\text{C}(\text{O})\text{OOH}$ ratios, observed in each experiment in the absence of SO_2 , would correspond to implausible high $[\text{HO}_2]/[\text{CH}_3\text{C}(\text{O})\text{O}_2]$ ratios comparative to the $[\text{HO}_2]/[\text{CH}_3\text{C}(\text{O})\text{CH}_2\text{O}_2]$ ratios estimated for the $4\text{M3P2} + \text{O}_3$ system. In summary, this remains rather uncertain due to the uncertainties assigned to the peroxide quantification. Vice versa, this does not allow to provide an appropriate estimate of the contribution of RO_2 reactions on the observed HCHO yield, although they will contribute at any rate.

By contrast, the acetic acid yield modelled for this upper limit scenario is minimally a factor of 2 lower than experimentally observed. This observation proves unequivocally an additional source of acetic acid, which is not explained by RO_2 reactions. Further, this finding is consistent with the results of the $4\text{M3P2} + \text{O}_3$ reaction, where the same carbonyl-substituted CI is formed, which further supports the proposed decomposition of the vibrational excited pyruvic acid, $[\text{CH}_3\text{C}(\text{O})\text{C}(\text{O})\text{OH}]^*$.

Another pathway, proposed for the decomposition of $[\text{CH}_3\text{C}(\text{O})\text{C}(\text{O})\text{OH}]^*$, provides ketene in conjunction with formic acid. Traces of ketene are indicated in experiments without OH scavenger, as mentioned above, which supports the proposed fragmentation route. However, since based on these preliminary results, the ketene yield is more than a factor of 10 smaller than the $\text{HC}(\text{O})\text{OH}$ yield, an additional source must be present in the

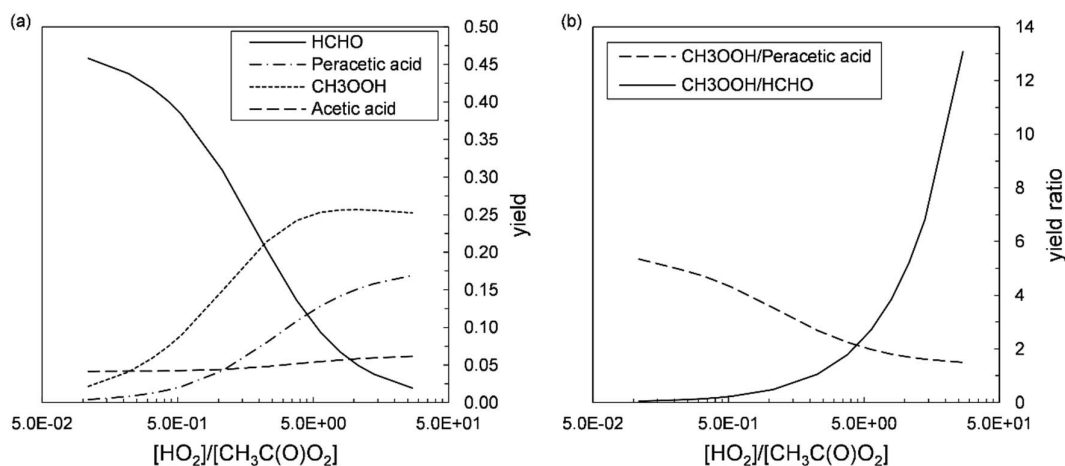


Figure 7.11. (a) Product yields of acetic acid, HCHO, methyl hydroperoxide, and peracetic acid and (b) translated yield ratios depending on the $[\text{HO}_2]/[\text{CH}_3\text{C}(\text{O})\text{O}_2]$ ratio obtained from modelling of an artificial reaction producing solely $\text{CH}_3\text{C}(\text{O})\text{O}_2$ radicals (yield = 0.5) using the corresponding kinetic data from Tab. 7.4.

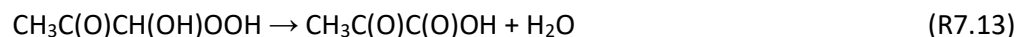
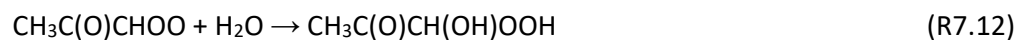
reaction system. Further, the presence of SO_2 minimizes bimolecular reactions of thermalized CIs. Hence, the only possibility to form $\text{HC}(\text{O})\text{OH}$ seems the formaldehyde oxide, which suggests that a fraction of $[\text{HC}(\text{O})\text{OH}]^*$, formed following the dioxirane route, is stabilized by collisional energy transfer:



This contrasts with the recent review article by Cox et al. (2020), where only fragmentation of $[\text{HC}(\text{O})\text{OH}]^*$ was presented. Regardless, this observation is in agreement with the high $\text{HC}(\text{O})\text{OH}$ yields observed here for the structurally similar ethyl vinyl ketone (see Chapter 6). This pathway will be further discussed in Sect. 7.3.2.4.

Grosjean et al. (1993b) identified pyruvic acid besides the primary carbonyls, although the authors report a yield of 0.05 based on the results of only one experiment. By contrast, the formation of the oxoacid is neither observed in the FTIR spectra nor in the PTR mass spectra recorded during the present experiments. Further, Ren et al., (2017) did not find pyruvic acid either (under dry conditions). All this suggests that a collisional stabilization of the excited oxoacid does not take place, in contrast to the observation of formic acid.

Another possibility of forming pyruvic acid in the MVK + O_3 system were potentially the reaction of thermalized methyl glyoxal oxide with H_2O and the subsequent decomposition of the intermediate hydroxyhydroperoxide:



However, although not explicitly mentioned, the experimental details provided by Grosjean et al. (1993b) suggest that the experiments were performed under dry conditions. There is currently no closing explanation for the contradicting results on pyruvic acid, although it is striking that both the observed primary carbonyl yields and the presence of pyruvic acid in the experiments performed by Grosjean et al. (1993b) are contradicted by both the observations of Ren et al. (2017) and the present results.

7.3.2.3 3-Penten-2-one

Besides the primary carbonyls, acetaldehyde and methyl glyoxal, also HCHO, glyoxal, methyl hydroperoxide, peracetic acid, methane, ketene, and formic acetic anhydride were positively identified and quantified in the experiments in the presence of CO as the OH scavenger (Tab. 7.6). Fig. 7.12 displays the yield plots derived from the FTIR data for the species those yields were found to be < 0.10 . When SO_2 was present in the reaction mixture the yields of HCHO, methyl hydroperoxide and methane decreased slightly, while peracetic acid was not indicated by the FTIR spectra. Although traces of glyoxal are at least indicated, the signal/noise ratio prevents any accurate quantification. An attempt would set an upper limit of ≈ 0.02 for the glyoxal yield. In addition, acetic acid and formic acid were observed with yields of about 0.13 ± 0.02 and 0.083 ± 0.037 , respectively (Tab. 7.6). Since the primary carbonyl yield indicates the $3\text{P2} + \text{O}_3$ reaction to proceed solely via the 1,3-dipolar cycloaddition and the subsequent POZ decomposition, the observed products evolve from the further reactions of either acetaldehyde oxide (C_2 fragment), CH_3CHOO , or methyl glyoxal oxide (C_3 fragment), $\text{CH}_3\text{C}(\text{O})\text{CHOO}$. The ratio of the primary carbonyls implies necessarily the acetaldehyde oxide to be the dominant CI in the reaction system, although the yield of the carbonyl-substituted CI is about a factor of 2 larger than for the $4\text{M3P2} + \text{O}_3$ reaction.

Both the glyoxal and the ketene yield possess large uncertainties due to the low absorption intensities exhibited by the two substances in the FTIR spectra recorded during the $3\text{P2} + \text{O}_3$ reaction which causes are larger scatter in the experimental data (Fig. 7.12). For instance, the quantification of ketene is achieved only by the absorption pattern in the range of $3100\text{--}3040\text{ cm}^{-1}$, which is much less intense than the main absorption in the range

Tab. 7.6. Quantified reaction products and assigned masses of the 3P2 + O₃ reaction in the presence of CO as an OH radical scavenger and in the presence of CO and SO₂. The uncertainties given for the product yields represent a combination of the 2 σ statistical error and the accuracy error.

Species	Yield ^a	Yield ^b	Assigned <i>m/z</i> ^a
Acetaldehyde	0.21 ± 0.07	0.60 ± 0.10	45.034
Methyl glyoxal	0.66 ± 0.16	0.68 ± 0.11	73.029, 45.034
HCHO	0.16 ± 0.04	0.11 ± 0.02	31.018
Formic acid		0.083 ± 0.037	47.013
Formic acetic anhydride ^c	0.065 ± 0.031		61.029, 47.013
Acetic acid		0.13 ± 0.02	61.029
Peracetic acid	0.027 ± 0.016		77.024, 61.029
CH ₃ OOH	0.075 ± 0.017	0.041 ± 0.011	49.029, 31.018
Glyoxal	0.030 ± 0.011		
Ketene	0.055 ± 0.028		43.018
CH ₄	0.076 ± 0.012	0.064 ± 0.008	
CO ₂ ^d	1.05 ± 0.31	0.47 ± 0.19	
sCl		0.40 ± 0.14	

^a Experiments were performed in the presence of CO as an OH radical scavenger, ^b experiments were performed in the presence of CO as and OH radical scavenger and SO₂, ^c the yields were determined from the linear range of the yield plot, ^d sum of CO₂ formed from 3P2 + O₃ and CO + OH.

2200–2100 cm⁻¹. However, preliminary data from experiments performed in the absence of an OH scavenger unambiguously confirm ketene as a reaction product.

In the case of acetaldehyde oxide two isomers are possibly formed in which the outer O atom of the Criegee moiety is either oriented towards the methyl group (*Z*-CH₃CHOO or *syn*-CH₃CHOO) or the H atom (*E*-CH₃CHOO or *anti*-CH₃CHOO) (Fig. 7.13). The latter isomer is expected to form a dioxirane intermediate via 1,3-ringclosure followed by an isomerization into excited acetic acid, [CH₃C(O)OH]^{*}, since the *E*-configuration prohibits an 1,4-H shift isomerization into an excited vinyl hydroperoxide. The decomposition of the excited acid via molecular fragmentation routes evolves either into ketene + H₂O, methanol + CO, or CH₄ + CO₂ (e. g. Martinez and Herron, 1988; Tuazon et al., 1997; Cox et al., 2020). In addition, the results of various studies (e. g. Horie and Moortgat, 1991; Tuazon et al., 1997) suggest the existence of radical-forming fragmentation routes that yield either CH₃ + CO₂ + H, CH₃ + CO + OH, or CH₃C(O) + OH, although the acetyl radical forming pathway was not proven experimentally to date (Tuazon et al., 1997; Cox et al., 2020).

The formation of CH₄ and ketene are therefore strong proofs for the presence of the *E*-CH₃CHOO in the 3P2 + O₃ system, although ketene might also be formed following the further reactions of the carbonyl-substituted CI (see below). Methanol, built potentially following a third molecular channel, could not be quantified, since the main absorption feature in the range 1080–980 cm⁻¹ is overlapped completely by the O₃ absorption.

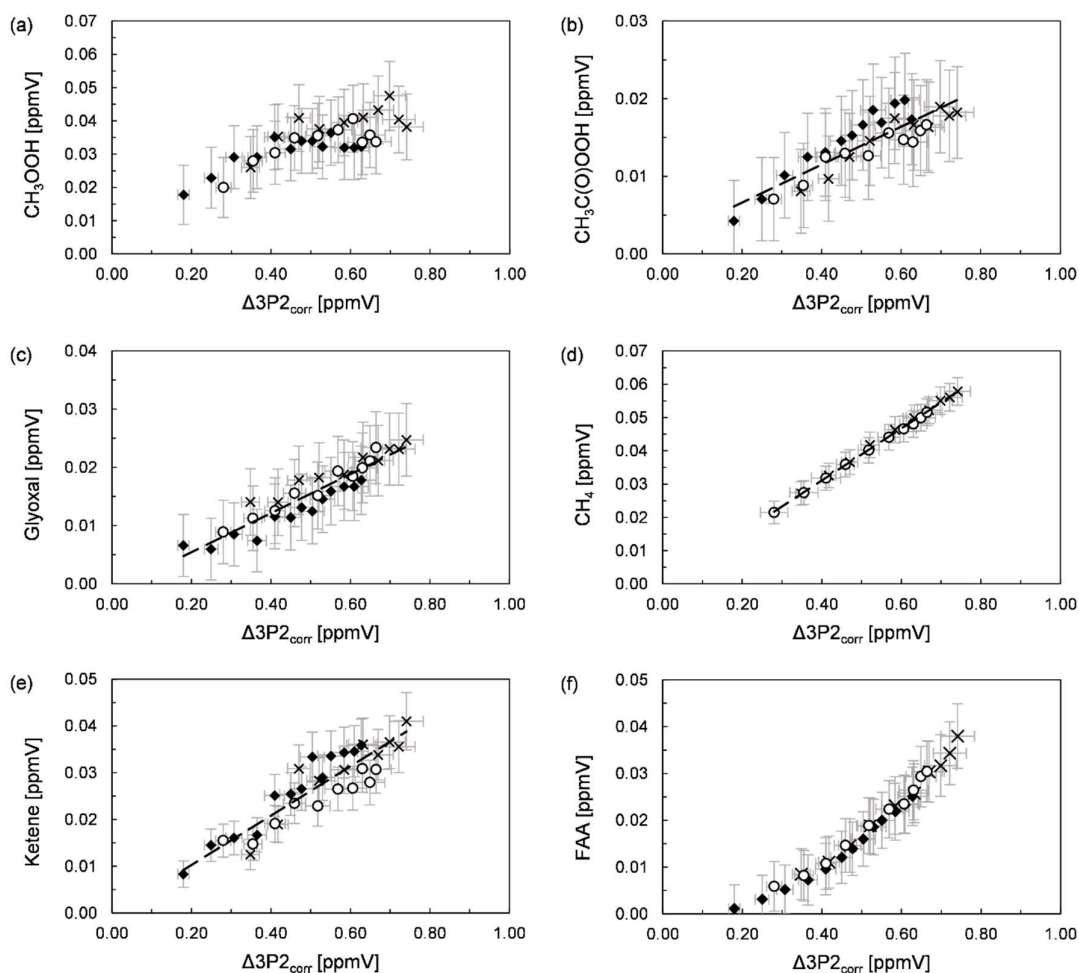


Figure 7.12. Yield plots for (a) methyl hydroperoxide, (b) peracetic acid, (c) glyoxal, (d) methane, (e) ketene, and (f) formic acetic anhydride obtained from experiments in the absence of a sCl scavenger. Different experimental runs are denoted with different symbols. The error bars represent the respective precision error under the experimental conditions.

However, there are two observations that support qualitatively the existence of the CH_3OH forming decomposition pathway. After subtraction of O_3 , the residual spectrum contains a small peak at 1033 cm^{-1} , which could belong to methanol. Though, the stronger point is the temporal evolution of the m/z 33 signal in the PTR mass spectra during the ozonolysis reaction. The time profile suggests that the formation of the m/z 33 ion occurs only in the first part of the reaction, while almost no additional formation is observed at higher 3P2 consumption levels. Depending on the wall conditions, methanol is known to exhibit a notable wall loss of up to $\approx 3 \times 10^{-4}\text{ s}^{-1}$ in the 1080 L chamber, which might hence cause the

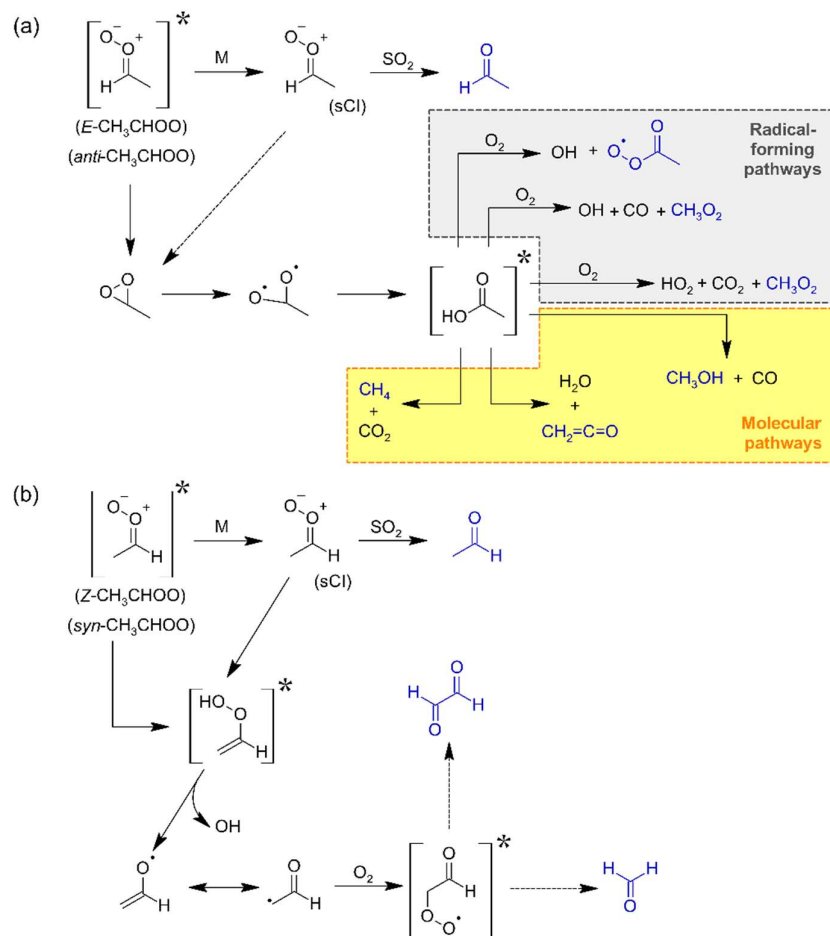


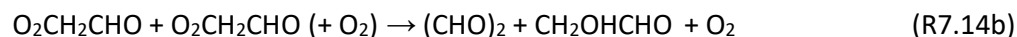
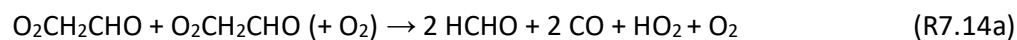
Figure 7.13. Fate of the (a) E - CH_3CHOO and (b) Z - CH_3CHOO according to available literature data. Identified structures are marked in blue, although the RO_2 species cannot be clearly assigned to the shown pathways.

observed temporal behaviour.

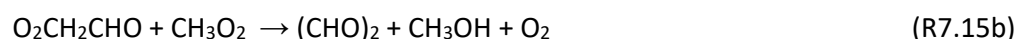
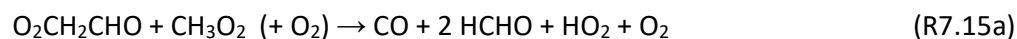
In the presence of SO_2 , the FTIR spectra do not allow to conclude whether ketene is formed due to a non-linear baseline shift resulting from particle formation (due to H_2SO_4 formed following the SO_2 oxidation), as discussed in Chapter 6. The CH_4 yield decreases minimally, which might indicate that a very small fraction of the E - CH_3CHOO is thermalized.

Glyoxal has also been identified in studies on the ozonolysis of propene, $E2$ -butene, and $Z2$ -butene (Tuazon et al., 1997). Its formation is attributed to the Z - CH_3CHOO (Cox et al., 2020), which hence suggests that both acetaldehyde oxide isomers are formed in the $3\text{P}2 + \text{O}_3$ reaction. However, due to the complexity of the reaction system and the undefined isomer ratio for $3\text{P}2$ it is not possible to decipher the E/Z isomer ratio for

CH₃CHOO. The Z-CH₃CHOO forms an excited vinyl hydroperoxide via an 1,4-H shift migration, which will subsequently release OH to yield a vinyloxy radical (CH₂CHO). The CH₂CHO + O₂ reaction has been investigated by several groups due its relevance in combustion processes. It was shown to yield initially an O₂-CH₂CHO adduct, which is subject of subsequent isomerization and decomposition processes in competition with collisional stabilization. Although branching ratios were scarcely determined, experimental and theoretical studies showed the formation of HCHO, glyoxal, and ketene via isomerization and subsequent decomposition of the chemically activated adduct (Gutman and Nelson, 1983; Lorenz et al., 1985; Zhu and Johnston, 1995; Lee and Bozzelli, 2003; Weidman et al., 2018). However, theoretical calculations indicate the pathways yielding the latter two products to be competitive only at extremely high temperatures (Weidman et al., 2018). In addition, experimental results suggest that glyoxal is not a direct product from the CH₂CHO + O₂ reaction (Zhu and Johnston, 1995). Lee and Bozzelli (2003) calculated that the stabilization of the peroxy adduct (O₂-CH₂CHO adduct) is the major reaction pathway at 1 atm and temperatures < 500 K. Accordingly, Cox et al. (2020) state that the vinyloxy radical, resulting from alkene ozonolysis at atmospheric conditions, is expected to form a stabilized RO₂ radical. Hence, the formation of glyoxal would be described by bimolecular reactions of the respective RO₂. In the case of the propene + O₃ or 2-butene + O₃ systems this were rationalized either by the RO₂ self-reaction or cross-reaction with methyl peroxy radicals, by analogy to available literature data on self- and cross-reactions of RO₂ radicals. The self-reaction would proceed via two channels, either conversion into the corresponding alkoxy radical, which, similar to the acetonyloxy radical (Orlando et al., 2000), is expected to decompose immediately, or a channel, which yields glyoxal in conjunction with glycolaldehyde.



The cross-reaction with methyl peroxy radicals were expected to proceed via three channels, yielding either the corresponding alkoxy radicals, glyoxal or glycolaldehyde.



Hence, the further reactions of a stabilized RO_2 , needed to explain the formation of glyoxal (and HCHO) would consequently account also for glycolaldehyde. Although the yield of glycolaldehyde could be lower than that of glyoxal, depending hypothetically on the branching ratios for the Reactions (R7.15b) and (R7.15c), one should observe also the formation of the α -hydroxyaldehyde in the ozonolysis systems. However, neither here nor in one of the preceding investigations, even for the *E*2-butene + O_3 system, where the glyoxal yield were the highest (Tuazon et al., 1997), the formation of glycolaldehyde has ever been identified.

In addition, the 1,4-H migration of the stabilized RO_2 , which yields finally HCHO, is predicted to be as fast as $\approx 2\text{--}3 \text{ s}^{-1}$ (Vereecken and Nozière, 2020), which is expected to be faster than $\text{RO}_2 + \text{RO}_2$ and $\text{RO}_2 + \text{HO}_2$ reactions under atmospheric conditions and at least competitive under the experimental conditions. However, this would account solely for the HCHO formed, whereas it cannot explain the formation of glyoxal. Given the still open questions, it is preferred not to provide a conclusive mechanism for the vinyloxy radical towards the formation of HCHO and glyoxal (Fig. 7.13).

Since glyoxal might be as well formed in the presence of SO_2 , the vinyloxy radical seems to originate at least partly from the excited *Z*- CH_3CHOO . These experiments show also the formation of organic acids, which may imply that the products accounted for the thermalized *Z*- CH_3CHOO are underestimated in the absence of a *s*Cl scavenger due to a fast reaction between the *Z*- CH_3CHOO and the acids.

The formation of both peracetic acid and methyl hydroperoxide proceeds solely through the reaction of their parent RO_2 , namely the acetyl peroxy and methyl peroxy radical, with HO_2 , as discussed in the beginning of Sect. 7.3.2. Observing the assigned uncertainties, the ratio between both peroxides does not allow to conclude whether both compounds evolve solely from the acetyl peroxy radical or whether an additional source of methyl peroxy radicals is present. However, in both cases the RO_2 cross-reaction may contribute to the observed HCHO formation. The slight decrease of the HCHO yield in the presence of SO_2 seems hence consistent with the lowering of the hydroperoxide yield. Since $[\text{CH}_3\text{C}(\text{O})\text{OH}]^*$, formed following the isomerization of the *E*- CH_3CHOO , was shown to produce CH_3 radicals, that are immediately converted into methyl peroxy radicals, it is not possible to assign CH_3 formation also to the carbonyl-substituted Cl. The same applies for the acetyl peroxy radical although its formation from the $[\text{CH}_3\text{C}(\text{O})\text{OH}]^*$ has only been postulated (Tuazon et al., 1997), but no experimental confirmation has been reported. Hence, the absence of peracetic acid in the presence of SO_2 , whereas methyl hydroperoxide is still observed, might indicate different sources of the RO_2 radicals. The observation of

CH₃OOH were further consistent with its formation from [CH₃C(O)OH]^{*}, given that other fragmentation products like CH₄ are found also in the presence of the sCl scavenger. Nevertheless, it should be emphasized that low amounts of peracetic acid might be below the detection limit due to a poorer signal/noise ratio in the corresponding spectral range when working with SO₂. Therefore the presence of acetyl peroxy radicals cannot be ruled out completely. However, the acetyl peroxy radical further reactions with HO₂ or methyl peroxy radicals were the only sources of acetic acid if formed from RO₂ radical reactions. The yield found for 3P2 + O₃ originates thus unequivocally from an additional source, which, in turn, is consistent with the observation for ethyl vinyl ketone (see Chapter 6) and 4M3P2 (see Sect. 7.3.2.1). The acetic acid formation is expected to proceed also through the decomposition of the vibrationally excited pyruvic acid, [CH₃C(O)C(O)OH]^{*}, built upon isomerization of the excited carbonyl-substituted CI (Fig. 7.8). Accordingly, the observation of formic acid is consistent with another molecular fragmentation route of [CH₃C(O)C(O)OH]^{*} (Fig. 7.8). Since ketene is supposed to be formed as the co-product, this pathway interferes with the ketene formation expected from [CH₃C(O)OH]^{*}.

The formic acetic anhydride is observed solely in the absence of the sCl scavenger. In contrast to the anhydride data of the MVK + O₃ system, here the yield plot of the FTIR data (Fig. 7.12) suggests unequivocally a higher FAA yield at longer reaction times, which indicates a delayed FAA formation. This is further supported by the fact that the regression line over the whole data in each experiment exhibits a small negative intercept beyond the statistical uncertainties. A contribution of a direct FAA formation seems possible from the isomerization of the methyl glyoxal oxide, as suggested from the 4M3P2 + O₃ system. However, the shape of the yield plots indicates a stronger source from secondary processes. Since the experiments in the presence of SO₂ show clearly the formation of both formic and acetic acid, this is likely rationalized also through the intermediate formation of a hydroperoxide ester and its subsequent decomposition into the mixed anhydride. In contrast to the FAA formation observed for MVK this is attributed to a hydroperoxide ester resulting from CH₃CHOO + HC(O)OH in the present reaction system. An analogue reaction with acetic acid would provide potentially acetic anhydride. However, although the SO₂ experiments indicated a slightly higher level of acetic acid than formic acid, there was no indication for the formation of acetic anhydride in experiments performed in the absence of a sCl scavenger.

7.3.2.4 3-Methyl-3-penten-2-one

In addition to the primary carbonyls, acetaldehyde and biacetyl, the formation of HCHO, glyoxal, ketene, and CH₄ was observed in the FTIR spectra of experiments, when only the OH scavenger (CO) was present (Tab. 7.7). Except for CH₄, the PTR mass spectra show the formation of ions corresponding to each protonated molar mass of the product identified via FTIR: m/z 31 for HCHO, m/z 43 for ketene, and m/z 59 for glyoxal. The acetyl ion (CH₃CO⁺), formed through fragmentation of acetyl-containing species, might interfere at m/z 43. Further, glyoxal was shown to produce mainly a fragment ion at m/z 31 (Stöner et al., 2017), which hence interferes with HCHO. Biacetyl, formed as one of the primary carbonyls, was shown to form fragment ions at m/z 59 and 73 (Holm et al., 2013). Therefore, the main fraction of the m/z 59 signal corresponds likely to a fragment ion of biacetyl (elimination of CO) rather than to glyoxal. Similar to the 3P2 + O₃ system, the FTIR residual spectra might indicate also the formation of methanol, although an unequivocal assignment is not possible. Additionally, the formation of a species with m/z 33 is observed, whose temporal evolution behaves as discussed in Sect. 7.3.2.3 and is hence assigned also to CH₃OH.

In contrast to the significant differences observed for the acetaldehyde and biacetyl yield comparative to the previous study of Wang et al. (2015), the HCHO yields are in perfect agreement. On the other hand, Wang et al. (2015) observed a 2–5 times larger glyoxal yield. Although the present yield exhibits a large relative error due to the spectral subtraction, this cannot account for the differences of a factor of 2–5. In the former study, the quantification was done by PTR-MS measurements, where the calibration of glyoxal was achieved by applying the rate constant of the proton transfer reaction (Wang et al., 2015). Based on the description of the experimental methods, the species were identified according to their protonated mass ($[M + H]^+$) and no fragmentation (except for H₂O elimination from glycolaldehyde) was considered. Hence, it seems possible that the biacetyl fragment ion at m/z 59 was erroneously taken as glyoxal.

In the present work, the FTIR spectra strongly indicate also the formation of acetic anhydride. The yield plots exhibit also a significant negative intercept suggesting a delayed formation. However, although this behaviour is observed in all experiments, the calculated yields possess significant scattering, which allows solely to provide an upper limit of 0.10 for the acetic anhydride yield. In the FTIR spectra no clear evidence for acetic acid was found and the peracetic acid absorption features were close to the detection limit. For this reason, the temporal evolution observed for the m/z 61 signal is a supportive indication for

Tab. 7.7. Quantified reaction products and assigned masses of the 3M3P2 + O₃ reaction in the presence of CO as an OH radical scavenger and in the presence of CO and SO₂ together with available literature data. The uncertainties given for the product yields determined within this work represent a combination of the 2 σ statistical error and the accuracy error.

Species	Yield ^a	Yield ^a	Yield ^b	Assigned m/z ^a
Acetaldehyde	0.21 ± 0.04	0.61 ± 0.07	0.80 ± 0.16	45.034
Biacetyl	0.59 ± 0.13	0.39 ± 0.04	0.74 ± 0.13	87.045, 59.050
HCHO	0.15 ± 0.04	0.15 ± 0.02	0.14 ± 0.02	31.018
Acetic acid			0.17 ± 0.02	61.029
Acetic anhydride	< 0.10			61.029
Glyoxal	0.015 ± 0.011	0.05 ± 0.01		31.018
Ketene	0.086 ± 0.023	0.21 ± 0.02		43.018
CH ₄	0.081 ± 0.011		0.062 ± 0.007	
Methanol		0.03 ± 0.005		33.034
Glycolaldehyde		0.07 ± 0.01		
Pyruvic acid		0.01 ± 0.002		
CO ₂ ^c	0.60 ± 0.14		0.50 ± 0.06	
sCl			0.52 ± 0.13	
Detection method	FTIR	PTR-MS	FTIR	PTR-MS
Reference	This work	Wang et al. (2015)	This work	This work

^a Experiments were performed in the presence of CO as an OH radical scavenger, ^b experiments were performed in the presence of CO as and OH radical scavenger and SO₂, ^c sum of CO₂ formed from 3M3P2 + O₃ and CO + OH.

the formation of acetic anhydride. In addition, the yield plot for m/z 61 is similar to that observed for the MVK + O₃ system (Fig. 7.10), which further suggests that acetic anhydride is formed rather from secondary reactions. Wang et al. (2015) observed also the m/z 61 ion as a minor product, which they, however, assigned to either acetic acid or glycolaldehyde. The yield plot of m/z 61 in the present experiments might further indicate a delayed formation and hence a secondary process yielding the species responsible for the ion signal.

In the presence of SO₂ the HCHO yield is essentially the same, while the CH₄ yield decreases minimally. Similar to the 3P2 + O₃ system, the FTIR spectra do not allow to conclude whether ketene is formed due to the non-linear change of the baseline. In the 3M3P2 + O₃ system the same applies also to glyoxal. In addition, acetic acid is observed unambiguously with an average yield of 0.17 ± 0.02 while for the formation of corresponding anhydride no evidence was found.

Although the sum of both primary carbonyls (acetaldehyde and biacetyl) accounts only for 80 ± 14 %, thus lower than expected considering the POZ formation and its subsequent decomposition as the only reaction pathway, there is no indication in both the FTIR spectra and the PTR-MS data for additional routes, for instance the formation of an epoxide. This

is further supported by the quantified reaction products in the presence of SO_2 , which account for about $85 \pm 10\%$ of the 3M3P2 carbon without observing the non-quantified co-products CO and CO_2 . Accordingly, the observed reaction products arise from the further reactions of either acetaldehyde oxide, CH_3CHOO , or biacetyl oxide, $\text{CH}_3\text{C}(\text{O})\text{C}(\text{CH}_3)\text{OO}$, formed in conjunction with the primary carbonyls following both POZ fragmentation routes. The acetaldehyde/biacetyl ratio, observed in the absence of SO_2 , reveals the C₂-CI (CH_3CHOO) to be the predominant CI in the reaction system similar to the $3\text{P}2 + \text{O}_3$ reaction. The formation of HCHO, glyoxal, ketene and methane is in agreement with the fate of both CH_3CHOO isomers as discussed above (Sect. 7.3.2.3). Interestingly, the HCHO and CH_4 yields are almost identical to the $3\text{P}2 + \text{O}_3$ reaction, in which the level of CH_3CHOO formed appears to be very similar based on the dicarbonyl/carbonyl ratio observed for the primary carbonyls in both reaction systems. The slight lowering of the CH_4 yield, when working with SO_2 , suggests a small fraction of thermalized *E*- CH_3CHOO in the reaction system. By contrast, observing the large increase of the acetaldehyde yield, this implies necessarily a large fraction of thermalized *Z*- CH_3CHOO , which might be consistent with the absence of glyoxal in the presence of the sCI scavenger (s. Fig. 7.9). The lower glyoxal yield in the absence of SO_2 comparative to $3\text{P}2 + \text{O}_3$ might indicate a different *E/Z* isomer ratio for the acetaldehyde oxide. However, this is not conclusive since the experiments in the presence of SO_2 show unambiguously the formation of organic acids and hence the products arising from the thermalized *Z*- CH_3CHOO are very likely underestimated in the absence of SO_2 due to bimolecular reactions, in particular with acetic acid.

The carbonyl-substituted CI is formed potentially in two isomers (Fig. 7.14), in which the outer O atom of the Criegee moiety is either oriented towards the CH_3 group (hereafter referred to as *Z*- $\text{CH}_3\text{C}(\text{O})\text{C}(\text{CH}_3)\text{OO}$ with respect to the orientation relative to the CH_3 group) or towards the C=O group (hereafter referred to as *E*- $\text{CH}_3\text{C}(\text{O})\text{C}(\text{CH}_3)\text{OO}$). Since the *E*-configuration exhibits no possibility for an 1,4-H shift isomerization, the further fate of the *E*- $\text{CH}_3\text{C}(\text{O})\text{C}(\text{CH}_3)\text{OO}$ proceeds likely through the initial 1,3-ringclosure according to the dioxirane route. It is proposed that the subsequently formed bis(oxy) biradical will either decompose into $\text{CO}_2 + \text{CH}_3 + \text{CH}_3(\text{O})$, as suggested from theoretical calculations on the ozonolysis of β -pinene and β -caryophyllene for thermally equilibrated dioxirane intermediates (Nguyen et al., 2009a; 2009b), or isomerize further into acetic anhydride (Fig. 7.10). Wang et al. (2015) did already mention a possible decomposition into $\text{CO}_2 + \text{CH}_3 + \text{CH}_3(\text{O})$. However, the authors did neither differentiate between both $\text{CH}_3\text{C}(\text{O})\text{C}(\text{CH}_3)\text{OO}$ isomers nor specify the mechanism.

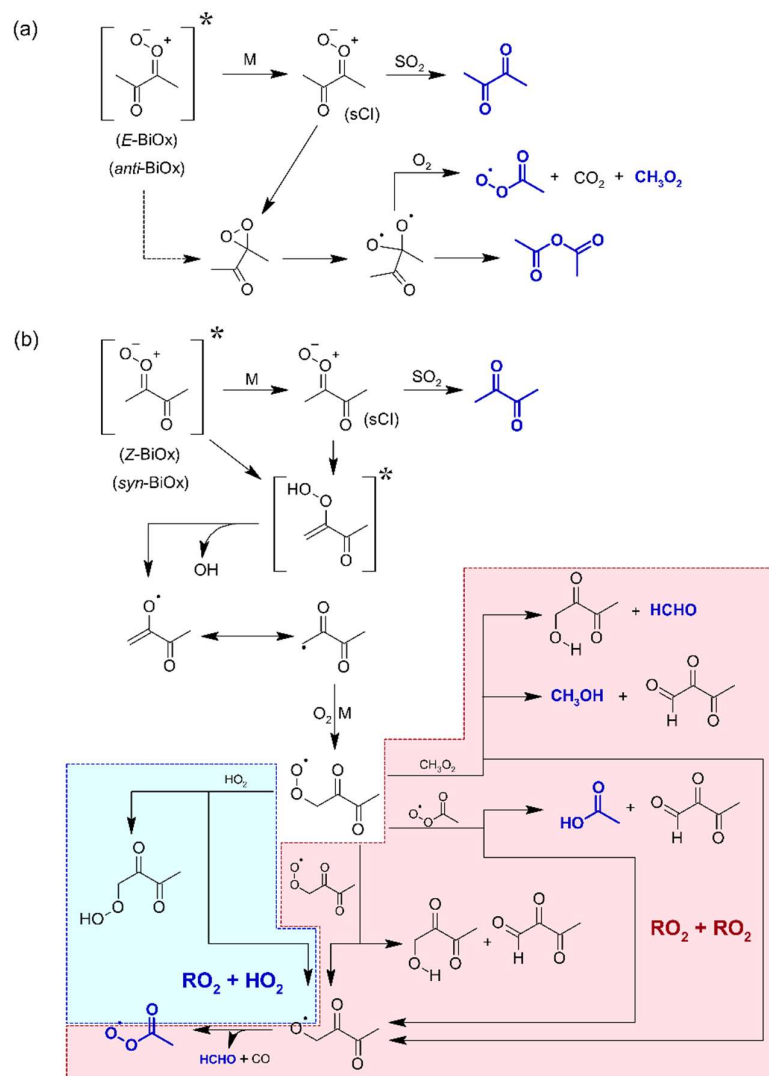


Figure 7.14. Proposed pathways for the further chemistry of both $\text{CH}_3\text{C}(\text{O})\text{C}(\text{CH}_3)\text{OO}$ isomers (= BiOx). Blue structures were clearly identified in the experiments. The existence of the dicarbonyl-containing RO_2 radical is at least supported by the PTR mass spectra, although further investigation is needed to prove unambiguously the results.

The existence of both pathways is difficult to demonstrate since methyl radicals are formed also (and probably predominantly) from the $[\text{CH}_3\text{C}(\text{O})\text{OH}]^*$. In addition, the above discussed results suggest a reaction between the thermalized Z- CH_3CHOO and acetic acid in the absence of a sCI scavenger, which, by analogy to the $\text{HC}(\text{O})\text{OH} + \text{CH}_2\text{OO}$ reaction, might yield a vibrationally excited hydroperoxide ester. This, in turn, will decompose to acetic anhydride, which would hence interfere with the suggested pathway following the

E-CH₃C(O)C(CH₃)OO isomerization route. The intermediate formation of the hydroperoxide ester were in agreement with a delayed anhydride formation or at least an enhanced anhydride formation at longer reaction times. However, the absence of acetic anhydride in the presence of SO₂ is not necessarily a proof for its source from bimolecular reactions (which are effectively suppressed in the presence of a sCl scavenger) either, since the same behaviour were found, if the isomerization via the dioxirane route evolved solely from thermally equilibrated *E*-CH₃C(O)C(CH₃)OO. The existence of a thermalized CH₃C(O)C(CH₃)OO fraction is at least strongly indicated by the increase of the biacetyl yield, when SO₂ is added to the reaction mixture. Consequently, any further statement on the contribution of unimolecular and bimolecular reactions on the acetic anhydride formation would be highly speculative.

Wang et al. (2015) hypothesized also the formation of pyruvic acid following a unimolecular process from the carbonyl-substituted Cl based experimentally on the detection of the *m/z* 89 ion. They further argued that the formation of carboxylic acids has been observed for structurally similar Cls. For instance, the authors cite a study of Grosjean and Grosjean (1999), in which the formation of 2-oxobutanoic acid from [CH₃CH₂C(O)CHOO]* was reported. However, there are three strong arguments against this hypothesis.

First, the isomerization into a (vibrationally excited) carboxylic acid requires a mono-substituted Cl and hence an H atom adjacent the C=O⁺-O⁻ moiety, which is not the case for biacetyl oxide, CH₃C(O)C(CH₃)OO. Therefore the comparison with [CH₃CH₂C(O)CHOO]* is not sound and, accordingly, the pathway drawn by Wang et al. (2015) lacks the carbon balance. Secondly, the authors give the impression that Grosjean and Grosjean (1999) observed experimentally the formation of 2-oxobutanoic acid, which is not the case. Among the investigated species, CH₃CH₂C(O)CHOO arises solely from 4-hexen-3-one, for which Grosjean and Grosjean (1999) identified acetaldehyde, 2-oxobutanal, glyoxal, HCHO and acetic acid as reaction products of the ozonolysis reaction in the presence of cyclohexane used to scavenge OH radicals. Grosjean and Grosjean (1999) assigned acetaldehyde oxide as the source of acetic acid and suggested this pathway to be a general feature of Criegee intermediates possessing an H atom adjacent the C=O⁺-O⁻ moiety, but in particular for carbonyl oxides those substitution pattern does not allow an 1,4-H shift isomerization. According to this, they listed the possible reaction products for the investigated reactions following this pathway. However, it is clearly written that besides 4-oxobutyric acid from the *Z*-4-heptenal ozonolysis (those Criegee intermediates are

structurally different from the 3M3P2 derived carbonyl oxides), there is no experimental proof for the carboxylic acid formation.

Thirdly, Wang et al. (2015) do not provide further information other than the nominal mass (m/z 89). Pyruvic acid would appear at m/z 89.024, which was not observed in the present experiments. Instead, an increase is visible at m/z 89.056, which is close to the m/z 89.049 ion, expected for biacetyl with a relative abundance of $\approx 0.4\%$ due to isotopes. Combining this, it seems more plausible to assume that the biacetyl signal at m/z 89 was erroneously interpreted as pyruvic acid in the former study.

Figure 7.15 depicts a residual spectrum of an experiment, performed in the absence of a sCl scavenger, obtained after the subtraction of all clearly identified species. Although a definitive assignment to one or more species is not possible due to a lack of reference spectra, the characteristic absorption features present allow to limit the possible chemical structures. Although the absorption bands in the range 3040–2870 cm^{-1} (C–H stretching) and centred on 1746 cm^{-1} (C=O stretching) are rather generic for carbonyl-containing VOCs, the most intense absorption band centred on 1122 cm^{-1} is characteristic for C–O stretching vibrations. Due to its position and intensity, it may correspond either to an ether, an anhydride or an alcohol. However, a conventional ether is unlikely formed from the carbonyl-substituted Cl, especially considering the presence of the C=O moiety. Anhydrides exhibit complex carbonyl absorptions, which consist of two, usually differentiable absorption bands owing to the symmetric and asymmetric C=O stretching vibration. Hence, observing the shape of the carbonyl absorption the presence of an additional unidentified anhydride can be ruled out. The intense band at 1122 cm^{-1} belongs thus more likely to either an alcohol or another species besides the common compound classes. For instance, investigations on ozonolysis reactions of alkenes in the presence of aldehydes at atmospheric pressure indicated the formation of secondary ozonides (SOZ), which possess three C–O bonds in one molecule (Niki et al., 1977; Horie et al., 1997; Neeb et al., 1998).

In the 3M3P2 + O₃ system this could potentially result from the reaction of acetaldehyde with the thermalized carbonyl oxides. In experiments with an initial acetaldehyde level of ≈ 2 ppm the biacetyl yield was found to be near to the value obtained in the presence of SO₂, although a larger scattering is observed for different experimental runs. Hence an increase of the biacetyl yield is also found comparative to experiments without any scavenger other than CO. The residual spectra contain mainly the absorption features as presented in panel (a) of Fig 7.15 and besides additional smaller absorption bands. If the spectrum of (a) is subtracted from the residual, obtained from an experiment in the presence of supplementary acetaldehyde, the remaining absorption features, as

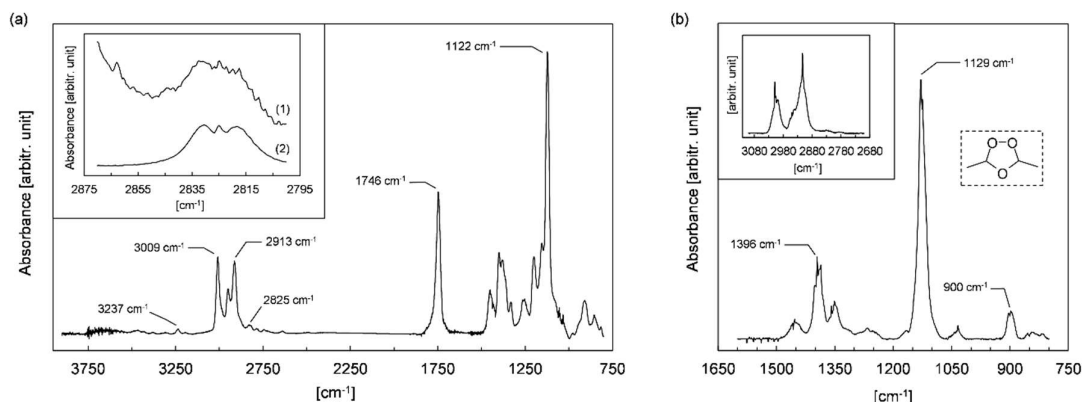
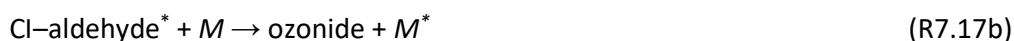


Figure 7.15. (a) Larger panel: Residual spectrum of a 3M3P2 + O₃ experiment performed in the absence of a sCl scavenger, obtained after subtraction of all clearly identified species. The spectrum was cut in the range 2400–1900 cm⁻¹ due to the saturated CO absorption. Upper left panel: (1) scaled residual spectrum in the range 2870–2800 cm⁻¹, and (2) scaled reference spectrum of 2-oxobutanal. (b) Residual spectrum assigned to 2-butene ozonide obtained from an experiment with supplementary addition of CH₃CHO after subtraction with the residual spectrum of (a).

presented in panel (b), are very close to a published spectrum assigned to 2-butene ozonide (Horie et al., 1997). Stone et al. (2014) investigated bimolecular reactions of the simplest Cl, CH₂OO, and employed a simple mechanism in order to describe the pressure dependence of the reaction of CH₂OO with acetaldehyde. This might be generalized as follows:



Hence, the increase of the biacetyl yield suggests that the initial adduct, formed following the reaction of thermalized biacetyl oxide with acetaldehyde, decomposes immediately to give biacetyl. Conversely, the residual spectrum indicates that the adduct from the reaction of acetaldehyde oxide with acetaldehyde is at least partially stabilized to form 2-butene ozonide. When subtracting the 2-butene ozonide spectrum generated as described above (see panel (b) of Fig. 7.15), from the residual spectra of the experiments, where only the OH scavenger was used, the presence of the ozonide cannot be thoroughly excluded. However, the amount present were unambiguously very much lower. All this suggests that the Cl + acetaldehyde reaction is very likely negligible in the present

experiments without an artificial increase of the aldehyde level. This is further supported by the fact, that without supplementary addition of one reaction partner, there is necessarily a competition for the bimolecular reactions with thermalized CIs between all potential reaction partners. Indeed, among the possible reaction partners the reaction with organic acids is expected to be the fastest (Cox et al., 2020). Accordingly, SOZ are not expected to account for the absorption features present in the residual spectrum.

Panel (a) of Fig. 7.15 shows also a small absorption band centred on 3237 cm^{-1} , which may correspond to an O–H stretching vibration. This band were fundamentally shifted towards lower wavenumbers comparative to the free O–H bonds absorption bands, for instance found for methanol and ethanol in the gas-phase. This, in turn, would indicate a strong intramolecular H bonding, which lowers the bond strength and hence the energy needed for vibrational transitions.

Upon scaling of the residual spectrum in the range $2870\text{--}2800\text{ cm}^{-1}$ (upper left panel of (a), Fig. 7.15), it can be seen that a small absorption band centred on 2825 cm^{-1} , although noisy, exhibits considerable similarities to the infrared spectrum of 2-oxobutanal, obtained from the ozonolysis of ethyl vinyl ketone (see Chapter 6). Traces of this absorption band are also indicated in the residual spectra of experiments performed in the presence of SO_2 . Although the intensity is rather low, this suggests the formation an α -oxoaldehyde in the $3\text{M3P2} + \text{O}_3$ reaction. By contrast, the absorption bands in the range $3040\text{--}2870\text{ cm}^{-1}$ and centred on 1746 cm^{-1} and 1122 cm^{-1} are virtually not present in the presence of SO_2 and the absorption band at 3237 cm^{-1} is not found in the residual spectra.

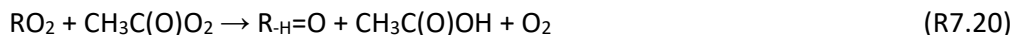
The configuration of the $Z\text{-CH}_3\text{C}(\text{O})\text{C}(\text{CH}_3)\text{OO}$ allows an 1,4-H shift isomerization, which is hence supposed to be the predominant fate of this carbonyl oxide isomer. The subsequently formed vinyloxy-type radical will most probably yield a stabilized RO_2 radical at atmospheric pressure, which undergoes bimolecular reactions with itself or either methyl peroxy, acetyl peroxy or HO_2 radicals. Based on available literature data on RO_2 self- and cross-reactions, one would expect the dicarbonyl- RO_2 to be at least partly converted into the corresponding alkoxy radical for both the self-reaction and the cross-reaction with either methyl peroxy or acetyl peroxy radicals. The structural analogue acetonyloxy radical was shown to undergo exclusively through decomposition (Orlando et al., 2000). Hence, it seems reasonable to assume the same behaviour for the dicarbonyl-containing alkoxy radical, which will ultimately break down into HCHO, CO, and acetyl radicals. An additional pathway of the RO_2 self-reaction might yield a vicinal tricarbonyl species in conjunction with a hydroxydicarbonyl, as shown schematically below (see also Fig. 7.14).



Both species may also be formed from the reaction with methyl peroxy radicals via two different pathways, forming either the tricarbonyl + CH₃OH or the hydroxydicarbonyl + HCHO.



In the case of the acetyl peroxy radical, only a tricarbonyl + acetic acid forming channel (R7.20) may exist besides the alkoxy forming pathway.



The alkoxy radical and the subsequent decomposition products may arise also partially from the reaction of the dicarbonyl-containing RO₂ with HO₂ (R7.21a). An additional channel might yield a multifunctional hydroperoxide (R7.21b).



Hence, besides the alkoxy radical decomposition products like HCHO and CO, the possible RO₂ reactions may yield a hydroxydicarbonyl species and/or a vicinal tricarbonyl.

In the case of the hydroxydicarbonyl species one would intuitively expect a stabilization of the structure due to intramolecular H bonding via a six-membered ring, as suggested from the residual spectrum. The absorption band is shifted for about 300 cm⁻¹ towards lower wavenumbers comparative to the simplest α -hydroxyketone, namely hydroxyacetone, which cannot exhibit a six-membered ring stabilization. For instance, a shift of the same order is observed when comparing the O–H stretching absorption band of acetic acid and peracetic acid, which has been attributed to strong intramolecular H bonding in peracetic acid. This shift is much larger than possible from the differences resulting from the O–H and O–O–H moiety, which was found to shift the O–H stretching absorption band up to about 80 cm⁻¹ towards lower wavenumbers (e. g. methanol vs. methyl hydroperoxide, and ethanol vs. ethyl hydroperoxide). Hence, the position of the absorption band at 3237 cm⁻¹ seems to be consistent with the molecular structure of the

hydroxydicarbonyl species. By contrast, the small absorption band centred on 2825 cm^{-1} seems to support the formation of the vicinal tricarbonyl species, which, in turn, is an α -oxoaldehyde.

The PTR mass spectra show additionally the formation of ions at m/z 73.030, 75.045, and 103.040, which, although noisy, are above the detection limit. The temporal profiles of these ion signals show a continuous increase in the case of m/z 75 and 103 during the ozonolysis reaction, which, by comparison with signals corresponding to the primary carbonyl biacetyl, might indicate a delayed formation or sampling line effects. By contrast, the temporal evolution of m/z 73 surpasses a maximum after a sharp increase in the beginning of the experiment. In the latter case, the behaviour is near to the temporal evolution of methanol (m/z 33), which hence suggests a large wall loss of the species responsible for m/z 73. The signal is possibly related to a fragment ion of the tricarbonyl species, built upon elimination of CO ($[\text{HC}(\text{O})\text{C}(\text{O})\text{CH}_3 + \text{H}]^+$). However, further fragmentation would probably result in $\text{CH}_3\text{C}(\text{O})^+$ ions and hence might contribute to the m/z 43 signal. The signals at m/z 103 and 75 were in agreement with the protonated hydroxydicarbonyl ($[\text{H}_2\text{C}(\text{OH})\text{C}(\text{O})\text{C}(\text{O})\text{CH}_3 + \text{H}]^+$) and the fragment ion after CO elimination ($[\text{H}_2\text{C}(\text{OH})\text{C}(\text{O})\text{CH}_3 + \text{H}]^+$), although further fragmentation would also possibly contribute to the m/z 43 signal. In principle, the m/z 103 ion might also correspond to protonated acetic anhydride, though two observations argue against this possibility. In test experiments, which contained only acetic anhydride in synthetic air, solely the m/z 61 signal was observed. In addition, it does not correlate with the m/z 61 signal, which is dominated by acetic anhydride.

The intensity of the absorption band centred on 3237 cm^{-1} increases linearly with the ketone consumption. A regression analysis yields a linear correlation with an intercept of zero within the uncertainties. If all, the IR-absorption band at 3237 cm^{-1} and the m/z 103 and 75 signals, observed in the PTR mass spectra, belong to the hydroxydicarbonyl, this suggests the temporal profile of the m/z 103 and 75 ion to be influenced by sampling line effects rather than a delayed formation.

Although a characterization of both the hydroxydicarbonyl and the tricarbonyl species is necessary to unambiguously prove their formation in the $3\text{M3P2} + \text{O}_3$ reaction, both the FTIR spectra and the PTR mass spectra support their formation. By contrast, there is no hint towards the formation of a hydroperoxide resulting from the dicarbonyl-containing RO_2 . However, it should be emphasized that only small parts of the FTIR residual spectra (the bands centred on 3237 cm^{-1} and 2825 cm^{-1}) could be assigned to these species. The most intense absorption bands are found to be structurally similar to the residual spectrum of

the 3P2 + O₃ system in the absence of SO₂, in which it is not feasible to observe the multifunctional species mentioned above. Therefore, in the absence of a sCI scavenger additional species seem to be present, which are not explained by the further reactions of the unimolecular loss of the carbonyl oxides.

Considerable amounts of acetic acid were observed solely in the presence of SO₂. As discussed in Chapter 6 and Sect. 7.3.2.2, Hatakeyama et al. (1986) suggested that the CH₂OO + SO₂ reaction leads partly to formic acid. Accordingly, if the CH₃CHOO + SO₂ reaction does not evolve quantitatively into acetaldehyde + SO₃, it might hypothetically account for the observed acetic acid formation. In order to prove this, an experiment was performed on the ozonolysis of propene under the same experimental conditions, since the branching ratio towards the formation of acetaldehyde oxide in the propene ozonolysis (Cox et al., 2020) is similar to 3M3P2. It was found that the CH₄ yield (0.089 ± 0.013) is slightly higher than for 3M3P2, whereas the acetic acid yield is < 0.02. Hence, CH₃CHOO + SO₂ cannot account for the acetic acid yield of 0.17 ± 0.02 found for 3M3P2. Following this, the observation of acetic acid in the presence of SO₂ permits two conclusions. First, the acid evolves unequivocally from excited carbonyl oxides. Secondly, this implies that the acetic acid formed is consumed in the absence of SO₂, which pinpoints its loss via bimolecular reactions with thermalized CIs. This is consistent with the observations found for ethyl vinyl ketone (see Chapter 6), 4M3P2 (see Sect. 7.3.2.1), and 3P2 (see Sect. 7.3.2.3). However, in contrast to the other ketone + O₃ systems, the carbonyl-substituted CI from 3M3P2 cannot isomerize into a vibrationally excited acid. On the other hand, among possible RO₂ reactions, acetic acid evolved solely from cross-reactions with the acetyl peroxy radical, observing the low level of hydroperoxides in the experimental system, which implies a negligible contribution of CH₃C(O)O₂ + HO₂. Taking into account the maximum level of excited biacetyl oxide in the system together with the fact that at least for the CH₃C(O)O₂ + CH₃O₂ the branching ratio towards the formation of acetic acid is fairly low (Tyndall et al., 2001), the (hypothetically) possible RO₂ reactions cannot account for the here determined yield of 0.17 ± 0.02. The only remaining source is the excited acetaldehyde oxide. Although fragmentation products of the vibrationally excited acetic acid were identified, the acetic acid yield observed in the presence of SO₂ suggests a fraction of the vibrationally excited acid is stabilized:



This may be interpreted in terms of a low excitation level that allows a stabilization by collisional energy transfer, as suggested for $[\text{HC}(\text{O})\text{OH}]^*$ formed following the $\text{EVK} + \text{O}_3$ reaction (see Chapter 6). The observation of the acetic acid contrasts with the recent review article by Cox et al. (2020), in which it is stated that the formation of stabilized acids was observed in particular for larger alkene systems. As discussed in Chapter 6, this may be intuitively attributed to a vibrational relaxation in larger molecules. The observation of an acid is thus surprising given the size of the potential parent carbonyl oxide, although this is consistent with previous reports. For instance, Wang et al. (2015) observed the m/z 61 ion in the $3\text{M3P2} + \text{O}_3$ reaction, as mentioned before. Formic acid and acetic acid were also previously found in simulation chamber experiments investigating the ozonolysis of oxygenated species and alkenes (Grosjean et al., 1994; Grosjean and Grosjean, 1999). However, although the acids were assigned to the corresponding carbonyl oxides, none of the above mentioned studies presents a detailed discussion on the mechanistic interpretation. For instance, Grosjean and Grosjean (1999) discussed the excitation of the Cl-derived intermediates solely for the vinyl hydroperoxide, whereas they suggest acetic acid to be formed from the acetaldehyde oxide without excitation. In addition, they do not consider the identified decomposition products of CH_3CHOO reported in advance of their study (e. g. Tuazon et al., 1997). In general, there exist different explanations towards acid formation from ozonolysis reactions, some of them contradictory. For instance, Chebbi and Carlier (1996) summarize that acids may evolve generally from a fraction of mono-substituted Cls after collisional stabilization and subsequent isomerization, whereas Cox et al. (2020) review solely fragmentation pathways of the acid (formic acid, acetic acid), which are formed vibrationally excited, as discussed above. They further state that this pathway is only significant for chemically activated Cls.

The different statements may be partly explained by the fact that previous studies reporting the formation of formic acid and acetic acid were performed under humid conditions. In the experiments of Grosjean et al. (1994) the relative humidity was 3–5 %. Later, Grosjean and Grosjean (1999) worked at a relative humidity of 55 ± 10 %. Wang et al. (2015) do not report explicitly the H_2O level, although the specifications of the zero air gas generator used suggest that the study was also not performed under dry conditions. Under humid conditions the thermalized Cls will react preferentially with H_2O . In the study of Grosjean et al. (1994) this will be the case at least partly. This, in turn, results in the intermediate formation of vibrationally excited hydroperoxides, those further reactions yield partly the corresponding acid, for example, acetic acid from *E*- CH_3CHOO (Cox et al, 2020). Hence, the acids observed in the former investigations cannot be assigned

unequivocally to a collisional stabilization of the excited acid, whereas the present results are not rationalized through the reaction of thermalized E -CH₃CHOO with H₂O.

7.4 Conclusion

The present investigation of the ozonolysis of the four selected α,β -unsaturated ketones exposes three key aspects.

First, all ozonolysis reactions were shown to yield anhydrides in different amounts in the absence of a sCI scavenger. Except for the 4M3P2 + O₃ system, the yield plots of all anhydrides suggest their formation from secondary sources, which is likely rationalized through the decomposition of intermediately formed hydroperoxide esters, following the reaction of thermalized carbonyl oxides with acids. In principle, a formation of the respective anhydrides could be also explained through an isomerization of the carbonyl-substituted CIs. In this respect, it is at least striking, that acetic anhydride (suggested to be formed from a secondary reaction due to the shape of the yield plot) was determined solely in a reaction system (3M3P2 + O₃), where a formation from the CI isomerization were also possible, whereas it is not observed in a system (3P2 + O₃), where only the secondary formation is possible. However, irrespective of the formation pathway, no anhydride formation was observed in the presence of a sCI scavenger, which suggests their formation from thermalized CIs. Since these will react preferentially with H₂O or (H₂O)₂ in the atmosphere, the processes yielding the anhydrides are rather of academic interest than atmospherically relevant. By contrast, the formation of acids (formic acid, acetic acid) arises clearly from the excited carbonyl oxides and can be hence transferred to atmospheric conditions.

A second important finding is that the results of the present chapter confirm the acid formation mechanism proposed following the examination of the EVK + O₃ reaction. The present results show, that for all ketones, where the carbonyl-substituted CI can isomerize into a vibrationally excited acid, one observes the formation of the corresponding acid after elimination of carbon monoxide. Further, considering the observed primary carbonyls ratio (and hence the CI ratio) the formation of the acid and the acetyl peroxy radical seem to be the dominant fragmentation routes of the vibrationally excited oxoacids. An additional decomposition pathway suggested for the excited pyruvic acid yields also formic acid. Although in chamber experiments very small yields of HC(O)OH result likely from wall contaminations, there are two observations supporting the existence of this pathway. On

one hand, in each reaction system the HC(O)OH yield was considerably reproducible, which speaks against an experimental artefact, since the wall conditions change with time. Moreover, HC(O)OH is not observed in the only reaction system, where this pathway is expectedly not existent, namely 3M3P2 + O₃.

A second acid forming mechanism was found for ketones where the *E*-isomer of the non-carbonyl-containing CI can isomerize into a vibrationally excited acid, which is partially stabilized; hence formic acid from CH₂OO and acetic acid from *E*-CH₃CHOO. This was interpreted in terms of a low excitation level of the excited acid after isomerization, which allows at least fractionally a stabilization by collisional energy transfer, which contradicts the statement of a recent review article (Cox et al., 2020). This implies that in the case of 3P2 both mechanism might be active. The observation of the acids as well as the assignment to unimolecular reactions were possible only due to scavenging sCIs with SO₂. This stresses the importance of varying the experimental conditions, in order to figure out mechanistic details. The third aspect regards the yield balance in the studied systems. Among the studied ketones the reaction of MVK exhibits the poorest carbon balance similar to the homologue EVK, as shown earlier in Chapter 6. For instance, when working with the OH scavenger solely, the sum of the primary carbonyls yields only 60 %, which remains unexplained and contradicts the results of previous reports. In contrast to the other ketones, in the ozonolysis of MVK the PTR mass spectra hinted towards an epoxide-forming pathway. However, together with the residual FTIR spectra this cannot account for about 40 % of the MVK consumed. Given the importance of MVK due its formation from the oxidation of isoprene, there is a clear need for a more in-depth investigation on the ozonolysis reaction.

Ozonolysis of α,β -unsaturated ketones: 3-alken-2-ones

8 Summary and outlook

In the present work a series of unsaturated oxygenated compounds were investigated with respect to their reaction with the OH radical and ozone in the gas-phase and the implication of these processes for the atmosphere. Additionally, several compounds needed for the characterization of the experimental systems were synthesized in situ, as they are not available commercially as pure standards. These were: 2-hydroxypropanal, 2-hydroxy-2-methylpropanal, 2-oxobutanal and perpropionic acid.

The results showed that, except for the minor formation of RONO₂ preserving the intact structure of the VOC, in particular suggested for 4-methyl-3-penten-2-one + OH, the OH-initiated oxidation of the investigated α,β -unsaturated ketones (3-penten-2-one, 3-methyl-3-penten-2-one, 4-methyl-3-penten-2-one) resulted solely in fragmentation of the molecule under conditions, where virtually all RO₂ formed react with NO_x. Further, it was shown that a significant fraction resulted directly in the formation of acetyl peroxy radicals, which consequently account for PAN formation at elevated NO₂ levels, for instance encountered within the plumes of biomass burning emissions. Nearly all reaction products form also acetyl peroxy radicals in their further gas-phase oxidations, which implies a huge potential of forming NO_x reservoir species from the overall OH-oxidation mechanism of α,β -unsaturated ketones. In this respect, the present work has shown that the sum parameter PAN + CO₂ gives a more comprehensive picture on the production of acetyl radicals (and consequently acetyl peroxy radicals) in a reaction system than considering the PAN yield alone. Combining the mechanistic information together with the fact that the rate coefficients for the OH reaction are all in the order of 10⁻¹¹–10⁻¹⁰ cm³ molecule⁻¹ s⁻¹, the unsaturated ketones fit well into the characteristics of unidentified VOCs, as defined by Alvarado et al. (2015), crucial to understand the chemistry within biomass burning plumes.

Among the reaction products two α -hydroxyaldehydes were identified, which were synthesized in situ for quantification purposes. Since these rely on the assumption that 100 % of the primary carbonyls are found in the experiments, which later on turned out to be not the case for MVK and EVK, a confirmation of the aldehyde quantification via other methods is advisable. However, at least the agreement of the α -hydroxyaldehyde yields and the yields obtained for the products formed in conjunction with the α -hydroxyaldehydes in the same reaction channel (PAN + CO₂) suggests any systematic error due to the quantification method to be rather small.

The mechanistic investigation of the OH reactions showed that reaction products were not only consumed by secondary processes but also formed from secondary sources. Since in this case common approaches for the correction of product yields can no longer be applied, a simple modelling approach was established, which accounts for both secondary consumption and formation processes by employing a simplified chemical mechanism.

In contrast to MVK + OH, the product distributions observed here for higher substituted α,β -unsaturated ketones did not allow to decipher precisely the branching ratios towards the addition of OH to either the α - or β -carbon of the C=C double bond. However, in order to investigate peroxy radical reactions other than $RO_2 + NO$, the precise knowledge of the ratio in between both RO_2 species initially formed is crucial. Therefore, follow-up work should be dedicated first to experiments that allow a differentiation between the pathways possible yielding the same reaction products.

The determination of rate coefficients of ozonolysis reactions for a series of α,β -unsaturated carbonyls and the consecutive systematic analysis of their reactivity yielded a surprisingly consistent correlation for esters and acids. The effect of a linear increase of the reactivity relative to an alkene core structure with longer n -alkyl chain length at the ester moiety needs further investigations in order to find out the fundamentals accounting for the observations, which intuitively contradict our understanding of inductive effects. The here proposed approach was shown to be able to predict rate coefficients for a series of α,β -unsaturated carbonyls. In particular, a much better predictability was shown for methyl tiglate, whose ozonolysis rate coefficient was determined within this work for the first time, comparative to a recently published SAR model (Jenkin et al., 2020), which failed by about a factor of 10. This might serve as a basis of an alternative SAR approach in future.

On the other hand, the analysis of the kinetic data for α,β -unsaturated ketones suggested their reactivity to be extremely complex. The mechanistic investigation of these ozonolysis reactions showed that the carbon balance was generally closer to unity, when working with SO_2 as a scavenger for sCIs, which suggests unidentified reaction products at least for some of the investigated reaction systems due to bimolecular reactions of sCIs. The carbon balance remained generally lower for less substituted ketones in the absence of a sCI scavenger, in particular for methyl vinyl ketone and ethyl vinyl ketone. In the latter case, it remained unexplained that for both ozonolysis systems the primary carbonyl yield was only about 60 % in the absence of SO_2 . The similarity between both systems suggests a structure-related effect, which was not resolved until now.

Based on the examination of the EVK + O_3 system a mechanism for the formation of organic acids was drawn, which was subsequently confirmed against other α,β -unsaturated

ketones ozonolysis systems. It was shown that the formation of organic acids seems to be a general feature of mono-substituted CIs possessing a carbonyl group in α -position to the $C=O^+-O^-$ moiety. This was attributed to the intermediate formation of a vibrationally excited oxoacid, whose fragmentation yields mainly the corresponding acid after elimination of a carbonyl group or forms an acyl radical. For instance, the acyl radical forming channel is necessary to explain partly the formation of propionyl peroxy radicals from EVK + O_3 and acetyl peroxy radicals from MVK + O_3 . Another molecular fragmentation pathway was shown to account for the formation of formic acid. Further, additional acid formation was observed for the systems, where the non-carbonyl-containing CIs can isomerize also into a vibrationally excited acid (formic acid from CH_2OO , acetic acid from *E*- CH_3CHOO). This was interpreted in terms of a low excitation level after the isomerization allowing the acid to be stabilized, which is surprising for such small fragments. Observing that the ozonolysis reactions account at least partly for the daytime and nighttime loss of α,β -unsaturated ketones, these reactions are a considerable source of organic acids, which was formerly not considered, particularly in the case of MVK.

Summary and outlook

9 Annex

9.1 Supplementary information to Chapter 4

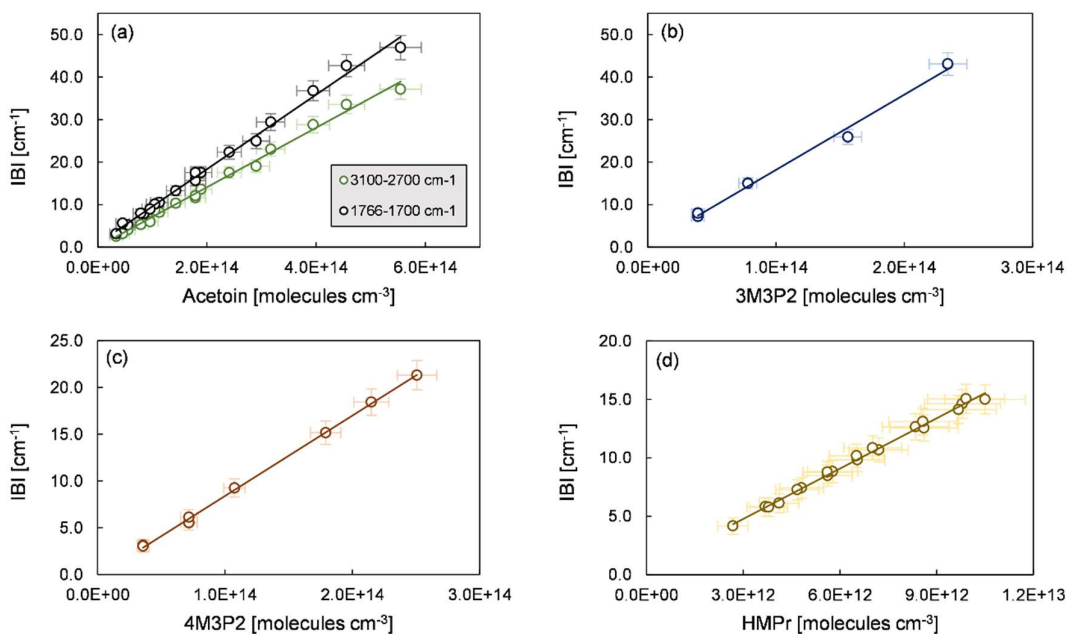


Figure 9.1. Calibration plots for (a) acetoin, (b) 3M3P2, (c) 4M3P2, and (d) HMPr. The calibrations were performed at an optical path length of 50.4 ± 0.2 m for acetoin, 3M3P2, and 4M3P2 and 484.7 ± 0.9 m for HMPr, respectively.

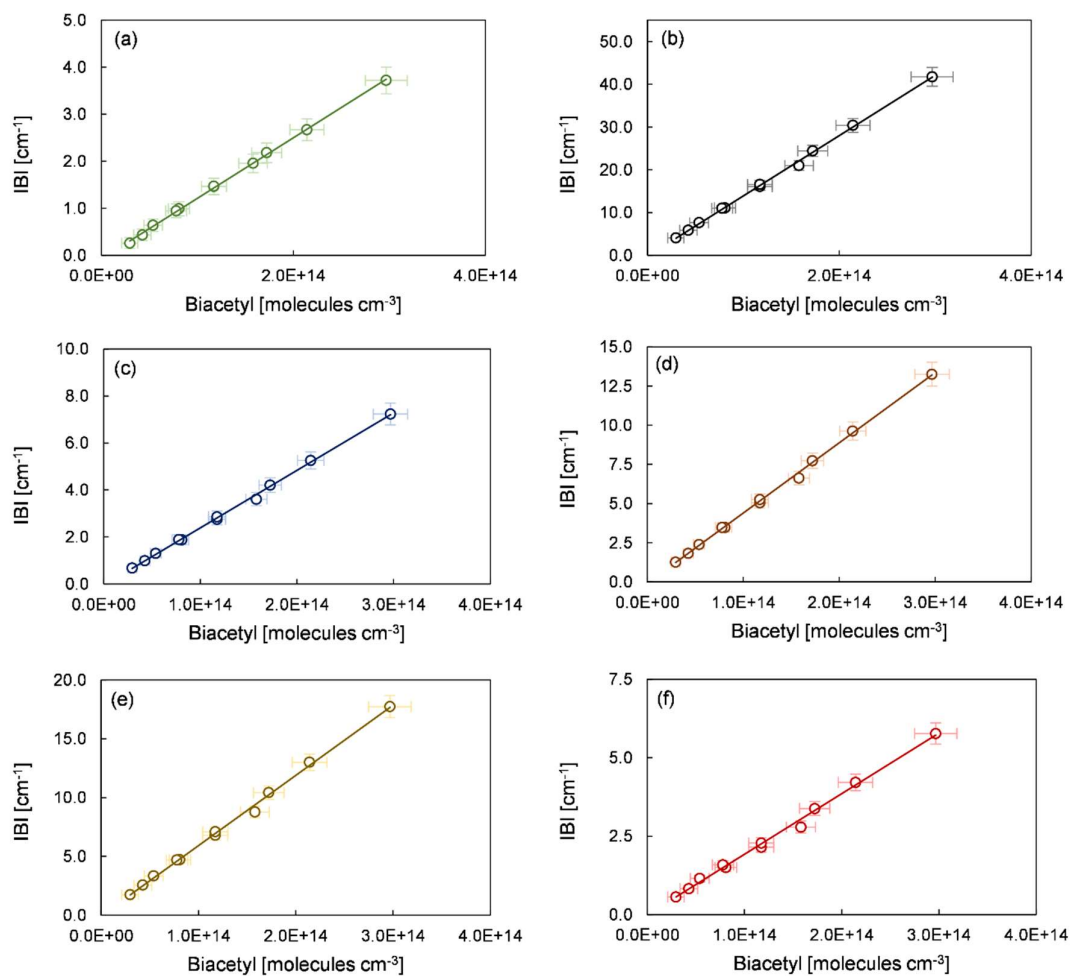


Figure 9.2. Calibration plots for biacetyl for absorption features in the range (a) 3053–2905 cm⁻¹, (b) 1769–1690 cm⁻¹, (c) 1492–1392 cm⁻¹, (d) 1392–1297 cm⁻¹, (e) 1154–1078 cm⁻¹, and (f) 994–870 cm⁻¹. All calibrations were performed at an optical path length of 50.4 ± 0.2 m.

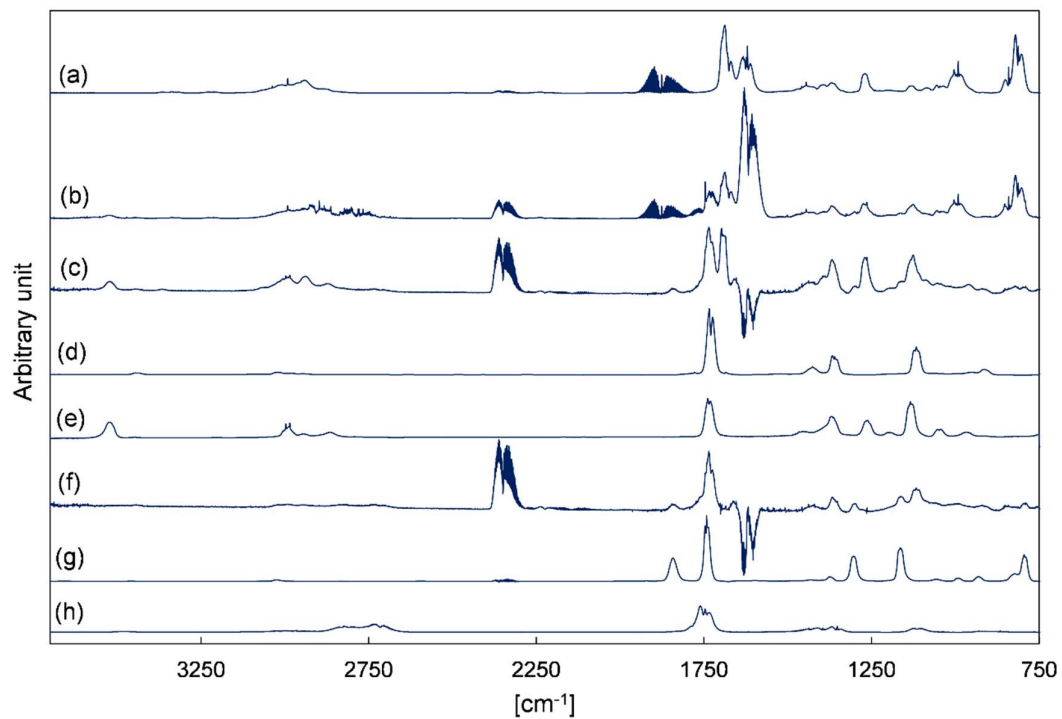


Figure 9.3. Exemplary FTIR spectra of a product study experiment of 3M3P2 + OH: (a) reaction mixture before irradiation, (b) reaction mixture at the end of the irradiation period, (c) residual spectrum after subtraction of methyl nitrite, methyl nitrate, HNO₃, HONO, NO, NO₂ and HCHO from (b), (d) reference spectrum of 2,3-butanedione (biacetyl), (e) reference spectrum of 3-hydroxy-2-butanone (acetoin), (f) residual spectrum after subtraction of 3M3P2 and acetoin from (c), (g) reference spectrum of peroxyacetyl nitrate (PAN), and (h) reference spectrum of acetaldehyde. The spectra are shifted and scaled individually for a better overview.

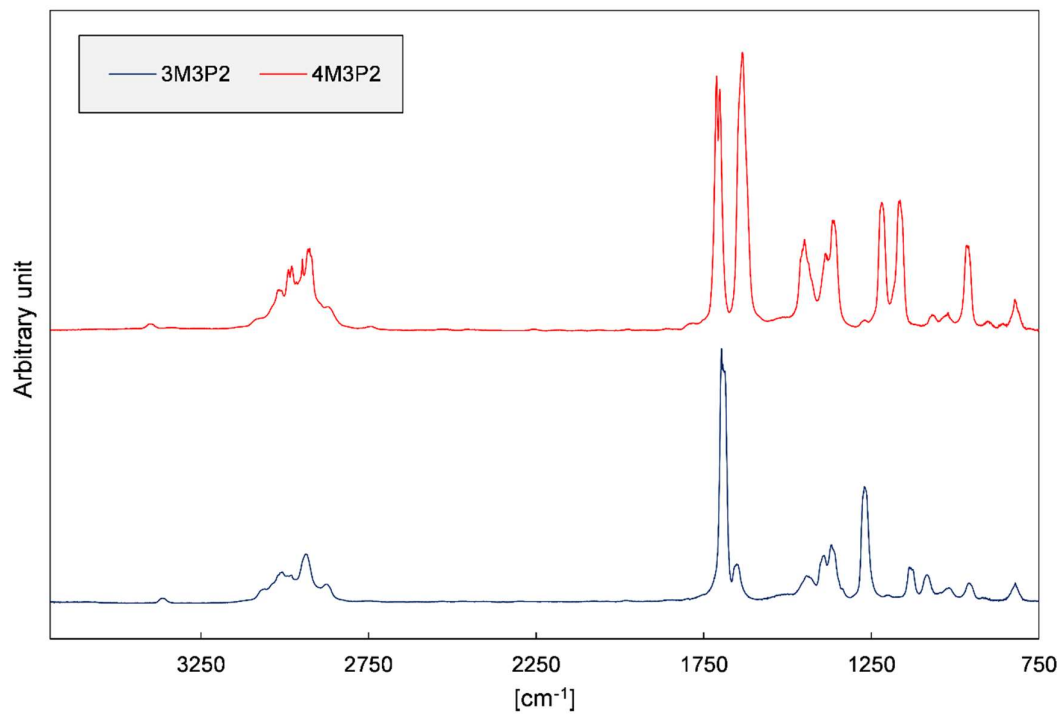


Figure 9.4. FTIR spectra of 3M3P2 and 4M3P2 in the gas-phase.

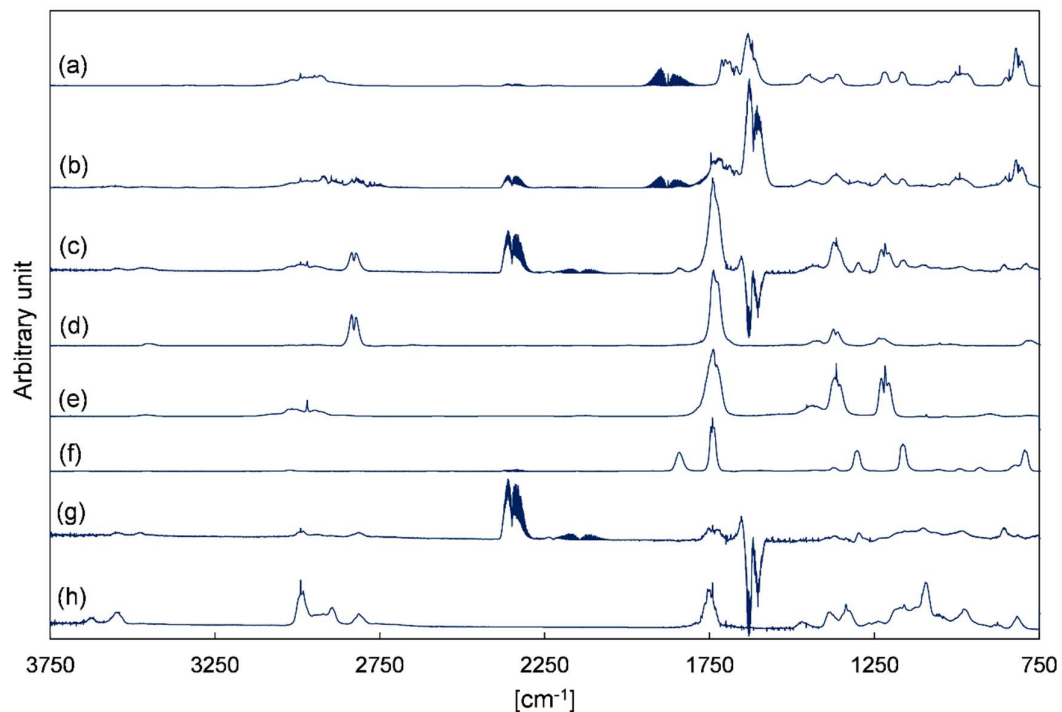


Figure 9.5. Exemplary FTIR spectra of a product study experiment of 4M3P2 + OH: (a) reaction mixture before irradiation, (b) reaction mixture at the end of the irradiation period, (c) residual spectrum after subtraction of 4M3P2, methyl nitrite, methyl nitrate, NO, NO₂ and HCHO from (b), (d) reference spectrum of methyl glyoxal, (e) reference spectrum of acetone, (f) reference spectrum of peroxyacetyl nitrate (PAN), (g) residual spectrum after subtracting methyl glyoxal, acetone and PAN from (c), and (h) reference spectrum of 2-hydroxy-2-methylpropanal generated in situ. The spectra are shifted and scaled individually for a better overview.

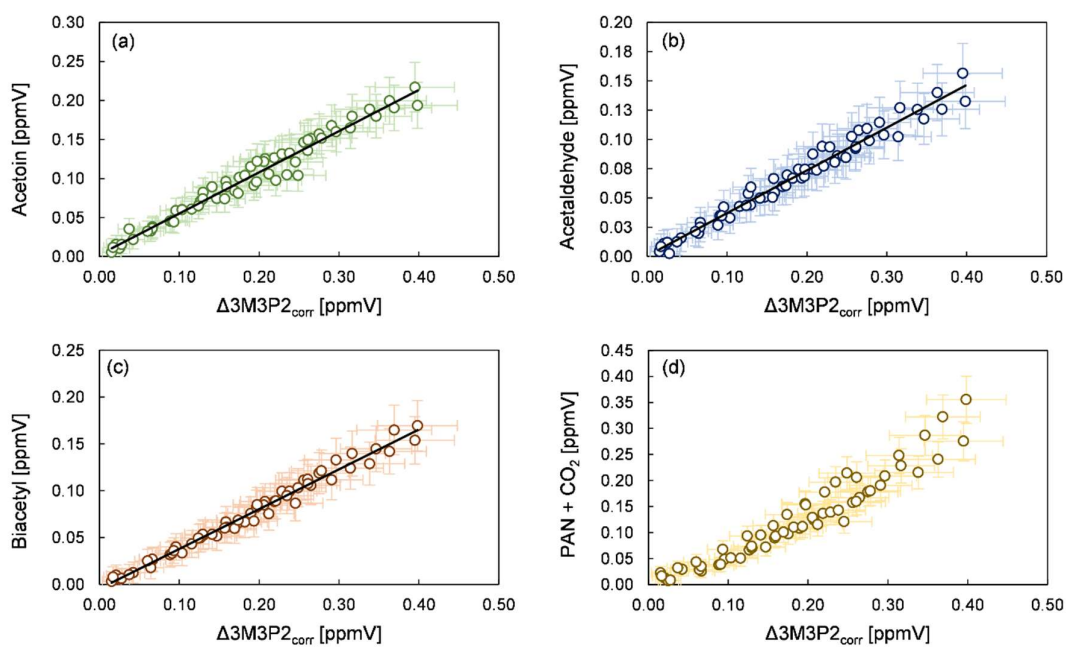


Figure 9.6. Yield plots of (a) acetoin, (b) acetaldehyde, (c) biacetyl, and (d) the sum of PAN and CO₂ in the 3M3P2 + OH reaction where the consumption of 3M3P2 is corrected for the wall loss. Mixing ratios of the 480 L chamber experiments are multiplied by a factor of 0.1 to fit within the scale of the 1080 L chamber experiments.

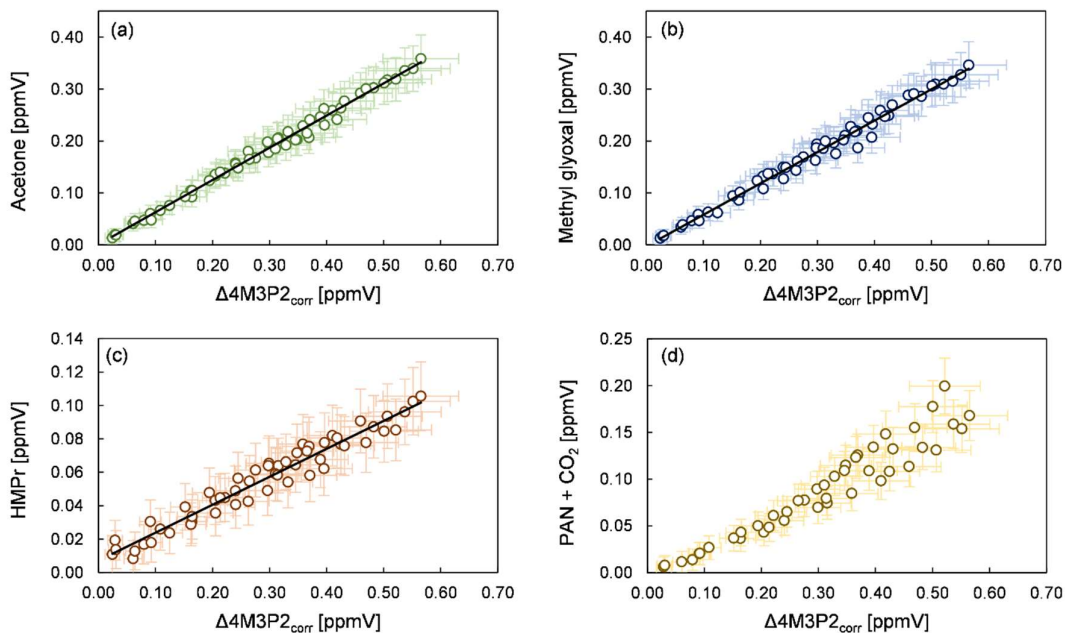


Figure 9.7. Yield plots of (a) acetone, (b) methyl glyoxal, (c) 2-hydroxy-2-methylpropanal (HMPPr), and (d) the sum of PAN and CO₂ in the 4M3P2 + OH reaction where the consumption of 4M3P2 is corrected for the wall loss. Mixing ratios of the 480 L chamber experiments are multiplied by a factor of 0.1 to fit within the scale of the 1080 L chamber experiments.

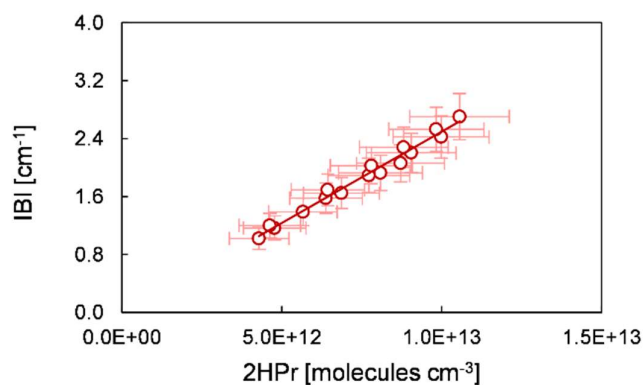
Table 9.1. Parameters used in the model for the correction for secondary reactions in the 3M3P2 + OH reaction system.

Reaction	k	γ	Reference
3M3P2 + wall	$\leq 6 \times 10^{-5} \text{ s}^{-1}$		
$\text{CH}_3\text{C}(\text{OH})\text{C}(\text{O})\text{CH}_3 + \text{OH} \rightarrow \text{CH}_3\text{C}(\text{O})\text{C}(\text{O})\text{CH}_3$	$1.0 \times 10^{-11} \text{ cm}^3 \text{ molecule}^{-1} \text{ s}^{-1}$	0.8	Aschmann et al., (2000)
CH ₃ C(OH)C(O)CH ₃ + wall	$\leq 2.5 \times 10^{-4} \text{ s}^{-1}$		
$\text{CH}_3\text{C}(\text{O})\text{H} + \text{OH} \rightarrow \text{CH}_3\text{C}(\text{O})$	$1.5 \times 10^{-11} \text{ cm}^3 \text{ molecule}^{-1} \text{ s}^{-1}$	0.95	Calvert et al., (2011)
CH ₃ C(O)H + wall	$\leq 3.5 \times 10^{-4} \text{ s}^{-1}$		
$\text{CH}_3\text{C}(\text{O})\text{C}(\text{O})\text{CH}_3 + h\nu \rightarrow \text{CH}_3\text{C}(\text{O})$	$3.6 \times 10^{-2} \times \text{J}(\text{NO}_2)$	2.0	Klotz et al., (2001)
CH ₃ C(O)C(O)CH ₃ + wall	$\leq 7 \times 10^{-5} \text{ s}^{-1}$		

Table 9.2. Parameters used in the model for the correction for secondary reactions in the 4M3P2 + OH reaction system.

Reaction	k	γ	Reference
4M3P2 + wall	$\leq 8 \times 10^{-5} \text{ s}^{-1}$		
$\text{CH}_3\text{C}(\text{O})\text{C}(\text{O})\text{H} + \text{OH} \rightarrow \text{CH}_3\text{C}(\text{O})$	$1.3 \times 10^{-11} \text{ cm}^3 \text{ molecule}^{-1} \text{ s}^{-1}$	1.0	Calvert et al., (2011)
$\text{CH}_3\text{C}(\text{O})\text{C}(\text{O})\text{H} + \text{wall}$	$\leq 1.0 \times 10^{-4} \text{ s}^{-1}$		
$\text{CH}_3\text{C}(\text{O})\text{CH}_3 + \text{OH} \rightarrow \text{CH}_3\text{C}(\text{O})$	$1.8 \times 10^{-13} \text{ cm}^3 \text{ molecule}^{-1} \text{ s}^{-1}$	1.0	Calvert et al., (2011)
$\text{CH}_3\text{C}(\text{O})\text{CH}_3 + \text{wall}$	$\leq 2.0 \times 10^{-4} \text{ s}^{-1}$		
$(\text{CH}_3)_2\text{C}(\text{OH})\text{C}(\text{O})\text{H} + \text{OH} \rightarrow \text{CH}_3\text{C}(\text{O})\text{CH}_3$	$1.5 \times 10^{-11} \text{ cm}^3 \text{ molecule}^{-1} \text{ s}^{-1}$	1.0	Carrasco et al., (2006)

9.2 Supplementary information to Chapter 5

**Figure 9.8** Correlation between the integrated absorption band of 2HPr in the range 3580–3500 cm^{-1} and the concentration of 2HPr. The experiments were carried out at an optical path length $484.7 \pm 0.8 \text{ m}$.

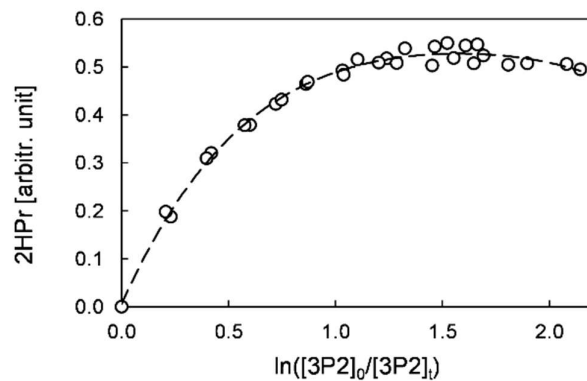


Figure 9.9. Non-linear plot for the formation of 2HPr from the 3P2 + OH reaction according to Baker et al. (2004) used to estimate the rate coefficient of 2HPr + OH.

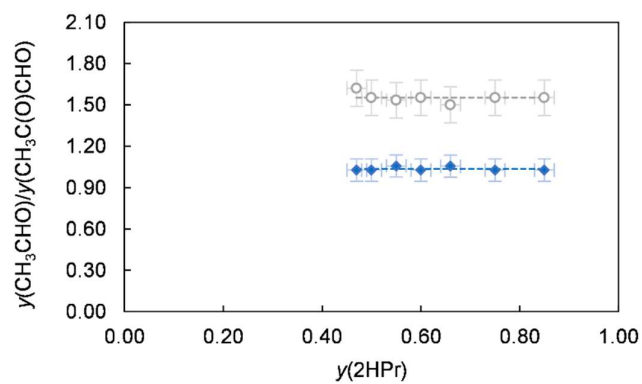


Figure 9.10. Ratio of the obtained yields of acetaldehyde and methyl glyoxal from 3P2 + OH in dependence of the 2HPr yield used in the model for scenario 1 (filled rhomb) and scenario 2 (open circles). The dashed lines represent the corresponding average ratio. The error bars include the precision error of the model.

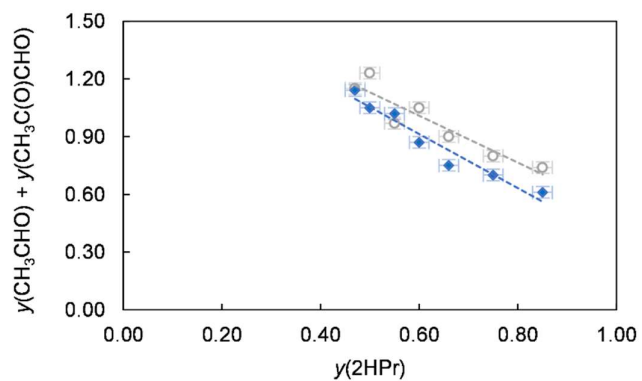


Figure 9.11. Sum of the obtained yields of acetaldehyde and methyl glyoxal from 2HPr + OH in dependence of the 2HPr yield used in the model for scenario 1 (filled rhomb) and scenario 2 (open circles). The error bars include the precision error of the model.

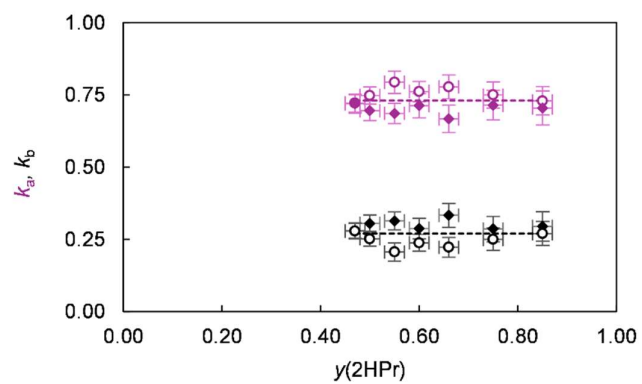


Figure 9.12. Obtained branching ratios k_a and k_b for the formation of acetaldehyde (purple) and methyl glyoxal (black) from 2HPr + OH in dependence of the 2HPr yield used in the model for scenario 1 (filled rhomb) and scenario 2 (open circles). The dashed lines represent the corresponding average branching ratio. The error bars include the precision error of the model.

9.3 Further supplementary material

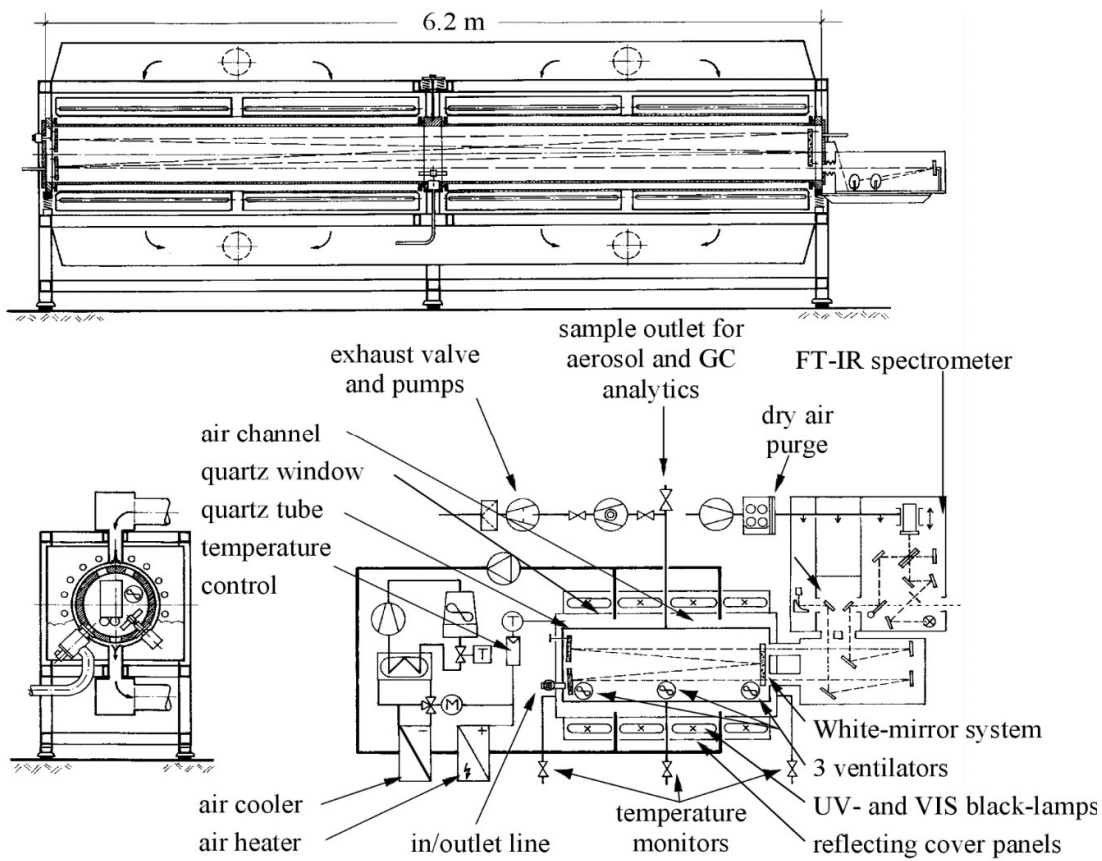


Figure 9.13. Scheme of the 1080 L chamber (QUAREC), adapted from Barnes et al. (1994).

Annex

References

- Allen, G., Remedios, J. J., Newnham, D. A., Smith, K. M., and Monks, P. S.: Improved mid-infrared cross-sections for peroxyacetyl nitrate (PAN) vapour, *Atmos. Chem. Phys.*, **5**, 47–56, <https://doi.org/10.5194/acp-5-47-2005>, 2005.
- Al Mulla, I., Viera, L., Morris, R., Sidebottom, H., Treacy, J., and Mellouki, A.: Kinetics and Mechanisms for the Reactions of Ozone with Unsaturated Oxygenated Compounds, *ChemPhysChem*, **11**, 4069–4078, <https://doi.org/10.1002/cphc.201000404>, 2010.
- Alvarado, M. J., Logan, J. A., Mao, J., Apel, E., Riemer, D., Blake, D., Cohen, R. C., Min, K.-E., Perring, A. E., Browne, E. C., Wooldridge, P. J., Diskin, G. S., Sachse, G. W., Fuelberg, H., Sessions, W. R., Harrigan, D. L., Huey, G., Liao, J., Case-Hanks, A., Jimenez, J. L., Cubison, M. J., Vay, S. A., Weinheimer, A. J., Knapp, D. J., Montzka, D. D., Flocke, F. M., Pollack, I. B., Wennberg, P. O., Kurten, A., Crouse, J., Clair, J. M. St., Wisthaler, A., Mikoviny, T., Yantosca, R. M., Carouge, C. C., and Le Sager, P.: Nitrogen oxides and PAN in plumes from boreal fires during ARCTAS-B and their impact on ozone: an integrated analysis of aircraft and satellite observations, *Atmos. Chem. Phys.*, **10**, 9739–9760, <https://doi.org/10.5194/acp-10-9739-2010>, 2010.
- Alvarado, M. J., Lonsdale, C. R., Yokelson, R. J., Akagi, S. K., Coe, H., Craven, J. S., Fischer, E. V., McMeeking, G. R., Seinfeld, J. H., Soni, T., Taylor, J. W., Weise, D. R., and Wold, C. E.: Investigating the links between ozone and organic aerosol chemistry in a biomass burning plume from a prescribed fire in California chaparral, *Atmos. Chem. Phys.*, **15**, 6667–6688, <https://doi.org/10.5194/acp-15-6667-2015>, 2015.
- Arey, J., Aschmann, S. A., Kwok, E. S. C., and Atkinson, R.: Alkyl Nitrate, Hydroxyalkyl Nitrate, and Hydroxycarbonyl Formation from the NO_x -Air Photooxidations of C_5 – C_8 *n*-Alkanes, *J. Phys. Chem. A*, **105**, 1020–1027, <https://doi.org/10.1021/jp003292z>, 2001.
- Aschmann, S. M., Arey, J., and Atkinson, R.: Atmospheric Chemistry of Selected Hydroxycarbonyls, *J. Phys. Chem. A*, **104**, 3998–4003, <https://doi.org/10.1021/jp9939874>, 2000.
- Atkinson, R.: Kinetics and Mechanisms of the Gas-Phase Reactions of the NO_3 Radical with Organic Compounds, *J. Phys. Chem. Ref. Data.*, **20**, 459–507, <https://doi.org/10.1063/1.555887>, 1991.
- Atkinson, R.: Rate constants for the atmospheric reactions of alkoxy radicals: An updated estimation method, *Atmos. Environ.*, **41**, 8468–8485, <https://doi.org/10.1016/j.atmosenv.2007.07.002>, 2007.
- Atkinson, R., Aschmann, S. M., Winer, A. M., and Pitts, J. N., Jr.: Rate constants for the gas-phase reactions of O_3 with a series of carbonyls at 296 K, *Int. J. Chem. Kinet.*, **13**, 1133–1142, <https://doi.org/10.1002/kin.550131104>, 1981.
- Atkinson, R., Carter, W. P. K., and Winer, A. M.: Effects of Temperature and Pressure on Alkyl Nitrate Yields in the NO_x Photooxidations of *n*-Pentane and *n*-Hexane, *J. Phys. Chem.*, **87**, 2012–2018, <https://doi.org/10.1021/j100234a034>, 1983.

References

- Atkinson, R., Arey, J., Aschmann, S. M., Corchnoy, S. B., and Shu, Y.: Rate constants for the gas-phase reactions of *cis*-3-Hexen-1-ol, *cis*-3-Hexenylacetate, *trans*-2-Hexenal, and Linalool with OH and NO₃ radicals and O₃ at 296 ± 2 K, and OH radical formation yields from the O₃ reactions, *Int. J. Chem. Kinet.*, 27, 941–955, <https://doi.org/10.1002/kin.550271002>, 1995.
- Atkinson, R., Baulch, D. L., Cox, R. A., Crowley, J. N., Hampson, R. F., Hynes, R. G., Jenkin, M. E., Rossi, M. J., Troe, J., and IUPAC Subcommittee: Evaluated kinetic and photochemical data for atmospheric chemistry: Volume II – gas phase reactions of organic species, *Atmos. Chem. Phys.*, 6, 3625–4055, <https://doi.org/10.5194/acp-6-3625-2006>, 2006.
- Avzianova, E. V., and Ariya, P. A.: Temperature-dependent kinetic study for ozonolysis of selected tropospheric alkenes, *Int. J. Chem. Kinet.*, 34, 678–684, <https://doi.org/10.1002/kin.10093>, 2002.
- Bacher, C., Tyndall, G. S., and Orlando, J. J.: The Atmospheric Chemistry of Glycolaldehyde, *J. Atmos. Chem.*, 39, 171–189, <https://doi.org/10.1023/A:1010689706869>, 2001.
- Baker, J., Arey, J., and Atkinson, R.: Rate Constants for the Gas-Phase Reactions of OH Radicals with a Series of Hydroxyaldehydes at 296 ± 2 K, *J. Phys. Chem. A*, 108, 7032–7037, <https://doi.org/10.1021/jp048979o>, 2004.
- Barnes, I., Becker, K. H., Fink, E. H., Reimer, A., Zabel, F., and Niki, H.: FTIR spectroscopic study of the gas-phase reaction of HO₂ with H₂CO, *Chem. Phys. Lett.*, 115, 1–8, [https://doi.org/10.1016/0009-2614\(85\)80091-9](https://doi.org/10.1016/0009-2614(85)80091-9), 1985.
- Barnes, I., Becker, K. H., and Zhu, T.: Near UV Absorption Spectra and Photolysis Products of Difunctional Organic Nitrates: Possible Importance as NO_x Reservoirs, *J. Atmos. Chem.*, 17, 353–373, <https://doi.org/10.1007/BF00696854>, 1993.
- Barnes, I., Becker, K.H., and Mihalopoulos, N.: An FTIR Product Study of the Photooxidation of Dimethyl Disulfide, *J. Atmos. Chem.*, 18, 267–289, <https://doi.org/10.1007/BF00696783>, 1994.
- Bauer, W., Jr.: Methacrylic Acid and Derivatives, in: Ullmann's Encyclopedia of Industrial Chemistry, (Ed.), https://doi.org/10.1002/14356007.a16_441.pub2, 2011.
- Berasategui, M., Amedro, D., Vereecken, L., Lelieveld, J., and Crowley, J. N.: Reaction between CH₃C(O)OOH (peracetic acid) and OH in the gas phase: a combined experimental and theoretical study of the kinetics and mechanism, *Atmos. Chem. Phys.*, 20, 13541–13555, <https://doi.org/10.5194/acp-20-13541-2020>, 2020.
- Bernard, F., Eyslunent, G., Daële, V., and Mellouki, A.: Kinetics and Products of Gas-Phase Reactions of Ozone with Methyl Methacrylate, Methyl Acrylate, and Ethyl Acrylate, *J. Phys. Chem. A*, 114, 8376–8383, <https://doi.org/10.1021/jp104451v>, 2010.
- Bianchi, F., Kurtén, T., Riva, M., Mohr, C., Rissanen, M. P., Roldin, P., Berndt, T., Crouse, J. D., Wennberg, P. O., Mentel, T. F., Wildt, J., Junninen, H., Jokinen, T., Kulmala, M., Worsnop, D. R., Thornton, J. A., Donahue, N., Kjaergaard, H. G., and Ehn, M.: Highly Oxygenated Organic Molecules (HOM) from Gas-Phase Autoxidation Involving Peroxy Radicals: A Key Contributor to Atmospheric Aerosol, *Chem. Rev.*, 119, 3472–3509, <https://doi.org/10.1021/acs.chemrev.8b00395>, 2019.

- Bickers, D. R., Calow, P., Greim, H. A., Hanifin, J. M., Rogers, A. E., Saurat, J.-H., Sipes, I. G., Smith, R. L., and Tagami, H.: The safety assessment of fragrance materials, *Regul. Toxicol. Pharmacol.*, **37**, 218–273, [https://doi.org/10.1016/S0273-2300\(03\)00003-5](https://doi.org/10.1016/S0273-2300(03)00003-5), 2003.
- Blanco, M. B., Barnes, I., and Wiesen, P.: Kinetic Investigation of the OH Radical and Cl Atom Initiated Degradation of Unsaturated Ketones at Atmospheric Pressure and 298 K, *J. Phys. Chem. A*, **116**, 6033–6040, <https://doi.org/10.1021/jp2109972>, 2012.
- Bloss, W. J., Evans, M. J., Lee, J. D., Sommariva, R., Heard, D. E., and Piling, M. J.: The oxidative capacity of the troposphere: Coupling of field measurements of OH and a global chemistry transport model, *Faraday Discuss.*, **130**, 425–436, <https://doi.org/10.1039/B419090D>, 2005.
- Bridier, I., Veyret, B., and Lesclaux, R.: Flash Photolysis Study of the UV Spectrum and Kinetics of Reactions of the Acetonylperoxy Radical, *J. Chem. Soc. Faraday Trans.*, **89**, 2993–2997, <https://doi.org/10.1039/FT9938902993>, 1993.
- Calvert, J. G., Atkinson, R., Kerr, J. A., Madronich, S., Moortgat, G. K., Wallington, T. J., and Yarwood, G.: The mechanisms of atmospheric oxidation of the alkenes, Oxford University Press, New York, 2000.
- Calvert, J. G., Mellouki, A., Orlando, J. J., Pilling, M. J., and Wallington, T. J.: The mechanisms of atmospheric oxidation of the oxygenates, Oxford University Press, New York, 2011.
- Calvert, J. G., Orlando, J. J., Stockwell, W. R., and Wallington, T. J.: The Mechanisms of Reactions Influencing Atmospheric Ozone, Oxford University Press, New York, 2015.
- Canosa-Mas, C. E., Flugge, M. L., King, M. D., and Wayne, R. P.: An experimental study of the gas-phase reaction of the NO₃ radical with α,β -unsaturated carbonyl compounds, *Phys. Chem. Chem. Phys.*, **7**, 643–650, <https://doi.org/10.1039/B416574H>, 2005.
- Carrasco, N., Doussin, J.-F., Picquet-Varrault, B., and Carlier, P.: Tropospheric degradation of 2-hydroxy-2-methylpropanal, a photo-oxidation product of 2-methyl-3-buten-2-ol: Kinetic and mechanistic study of its photolysis and its reaction with OH radicals, *Atmos. Environ.*, **40**, 2011–2019, <https://doi.org/10.1016/j.atmosenv.2005.11.042>, 2006.
- Carrasco, N., Doussin, J. F., O'Connor, M., Wenger, J. C., Picquet-Varrault, B., Durand-Jolibois, R., and Carlier, P.: Simulation Chamber Studies of the Atmospheric Oxidation of 2-Methyl-3-buten-2-ol: Reaction with Hydroxyl Radicals and Ozone Under a Variety of Conditions, *J. Atmos. Chem.*, **56**, 33–55, <https://doi.org/10.1007/s10874-006-9041-y>, 2007.
- Carter, W. L. P., and Atkinson, R.: Alkyl Nitrate Formation from the Atmospheric Photooxidation of Alkanes; a Revised Estimation Method, *J. Atmos. Chem.*, **8**, 165–173, <https://doi.org/10.1007/BF00053721>, 1989.
- Chapuis, C., and Jacoby, D.: Catalysis in the preparation of fragrances and flavours, *Appl. Catal.*, **A**, **221**, 93–117, [https://doi.org/10.1016/S0926-860X\(01\)00798-0](https://doi.org/10.1016/S0926-860X(01)00798-0), 2001.
- Chebbi, A., and Carlier, P.: Carboxylic acids in the troposphere, occurrence, sources, and sinks: a review, *Atmos. Environ.*, **30**, 4233–4249, 1996.

References

- Chhantyal-Pun, R., Rotavera, B., McGillen, M. R., Khan, M. A. H., Eskola, A. J., Caravan, R. L., Blacker, L., Tew, D. P., Osborn, D. L., Percival, C. J., Taatjes, C. A., Shallcross, D. E., and Orr-Ewing, A. J.: Criegee Intermediate Reactions with Carboxylic Acids: A Potential Source of Secondary Organic Aerosol in the Atmosphere, *ACS Earth Space Chem.*, **2**, 833–842, <https://doi.org/10.1021/acsearthspacechem.8b00069>, 2018.
- Ciccioli, P., Brancaleoni, E., Frattoni, M., Cecinato, A., and Pinciarelli, L.: Determinations of volatile organic compounds (VOC) emitted from biomass burning of mediterranean vegetation species by GC-MS, *Anal. Lett.*, **34**, 937–955, <https://doi.org/10.1081/AL-100103604>, 2001.
- Colomer, J. P., Blanco, M. B., Peñeñory, A. B., Barnes, I., Wiesen, P., and Teruel, M. A.: FTIR gas-phase kinetic study on the reactions of OH radicals and Cl atoms with unsaturated esters: Methyl-3,3-dimethyl acrylate, (*E*)-ethyl tiglate and methyl-3-butenoate, *Atmos. Environ.*, **79**, 546–552, <https://doi.org/10.1016/j.atmosenv.2013.07.009>, 2013.
- Cox, R. A., and Penkett, S. A.: Oxidation of atmospheric SO₂ by products of the ozone–olefin reaction, *Nature*, **230**, 321–322, <https://doi.org/10.1038/230321a0>, 1971.
- Cox, R. A., Ammann, M., Crowley, J. N., Herrmann, H., Jenkin, M. E., McNeill, V. F., Mellouki, A., Troe, J., and Wallington, T. J.: Evaluated kinetic and photochemical data for atmospheric chemistry: Volume VII – Criegee intermediates, *Atmos. Chem. Phys.*, **20**, 13497–13519, <https://doi.org/10.5194/acp-20-13497-2020>, 2020.
- Crawford, M. A., Wallington, T. J., Szente, J. J., Maricq, M. M., and Francisco, J. S: Kinetics and Mechanism of the Acetylperoxy + HO₂ Reaction, *J. Phys. Chem. A*, **103**, 365–378, <https://doi.org/10.1021/jp983150t>, 1999.
- Criegee, R.: Mechanismus der Ozonolyse, *Angew. Chem.*, **87**, 765–771, <https://doi.org/10.1002/ange.19750872104>, 1975a.
- Criegee, R.: Mechanism of Ozonolysis, *Angew. Chem.*, **14**, 745–752, <https://doi.org/10.1002/anie.197507451>, 1975b.
- Crouse, J. D., Paulot, F., Kjaergaard, H. G., and Wennberg, P. O.: Peroxy radical isomerization in the oxidation of isoprene, *Phys. Chem. Chem. Phys.*, **13**, 13607–13613, <https://doi.org/10.1039/C1CP21330J>, 2011.
- Crouse, J. D., Nielsen, L. B., Jørgensen, S., Kjaergaard, H. G., and Wennberg, P. O.: Autoxidation of Organic Compounds in the Atmosphere, *J. Phys. Chem. Lett.*, **4**, 3513–3520, <https://doi.org/10.1021/jz4019207>, 2013.
- Dillon, T. J. and Crowley, J. N.: Direct detection of OH formation in the reactions of HO₂ with CH₃C(O)O₂ and other substituted peroxy radicals, *Atmos. Chem. Phys.*, **8**, 4877–4889, <https://doi.org/10.5194/acp-8-4877-2008>, 2008.
- Dunlea, E. J., Herndon, S. C., Nelson, D. D., Volkamer, R. M., Lamb, B. K., Allwine, E. J., Grutter, M., Ramos Villegas, C. R., Marquez, C., Blanco, S., Cardenas, B., Kolb, C. E., Molina, L. T., and Molina, M. J.: Technical note: Evaluation of standard ultraviolet absorption ozone monitors in a polluted urban environment, *Atmos. Chem. Phys.*, **6**, 3163–3180, <https://doi.org/10.5194/acp-6-3163-2006>, 2006.

- Ehn, M., Kleist, E., Junninen, H., Petäjä, T., Lönn, G., Schobesberger, S., Dal Maso, M., Trimborn, A., Kulmala, M., Worsnop, D. R., Wahner, A., Wildt, J., and Mentel, Th. F.: Gas phase formation of extremely oxidized pinene reaction products in chamber and ambient air, *Atmos. Chem. Phys.*, 12, 5113–5127, <https://doi.org/10.5194/acp-12-5113-2012>, 2012.
- Ehrenson, S., Brownlee, R. T. C., and Taft, R. W.: A Generalized Treatment of Substituent Effects in the Benzene Series. A Statistical Analysis by the Dual Substituent Parameter Equation (1), in: *Progress in Physical Organic Chemistry*, 10, 1–80, <https://doi.org/10.1002/9780470171899.ch1>, 1973.
- Elrod, M. J., Ranschaert, D. L., Schneider, N. J.: Direct Kinetics Study of the Temperature Dependence of the CH₂O Branching Channel for the CH₃O₂ + HO₂ Reaction, *Int. J. Chem. Kinet.*, 33, 363–376, <https://doi.org/10.1002/kin.1030>, 2001.
- Emrich, M., and Warneck, P.: Branching Ratio for the Self-Reaction of Acetonyl Peroxy Radicals, *Z. Naturforsch.*, 58a, 429–433, <https://doi.org/10.1515/zna-2003-7-807>, 2003.
- Etzkorn, T., Klotz, B., Sørensen, S., Patroescu, I. V., Barnes, I., Becker, K. H., and Platt, U.: Gas-phase absorption cross sections of 24 monocyclic hydrocarbons in the UV and IR spectral ranges, *Atmos. Environ.*, 33, 525–540, [https://doi.org/10.1016/S1352-2310\(98\)00289-1](https://doi.org/10.1016/S1352-2310(98)00289-1), 1999.
- Exner, O.: The inductive effect: theory and quantitative assessment, *J. Phys. Org. Chem.*, 12, 265–274, [https://doi.org/10.1002/\(SICI\)1099-1395\(199904\)12:4<265::AID-POC124>3.0.CO;2-O](https://doi.org/10.1002/(SICI)1099-1395(199904)12:4<265::AID-POC124>3.0.CO;2-O), 1999.
- Ezell, M. J., Wang, W., Ezell, A. A., Soskin, G., and Finlayson-Pitts, B. J.: Kinetics of reactions of chlorine atoms with a series of alkenes at 1 atm and 298 K: structure and reactivity, *Phys. Chem. Chem. Phys.*, 4, 5813–5820, <https://doi.org/10.1039/B207529F>, 2002.
- Fall, R., Karl, T., Jordan, A., and Lindinger, W.: Biogenic C5 VOCs: release from leaves after freeze-thaw wounding and occurrence in air at high mountain observatory, *Atmos. Environ.* 35, 3905–3916, [https://doi.org/10.1016/S1352-2310\(01\)00141-8](https://doi.org/10.1016/S1352-2310(01)00141-8), 2001.
- Fiedrich, M., Kurtenbach, R., Wiesen, P., and Kleffmann, J.: Artificial O₃ formation during fireworks, *Atmos. Environ.*, 165, 57–61, <https://doi.org/10.1016/j.atmosenv.2017.06.028>, 2017.
- Fischer, E. V., Jacob, D. J., Yantosca, R. M., Sulprizio, M. P., Millet, D. B., Mao, J., Paulot, F., Singh, H. B., Roiger, A., Ries, L., Talbot, R. W., Dzepina, K., and Pandey Deolal, S.: Atmospheric peroxyacetyl nitrate (PAN): a global budget and source attribution, *Atmos. Chem. Phys.*, 14, 2679–2698, <https://doi.org/10.5194/acp-14-2679-2014>, 2014.
- Frost, M. J., and Smith, I. W. M.: Rate Constants for the Reactions of CH₃O and C₂H₅O with NO₂ over a Range of Temperature and Total Pressure, *J. Chem. Soc. Faraday Trans.*, 86, 1751–1756, <https://doi.org/10.1039/FT9908601751>, 1990.
- Fu, T.-M., Jacob, D. J., Wittrock, F., Burrows, J. P., Vrekoussis, M. and Henze, D. K.: Global budgets of atmospheric glyoxal and methylglyoxal, and implications for formation of secondary organic aerosols, *J. Geophys. Res. Atmos.*, 113, 1–17, <https://doi.org/10.1029/2007JD009505>, 2008.

References

- Fuchs, H., Albrecht, S., Acir, I.-H., Bohn, B., Breitenlechner, M., Dorn, H.-P., Gkatzelis, G. I., Hofzumahaus, A., Holland, F., Kaminski, M., Keutsch, F. N., Novelli, A., Reimer, D., Rohrer, F., Tillmann, R., Vereecken, L., Wegener, R., Zaytsev, A., Kiendler-Scharr, A., and Wahner, A.: Investigation of the oxidation of methyl vinyl ketone (MVK) by OH radicals in the atmospheric simulation chamber SAPHIR, *Atmos. Chem. Phys.*, **18**, 8001–8016, <https://doi.org/10.5194/acp-18-8001-2018>, 2018.
- Gai, Y., Ge, M., and Wang, W.: Rate constants for the gas phase reaction of ozone with *n*-butyl acrylate and ethyl methacrylate, *Chem. Phys. Lett.*, **473**, 57–60, <https://doi.org/10.1016/j.cplett.2009.03.070>, 2009.
- Gallego-Iniesta, M. P., Cabañas, B., Salgado, S., Martínez, E., and Martín, P.: Estimation of gas-phase rate coefficients for the reactions of a series of α,β -unsaturated esters with OH, NO₃, O₃ and Cl, *Atmos. Environ.*, **90**, 133–145, <https://doi.org/10.1016/j.atmosenv.2014.03.036>, 2014.
- Galloway, M. M., Huisman, A. J., Yee, L. D., Chan, A. W. H., Loza, C. L., Seinfeld, J. H., and Keutsch, F. N.: Yields of oxidized volatile organic compounds during the OH radical initiated oxidation of isoprene, methyl vinyl ketone, and methacrolein under high-NO_x conditions, *Atmos. Chem. Phys.*, **11**, 10779–10790, <https://doi.org/10.5194/acp-11-10779-2011>, 2011.
- Gaona Colmán, E., Blanco, M. B., Barnes, I., and Teruel, M. A.: Gas phase kinetics for the ozonolysis of *n*-butyl methacrylate, ethyl crotonate and vinyl propionate under atmospheric conditions, *Chem. Phys. Lett.*, **579**, 11–15, <https://doi.org/10.1016/j.cplett.2013.05.049>, 2013.
- Gaona Colmán, E., Blanco, M. B., Barnes, I., and Teruel, M. A.: Kinetics of the gas-phase reaction between ozone and three unsaturated oxygenated compounds: Ethyl 3,3-dimethyl acrylate, 2-methyl-2-pentenal and 6-methyl-5-hepten-2-one at atmospheric pressure, *Atmos. Environ.*, **109**, 272–278, <https://doi.org/10.1016/j.atmosenv.2015.03.011>, 2015a.
- Gaona Colmán, E., Blanco, M. B., Barnes, I., and Teruel, M. A.: Ozonolysis of a series of C7–C9 unsaturated biogenic aldehydes: reactivity study at atmospheric pressure, *RSC Adv.*, **5**, 30500–30506, <https://doi.org/10.1039/C4RA17283C>, 2015b.
- Gaona-Colmán, E., Blanco, M. B., and Teruel, M. A.: Kinetics and product identification of the reactions of (*E*)-2-hexenyl acetate and 4-methyl-3-penten-2-one with OH radicals and Cl atoms at 298 K and atmospheric pressure, *Atmos. Environ.*, **161**, 155–166, <https://doi.org/10.1016/j.atmosenv.2017.04.033>, 2017.
- Giguère, P. A., and Weingartshofer Olmas, A.: A spectroscopic study of hydrogen bonding in performic and peracetic acids, *Can. J. Chem.*, **30**, 821–830, <https://doi.org/10.1139/v52-099>, 1952.
- Gratien, A., Nilsson, E., Doussin, J.-F., Johnson, M. S., Nielsen, C. J., Stenstrøm, Y., and Picquet-Varrault, B.: UV and IR Absorption Cross-sections of HCHO, HCDO, and DCDO, *J. Phys. Chem. A*, **111**, 11506–11513, <https://doi.org/10.1021/jp074288r>, 2007.

- Green, M., Yarwood, G., and Niki, H.: FTIR Study of the Cl-Atom Initiated Oxidation of Methylglyoxal, *Int. J. Chem. Kinet.*, 22, 689–699, <https://doi.org/10.1002/kin.550220705>, 1990.
- Greene, C. R.; and Atkinson, R.: Rate constants for the gas-phase reactions of O₃ with a series of cycloalkenes and α,β -unsaturated ketones at 296 ± 2 K, *Int. J. Chem. Kinet.*, 26, 37–44, <https://doi.org/10.1002/kin.550260106>, 1994.
- Grosjean, E., and Grosjean, D.: Rate constants for the gas-phase reaction of ozone with unsaturated oxygenates, *Int. J. Chem. Kinet.*, 30, 21–29, [https://doi.org/10.1002/\(SICI\)1097-4601\(1998\)30:1<21::AID-KIN3>3.0.CO;2-W](https://doi.org/10.1002/(SICI)1097-4601(1998)30:1<21::AID-KIN3>3.0.CO;2-W), 1998.
- Grosjean, E., and Grosjean, D.: The Reaction of Unsaturated Aliphatic Oxygenates with Ozone, *J. Atmos. Chem.*, 32, 205–232, <https://doi.org/10.1023/A:1006122000643>, 1999.
- Grosjean, D., and Williams II, E. L.: Environmental persistence of organic compounds estimated from structure-reactivity and linear free-energy relationships. Unsaturated Aliphatics, *Atmos. Environ. A, Gen. Top.*, 26, 1395–1405, [https://doi.org/10.1016/0960-1686\(92\)90124-4](https://doi.org/10.1016/0960-1686(92)90124-4), 1992.
- Grosjean, D., Grosjean, E., and Williams, E. L., II.: Rate constants for the gas-phase reactions of ozone with unsaturated alcohols, esters, and carbonyls, *Int. J. Chem. Kinet.*, 25, 783–794, <https://doi.org/10.1002/kin.550250909>, 1993a.
- Grosjean, D., Williams, E. L., II, and Grosjean, E.: Atmospheric chemistry of isoprene and of its carbonyl products, *Environ. Sci. Technol.*, 27, 830–840, <https://doi.org/10.1021/es00042a004>, 1993b.
- Grosjean, E., Grosjean, D., and Seinfeld, J. H.: Gas-Phase Reaction of Ozone with Trans-2-Hexenal, Trans-2-Hexenyl Acetate, Ethylvinyl Ketone, and 6-Methyl-5-Hepten-2-One, *Int. J. Chem. Kinet.*, 28, 373–382, [https://doi.org/10.1002/\(SICI\)1097-4601\(1996\)28:5<373::AID-KIN6>3.0.CO;2-S](https://doi.org/10.1002/(SICI)1097-4601(1996)28:5<373::AID-KIN6>3.0.CO;2-S), 1996.
- Groß, C. B. M., Dillon, T. J., Schuster, G., Lelieveld, J., and Crowley, J. N.: Direct Kinetic Study of OH and O₃ Formation in the Reaction of CH₃C(O)O₂ with HO₂, *J. Phys. Chem. A*, 118, 974–985, <https://doi.org/10.1021/jp412380z>, 2014.
- Guenther, A., Karl, T., Harley, P., Wiedinmyer, C., Palmer, P. I., and Geron, C.: Estimates of global terrestrial isoprene emissions using MEGAN (Model of Emissions of Gases and Aerosols from Nature), *Atmos. Chem. Phys.*, 6, 3181–3210, <https://doi.org/10.5194/acp-6-3181-2006>, 2006.
- Gutman, D., and Nelson, H. H.: Gas-Phase Reactions of the Vinyloxy Radical with O₂ and NO, *J. Phys. Chem.*, 87, 3902–3905, <https://doi.org/10.1021/j100243a023>, 1983.
- Hasson, A. S., Tyndall, G. S., Orlando, J. J.: A Product Yield Study of the Reaction of HO₂ Radicals with Ethyl Peroxy (C₂H₅O₂), Acetyl Peroxy (CH₃C(O)O₂), and Acetonyl Peroxy (CH₃C(O)CH₂O₂) Radicals, *J. Phys. Chem. A*, 108, 5979–5989, <https://doi.org/10.1021/jp048873t>, 2004.
- Hasson, A. S., Tyndall, G. S., Orlando, J. J., Singh, S., Hernandez, S. Q., Campbell, S., and Ibarra, Y.: Branching Ratios for the Reaction of Selected Carbonyl-Containing Peroxy

References

- Radicals with Hydroperoxy Radicals, *J. Phys. Chem. A*, **116**, 6264–6281, <https://doi.org/10.1021/jp211799c>, 2012.
- Hatakeyama, S., Kobayashi, H., and Akimoto, H.: Gas-Phase Oxidation of SO₂ in the Ozone-Olefine Reactions, *J. Phys. Chem.*, **88**, 4736–4739, <https://doi.org/10.1021/j150664a058>, 1984.
- Hatakeyama, S., Kobayashi, H., Lin, Z.-Y., Takagi, H., and Akimoto, H.: Mechanism for the Reaction of CH₂OO with SO₂, *J. Phys. Chem.*, **90**, 4131–4135, <https://doi.org/10.1021/j100408a059>, 1986.
- Hatch, L. E., Yokelson, R. J., Stockwell, C. E., Veres, P. R., Simpson, I. J., Blake, D. R., Orlando, J. J., and Barsanti, K. C.: Multi-instrument comparison and compilation of non-methane organic gas emissions from biomass burning and implications for smoke-derived secondary organic aerosol precursors, *Atmos. Chem. Phys.*, **17**, 1471–1489, <https://doi.org/10.5194/acp-17-1471-2017>, 2017.
- Holm, E. S., Adamsen, A. P. S., Feilberg, A., Schäfer, A., Løkke, M. M., Petersen, M. A.: Quality changes during storage of cooked and sliced meat products measured with PTR-MS and HS-GC-MS, *Meat Sci.*, **95**, 302–310, <https://doi.org/10.1016/j.meatsci.2013.04.046>, 2013.
- Honrath, R. E., Owen, R. C., Val Martín, M., Reid, J. S., Lapina, K., Fialho, P., Dziobak, M. P., Kleissl, J., Westphal, D. L.: Regional and hemispheric impacts of anthropogenic and biomass burning emissions on summertime CO and O₃ in the North Atlantic lower free troposphere, *J. Geophys. Res. Atmos.*, **109**, D24310, <https://doi.org/10.1029/2004JD005147>, 2004.
- Horie, O., and Moortgat, G. K.: Decomposition pathways of the excited Criegee intermediates in the ozonolysis of simple alkenes, *Atmos. Environ.*, **25A**, 1881–1896, [https://doi.org/10.1016/0960-1686\(91\)90271-8](https://doi.org/10.1016/0960-1686(91)90271-8), 1991.
- Horie, O., and Moortgat, G. K.: Reactions of CH₃C(O)O₂ radicals with CH₃O₂ and HO₂ between 263 and 333 K. A product study, *J. Chem. Soc., Faraday Trans.*, **88**, 3305–3312, <https://doi.org/10.1039/FT9928803305>, 1992.
- Horie, O., Neeb, P., and Moortgat, G. K.: The Reactions of the Criegee Intermediates CH₃CHOO in the Gas-Phase Ozonolysis of 2-Butene Isomers, *Int. J. Chem. Kinet.*, **29**, 461–468, [https://doi.org/10.1002/\(SICI\)1097-4601\(1997\)29:6<461::AID-KIN8>3.0.CO;2-S](https://doi.org/10.1002/(SICI)1097-4601(1997)29:6<461::AID-KIN8>3.0.CO;2-S), 1997.
- Hui, A. O., Fradet, M., Okumura, M., and Sander, S. P.: Temperature Dependence Study of the Kinetics and Product Yields of the HO₂ + CH₃C(O)O₂ Reaction by Direct Detection of OH and HO₂ Radicals Using 2f-IR Wavelength Modulation Spectroscopy, *J. Phys. Chem. A*, **123**, 3655–3671, <https://doi.org/10.1021/acs.jpca.9b00442>, 2019.
- Illmann, J. N., Patroescu-Klotz, I., and Wiesen, P.: Gas-phase reactivity of acyclic α,β-unsaturated carbonyls towards ozone, *Phys. Chem. Chem. Phys.*, **23**, 3455–3466, <https://doi.org/10.1039/D0CP05881E>, 2021a.
- Illmann, N., Gibilisco, R. G., Bejan, I. G., Patroescu-Klotz, I., and Wiesen, P.: Atmospheric oxidation of α,β-unsaturated ketones: kinetics and mechanism of the OH radical

- reaction, *Atmos. Chem. Phys.*, **21**, 13667–13686, <https://doi.org/10.5194/acp-21-13667-2021>, 2021b.
- Illmann, N., Patroescu-Klotz, I., and Wiesen, P.: Biomass burning plume chemistry: OH radical initiated oxidation of 3-penten-2-one and its main oxidation product 2-hydroxypropanal, *Atmos. Chem. Phys. Discuss.* [preprint], <https://doi.org/10.5194/acp-2021-575>, in review, 2021c.
- Illmann, N., Patroescu-Klotz, I., and Wiesen, P.: Biomass burning plume chemistry: OH-radical-initiated oxidation of 3-penten-2-one and its main oxidation product 2-hydroxypropanal, *Atmos. Chem. Phys.*, **21**, 18557–18572, <https://doi.org/10.5194/acp-21-18557-2021>, 2021d.
- Jaffe, D. A., and Wigder, N. L.: Ozone production from wildfires: A critical review, *Atmos. Environ.*, **51**, 1–10, <https://doi.org/10.1016/j.atmosenv.2011.11.063>, 2012.
- Jaffe, D., Chand, D., Hafner, W., Westerling, A., and Spracklen, D.: Influence of Fires on O₃ Concentrations in the Western U.S., *Environ. Sci. Technol.*, **42**, 5885–5891, <https://doi.org/10.1021/es800084k>, 2008.
- Jenkin, M. E., Cox, R. A., Emrich, M., and Moortgat, G. K.: Mechanisms of the Cl-atom-initiated Oxidation of Acetone and Hydroxyacetone in Air, *J. Chem. Soc. Faraday Trans.*, **89**, 2983–2991, <https://doi.org/10.1039/FT9938902983>, 1993.
- Jenkin, M. E., Hurley, M. D., and Wallington, T. J.: Investigation of the radical product channel of the CH₃C(O)O₂ + HO₂ reaction in the gas phase, *Phys. Chem. Chem. Phys.*, **9**, 3149–3162, <https://doi.org/10.1039/B702757E>, 2007.
- Jenkin, M. E., Young, J. C., and Rickard, A. R.: The MCM v3.3.1 degradation scheme for isoprene, *Atmos. Chem. Phys.*, **15**, 11433–11459, <https://doi.org/10.5194/acp-15-11433-2015>, 2015.
- Jenkin, M. E., Valorso, R., Aumont, B., Rickard, A. R., and Wallington, T. J.: Estimation of rate coefficients and branching ratios for gas-phase reactions of OH with aliphatic organic compounds for use in automated mechanism construction, *Atmos. Chem. Phys.*, **18**, 9297–9328, <https://doi.org/10.5194/acp-18-9297-2018>, 2018a.
- Jenkin, M. E., Valorso, R., Aumont, B., Rickard, A. R., and Wallington, T. J.: Estimation of rate coefficients and branching ratios for gas-phase reactions of OH with aromatic organic compounds for use in automated mechanism construction, *Atmos. Chem. Phys.*, **18**, 9329–9349, <https://doi.org/10.5194/acp-18-9329-2018>, 2018b.
- Jenkin, M. E., Valorso, R., Aumont, B., Newland, M. J., and Rickard, A. R.: Estimation of rate coefficients for the reactions of O₃ with unsaturated organic compounds for use in automated mechanism construction, *Atmos. Chem. Phys.*, **20**, 12921–12937, <https://doi.org/10.5194/acp-20-12921-2020>, 2020.
- Johnson, D., and Marston, G.: The gas-phase ozonolysis of unsaturated volatile organic compounds in the troposphere, *Chem. Soc. Rev.*, **37**, 699–716, <https://doi.org/10.1039/B704260B>, 2008.

References

- Kalalian, C., Roth, E., and Chakir, A.: Rate Coefficients for the Gas-Phase Reaction of Ozone with C5 and C6 Unsaturated Aldehydes, *Int. J. Chem. Kinet.*, 50, 47–56, <https://doi.org/10.1002/kin.21139>, 2018.
- Kanakidou, M., Seinfeld, J. H., Pandis, S. N., Barnes, I., Dentener, F. J., Facchini, M. C., Van Dingenen, R., Ervens, B., Nenes, A., Nielsen, C. J., Swietlicki, E., Putaud, J. P., Balkanski, Y., Fuzzi, S., Horth, J., Moortgat, G. K., Winterhalter, R., Myhre, C. E. L., Tsigaridis, K., Vignati, E., Stephanou, E. G., and Wilson, J.: Organic aerosol and global climate modelling: a review, *Atmos. Chem. Phys.*, 5, 1053–1123, <https://doi.org/10.5194/acp-5-1053-2005>, 2005.
- King, M. D., Canosa-Mas, C. E., and Wayne, R. P.: Frontier molecular orbital correlations for predicting rate constants between alkenes and the tropospheric oxidants NO₃, OH and O₃, *Phys. Chem. Chem. Phys.*, 1, 2231–2238, <https://doi.org/10.1039/A901192G>, 1999.
- Klotz, B., Graedler, F., Sørensen, S., Barnes, I., and Becker, K.-H.: A kinetic study of the atmospheric photolysis of α -dicarbonyls, *Int. J. Chem. Kinet.*, 33, 9–20, [https://doi.org/10.1002/1097-4601\(20010101\)33:1<9::AID-KIN2>3.0.CO;2-V](https://doi.org/10.1002/1097-4601(20010101)33:1<9::AID-KIN2>3.0.CO;2-V), 2001.
- Knap, H. C., and Jørgensen, S.: Rapid Hydrogen Shift Reactions in Acyl Peroxy Radicals, *J. Phys. Chem. A*, 121, 1470–1479, <https://doi.org/10.1021/acs.jpca.6b12787>, 2017.
- Kroll, J. H., Donahue, N. M., Cee, V. J., Demerjian, K. L., and Anderson, J. G.: Gas-Phase Ozonolysis of Alkenes: Formation of OH from Anti Carbonyl Oxides, *J. Am. Chem. Soc.*, 124, 8518–8519, <https://doi.org/10.1021/ja0266060>, 2002.
- Kwok, E. S. C., and Atkinson, R.: Estimation of hydroxyl radical reaction rate constants for gas-phase organic compounds using a structure-reactivity relationship: An update, *Atmos. Environ.*, 29, 1685–1695, [https://doi.org/10.1016/1352-2310\(95\)00069-B](https://doi.org/10.1016/1352-2310(95)00069-B), 1995.
- Lee, J., and Bozzelli, J. W.: Thermochemical and Kinetic Analysis of the Formyl Methyl Radical + O₂ Reaction System, *J. Phys. Chem. A*, 107, 3778–3791, <https://doi.org/10.1021/jp030001o>, 2003.
- Le Crâne, J.-P., Villenave, E., Hurley, M. D., Wallington, T. J., and Ball, J. C.: Atmospheric Chemistry of Propionaldehyde: Kinetics and Mechanisms of Reactions with OH Radicals and Cl Atoms, UV Spectrum, and Self-Reaction Kinetics of CH₃CH₂C(O)O₂ Radicals at 298 K, *J. Phys. Chem. A*, 109, 11837–11850, <https://doi.org/10.1021/jp0519868>, 2005.
- Li, W., Dan, G., Chen, M., Wang, Z., Zhao, Y., Wang, F., Li, F., Tong, S., and Ge, M.: The gas-phase reaction kinetics of different structure of unsaturated alcohols and ketones with O₃, *Atmos. Environ.*, 254, 118394, <https://doi.org/10.1016/j.atmosenv.2021.118394>, 2021.
- Logan, J. A.: Tropospheric Ozone: Seasonal Behavior, Trends, and Anthropogenic Influence, *J. Geophys. Res.*, 90, 10463–10482, <https://doi.org/10.1029/JD090iD06p10463>, 1985.
- Lorenz, K., Rhasa, D., Zellner, R., and Fritz, B.: Laser Photolysis – LIF Kinetic Studies of the Reactions of CH₃O and CH₂CHO with O₂ between 300 and 500 K, *Ber. Bunsenges. Phys. Chem.*, 89, 341–342, <https://doi.org/10.1002/bbpc.19850890346>, 1985.

- Ma, S., Barnes, I., and Becker, K. H.: Atmospheric Degradation of Glycidaldehyde: Photolysis and Reaction with OH Radicals, *Environ. Sci. Technol.*, 32, 3515–3521, <https://doi.org/10.1021/es9804159>, 1998.
- Magneron, I., Mellouki, A., Le Bras, G., Moortgat, G. K., Horowitz, A., Wirtz, K.: Photolysis and OH-Initiated Oxidation of Glycolaldehyde under Atmospheric Conditions, *J. Phys. Chem. A*, 109, 4552–4561, <https://doi.org/10.1021/jp044346y>, 2005.
- Maricq, M. M., and Szente, J. J.: The $\text{CH}_3\text{C}(\text{O})\text{O}_2$ Radical. Its UV Spectrum, Self-Reaction Kinetics, and Reaction with CH_3O_2 , *J. Phys. Chem.*, 100, 4506–4513, <https://doi.org/10.1021/jp9533234>, 1996.
- Martinez, R. I., and Herron, J. T.: Stopped-Flow Studies of the Mechanisms of Ozone-Alkene Reactions in the Gas Phase: *trans*-2-Butene, *J. Phys. Chem.*, 92, 4644–4648, <https://doi.org/10.1021/j100327a017>, 1988.
- Matsunaga, A., and Ziemann, P. J.: Yields of β -hydroxynitrates, dihydroxynitrates, and trihydroxynitrates formed from OH radical-initiated reactions of 2-methyl-1-alkenes, *Proc. Natl. Acad. Sci. USA*, 107, 6664–6669, <https://doi.org/10.1073/pnas.0910585107>, 2010.
- Mauzerall, D. L., Logan, J. A., Jacob, D. J., Anderson, B. E.; Blake, D. R.; Bradshaw, J. D.; Heikes, B.; Sachse, G. W.; Singh, H.; Talbot, B.: Photochemistry in biomass burning plumes and implications for tropospheric ozone over the tropical South Atlantic, *J. Geophys. Res. Atmos.*, 103, 8401–8423, <https://doi.org/10.1029/97JD02612>, 1998.
- McGillen, M. R., Archibald, A. T., Carey, T., Leather, K. E., Shallcross, D. E., Wenger, J. C., and Percival, C. J.: Structure–activity relationship (SAR) for the prediction of gas-phase ozonolysis rate coefficients: an extension towards heteroatomic unsaturated species, *Phys. Chem. Chem. Phys.*, 13, 2842–2849, <https://doi.org/10.1039/C0CP01732A>, 2011a.
- McGillen, M. R., Ghalaieny, M., and Percival, C. J.: Determination of gas-phase ozonolysis rate coefficients of C_{8-14} terminal alkenes at elevated temperatures using the relative rate method, *Phys. Chem. Chem. Phys.*, 13, 10965–10969, <https://doi.org/10.1039/C0CP02643C>, 2011b.
- Mellouki, A., Le Bras, G., and Sidebottom, H.: Kinetics and Mechanisms of the Oxidation of Oxygenated Organic Compounds in the Gas Phase, *Chem. Rev.*, 103, 5077–5096, <https://doi.org/10.1021/cr020526x>, 2003.
- Mellouki, A., Wallington, T. J., and Chen, J.: Atmospheric Chemistry of Oxygenated Volatile Organic Compounds: Impacts on Air Quality and Climate, *Chem. Rev.*, 115, 3984–4014, <https://doi.org/10.1021/cr500549n>, 2015.
- Mellouki, A., Ammann, M., Cox, R. A., Crowley, J. N., Herrmann, H., Jenkin, M. E., McNeill, V. F., Troe, J., and Wallington, T. J.: Evaluated kinetic and photochemical data for atmospheric chemistry: volume VIII – gas-phase reactions of organic species with four, or more, carbon atoms ($\geq \text{C}_4$), *Atmos. Chem. Phys.*, 21, 4797–4808, <https://doi.org/10.5194/acp-21-4797-2021>, 2021.

References

- Méreau, R., Rayez, M.-T., Rayez, J.-C., Caralp, F., Lesclaux, R.: Theoretical study on the atmospheric fate of carbonyl radicals: kinetics of decomposition reactions, *Phys. Chem. Chem. Phys.*, **3**, 4712–4717, <https://doi.org/10.1039/B105824J>, 2001.
- Moortgat, G., Veyret, B., and Lesclaux, R.: Absorption spectrum and kinetics of reactions of the acetylperoxy radical, *J. Phys. Chem.*, **93**, 2362–2368, <https://doi.org/10.1021/j100343a032>, 1989.
- Mund, C., Fockenberg, C., and Zellner, R.: LIF Spectra of *n*-Propoxy Radicals and Kinetics of their Reactions with O₂ and NO₂, *Ber. Bunsenges. Phys. Chem.*, **102**, 709–715, <https://doi.org/10.1002/bbpc.19981020502>, 1998.
- Müller, M., Graus, M., Wisthaler, A., Hansel, A., Metzger, A., Dommen, J., and Baltensperger, U.: Analysis of high mass resolution PTR-TOF mass spectra from 1,3,5-trimethylbenzene (TMB) environmental chamber experiments, *Atmos. Chem. Phys.*, **12**, 829–843, <https://doi.org/10.5194/acp-12-829-2012>, 2012.
- Müller, M., Anderson, B. E., Beyersdorf, A. J., Crawford, J. H., Diskin, G. S., Eichler, P., Fried, A., Keutsch, F. N., Mikoviny, T., Thornhill, K. L., Walega, J. G., Weinheimer, A. J., Yang, M., Yokelson, R. J., and Wisthaler, A.: In situ measurements and modeling of reactive trace gases in a small biomass burning plume, *Atmos. Chem. Phys.*, **16**, 3813–3824, <https://doi.org/10.5194/acp-16-3813-2016>, 2016.
- Nakanaga, T., Kondo, S., and Saëki, S.: Infrared band intensities of formaldehyde and formaldehyde-d₂, *J. Chem. Phys.*, **76**, 3860–3865, <https://doi.org/10.1063/1.443527>, 1982.
- Neeb, P., Horie, O., and Moortgat, G. K.: The nature of the transitory product in the gas-phase ozonolysis of ethene, *Chem. Phys. Lett.*, **246**, 150–156, [https://doi.org/10.1016/0009-2614\(95\)01073-I](https://doi.org/10.1016/0009-2614(95)01073-I), 1995.
- Neeb, P., Horie, O., and Moortgat, G. K.: Gas-Phase Ozonolysis of Ethene in the Presence of Hydroxylic Compounds, *Int. J. Chem. Kinet.*, **28**, 721–730, [https://doi.org/10.1002/\(SICI\)1097-4601\(1996\)28:10<721::AID-KIN2>3.0.CO;2-P](https://doi.org/10.1002/(SICI)1097-4601(1996)28:10<721::AID-KIN2>3.0.CO;2-P), 1996.
- Neeb, P., Sauer, F., Horie, O., and Moortgat, G. K.: Formation of hydroxymethyl hydroperoxide and formic acid in alkene ozonolysis in the presence of water vapour, *Atmos. Environ.*, **31**, 1417–1423, [https://doi.org/10.1016/S1352-2310\(96\)00322-6](https://doi.org/10.1016/S1352-2310(96)00322-6), 1997.
- Neeb, P., Horie, O., and Moortgat, G. K.: The Ethene–Ozone Reaction in the Gas Phase, *J. Phys. Chem. A*, **102**, 6778–6785, <https://doi.org/10.1021/jp981264z>, 1998.
- Neeb, P., Kolloff, A., Koch, S., and Moortgat, G. K.: Rate constants for the reactions of methylvinyl ketone, methacrolein, methacrylic acid, and acrylic acid with ozone, *Int. J. Chem. Kinet.*, **30**, 769–776, [https://doi.org/10.1002/\(SICI\)1097-4601\(1998\)30:10<769::AID-KIN9>3.0.CO;2-T](https://doi.org/10.1002/(SICI)1097-4601(1998)30:10<769::AID-KIN9>3.0.CO;2-T), 1999.
- Nguyen, T. L., Winterhalter, R., Moortgat, G., Kanawati, B., Peeters, J., and Vereecken, L.: The gas-phase ozonolysis of β -caryophyllene (C₁₅H₂₄). Part II: A theoretical study, *Phys. Chem. Chem. Phys.*, **11**, 4173–4183, <https://doi.org/10.1039/B817913A>, 2009a.

- Nguyen, T. L., Peeters, J., and Vereecken, L.: Theoretical study of the gas-phase ozonolysis of β -pinene ($C_{10}H_{16}$), *Phys. Chem. Chem. Phys.*, **11**, 5643–5656, <https://doi.org/10.1039/B822984H>, 2009b.
- Nguyen, T. B., Tyndall, G. S., Crouse, J. D., Teng, A. P., Bates, K. H., Schwantes, R. H., Coggon, M. M., Zhang, L., Feiner, P., Miller, D. O., Skog, K. M., Rivera-Rios, J. C., Dorris, M., Olson, K. F., Koss, A., Wild, R. J., Brown, S. S., Goldstein, A. H., de Gouw, J. A., Brune, W. H., Keutsch, F. N., Seinfeld, J. H., and Wennberg, P. O.: Atmospheric fates of Criegee intermediates in the ozonolysis of isoprene, *Phys. Chem. Chem. Phys.*, **18**, 10241–10254, <https://doi.org/10.1039/C6CP00053C>, 2016.
- Niki, H., Maker, P. D., Savage, C. M., and Breitenbach, L. P.: Fourier transform IR spectroscopic observation of propylene ozonide in the gas phase reaction of ozone–cis-2-butene–formaldehyde, *Chem. Phys. Lett.*, **46**, 327–330, [https://doi.org/10.1016/0009-2614\(77\)85273-1](https://doi.org/10.1016/0009-2614(77)85273-1), 1977.
- Niki, H., Maker, P. D., Savage, C. M., and Breitenbach, L. P.: FTIR Study of the Kinetics and Mechanism for Cl-Atom-Initiated Reactions of Acetaldehyde, *J. Phys. Chem.*, **89**, 588–591, <https://doi.org/10.1021/j100250a008>, 1985.
- Niki, H., Maker, P. D., Savage, C. M., Breitenbach, L. P., and Hurley, M. D.: FTIR spectroscopic study of the mechanism for the gas-phase reaction between ozone and tetramethylethylene, *J. Phys. Chem.*, **91**, 941–946, <https://doi.org/10.1021/j100288a035>, 1987a.
- Niki, H., Maker, P. D., Savage, C. M., Hurley, M. D.: Fourier Transform Infrared Study of the Kinetics and Mechanisms for the Cl-Atom and HO-Radical-Initiated Oxidation of Glycolaldehyde, *J. Phys. Chem.*, **91**, 2174–2178, <https://doi.org/10.1021/j100292a038>, 1987b.
- Noda, J., Hallquist, M., Langer, S., and Ljungström, E.: Products from the gas-phase reaction of some unsaturated alcohols with nitrate radicals, *Phys. Chem. Chem. Phys.*, **2**, 2555–2564, <https://doi.org/10.1039/B000251H>, 2000.
- Noell, A. C., Alconcel, L. S., Robichaud, D. J., Okumura, M., and Sander, S. P.: Near-Infrared Kinetic Spectroscopy of the HO_2 and $C_2H_5O_2$ Self-reactions and Cross-Reactions, *J. Phys. Chem. A*, **114**, 6983–6995, <https://doi.org/10.1021/jp912129j>, 2010.
- Notario, A., Le Bras, G., and Mellouki, A.: Absolute Rate Constants for the Reactions of Cl Atoms with a Series of Esters, *J. Phys. Chem. A*, **102**, 3112–3117, <https://doi.org/10.1021/jp980416n>, 1998.
- O'Dwyer, M. A., Carey, T. J., Healy, R. M., Wenger, J. C., Picquet-Varrault, B. and Doussin, J. F.: The Gas-phase Ozonolysis of 1-Penten-3-ol, (Z)-2-Penten-1-ol and 1-Penten-3-one: Kinetics, Products and Secondary Organic Aerosol Formation, *Z. Phys. Chem.*, **224**, 1059–1080, <https://doi.org/10.1524/zpch.2010.6141>, 2010.
- Orlando, J. J., and Tyndall, G. S.: Laboratory studies of organic peroxy radical chemistry: an overview with emphasis on recent issues of atmospheric significance, *Chem. Soc. Rev.*, **41**, 6294–6317, <https://doi.org/10.1039/C2CS35166H>, 2012.

References

- Orlando, J. J., Tyndall, G. S., Vereecken, L., and Peeters, J.: The Atmospheric Chemistry of the Acetonyl Radical, *J. Phys. Chem. A*, 104, 11578–11588, <https://doi.org/10.1021/jp0026991>, 2000.
- Orlando, J. J., Tyndall, G. S., and Wallington, T. J.: The Atmospheric Chemistry of Alkoxy Radicals, *Chem. Rev.*, 103, 4657–4689, <https://doi.org/10.1021/cr020527p>, 2003.
- Paulot, F., Crounse, J. D., Kjaergaard, H. G., Kroll, J. H., Seinfeld, J. H., and Wennberg, P. O.: Isoprene photooxidation: new insights into the production of acids and organic nitrates, *Atmos. Chem. Phys.*, 9, 1479–1501, <https://doi.org/10.5194/acp-9-1479-2009>, 2009.
- Pfrang, C., King, M. D., Canosa-Mas, C. E., and Wayne, R. P.: Correlations for gas-phase reactions of NO₃, OH and O₃ with alkenes: An update, *Atmos. Environ.*, 40, 1170–1179, <https://doi.org/10.1016/j.atmosenv.2005.10.019>, 2006a.
- Pfrang, C., King, M. D., Canosa-Mas, C. E., and Wayne, R. P.: Structure–activity relations (SARs) for gas-phase reactions of NO₃, OH and O₃ with alkenes: An update, *Atmos. Environ.*, 40, 1180–1186, <https://doi.org/10.1016/j.atmosenv.2005.09.080>, 2006b.
- Pfrang, C., King, M. D., Canosa-Mas, C. E., Flugge, M., and Wayne, R. P.: Gas-phase rate coefficients for the reactions of NO₃, OH and O₃ with α,β -unsaturated esters and ketones: Structure–activity relations (SARs), *Atmos. Environ.*, 41, 1792–1802, <https://doi.org/10.1016/j.atmosenv.2006.11.026>, 2007.
- Pfrang, C., King, M. D., Braeckvelt, M., Canosa-Mas, C. E., and Wayne, R. P.: Gas-phase rate coefficients for reactions of NO₃, OH, O₃ and O(³P) with unsaturated alcohols and ethers: Correlations and structure–activity relations (SARs), *Atmos. Environ.*, 42, 3018–3034, <https://doi.org/10.1016/j.atmosenv.2007.12.046>, 2008.
- Picquet-Varrault, B., Doussin, J.-F., Durand-Jolibois, R., Pirali, O., and Carlier, P.: Kinetic and Mechanistic Study of the Atmospheric Oxidation by OH Radicals of Allyl Acetate, *Environ. Sci. Technol.*, 36, 4081–4086, <https://doi.org/10.1021/es0200138>, 2002.
- Picquet-Varrault, B., Suarez-Bertoa, R., Duncianu, M., Cazaunau, M., Pangui, E., David, M., and Doussin, J.-F.: Photolysis and oxidation by OH radicals of two carbonyl nitrates: 4-nitrooxy-2-butanone and 5-nitrooxy-2-pentanone, *Atmos. Chem. Phys.*, 20, 487–498, <https://doi.org/10.5194/acp-20-487-2020>, 2020.
- Praske, E., Crounse, J. D., Bates, K. H., Kurtén, T., Kjaergaard, H. G., and Wennberg, P. O.: Atmospheric Fate of Methyl Vinyl Ketone: Peroxy Radical Reactions with NO and HO₂, *J. Phys. Chem. A*, 119, 4562–4572, <https://doi.org/10.1021/jp5107058>, 2015.
- Profeta, L. T. M., Sams, R. L., and Johnson, T. J.: Quantitative Infrared Intensity Studies of Vapor-Phase Glyoxal, Methylglyoxal, and 2,3-Butanedione (Diacetyl), with Vibrational Assignments, *J. Phys. Chem. A*, 115, 9886–9900, <https://doi.org/10.1021/jp204532x>, 2011.
- Ren, Y., Grosselin, B., Daële, V., and Mellouki, A.: Investigation of the reaction of ozone with isoprene, methacrolein and methyl vinyl ketone using the HELIOS chamber, *Faraday Discuss.*, 200, 289–311, <https://doi.org/10.1039/C7FD00014F>, 2017.

- Ren, Y., Cai, M., Daële, V., and Mellouki, A.: Rate coefficients for the reactions of OH radical and ozone with a series of unsaturated esters, *Atmos. Environ.*, 200, 243–253, <https://doi.org/10.1016/j.atmosenv.2018.12.017>, 2019.
- Roehl, C. M., Bauer, D., and Moortgat, G. K.: Absorption Spectrum and Kinetics of the Acetylperoxy Radical, *J. Phys. Chem.*, 100, 4038–4047, <https://doi.org/10.1021/jp9526298>, 1996.
- Rossiter, B. E., and Swingle, N. M.: Asymmetric conjugate addition, *Chem. Rev.*, 92, 771–806, <https://doi.org/10.1021/cr00013a002>, 1992.
- Sato, K., Klotz, B., Taketsuga, T., and Takaynagi, T.: Kinetic measurements for the reactions of ozone with crotonaldehyde and its methyl derivatives and calculations of transition-state theory, *Phys. Chem. Chem. Phys.*, 6, 3696–3976, <https://doi.org/10.1039/B402496F>, 2004.
- Sheps, L., Rotavera, B., Eskola, A. J., Osborn, D. L., Taatjes, C. A., Au, K., Shallcross, D. E., Khan, M. A. H., and Percival, C. J.: The reaction of Criegee intermediate CH₂OO with water dimer: primary products and atmospheric impact, *Phys. Chem. Chem. Phys.*, 19, 21970–21979, <https://doi.org/10.1039/C7CP03265J>, 2017.
- Siegel, H., and Eggersdorfer, M.: Ketones, *Ullmann's Encyclopedia of Industrial Chemistry*, Wiley-VCH Verlag, Weinheim, https://doi.org/10.1002/14356007.a15_077, 2000.
- Sifniades, S., Levy, A. B., and Bahl, H.: Acetone, in: *Ullmann's Encyclopedia of Industrial Chemistry*, Wiley-VCH Verlag, Weinheim, https://doi.org/10.1002/14356007.a01_079.pub3, 2011.
- Smith, I. W. M., and Ravishankara, A. R.: Role of Hydrogen-Bonded Intermediates in the Bimolecular Reactions of the Hydroxyl Radical, *J. Phys. Chem. A*, 106, 4798–4807, <https://doi.org/10.1021/jp014234w>, 2002.
- Španěl, P., Diskin, A. M., Wang, T., Smith, D.: A SIFT study of reactions of H₃O⁺, NO⁺, and O₂⁺ with hydrogen peroxide and peroxyacetic acid, *Int. J. Mass Spectrom.*, 228, 269–283, [https://doi.org/10.1016/S1387-3806\(03\)00214-8](https://doi.org/10.1016/S1387-3806(03)00214-8), 2003.
- Spittler, M.: Untersuchungen zur troposphärischen Oxidation von Limonen: Produktanalysen, Aerosolbildung und Photolyse von Produkten, Ph.D. thesis, Bergische Universität Wuppertal, Germany, 2001.
- Stewart, D. J., Altabrok, S. H., Lockhart, J. P., Mohamed, O. M., Nutt, D. R., Pfrang, C., and Marston, G.: The kinetics of the gas-phase reactions of selected monoterpenes and cyclo-alkenes with ozone and the NO₃ radical, *Atmos. Environ.*, 70, 227–235, <https://doi.org/10.1016/j.atmosenv.2013.01.036>, 2013.
- Stone, D., Blitz, M., Daubney, L., Howes, N. U. M., and Seakins, P.: Kinetics of CH₂OO reactions with SO₂, NO₂, NO, H₂O and CH₃CHO as a function of pressure, *Phys. Chem. Chem. Phys.*, 16, 1139–1149, <https://doi.org/10.1039/C3CP54391A>, 2014.
- Stöner, C., Derstroff, B., Klüpfel, T., Crowley, J. N., and Williams, J.: Glyoxal measurement with a proton transfer reaction time of flight mass spectrometer (PTR-TOF-MS): characterization and calibration, *J. Mass. Spectrom.*, 52, 30–35, <https://doi.org/10.1002/jms.3893>, 2017.

References

- Suarez-Bertoa, R., Picquet-Varrault, B., Tamas, W., Pangui, E., and Doussin, J.-F.: Atmospheric Fate of a Series of Carbonyl Nitrates: Photolysis Frequencies and OH-Oxidation Rate Constants, *Environ. Sci. Technol.*, **46**, 12502–12509, <https://doi.org/10.1021/es302613x>, 2012.
- Sulbaek Andersen, M. P., Hurley, M. D., Wallington, T. J., Ball, J. C., Martin, J. W., Ellis, D. A., and Mabury, S. A.: Atmospheric chemistry of C₂F₅CHO: mechanism of the C₂F₅(O)O₂ + HO₂ reaction, *Chem. Phys. Lett.*, **381**, 14–21, <https://doi.org/10.1016/j.cplett.2003.09.085>, 2003.
- Taft, R. W.: Polar and Steric Substituent Constants for Aliphatic and o-Benzoate Groups from Rates of Esterification and Hydrolysis of Esters, *J. Am. Chem. Soc.*, **74**, 3120–3128, <https://doi.org/10.1021/ja01132a049>, 1952.
- Talukdar, R. K., Zhu, L., Feierabend, K. J., and Burkholder, J. B.: Rate coefficients for the reaction of methylglyoxal (CH₃COCHO) with OH and NO₃ and glyoxal (HCO)₂ with NO₃, *Atmos. Chem. Phys.*, **11**, 10837–10851, <https://doi.org/10.5194/acp-11-10837-2011>, 2011.
- Takahashi, H., Kobayashi, Y., and Kaneko, N.: Conformational studies of DL-lactaldehyde by ¹H-NMR, Raman and i.r. spectroscopy, *Spectrochim. Acta A Mol. Spectrosc.*, **39**, 569–572, [https://doi.org/10.1016/0584-8539\(83\)80108-1](https://doi.org/10.1016/0584-8539(83)80108-1), 1983.
- Taylor, W. D., Allston, T. D., Moscato, M. J., Fazekas, G. B., Kozlowski, R., and Takacs, G. A.: Atmospheric photodissociation lifetimes for nitromethane, methyl nitrite, and methyl nitrate, *Int. J. Chem. Kinet.*, **12**, 231–240, <https://doi.org/10.1002/kin.550120404>, 1980.
- Thomas, W.: Mechanistische und kinetische Studie zur Ozonolyse von Ethen in der Gasphase, Ph.D. thesis, Bergische Universität Wuppertal, Germany, 1997.
- Treacy, J., Hag, M. E., O'Farrell, D., and Sidebottom, H.: Reactions of Ozone with Unsaturated Organic Compounds, *Ber. Bunsenges. Phys. Chem.*, **96**, 422–427, <https://doi.org/10.1002/bbpc.19920960337>, 1992.
- Tuazon, E. C., and Atkinson, R.: A Product Study of the Gas-Phase Reaction of Methyl Vinyl Ketone with the OH Radical in the Presence of NO_x, *Int. J. Chem. Kinet.*, **21**, 1141–1152, <https://doi.org/10.1002/kin.550211207>, 1989.
- Tuazon, E. C., MacLeod, H., Atkinson R., and Carter, W. P. L.: α-Dicarbonyl yields from the NO_x-air photooxidation of a series of aromatic hydrocarbons in air, *Environ. Sci. Technol.*, **20**, 383–387, <https://doi.org/10.1021/es00146a010>, 1986.
- Tuazon, E. C., Aschmann, S. M., Arey, J., and Atkinson, R.: Products of the Gas-Phase Reactions of O₃ with a Series of Methyl-Substituted Ethenes, *Environ. Sci. Technol.*, **31**, 3004–3009, <https://doi.org/10.1021/es970258y>, 1997.
- Turnipseed, A. A., Andersen, P. C., Williford, C. J., Ennis, C. A., and Birks, J. W.: Use of a heated graphite scrubber as a means of reducing interferences in UV-absorbance measurements of atmospheric ozone, *Atmos. Meas. Tech.*, **10**, 2253–2269, <https://doi.org/10.5194/amt-10-2253-2017>, 2017.

- Tyndall, G. S., Cox, R. A., Granier, C., Lesclaux, R., Moortgat, G. K., Pilling, M. J., Ravishankara, A. R., and Wallington, T. J.: Atmospheric chemistry of small organic peroxy radicals, *J. Geophys. Res.*, 106, 12157, <https://doi.org/10.1029/2000JD900746>, 2001.
- US EPA, 2021. Estimation Programs Interface Suite™ for Microsoft® Windows, v 4.11. United States Environmental Protection Agency, Washington, DC, USA.
- Vereecken, L. and Nozière, B.: H migration in peroxy radicals under atmospheric conditions, *Atmos. Chem. Phys.*, 20, 7429–7458, <https://doi.org/10.5194/acp-20-7429-2020>, 2020.
- Vereecken, L., and Peeters, J.: Decomposition of substituted alkoxy radicals – part I: a generalized structure-activity relationship for reaction barrier heights, *Phys. Chem. Chem. Phys.*, 11, 9062–9074, <https://doi.org/10.1039/B909712K>, 2009.
- Vereecken, L., Harder, H., and Novelli, A.: The reaction of Criegee intermediates with NO, RO₂, and SO₂, and their fate in the atmosphere, *Phys. Chem. Chem. Phys.*, 14, 14682–14695, <https://doi.org/10.1039/C2CP42300F>, 2012.
- Vereecken, L., Novelli, A., and Taraborrelli, D.: Unimolecular decay strongly limits the atmospheric impact of Criegee intermediates, *Phys. Chem. Chem. Phys.*, 19, 31599–31612, <https://doi.org/10.1039/C7CP05541B>, 2017.
- Veyret, B., Lesclaux, R., Rayez, M.-T., Rayez, J.-C., Cox, R. A., and Moortgat, G. K.: Kinetic and Mechanism of the Photooxidation of Formaldehyde. 1. Flash Photolysis Study, *J. Phys. Chem.*, 93, 2368–2374, <https://doi.org/10.1021/j100343a033>, 1989.
- Vyskocil A., Viau C., and Lamy S.: Peroxyacetyl nitrate: review of toxicity, *Hum. Exp. Toxicol.*, 17, 212–220, <https://doi.org/10.1177/096032719801700403>, 1998.
- Wallington, T. J.: Fourier-transform infrared product study of the reaction of CH₃O₂ + HO₂ over the pressure range 15–700 torr at 295 K, *J. Chem. Soc., Faraday Trans.*, 87, 2379–2382, <https://doi.org/10.1039/FT9918702379>, 1991.
- Wallington, T. J., and Japar, S. M.: FTIR product study of the reaction of C₂H₅O₂ + HO₂ in air at 295 K, *Chem. Phys. Lett.*, 166, 495–499, [https://doi.org/10.1016/0009-2614\(90\)87140-M](https://doi.org/10.1016/0009-2614(90)87140-M), 1990.
- Wang, J., Zhou, L., Wang, W., and Ge, M.: Gas-phase reaction of two unsaturated ketones with atomic Cl and O₃: kinetics and products, *Phys. Chem. Chem. Phys.*, 17, 12000–12012, <https://doi.org/10.1039/C4CP05461J>, 2015.
- Wang, X., Sun, J., Bao, L., Mei, Q., Wie, B., An, Z., Xie, J., and He, M.: Mechanisms and Kinetic Parameters for the Gas-Phase Reactions of 3-Methyl-3-buten-2-one and 3-Methyl-3-penten-2-one with Ozone, *J. Phys. Chem. A*, 123, 2745–2755, <https://doi.org/10.1021/acs.jpca.8b12025>, 2019.
- Wang, X., Hong, P., Kiss, A. A., Wang, Q., Li, L., Wang, H., and Qiu, T.: From Batch to Continuous Sustainable Production of 3-Methyl-3-penten-2-one for Synthetic Ketone Fragrances, *ACS Sustainable Chem. Eng.*, 8, 17201–17214, <https://doi.org/10.1021/acssuschemeng.0c05908>, 2020.
- Weidman, J. D., Allen, R. T., Moore, K. B. III, and Schaefer, H. F. III: High-level theoretical characterization of the vinoxy radical (CH₂CHO) + O₂ reaction, *J. Chem. Phys.*, 148, 184308, <https://doi.org/10.1063/1.5026295>, 2018.

References

- Wennberg, P. O., Bates, K. H., Crouse, J. D., Dodson, L. G., McVay, R. C., Mertens, L. A., Nguyen, T. B., Praske, E., Schwantes, R. H., Smarte, M. D., St Clair, J. M., Teng, A. P., Zhang, X., and Seinfeld, J. H.: Gas-Phase Reactions of Isoprene and Its Major Oxidation Products, *Chem. Rev.*, 118, 3337–3390, <https://doi.org/10.1021/acs.chemrev.7b00439>, 2018.
- Williams, E. J., Fehsenfeld, F. C., Jobson, B. T., Kuster, W. C., Goldan, P. D., Stutz, J., and McClenny, W. A.: Comparison of Ultraviolet Absorbance, Chemiluminescence, and DOAS Instruments for Ambient Ozone Monitoring, *Environ. Sci. Technol.*, 40, 5755–5762, <https://doi.org/10.1021/es0523542>, 2006.
- Wingenter, O. W., Kubo, M. K., Blake, N. J., Smith Jr., T. W., Blake, D. R., and Rowland, F. S.: Hydrocarbon and halocarbon measurements as photochemical and dynamical indicators of atmospheric hydroxyl, atomic chlorine, and vertical mixing obtained during Lagrangian flights, *J. Geophys. Res.*, 101, 4331–4340, <https://doi.org/10.1029/95JD02457>, 1996.
- Winiberg, F. A. F., Dillon, T. J., Orr, S. C., Groß, C. B. M., Bejan, I., Brumby, C. A., Evans, M. J., Smith, S. C., Heard, D. E., and Seakins, P. W.: Direct measurements of OH and other product yields from the HO₂ + CH₃C(O)O₂ reaction, *Atmos. Chem. Phys.*, 16, 4023–4042, <https://doi.org/10.5194/acp-16-4023-2016>, 2016.
- Winterhalter, R., Herrmann, F., Kanawati, B., Nguyen, T. L., Peeters, J., Vereecken, L., and Moortgat, G. K.: The gas-phase ozonolysis of of β-caryophyllene (C₁₅H₂₄). Part I: an experimental study, *Phys. Chem. Chem. Phys.*, 11, 4152–4172, <https://doi.org/10.1039/B817824K>, 2009.
- Yokelson, R. J., Crouse, J. D., DeCarlo, P. F., Karl, T., Urbanski, S., Atlas, E., Campos, T., Shinozuka, Y., Kapustin, V., Clarke, A. D., Weinheimer, A., Knapp, D. J., Montzka, D. D., Holloway, J., Weibring, P., Flocke, F., Zheng, W., Toohey, D., Wennberg, P. O., Wiedinmyer, C., Mauldin, L., Fried, A., Richter, D., Walega, J., Jimenez, J. L., Adachi, K., Buseck, P. R., Hall, S. R., and Shetter, R.: Emissions from biomass burning in the Yucatan, *Atmos. Chem. Phys.*, 9, 5785–5812, <https://doi.org/10.5194/acp-9-5785-2009>, 2009.
- Zhu, L., and Johnston, G.: Kinetics and Products of the Reaction of the Vinyloxy Radical with O₂, *J. Phys. Chem.*, 99, 15114–15119, <https://doi.org/10.1021/j100041a030>, 1995.